

A Thesis Submitted for the Degree of PhD at the University of Warwick

Permanent WRAP URL:

<http://wrap.warwick.ac.uk/162333>

Copyright and reuse:

This thesis is made available online and is protected by original copyright.

Please scroll down to view the document itself.

Please refer to the repository record for this item for information to help you to cite it.

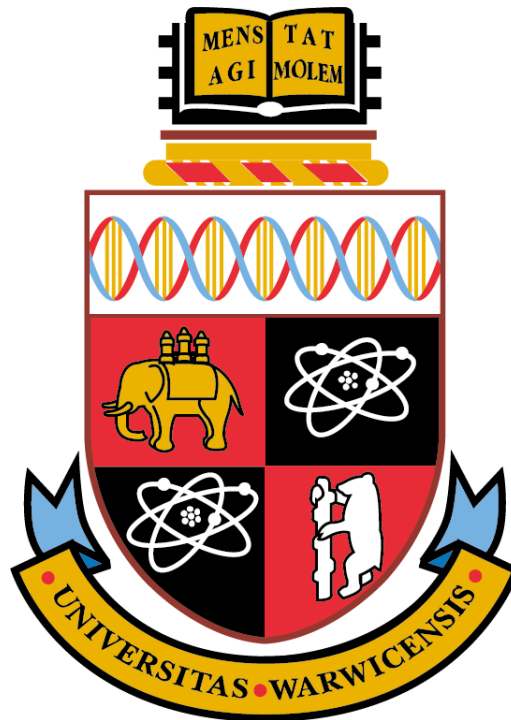
Our policy information is available from the repository home page.

For more information, please contact the WRAP Team at: wrap@warwick.ac.uk

Functional Organisation of the human kinetochore and roles of the Ska complex

submitted for qualification of Doctor of Philosophy in
Interdisciplinary Biomedical Research

University of Warwick



by Tsvetelina Germanova

Division of Biomedical Sciences, Warwick Medical School, University of Warwick

**Supervisors: Prof. Andrew McAinsh and Prof. Nigel
Burroughs**

March, 2021

Dedication

I dedicate this thesis to my family, my boyfriend and cat whose continuous support has made this work possible. I want to thank my grandparents: Violetka Qneva and Tsvetan Qnev, for supporting my choice to study biology even though I have been prepared to be a mathematician from young age. I want to thank my parents: Emiliya Germanova and Emil Germanov for their love, continuous support and for being my friends throughout the years. Without their support and believe in me, it would not have been possible for me to pursue a Bachelors degree in Biology, let alone a PhD degree. I want to also thank my boyfriend: Miroslav Ivanov, for his love, guidance, and support in the hard times of dealing with Covid19 pandemic and finishing my PhD degree. Finally, I would like to thank my cat Mika for providing the best mental support in these difficult times.

Declaration

This thesis is submitted to the University of Warwick in support of my application for the degree of Doctor of Philosophy. It has been composed by myself and has not been submitted in any previous application for any degree.

The work presented (including data generation and analysis) was carried out by the author except in the cases outlined below:

(1) Chapter 3 outlines the development of methodology for 3D inflation-corrected Delta Euclidian distance measurements, where I contributed to development of the methodology and prepared a step-by-step guide on the methodology. The correction algorithm was written by Nigel Burroughs, and the methodology development was also driven by Emanuele Roscioli.

(2) Chapter 4, subsections 4.2.1, 4.2.2, and 4.2.3, presents a summary of the experiments in Roscioli et al., 2020, which were performed by Emanuele Roscioli. For these experiments, I aided Emanuele Roscioli with data analysis and interpretation.

(3) In Chapter 4, subsection 4.2.6, Peter Embacher wrote the kinetochore state un-mixing algorithm and applied the algorithm.

(4) In Chapter 5, part of the data is analysed via the TEDCA algorithm for inflation-correction, who was developed and applied by Peter Embacher.

The data presented in Chapter 3 relates to a publication in revision by the author and is attached in Appendix B.

The data presented in sub-sections 4.2.1, 4.2.2, and 4.2.3 of Chapter 4 has been published where the author of this thesis is second author and can be found here:

Roscioli, E., Germanova, T.E., Smith, C.A., Embacher, P.A., Erent, M., Thompson, A.I., Burroughs, N.J., McAinsh, A.D., 2020. Ensemble-Level Organization of

Human Kinetochores and Evidence for Distinct Tension and Attachment Sensors.
Cell Reports 31, 107535. <https://doi.org/10.1016/j.celrep.2020.107535>

Inclusion of Published Work

In Appendix B I have included a published paper to which I have contributed and on which I am named a second author: Ensemble-Level Organization of Human Kinetochores and Evidence for Distinct Tension and Attachment Sensors (Roscioli et al., 2020); and a paper under revision where I am the named first author: Subcellular Euclidean distance measurements with Multicolor Fluorescence localization imaging (Germanova et al., 2021, under revision).

Acknowledgements

I want to thank my supervisors: Prof. Andrew McAinsh and Prof. Nigel Burroughs for their mentoring, support and guidance. I want to further thank them for their always positive attitude and believe in me, which has made this PhD a truly amazing experience for me. I am very grateful and lucky that in these four years, albeit challenging at times, my supervisors have always maintained a very positive environment which helped me to grow as a scientist and a person. I can truly say that I will always feel very lucky and proud to have had them as supervisors and mentors in my PhD. This PhD further allowed me to take on inspiring opportunities such as the AQLM training, the BSCB and ASCB conferences, which have become some of my favourite memories. This would not have been possible without my supervisors and without the amazing IBR DTP coordinator Sally Blakeman and the help of the IBR DTP course leader Jonathan Miller. I further want to thank Anne Straube for her support in my conference preparation endeavours.

I would also like to thank the current and previous lab members of the McAinsh and Burroughs labs for their friendship, support and understanding. I want to thank Dr. Philip Auckland for giving me the fundamentals of experimental work and writing, and for his support in the early years of my PhD. He has been an invaluable mentor for me and this work would not have been possible without him. I want to also thank Dr. Emanuele Roscioli who helped further forge my lab skills, for being my friend in difficult times when I needed to change direction, and for always being understanding and supportive of me. I want to thank Dr. Cerys Currie for her ever positive attitude, her invaluable advice and her help. I want to also thank Dr. Alessio Inchingolo for always bringing us together as a group, for helping me grow as scientist and for making the coffee breaks always very enjoyable and social. Finally, I want to thank Dr. Muriel Erent who have always been very helpful and

who has always made our work so much more easy and enjoyable. Finally, I want to thank Dr. Peter Embacher and Dr. Jonathan Harrison for being great collaborators with always new insight into the matter and never ending energy to pursue new directions.

Abstract

Accurate chromosome segregation demands that sister kinetochores form force-generating attachments to microtubules nucleated from opposite poles of the mitotic spindle (Bi-orientation). Kinetochores are assembled from hundreds of protein components with the Ndc80 complex providing the main attachment activity, and auxiliary load bearing provided by the Ska complex. Bi-orientation is monitored by the spindle assembly checkpoint (SAC) and catalysed by error correction processes that detect and eliminate incorrect attachments. However, our understanding of how the kinetochore is organised *in vivo*, and how this structure adapts to chemical and mechanical stimuli is poorly understood. This will be crucial to understanding how the SAC and error correction systems operate. Here, in collaboration with the Burroughs Lab, we developed a method for measuring the 3D euclidian-corrected distances between kinetochore components (ΔEC). We have used this approach to map the 3D architecture of the human kinetochore. We also show that the Ndc80 complex jack-knives at unattached kinetochores and how this is coordinated with SAC signalling. Our data support a model by which jack-knifing initiates after SAC silencing, and completes as the final checkpoint proteins unbind. We further used endogenously labeled Ska to provide evidence of how the Ska complex is flexibly linked to Ndc80 *in vivo*. These data provide a blueprint for the human kinetochore and new insight into how structural adaptation is coupled to checkpoint and error correction processes.

Abbreviations

AP kinetochore - away-from-the-pole-moving kinetochore

BEDCA - Bayesian euclidian distance correction algorithm

CRISPR - clustered regularly interspaced short palindromic repeats

Δ EC distance - inflation-corrected Delta euclidian distance

GDP - guanosine diphosphate

GTP - guanosine triphosphate

GUI - Graphic user interphase

HeLa K cells - Henrietta Lacks Kyoto cells

hTERT-Rpe1 cells- human telomerase reverse transcriptase retinal pigment epithelial 1 cells

K-fibre - kinetochore fibre

KiD - Kinetochore Delta Software (KiT2.1.10)

KiT - Kinetochore Tracking Software

MCC - mitotic checkpoint complex

NEB - nuclear envelope break-down

P kinetochore - poleward-moving kinetochore

RZZ - Rod-Zwilch-ZW10

SAC - spindle assembly checkpoint

TEDCA - triangle euclidian distance correction algorithm

Contents

1	Introduction	15
1.1	Overview of mitosis	15
1.2	Kinetochores	19
1.2.1	Overview	19
1.2.2	Kinetochores Assembly	22
1.3	The KMN (Knl1-Mis12-Ndc80 complex) network and the Ska complex	26
1.3.1	The Mis12 complex	26
1.3.2	The Ndc80 complex	29
1.3.3	The Spindle and kinetochores associated (Ska) complex	34
1.3.4	Knl1	42
1.4	The Spindle assembly checkpoint signaling	46
1.4.1	Overview	46
1.4.2	SAC assembly	47
1.4.3	SAC silencing upon microtubule attachment	49
1.5	Studies of kinetochores architecture in intact mammalian cells: Intra-kinetochores (Delta) measurement	51
1.6	Rationale and Aims of Thesis	58
2	Materials and methods	60
2.0.1	Cell culture and treatments	60
2.0.2	Indirect Immunofluorescence	61
2.0.3	Antibodies	62
2.0.4	DNA constructs and cloning	62
2.0.5	Transient transfection	63
2.0.6	Genomic DNA PCR analysis	64
2.0.7	Genomic DNA PCR product preparation for sequencing	64
2.0.8	Fluorescent In-situ Hybridisation (FISH)	65

2.0.9	Fluorescence-activated cell sorting	66
2.0.10	Generation of Halo-tag CenpA stable expression, Ska1 knock- in cell line (MC206)	67
2.0.11	Fixed-cell imaging	67
2.0.12	Live-cell imaging	68
2.0.13	Lattice light sheet Microscopy	68
2.0.14	Delta measurements and Statistical Analysis	68
3	Protocol for Subcellular Euclidean distance measurements with Multicolour Fluorescence localization imaging	70
3.1	Background	70
3.2	Results	76
3.2.1	Inflation correction of 3D Delta distances	76
3.2.2	Sample preparation	79
3.2.3	Kinetochores spot detection	80
3.2.4	Approximate chromatic shift correction (ACS) and fine chro- matic shift correction (centralisation)	81
3.2.5	Kinetochores spot quality control	83
3.2.6	3D Delta measurements at kinetochores categories	88
3.2.7	Protocol for inflation-corrected 3D Delta measurements	90
3.3	Summary	90
4	Architecture and plasticity of the human kinetochores in non- transformed hTERT-Rpe1 cells	91
4.1	Background	91
4.2	Results	94
4.2.1	3D mapping of the human kinetochores architecture via Δ EC measurements	94
4.2.2	Differential kinetochores architecture changes in response to loss of attachment and tension	101
4.2.3	Ndc80 jack-knifing correlates with Mad2 status	104
4.2.4	Visual kinetochores categorisation vs Quantitative analysis of kinetochores Mad2 status	106

4.2.5	Mad2 unloading precedes the switch of Ndc80 into the ordered state	109
4.2.6	Development of kinetochore state un-mixing algorithm	116
4.3	Conclusions	118
5	Defining the sub-kinetochore position and organisational state of the Ska complex in human cells.	119
5.1	Background	119
5.2	Results	124
5.2.1	Positioning of Ska complex within the architectural map of a human (Rpe1) kinetochore	124
5.2.2	Generation of endogenously tagged Ska1 HeLa K cell lines by CRISPR/Cas9 genome editing	127
5.2.3	Architecture of kinetochores in human HeLa cells	134
5.2.4	Mapping of the Ska complex position in HeLa cells	140
5.2.5	The Ska1(N) offset from the Mis12-Ndc80 complex axis is not dependent on microtubule dynamics	146
5.2.6	mNeonGreen-Ska1 as a tool for live-cell imaging of Ska dynamics	148
5.3	Conclusions	150
6	Discussion	151
6.1	<i>In vivo</i> investigation of the 3D human kinetochore architecture	151
6.2	Interplay between Ndc80 jack-knife and SAC activation-silencing	157
6.3	Ska Architecture at human kinetochores and its implications in Ska kinetochore recruitment mechanisms	165
A	Supplemental Figures	171
B	Manuscripts	173
B.1	Ensemble-Level Organization of Human Kinetochores and Evidence for Distinct Tension and Attachment Sensors	173
B.2	Subcellular Euclidean distance measurements with Multicolor Fluorescence localization imaging	218

List of Figures

Figure 1.1:	Early studies of Karyomitosis by Flemming.	16
Figure 1.2:	Stages of mitosis.	18
Figure 1.3:	Depolymerisation-coupled pulling (DCP) congression mechanism	22
Figure 1.4:	Kinetochores assembly.	25
Figure 1.5:	Structure of the Mis12 complex	27
Figure 1.6:	Structure of the Ndc80 complex	30
Figure 1.7:	Structure of the Ska complex	35
Figure 1.8:	Model for Ska kinetochore loading dynamics and function at kinetochores	43
Figure 1.9:	Functional organisation of Knl1.	44
Figure 1.10:	Kinetochores protein-protein distance measurements (Δ)	54
Figure 3.1:	Kinetochores protein-protein distance measurements (Δ): Projection and Inflation effects	73
Figure 3.2:	Posterior distributions of the mean Δ_{EC} distance (μ parameter) between CenpC and Ndc80(N) after BEDCA correction with parameter a set to 10 and 3.	78
Figure 3.3:	Representative images of the fluorescent signal in cells used for Δ measurements.	80
Figure 3.4:	Spot quality control removes outlier 3D Δ distances.	84
Figure 3.5:	Quality control in the Coordinate system channel (CSC): kinetochores sister-sister pairing and spot quality control.	85
Figure 3.6:	Kinetochores spot quality control in the non-coordinate system (NCS) channels.	87
Figure 3.7:	Accuracy of the Δ_{EC} measurement at 0 nm true intra-kinetochores distance.	89
Figure 4.1:	3D Architecture of bi-oriented kinetochores.	95

Figure 4.2:	Simulations of bi-oriented kinetochore architecture.	97
Figure 4.3:	Nematic order of the outer kinetochore.	100
Figure 4.4:	Ndc80 and Knl1 are distinct microtubule occupancy and tension sensors.	103
Figure 4.5:	Ndc80 jack-knife correlates with Mad2 status.	105
Figure 4.6:	Quantification of Mad2 kinetochore intensity.	108
Figure 4.7:	Miss-categorisation of kinetochores in qualitative Mad2 status analysis.	109
Figure 4.8:	Ndc80 jack-knife to straight conformation transition relative to Mad2 unloading.	112
Figure 4.9:	Ndc80 jack-knife to straight conformation transition relative to Mad2 unloading.	114
Figure 4.10:	Relationship between Ndc80 conformation and Mad2 unloading.	115
Figure 5.1:	Structure of the Ska, Mis12 and Ndc80 complexes.	123
Figure 5.2:	Position of Ska3(M) in hTERT Rpe1 cells.	126
Figure 5.3:	Chromosome 18 copy number in HeLa K cells.	128
Figure 5.4:	Characterisation of Ska1(N) endogenous fluorescent label cell lines.	130
Figure 5.5:	Kinetochore localisation of endogenous 2xmNeonGreen-Ska1.	133
Figure 5.6:	Δ EC positions of CenpC, Nnf1 and Ndc80(N) in HeLa K cells.	135
Figure 5.7:	Nematic order of the outer kinetochore Mis12-Ndc80 complex molecules in hTERT Rpe1 and HeLa K cell lines.	137
Figure 5.8:	Δ EC positions of CenpC, Nnf1 and Ndc80(N) in HeLa K cells. Fixation with "pre-extraction".	139
Figure 5.9:	Δ EC positions of Ska1(N), Nnf1 and Ndc80(N) in HeLa K cells. MC200 cell line.	141
Figure 5.10:	Δ EC positions of Ska1(N), CenpC and Ndc80(N) in HeLa K cells. MC200 cell line.	143
Figure 5.11:	Δ EC positions of Ska1(N), CenpC and Nnf1 in HeLa K cells. Cell line MC177.	144
Figure 5.12:	Δ EC positions of Ska1(N), CenpC and Nnf1 at tension-less kinetochores (taxol) in HeLa K cells. Cell line MC200.	147

Figure 5.13: Live-cell imaging of endogenously labelled Ska1(N) (MC206 cell line) on Lattice Light Sheet microscope.	149
Figure 6.1: Structured illumination microscopy (SIM) of hTERT Rpe1 kinetochores.	157
Figure 6.2: Schematic representing the distinct Ndc80 architecture changes as Mad2 is unloaded, and how they may integrate overall in the kinetochore bi-orientation and maturation processes. . . .	165
Figure 6.3: Schematic showing a putative model for Ska architectural changes in the process of Ska kinetochore recruitment.	170
Figure A.1: PCR products of Ska1 N-terminal region amplification in MC177 and MC200 cell lines.	172

List of Tables

Table 3.1 Kinetochore spot detection improvement via "Neighbour" Spot detection method.	82
Table 4.1 Parameters used for kinetochore ensemble simulations	98
Table 4.2 CenpC-to-Ndc80(N) ΔEC distance at kinetochores binned based on Mad2 intensity	111
Table 5.1 Ska architecture in HeLa kinetochores: ΔEC measurements in HeLa K cells, and their comparison to $\Delta 1D$ and $\Delta 3D$ measurements.	145

Chapter 1

Introduction

1.1 Overview of mitosis

Mitosis has intrigued scientists ever since its first description in the 1880s by a German scientist named Walther Flemming (Flemming, 1882; Paweletz, 2001). Flemming observed distinct arrangements of thick thread-like structures in cell division and proposed the process of ‘karyomitosis’ (see Figure 1.1). Karyomitosis consisted of two steps – a progressive and a regressive phase. The progressive phase began with condensation of the nuclear ‘framework’ into thick filaments that then migrated and aligned in an equatorial plate. In the regressive phase, the filamentous equatorial matter separated to opposite sides of the cell in two roughly equal masses. This phase concluded with constriction of the cell in the middle and generation of two daughter cells.

We now understand that mitosis is a highly regulated process in which the duplicated genetic material of the parental cell is equally segregated to two identical progeny cells (McIntosh, 2016). This process consists of five distinct phases that are followed by a cleavage division (see Figure 1.2). During prophase the genetic material condenses into the mitotic chromosomes, which are visible under a light microscope. The duplicated centrosomes begin nucleating multiple microtubules (long tubular polymers that grow and shrink at their +end and are relatively stable at their –end) giving rise to the two asters. The asters then migrate around the nucleus to opposite sides of the cell ready to form the nascent mitotic spindle. The spindle will function as the force generating machine that moves and segregates chromosomes

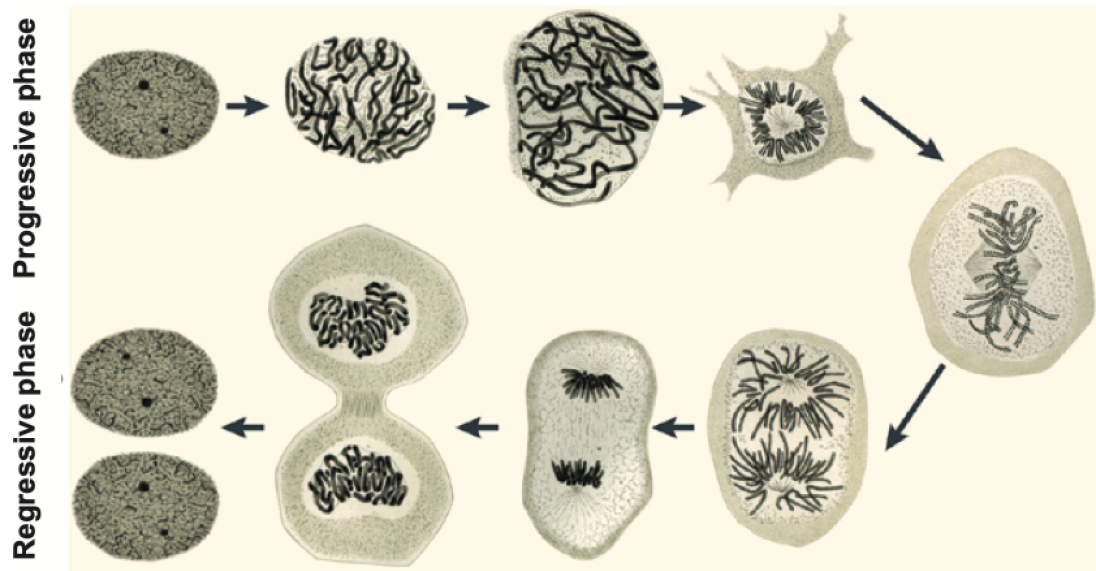


Figure 1.1: Early studies of Karyomitosis by Flemming. Karyomitosis consists of a progressive and a regressive phase. The progressive phase begins with the appearance of the nuclear threads and continues until they become aligned at an equatorial plate. The regressive phase describes the roughly equal separation of the filamentous equatorial mass to opposite sides of the cell, and the following formation of the daughter cell nuclei. Flemming 1882; Paweletz, 2001.

during mitosis. In metazoans, the beginning of prometaphase is marked by nuclear envelope breakdown (NEB), which allows microtubules access to the chromosomes. The dispersed chromosomes are captured by spindle microtubules at the kinetochore, a multi-protein complex that assembles on the two sister centromeres. At the same time the two interacting microtubule asters form the mature bipolar mitotic spindle. It is the spindle-attached kinetochores that harness the energy from microtubule dynamics to power the directed migration of chromosomes to the spindle equator, a process termed congression. During prometaphase, kinetochores undergo multiple rounds of microtubule binding and detachment until the two sister kinetochores ultimately form ‘end-on’ attachments to microtubule bundles (K-fibres) from opposite spindle poles, an event termed bi-orientation. Bi-orientation is vital for the re-distribution of the genetic material and is monitored by the spindle assembly checkpoint (SAC; discussed in section 1.4). Once congression is complete cells enter metaphase and kinetochores oscillate perpendicular to the spindle equator. This is thought to allow for final kinetochore-microtubule attachment maturation and for SAC signalling to occur. Silencing allows activation of the anaphase promoting

complex, destruction of the physical links holding sister chromatids together and initiation of chromosome segregation. During anaphase A, the sister chromatids move to opposite ends of the spindle driven by depolymerisation of kinetochore microtubules. In anaphase B, the two spindle poles are pushed apart as microtubule slide over each other in the spindle mid-zone. This moves the chromatids further apart into what will become the two new daughter cells. During anaphase, the division of the cell (cytokinesis) is initiated. Here, a membrane-tethered acto-myosin ring forms at the cell equator and its constriction divides the cytoplasm into two daughter cells (Green et al., 2012). Next, in telophase, the two DNA masses de-condense and a nuclear envelope is re-formed around each. The cell division process ends with the physical separation of the two progeny cells in a process called abscission.

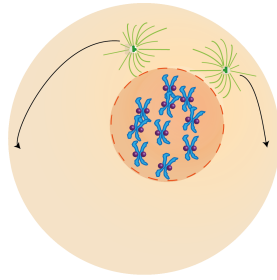
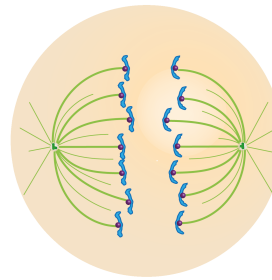
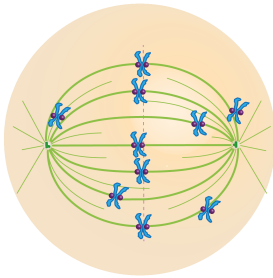
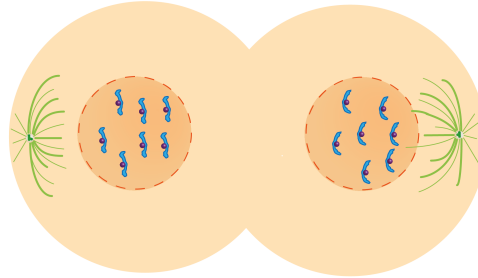
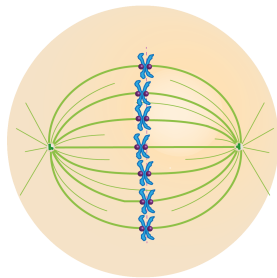
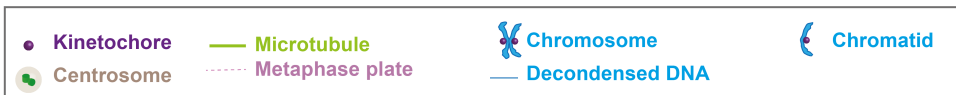
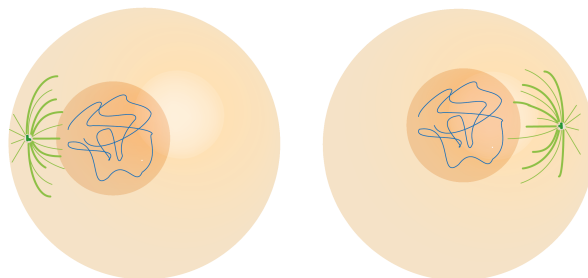
1) Prophase**4) Anaphase****2) Prometaphase****5) Telophase****3) Metaphase****Cytokinesis**

Figure 1.2: Stages of mitosis. Mitosis begins with Prophase, where the DNA condenses and the two centrosomes form asters by high rates of microtubule nucleation. Also, the two asters begin to migrate to opposite sides of the cell and the nuclear envelope starts to break down. Prometaphase begins with the dispersion of chromosomes that coincides with nuclear envelope break down. Here, chromosomes interact with microtubules from the nascent mitotic spindle via the kinetochore, multi-protein centromere associated complex. The kinetochore in turn powers the motion of the dispersed chromosomes to a plane equidistant from the two spindle poles, where the chromosomes align in metaphase plate. Metaphase entry occurs at formation of the metaphase plate. Here, the kinetochore-microtubule attachments mature. In Anaphase, the cohesion between the sister chromatids is broken and they migrate to the opposite poles. In Telophase, the nuclear envelope reforms around each of the two DNA masses and the DNA decondenses. Finally, the two progeny cells are physically separated in Cytokinesis.

1.2 Kinetochores

1.2.1 Overview

The kinetochore is a multi-megadalton protein assembly built from hundreds of protein molecules - many organised into distinct subcomplexes that mediate defined functions (McAinsh et al, 2003). Early transmission electron microscopy (EM) studies of fixed cells showed that these kinetochore proteins and complexes are broadly organised into three kinetochore layers: two electron-dense layers, separated by a translucent middle layer (Brinkley and Stubblefield, 1966). However, later thin-section EM studies of specimens frozen by high pressure instead of fixative showed only the two electron-dense layers and suggested that the middle translucent layer is an artefact (Dong et al., 2007). Therefore, now we know that the kinetochore is organised in two layers: an inner and outer kinetochore layers. The inner kinetochore layer interfaces directly with the chromosome at a specialised region, termed the centromere - specified through DNA sequence and/or epigenetic mechanisms depending on the organism. This is visualised as the primary constriction in electron micrographs of metaphase chromosomes. The inner kinetochore layer then serves as a platform for the assembly of the outer kinetochore layer which contacts with the tips of mitotic spindle microtubules. This way, the kinetochore forms the interface between the chromosome and mitotic spindle. In addition, another layer of the kinetochore, termed the fibrous corona, assembles outside of the outer kinetochore in absence of microtubule binding (Rieder, 1982). The kinetochore must perform three main functions during chromosome segregation:

(1) Kinetochores must capture the dynamic plus-ends of spindle microtubules in order to form end-on attachments, and ultimately, bi-orientation (also termed amphitelic attachment). Bi-orientation is complete when the kinetochores assembled on the two sister chromatids are end-on attached to K-fibres (microtubule bundles) emanating from opposite spindle poles. This attachment geometry is the only one compatible with sister chromatids being pulled to opposite spindle poles during anaphase. How do the sister kinetochores capture K-fibres specifically emanating from opposite spindle poles? Kinetochores first undergo a "Search-and-capture" process where they randomly encounter microtubules of the mitotic spindle (Heald and

Khodjakov, 2015). Further, the attachments that are compatible with kinetochore bi-orientation are stabilised. In contrast, erroneous attachments, such as attachment of both kinetochores to the same pole (syntely), are selectively destabilised by the error-correction machinery and the kinetochore can attempt again to form a bi-oriented attachment. However, kinetochores that are in very close proximity to the pole or behind the pole are unlikely to encounter microtubules from opposite spindle poles despite rounds of "Search-and-capture" (Auckland and McAinsh, 2015). Such kinetochores thus first bind laterally to the microtubule lattice (lateral attachment) and use this interaction to migrate to position more suitable for bi-orientation (as will be discussed next). These lateral attachments must then be converted to end-on attachments in order to complete chromosome bi-orientation.

(2) Kinetochores power the directed migration of all chromosomes to the spindle equator, a process termed congression. The importance of congression is not well understood: it may provide an equal starting position for the chromosomes before they segregate in anaphase. If, for example, the process of congression is abrogated, some of the chromosomes need to travel greater distance in anaphase, and thus arrive late at the pole (Fonseca et al., 2018). This slows anaphase and can cause formation of micronuclei and abnormal structure of the nucleus (Fonseca et al., 2018). On the other hand, congression may be an emergent property of the underlying mechanism that ensures kinetochore bi-orientation, equal forces across all sister kinetochores and satisfying of the spindle assemble checkpoint (Nicklas and Arana, 1992).

How do kinetochores power chromosome congression? Kinetochores use one of two mechanisms depending on the kinetochore location after NEB and their attachment status (Auckland and McAinsh, 2015). 1) Kinetochores that are proximal to the pole bind to the microtubule lattice via molecular motors that are located in the fibrous corona. These molecular motors (CenpE) can then walk to the plus-end of microtubules to transport the chromosome to the equator where bi-orientation is more favorable. If a kinetochore is behind the spindle pole then minus-end directed motors (Dynein) can transport the chromosome to the centrosome where it can switch to microtubules directed towards the equator and undergo plus-end directed lateral sliding. 2) Bi-oriented kinetochores utilise the dynamics of the microtubule plus ends in the end-on attached K-fibre to generate force. To understand this mechanism we need to first outline the nature of microtubules and how their dynamic

properties can store mechanical energy: Microtubules are stiff tube-like structures that alternate between growth and shrinkage states, and thus govern mechanical energy that can be harnessed for pushing or pulling (Brouhard and Rice, 2018). The microtubule is built from thirteen protofilaments of alpha- and beta-tubulin heterodimers (protofilaments). Microtubules grow by incorporation of GTP-tubulin dimers to the microtubule +end. The GTP-tubulin is subsequently hydrolysed to GDP-tubulin, creating a small GTP-tubulin cap and GDP-tubulin lattice. If the GTP-tubulin cap is lost (catastrophe), the microtubule can then switch to depolymerisation state where GDP-tubulin dissociates from the +end. Switch to microtubule polymerisation (rescue) occurs with GTP-tubulin addition and reformation of the cap. During microtubule +end depolymerisation, individual protofilaments peel off the microtubule lattice in ‘rams horn’ conformation and create force that has been estimated to be sufficient for powering congression (Simon and Salmon, 1990; Desai and Mitchison, 1997; Grishchuk et al., 2005; Nicklas, 1988; McEwan et al., 1997).

How can the bi-orientated kinetochore utilise those dynamics? The bi-orientated kinetochores employ a depolymerisation-coupled pulling mechanism of congression, where the kinetochore orientated towards the equator (the Poleward, [P] kinetochore) binds to a depolymerising K-fibre, tracks with shortening K-fibre end and thus generates a poleward pulling force (Auckland and McAinsh, 2015; See Figure 1.3). The sister kinetochore (the away-from-the-pole [AP] kinetochore) binds to an overall polymerising K-fibre and follows the motions of the P kinetochore.

(3) How does the cell monitor the completion of bi-orientation and congression and couple this to anaphase onset? For this the kinetochore also functions as a platform for assembly of the Spindle assembly checkpoint (SAC) signaling system (the SAC will be discussed in more detail in section 1.4). The SAC monitors the attachment status of kinetochores and prevents anaphase onset until all kinetochores have formed mature bi-orientated attachments. However, how the SAC detects kinetochore bi-orientation and what constitutes a mature kinetochore-K-fibre attachment remain open questions.

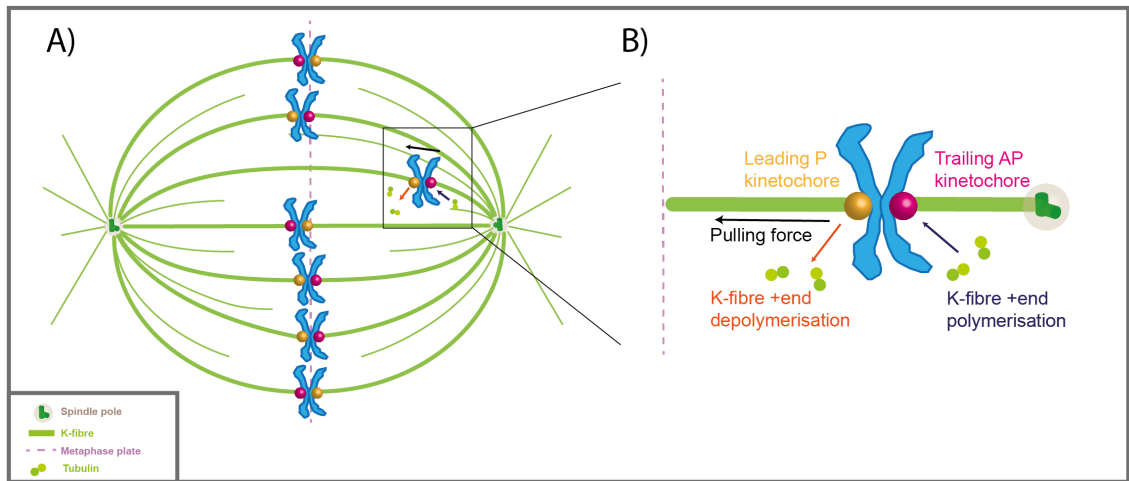


Figure 1.3: Depolymerisation-coupled pulling (DCP) congression mechanism

A) Cartoon representation showing two uncongressed kinetochores that are situated between the spindle poles and congress via DCP. B) The DCP congression mechanism. Here, the leading (poleward-moving, [P]) kinetochore induces depolymerisation at its associated K-fibre and tracks with the depolymerising end, thus generating pulling force. The sister kinetochore, termed trailing (away-from-the-pole-moving, [AP]) kinetochore, induces polymerisation at its associated K-fibre and trails behind the leading kinetochore, following its motions. Auckland and McAinsh, 2015.

1.2.2 Kinetochore Assembly

How do the hundreds of kinetochore molecules interact with each other to assemble the kinetochore at the centromere and to allow for its various functions? To assemble the kinetochore firstly the inner kinetochore layer, that is termed the constitutive centromere associated network (CCAN), assembles on the chromosome centromere (Hara and Fukagawa, 2020; see Figure 1.4). How does the CCAN specifically recognise the centromere? In *S. cerevisiae*, the centromere is specified by ~ 125 bp DNA sequence specific region, and is thus termed "point" centromere (Musacchio and Desai, 2017). In eukaryotes, however, the centromere spans much larger DNA region, and is termed "regional" centromere. The specification of regional centromeres occurs epigenetically by the incorporation of the histone H3 variant Centromere protein A (CenpA). The CenpA kinetochore protein further serves as the seed for kinetochore assembly and recruits the kinetochore protein CenpC and the CenpN-CenpL sub-complex (Trazzi et al., 2009; Pentakota et al., 2017; Kato et al., 2013; Allu et al., 2019).

CenpC is 943 amino acid protein that has been predicted to be elongated and largely unstructured (Screpanti, 2011). CenpC specifically recognises and binds CenpA via the CenpC Central Domain (amino acids 519-537), an interaction that is also facilitated by another CenpC region - the CenpC motif (amino acids 737-759) (Kato et al., 2013; Allu et al., 2019). CenpC further promotes its own kinetochore localisation by CenpC:CenpC dimerisation via the CenpC C-terminal Cupin Domain (Chick et al., 2019). CenpC also binds to the CenpN-L sub-complex via the PEST rich CenpC domain (Pentakota et al., 2017), an interaction that further stabilises CenpC incorporation at the kinetochore.

CenpC and the CenpN-CenpL subcomplex further bind to and recruit the CenpH-CenpI-CenpK-CenpM sub-complex (Musacchio and Desai, 2017). The CenpH-CenpI-CenpK-CenpM sub-complex is suggested to act in maintenance and the stability of the inner kinetochore. Then, the CenpO-CenpP-CenpQ-CenpU kinetochore sub-complex binds to the joint surface of CenpN-CenpL and CenpH-CenpI-CenpK-CenpM. In this manner, the inner kinetochore forms an intricate stable assembly while also branches out from the CenpA site in the centromere, and thus provides a stable platform with multiple interaction sites for assembly of the outer kinetochore.

In addition, the kinetochore provides a second linker between the chromosome and the outer kinetochore - CenpT. CenpT is 561 amino acid protein that is essential for robust formation of the outer kinetochore plate (Gascoigne, et al., 2011). CenpT has been found to directly bind to DNA via its C-terminal domain and to specifically target centromeric DNA adjacent to the CenpA incorporation region (Hori et al., 2008). CenpT is recruited to kinetochores at the beginning of each cell cycle during S phase and requires CenpA for centromeric localisation (Prendergast, et al., 2015). CenpT forms a tight complex with CenpW to form a heterodimer structurally homologous to the H2A/H2b and H3/H4 heterodimers (Hori et al., 2008). Further, the CenpT-CenpW sub complex binds the CenpS-CenpX sub-complex. The CenpT-CenpW-CenpS-CenpX heterotetramer was identified to bend ~ 100 bp of DNA where the DNA wraps around the heterotetramer core, and thus was suggested to incorporate into the chromosome similar to a histone (Nishino et al., 2012). Two heterotetramers of CenpT-CenpW-CenpS-CenpX have also been observed to dimerise into an octameric histone-like core and to also bend ~ 100 bp linear DNA (Takeuchi, et al., 2014). However, it remains unknown as to whether the complex

is heterodimeric or heterotetrameric in cells. In either case, the CenpT-CenpW-CenpX-CenpS sub-complex is thought to interact with free DNA at the centromere in a histone-like mode.

CenpT has also been suggested to bind to the CenpH-CenpI-CenpK-CenpM complex and thus indirectly interact with CenpC (Altunkaya et al., 2016; Zhang et al., 2020.; Walstein et al., 2020). This further shows that the inner kinetochore assembly and protein-protein interaction sites are highly redundant. This redundancy is likely an important evolutionary feature that prevents kinetochore collapse in case of a kinetochore protein mutation.

The CenpC and CenpT proteins further act as inner-outer kinetochore linkers and are critical for the outer kinetochore assembly. The outer kinetochore has four main components: the Mis12 complex, the Ndc80 complex, and Knl1 (collectively known as the KMN network), and the Ska complex. To scaffold the outer kinetochore assembly, CenpC and CenpT each recruit about 50% of the outer kinetochore complex Mis12 (Suzuki et al., 2015). CenpC binds Mis12 with its most N-terminal region (Screpanti, et al., 2011). The C-terminal and middle regions of CenpC associate with CenpA as discussed above. The CenpA and Mis12 binding site are interspersed by about 700 amino acid flexible region in CenpC. Therefore, Mis12 may be positioned flexibly by the CenpC linkage outward of the inner kinetochore. However, how exactly this flexible linkage positions Mis12 within the kinetochore remains an open question. CenpT also binds to and recruits the Mis12 complex. CenpT binds the Mis12 complex via 100 amino acid region at its most N-terminus (Gascoigne et al., 2011). The C-terminal region of CenpT targets CenpT to the chromosome as discussed above. The domain in CenpT responsible for its chromosome association and the CenpT Mis12-binding domains are interspersed by about 350 amino acid flexible region in CenpT (Huis In't Veld et al., 2016). Therefore, the CenpT connection of Mis12 to the inner kinetochore is also flexible. However, how the CenpT linker positions Mis12 in the kinetochore also remains unclear. Further, an open question remains as to whether the flexibility in the CenpC and CenpT Mis12 linkers allows for branching of the outer kinetochore and whether it is further required for capture of microtubules by the outer kinetochore.

The next component of the outer kinetochore that is recruited is the Ndc80 complex (the structure of the Ndc80 complex will be described in detail in the next section).

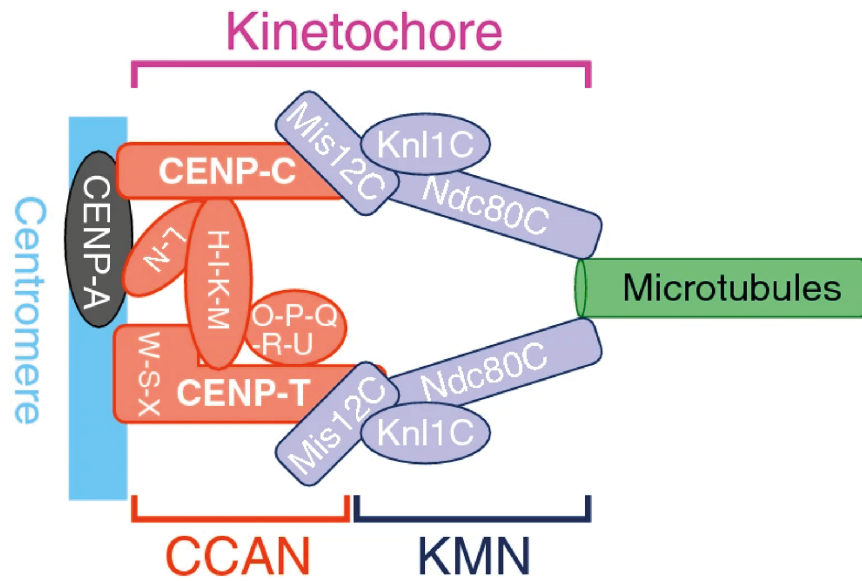


Figure 1.4: Kinetochore assembly. The kinetochore is broadly organised in inner kinetochore layer, also termed Constitutive centromere assembly network (CCAN, orange), and an outer kinetochore layer that includes the Knl1/Mis12/Ndc80 network (KMN, blue). The CCAN assembles at a specified region of the metaphase chromosomes, termed the centromere. In vertebrates, the centromere is specified epigenetically by incorporation of nucleosomes containing the Histone H3 variant CenpA. Then, to assemble the CCAN, CenpA recruits CenpC and CenpN-L to kinetochores. Then CenpH-I-K-M binds to the joint surface of CenpC and CenpN-L. The CenpH-I-K-M sub-complex further recruits the CenpO-P-Q-R-U sub-complex to kinetochores. A second pathway of inner kinetochore assembly stems from the inner kinetochore protein CenpT. CenpT binds to the DNA region proximal to the centromere, most likely in histone-like manner. CenpT further interacts with the CenpH-I-K-M sub-complex. This interaction is suggested to facilitate the CenpT kinetochore localisation. The CCAN then provides the platform for assembly of the KMN network. Here, CenpC and CenpT provide the two linkers between the inner and outer kinetochore layers. CenpC and CenpT each recruits about 50% of the outer kinetochore protein Mis12 complex. Further, the Mis12 complex binds to Knl1 and the Ndc80 complex and recruits the two kinetochore components to kinetochores. CenpT can also directly bind and recruit the Ndc80 complex to kinetochores. The Ndc80 complex binds to microtubules and establishes the kinetochore-microtubule end-on attachment. Hara and Fukagawa, 2020.

The Ndc80 complex is recruited via binding to Mis12 in 1:1 ratio and via direct binding to CenpT in 1:2, CenpT:Ndc80 ratio (Huis In't Veld et al., 2016). Therefore, the CenpC: Mis12 linkage recruits one Ndc80 complex, and the CenpT: Mis12 linkage recruits three Ndc80 complex molecules. The Ndc80 complex is essential for end-on capture of microtubules. The Ndc80 complex has also been implicated in the coupling of the microtubule dynamics to kinetochore motion in congression via DCP (Powers et al., 2009; Helgeson et al., 2018). However, the Ndc80 complex alone has been shown to be insufficient to sustain the kinetochore-K-fibre attachment under high force in congression via DCP (Auckland et al., 2017). To maintain stable kinetochore-microtubule attachments, the Ndc80 complex recruits the Ska complex to kinetochores. The Ska complex has been shown to be essential for stable mature kinetochore-microtubule end-on attachments. However, how Ndc80 and Ska interact and how Ska provides attachment stability remains unclear and under debate in the field. The functions, structure, and possible interplay between the Ndc80 and Ska complexes will be discussed in the next section.

The Mis12 complex also recruits Knl1 to kinetochores (Petrovic, et al., 2010). Knl1 is a 2342 amino acid protein that provides the scaffold for SAC assembly. The structural organisation and functions of Knl1 will be discussed in sections 1.3 and 1.4, respectively.

1.3 The KMN (Knl1-Mis12-Ndc80 complex) network and the Ska complex

1.3.1 The Mis12 complex

Structural organisation of the Mis12 complex

The Mis12 complex is ~20nm rod-shaped molecule and is composed of four proteins: Mis12 (aa 1-205), PMF1 (Nnf1, aa 1-205), NSL1 (aa 1-281), and DSN1 (aa 1-356) (Kline et al., 2006; Maskell et al., 2010; Petrovic et al., 2010; Huis In't Veld, 2016)). The Mis12, Nnf1, NSL1, and DSN1 proteins have similar topologies and span the full length of the Mis12 complex in the same direction, i.e. the N-termini and the C-termini of the proteins lie at opposite sites of the extended rod (Petrovic et al., 2016; see Figure 1.5). The N-termini of Mis12 and Nnf1 cluster together in

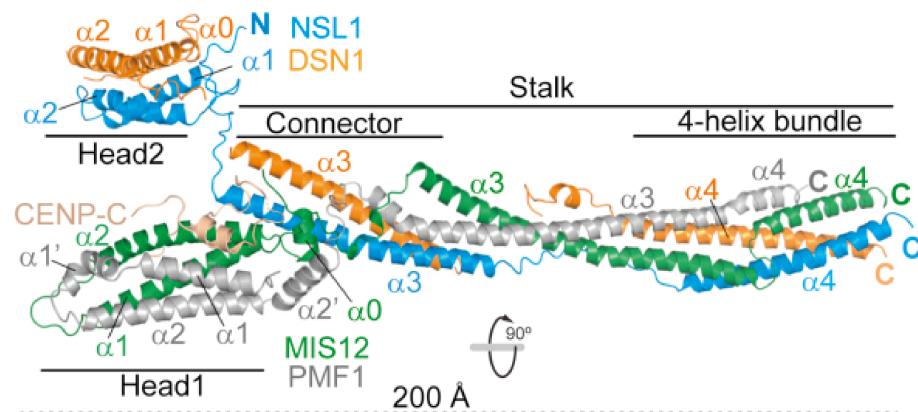


Figure 1.5: Structure of the Mis12 complex The Mis12 complex is composed of four proteins: DSN1, NSL1, PMF1 (Nnf1), and Mis12. The N-terminal regions of PMF1 and Mis12 form helical pins that further assemble in a four-helix bundle, termed the Mis12 complex Head1. The N-terminal regions of DSN1 and NSL1 pair in a helical segment and form the Mis12 complex Head2. Head2 is connected to the rest of the Mis12 complex via a helical connector segment that can allow for flexibility of Head2. The middle and C-terminal regions of the four Mis12 complex components form the Mis12 complex stalk. The middle region of the Mis12 complex stalk is composed of the alpha helices of Mis12 and PMF1, and the disordered side-chains of DSN1 and NSL1. In the C-terminal region of the stalk, the four proteins resume helical conformation and form a four-helix bundle. Petrovic et al., 2016.

structure termed Head1 and the N-termini of DSN1 and NSL1 cluster together in structure termed Head2. To form Head1, the N-termini of Mis12 and Nnf1 form helical hairpins that interact in four helix bundle. To form Head2, the $\alpha 3$ helices of DSN1 and NSL1 pair in a helical segment. Head1 progresses directly into the Mis12 complex stalk - region formed of the middle and C-terminal parts of the four Mis12 complex components. Head2 is followed by a helical connector segment and then progresses into the Mis12 complex stalk. The connection between the helical connector and Head2 is less restrained as compared to the continuation of Head1 into the stalk. Therefore, the helical connector may confer flexibility between Head2 and the rest of the Mis12 complex. The middle part of the stalk is formed of the long and tightly interacting $\alpha 3$ helices of Mis12 and Nnf1, and the extended and partially disorganised side chains of DSN1 and NSL1. At the C-terminal end of the Mis12 complex stalk, the four Mis12 components resume helical conformation and form a four-helix bundle.

Functions of the Mis12 complex

The Mis12 complex is targeted to kinetochore by binding to CenpC or CenpT, and further recruits the Ndc80 complex and Knl1 to kinetochores.

The Mis12 complex interacts with CenpC and CenpT via its N-terminal region as follows. The Mis12 complex binds to CenpC via a shallow groove in Head1 and further contacts CenpC via the interface of Head1 with the helical connector (Petrovic, et al., 2016). The interactions between the Mis12 complex and CenpC are stabilised by Mis12 $\alpha 0$ (part of Head1) and by Aurora B phosphorylation of DSN1 residues S100 and S109 (residues in Head2) (Petrovic, et al., 2016). The Mis12 complex interaction sites with CenpT remain unclear. The interactions between Mis12 and CenpC, and Mis12 and CenpT are mutually exclusive *in vitro* (Huis In't Veld et al., 2016). Therefore, the binding site of the Mis12 complex for CenpT is likely the same as the binding site of the Mis12 complex for CenpC. However, we cannot exclude that binding of one of the proteins to the Mis12 complex prevents binding of the other due to steric hindrance.

The Mis12 complex recruits Knl1 and the Ndc80 complex to kinetochores in 1:1 stoichiometry via its C-terminal region (Petrovic, et al., 2010; Kline et al., 2016; Cheesman et al., 2004, Obuse et al., 2004). To bind the Mis12 complex, the Knl1

RWD domain interacts tightly with a single tight helical turn in the NSL1 C-terminal region (amino acids 266-269) and forms extended contacts with the C-terminal end of the Mis12/Nnf1/NSL1/DSN1 four-helix bundle (Petrovic, et al., 2010; Petrovic et al., 2014, Petrovic et al., 2016, Cifferi et al., 2008; Cheeseman et al., 2006; Kiyomitsu et al., 2007). The Knl1 RWD domain further emerges at about 65° from the Mis12 complex long axis (Petrovic et al., 2014). The Mis12 complex binds to the Ndc80 complex via head-on interaction between the Mis12 complex C-terminus and the RWD domains in the Ndc80 complex Spc24 and Spc25 components (Petrovic, et al., 2010; Petrovic et al., 2016; Cheesman et al., 2004, Obuse et al., 2004). The Mis12 complex binding site for the Ndc80 complex has been mapped to a DSN1 region, amino acids 209 to 222, that is modelled to form an alpha helix and extend from the Mis12 complex stalk (Petrovic, et al., 2010; Petrovic et al., 2016).

1.3.2 The Ndc80 complex

Structural organisation of the Ndc80 complex

The Ndc80 complex is formed of two dimers: (1) Spc24 and Spc25, and (2) Ndc80 and Nuf2 (Wei, Sorger and Harrison, 2005; Bharadwaj, Qi and Yu, 2003, Ciferri et al., 2008; Valverde, Ingram and Harrison, 2016).

The full Ndc80 complex has length of ~57 nm in yeast and ~62nm in humans (EM studies) (Wei, Sorger and Harrison, 2005, Huis In't Veld, et al., 2016). The complex has a dumbbell shape, with a rod of ~51-56 nm flanked by a globular head on each side (Figure 1.6; Wei, Sorger and Harrison, 2005, Huis In't Veld, et al., 2016, Wang et al., 2008). Each of the two heterodimers, Spc24/Spc25 and Ndc80/Nuf2, contains N-terminal head and C-terminal coiled-coil (Wei, Sorger and Harrison, 2005). To assemble the complex the coiled-coils of each dimer interact anti-parallel via their C-termini.

The N-terminal regions of Spc24 and Spc25 fold into RING finger, WD repeat, DEAD-like helicases (RWD) domains (Malvezzi et al., 2013). The RWD domains of Spc24 and Spc25 target the Ndc80 complex to kinetochores via interactions with the CenpT N-terminus, and the Mis12 complex C-terminus (Huis In't Veld et al., 2016, Petrovic et al., 2016). After the RWD domains of Spc24 and Spc25, the Spc24/Spc25 C-terminal coiled-coil region contributes to about one third of the Ndc80 complex

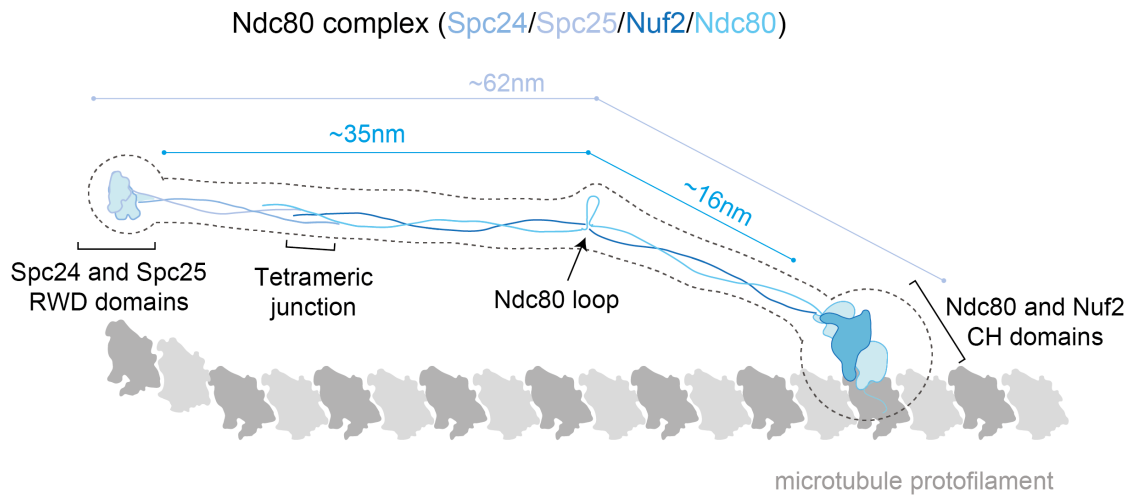


Figure 1.6: Structure of the Ndc80 complex Schematic showing the structure of the Ndc80 complex as modelled by Musacchio and Desai (2017). The Ndc80 structure model is based on available crystal structures of truncated versions of the Ndc80 complex and EM studies. The Ndc80 complex is composed of four proteins: Spc24, Spc25, Nuf2 and Ndc80. To form the complex, first Spc24 and Spc25, and Nuf2 and Ndc80 form heterodimers in which protein N- and C-termini orient in the same direction. Next, the Spc24/Spc25 and Nuf2/Ndc80 heterodimers interact at their C-terminal regions to form a four-helix bundle, termed the tetrameric junction. The N-termini of Spc24 and Spc25 fold into RWD domains that target Ndc80 to kinetochores. The N-termini of Nuf2 and Ndc80 fold into CH domains and confer microtubule-binding ability to the Ndc80 complex. The Ndc80 most N-terminal 100 amino acids, after the Ndc80 CH domain, are unstructured and termed the Ndc80 N-terminal tail. Between the Spc24/Spc25 RWD domain and the Nuf2/Ndc80 CH domains, the Ndc80 complex is formed by the Spc24/Spc25 coiled-coil prior to the tetrameric junction, and by the Nuf2/Ndc80 coiled-coil after the tetrameric junction. The Nuf2/Ndc80 coiled-coil is interrupted at ~15-20 nm from the Ndc80/Nuf2 CH domains by a short unstructured segment, termed the Ndc80 loop. The dimensions of the complex estimated from single molecule EM (dashed line) are indicated above.

coiled-coil region. At about one third of the Ndc80 complex length, the C-terminal end of the Spc24/Spc25 coiled-coil forms a groove into which the C-terminal end of the Ndc80/Nuf2 coiled-coil intercalates (Valverde et al., 2016). This region of intercalation between the two heterodimers is termed the Ndc80 complex tetrameric junction. The Nnf1 coil terminates within the tetrameric junction. The Ndc80 coil continues shortly after the tetrameric junction toward the Spc24/Spc25 RWD domains. After the tetrameric junction, the Ndc80 and Nuf2 proteins coiled coils form the rest of the Ndc80 complex coiled-coil region. The Ndc80/Nuf2 coiled-coil is interrupted at ~ 15 - 16 nm from the Ndc80/Nuf2 heads by a ~ 40 amino acid unstructured region in the Ndc80 protein (Maiolica et al., 2007). That interruption in the coiled coil is termed "loop" or "hinge" and allows the Ndc80 complex to hinge (Wang et al., 2009). The loop is not required for Ndc80 complex microtubule binding (Zhang et al., 2012). However, *in vivo*, deletion of the loop results in miss-localisation of outer kinetochore proteins and abolished kinetochore-microtubule end-on attachment formation. The Ndc80 region between the loop and the Ndc80/Nuf2 head is termed the Ndc80 complex lever arm. Bending of the lever arm towards the Ndc80 complex RWD domains has been suggested to represent an auto-inhibited state of the complex (Scarborough et al., 2019). Scarborough and colleagues assayed the conformation of the Ndc80 complex by testing for Förster resonance energy transfer (FRET) between the Ndc80 complex RWD domains and CHD domains. The authors observed FRET between the Ndc80 RWD and CHD domains, showing that the N- and C-termini of the complex are within 10 nm of each other. These data further showed that *in vitro* the Ndc80 complex lever arm is bent at the Ndc80 loop region, thus bringing the Ndc80 complex N- and C-termini in close proximity. Further, the authors aimed to test if Ndc80 complex N- and C-termini interact with each other in this conformation, leading to auto-inhibition of the Ndc80 complex. Incubation of the Ndc80 complex with excess of Spc24 or Spc25 alleviated the FRET signal between the Ndc80 complex N- and C-termini. Therefore, in these *in vitro* conditions, the Ndc80 complex N- and C-terminal domains can bind and cause a conformational change in the complex. However, we cannot exclude that the excess amounts of Spc24 and Spc25 may be facilitating an interaction that does not occur *in vivo*, and thus the observed conformation is not a stable auto-inhibited state in result of Ndc80 complex N- and C-termini binding. An alternate hypothesis that explains the observed FRET signal in absence of Ndc80 complex N- and C-termini

binding is that the Ndc80 lever arm pivots at the point of the Ndc80 loop, thus leading to periods of proximity between the Ndc80 complex N- and C-terminal domains, and FRET generation in the assay by Scarborough and colleagues. Further, the FRET between the Ndc80 complex N- and C-termini was alleviated by incubation the Ndc80 complex with the Mis12 complex, and microtubules. Therefore, binding of the Ndc80 complex to the Mis12 complex or microtubules affects the Ndc80 complex conformation *in vitro*, and may be inhibiting the Ndc80 complex auto-inhibition, if such occurs. However, it is unclear as to whether Ndc80 complex conformational changes and auto-inhibition occurs in cells and what may be the functionality of this re-organisation.

The N-terminal regions of Ndc80 and Nuf2 fold in Calponin homology domains (Wei, Al-Bassam, and Harrison, 2007). The Ndc80 and Nuf2 CH domains together form the second Ndc80 complex head with ~ 7.5 nm lateral dimension and ~ 3.5 nm vertical dimension, as orientated relative to the rod in straightened Ndc80 complex (Ciferri et al., 2008). The CH domains of Ndc80 and Nuf2 bind to microtubules and thus confer to the Ndc80 complex its microtubule-binding ability. The Ndc80 and Nuf2 CH domains bind the groove between two alpha/beta tubulin dimers, and alpha/beta tubulin subunits in a dimer on the microtubule lattice (Alushin et al., 2012). The Ndc80 complex head has also been suggested to bind to the microtubule at an angle, such that head long dimension is at ~ 20 - 60 degrees relative to the microtubule axis (Wilson-Kubalek, et al., 2008, Cheesman et al., 2006). The Ndc80 protein CH domain continues in 80 amino acid unstructured tail at the most N-terminus of Ndc80 (Wei, Sorger, Harrison, 2005). The Ndc80 tail can bind the acidic C-terminal tails of tubulin, termed E-hooks, and thus also contribute to the Ndc80 microtubule-binding affinity. (Alushin et al., 2012). The Ndc80 N-terminal tail has been shown to be phosphoregulated by Aurora B and Aurora A at nine residues. Ndc80 N-terminal tail with residue mutations that mimic phosphorylation at all nine residues abolished kinetochore-K-fibre end-on attachment formation *in vivo* (Umbreit et al., 2012, Wimbish et al., 2020). The phosphorylation of the nine residues further was shown to have additive effect, where as more residues are phosphorylated, less microtubules form end-on attachment to the kinetochore (Zaytsev et al., 2015). Mutagenesis of the nine residues to non-phosphorylatable residues resulted in hyper-stable attachments between the kinetochore and microtubules (DeLuca et

al., 2011). Therefore, dynamic phosphorylation of the tail is essential for wild type function of the complex and successful kinetochore congression *in vivo*. The Ndc80 N-terminal tail has also been implicated in Ndc80 oligomerisation (Alushin et al., 2010, Jankzyk et al., 2017) based on the following evidence: (1) truncated Ndc80 complexes (Ndc80 lacking 68 percent of the coiled-coil region, Ndc80 "Bonsai") were shown to cluster on microtubules *in vitro* (Alushin et al., 2010), and (2) the clustering behaviour was abolished by deletion of the Ndc80 Bonsai N-terminal. However, as to whether the Ndc80 complex can also cluster *in vivo* and what are the clustering functions remain open questions.

Roles of the Ndc80 complex

The Ndc80 complex has three main functions: (1) The Ndc80 complex is essential for kinetochore end-on attachment to K-fibres, (2) The Ndc80 complex N-terminal head provides a platform for the binding of the master SAC kinase MPS1 (this Ndc80 function will be discussed in section 1.4), and (3) The Ndc80 complex likely contributes to kinetochore-microtubule force-coupling (Ciferri, Mussachio and Petrovic, 2007). Here, I will focus on the proposed roles of Ndc80 in force-coupling. Ndc80 was first implicated as a force-coupling molecule based on the following evidence: (1) optical trap experiments showed that the Ndc80 complex can transduce the force of depolymerising microtubule +end to Ndc80-covered polystyrene bead under load (Powers et al, 2009; Helgeson et al., 2018). (2) Ndc80 complex ensembles were shown to diffuse on the microtubule lattice and at encounter of the depolymerising microtubule +end appeared to predominantly 'bounce off' and remain bound to the lattice (Powers et al, 2009).

Further, the above Ndc80 complex ensemble behaviour resembles a proposed theoretical model for microtubule +end tracking in which an energy gradient at the microtubule +end makes diffusion on the lattice away from the tip more favourable than molecule unbinding (biased diffusion) (Hill, 1985; Powers et al., 2009). The theoretical model further suggested biased diffusion to be sufficient for coupling microtubule +end depolymerisation to congression while also posed the requirements of (1) weak binding by the individual molecules and (2) ensemble formation (Hill, 1985). Consistent with the first model requirement, the Ndc80 complex interacts weakly with microtubules via transient electrostatic interaction of the Ndc80 and Nuf2 N-termini with the tubulin dimeric interface (Alushin et al, 2010; Alushin et al,

2012). Further, the following data argue that the Ndc80 complex behaviour is consistent with the second model requirement: (1) single Ndc80 complex molecules did not track with depolymerising microtubule + ends and diffused on the microtubule lattice (Powers et al., 2009). (2) when Ndc80 oligomerisation was promoted incubation with an Ab against Spc24, the Ndc80 complex large excursion were abolished and the complex ensemble tracked prominently with depolymerising microtubule +ends (Powers et al., 2009). Can the Ndc80 complex form ensembles *in vivo*? The human kinetochore contains 8 – 10 Ndc80 complex molecules per kinetochore microtubule and thus Ndc80 ensemble formation is theoretically possible (Johnston et al., 2010). How may the Ndc80 complexes form an ensemble? The Ndc80 complex may self-assemble into oligomeric ensembles (clusters) on microtubules, as suggested by *in vitro* data (Alushin et al., 2010). Alternatively, the two Ndc80-inner kinetochore linkers: phosphorylated CenpT and CenpC/Mis12, each bind several Ndc80 complex molecules, and thus can lead to an Ndc80 complex ensemble (Huis In 't Veld et al., 2016; Gascoigne et al., 2011; Kim and Yu, 2015; Suzuki et al., 2015; Malvezzi et al., 2013; Nishino et al., 2012; Przewloka et al., 2011; Screpanti et al., 2011; Volkov et al., 2018). Therefore, the Ndc80 complex can theoretically provide force-coupling between the depolymerising microtubule end and the kinetochore. However, this role of Ndc80 is not yet confirmed in cells. Further, in absence of the Ska complex, the Ndc80 complex alone is not sufficient to provide the attachment stability between kinetochores and depolymerising K-fibres required for successful congression and anaphase onset. The Ndc80 complex targets the Ska complex to kinetochores (see next section). The Ska complex is currently the prime candidate for kinetochore-K-fibre force-coupling molecule *in vivo*, albeit its interplay with Ndc80 in achieving force-coupling remains unclear.

1.3.3 The Spindle and kinetochore associated (Ska) complex

Structure of the Ska complex

The Ska complex is a homodimer of two assemblies of Ska1, Ska2 and Ska3 (Figure 1.7). To form the complex, the first helical domains in Ska1, Ska2 and Ska3 interwind and form two roughly parallel bundles of three helices (Jeyaprakash, et al., 2012). The resulting molecule is L-shaped with a shorter N-terminal helical bundle and longer C-terminal helical bundle, which are connected by a flexible loop region

(Jeyaprakash, et al, 2012). The full Ska complex forms from two of these L-shaped Ska1/Ska2/Ska3 molecules through an interaction between their short N-terminal bundles in a face-to-face orientation. This creates a W-shaped molecule with the Ska1 and Ska3 C-termini protruding from each arm, see Fig. 4 (Jeyaprakash, et al, 2012). The Ska1 C-terminus contains a loop (Ska192-132) and a following winged helix motif (Ska1 132-255) (Abad et al, 2014). The Ska3 C-terminus (Ska3 102-412) structure is unknown. The Ska3 C-terminus cross-links internally at many residues in cross-linking mass spectrometry, suggesting proximity of regions of the Ska3 C-terminus, and disordered or globular organisation of the domain. Further, the Ska3 C-terminus is suggested to attain extended unstructured conformation when phosphorylated at amino acids 358 and T360 by CDK1.

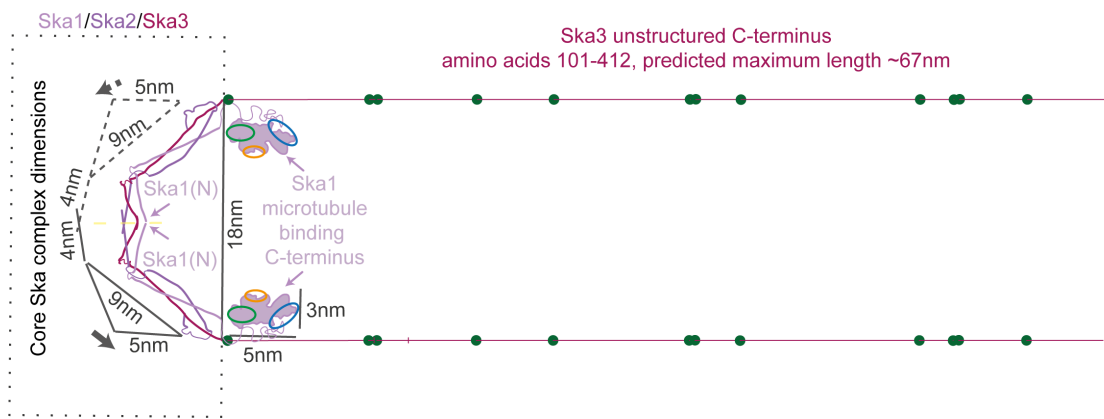


Figure 1.7: Structure of the Ska complex Schematic of the available structural information on the Ska complex. Abad et al., 2014; Abad et al., 2016. The Ska1 microtubule interaction sites are denoted with ellipses. Phosphorylation sites in the Ska3(C) are labelled with green dots. Zhang et al., 2017; Huis In't Veld et al., 2019. Ska3 unstructured C-terminus length is estimated based on 0.214 nm distance between the residues of two amino acid (Heyrovska, 2008).

Ska complex interactions with microtubules

The Ska complex interacts with microtubules through the Ska1 and Ska3 C-terminal domains (Jeyaprakash, et al, 2012). Both domains have been shown to interact with surface residues of alpha- and beta-tubulin (Abad et al, 2014; Abad et al, 2016; Schmidt et al, 2012). The Ska1 C-terminal winged helix motif is responsible for the high-affinity binding of the complex to microtubules via three interacting regions (see Figure 1.7; Abad et al, 2014; Jeyaprakash, et al, 2012). In its absence,

the full complex assembles but binding to microtubules is almost fully abolished (Jeyaprakash, et al, 2012). In contrast, the Ska3 C-terminal domain interacts only weakly with microtubules and its deletion results in only a slight reduction in the microtubule binding affinity (Abad et al, 2016; Jeyaprakash, et al, 2012). The Ska1 and Ska3 C-terminal domains also form interactions with each other that moderately increase the microtubule-binding properties of the complex (Abad et al, 2016). Therefore, the Ska1 C-terminal winged helix motif is the major microtubule-binding region while the Ska3 C-terminal domain and the interactions between these two regions only facilitate microtubule-binding.

Targeting of the Ska complex to kinetochores

The complete mechanism of Ska complex recruitment to kinetochores is currently unclear and likely involves several factors. Ska is thought to be recruited to kinetochores by directly binding the Ndc80 complex as removal of Ndc80 leads to undetectable kinetochores amounts of Ska *in vivo* (Zhang et al., 2012). The interaction between Ska and the Ndc80 complex is further supported by the following *in vitro* evidence: (1) Ndc80 covered beads to which Ska is added in solution form microtubule attachments with increased rupture force (Helgeson, et al, 2018), (2) Ndc80 ‘Broccoli’ tracks with depolymerising microtubule +ends if Ska is added in solution but not on its own (Schmidt et al., 2012), and (3) electron microscopic tomography study showed that Ndc80 ‘Bonsai’ (Ndc80 complex from which most of the rod-like region is truncated) recruits Ska to microtubules and induces Ska conformational change such that the Ska N-terminus is closer to the microtubule lattice (Janczyk et al., 2017). However, what are the interaction sites in Ska and the Ndc80 complex remains unknown.

The Ska3 C-terminus is the prime candidate for the Ndc80 binding site of Ska based on the following evidence: (1) Ska complex with truncated Ska3 C-terminus (Ska1/Ska2/Ska3 Δ C) does not localise to kinetochores *in vivo* (Jeyaprakash, et al, 2012), (2) Ska1/Ska2/Ska3 Δ C added in solution does not increase the microtubule attachment rupture force of Ndc80-coupled beads, in contrast to wild type Ska complex (Helgeson, et al, 2018). The Ska3 C-terminal domain does not significantly contribute to Ska microtubule binding, and thus the change in attachment stability is likely due to abolished interaction between Ska and Ndc80 (Helgeson, et al, 2018; Abad et al, 2016; Jeyaprakash, et al, 2012). (4) phosphorylation of the Ska3 C-

terminus residues T358 and T360 by Cdk1 is required for high affinity Ska-Ndc80 interaction *in vitro*, and for Ska kinetochore localisation *in vivo* (Huis In't Veld et al., 2019; Zhang et al., 2017). Further, phosphorylation of Ska3 at these residues does not affect the Ska microtubule binding *in vivo* (Zhang et al., 2017). Therefore, Ska3 phosphorylation directly mediates the Ndc80-Ska interaction.

Another candidate for kinetochore targeting of the Ska complex is the Ska1 MTBD. Ska complex with Ska1 lacking the MTBD has reduced kinetochore localisation, equal to about 30% of the kinetochore localisation of the wild type Ska complex at metaphase kinetochores (Auckland et al., 2017; Jeyaprakash et al., 2012; Janczyk et al., 2017). However, the Ska1 MTBD may facilitate Ska kinetochore localisation indirectly as it is essential for Ska microtubule-binding. Indeed, the reduction of kinetochore Ska levels observed after deletion of the Ska1 MTBD is similar to the kinetochore Ska reduction observed in absence of microtubules after Nocodazole treatment (Auckland et al., 2017; Chan et al., 2012; Sivakumar et al., 2014). Furthermore, *in vivo* the Ska complex accumulates at kinetochores as they congress by DCP and acquire microtubule attachments (Auckland et al., 2017). Therefore, it is likely that the Ska1 MTBD enables Ska microtubule binding that in turn allows for Ska accumulation at kinetochores. The current view of how microtubule binding drives Ska accumulation at kinetochores is that kinetochores 'swipe off' Ska from the microtubule during DCP (Auckland et al., 2017).

Another region implicated in Ska kinetochore targeting is the Ska1 C-terminal loop (Ska192-132). Deletion of the Ska1 C-terminal loop and its replacement with a short linker (GSSG) abolishes Ska targeting to kinetochores *in vivo* (Abad et al., 2014). One hypothesis is that the Ska1 loop may abolish Ska kinetochore localisation indirectly by preventing the attachment of Ska to microtubules. However, truncation of the Ska1 MTBD reduces but does not abolish the kinetochore localisation of the Ska complex (Auckland et al., 2017; Jeyaprakash et al., 2012; Janczyk et al., 2017). Therefore, the Ska1 C-terminal may be involved in direct interaction with Ndc80 complex or another kinetochore protein.

In addition, Ska may be promoting its own kinetochore targeting by self-oligomerisation (Welburn et al., 2009). Welburn and colleagues observed clusters of Ska complex when incubated with microtubules (electron microscopy). However, self-oligomerisation of Ska has been observed only *in vitro*, and has not been reported in other Ska *in*

in vitro studies. Therefore, whether Ska can self-oligomerise and facilitate its own kinetochore recruitment *in vivo* remain open questions.

What are the regions in the Ndc80 complex that interact with Ska? The Ndc80 coiled-coil region, the Ndc80 loop and the Ndc80 N-terminal tail have all been implicated as Ska interacting regions. However, the data in the field is currently controversial.

One hypothesis is that the phosphorylated unstructured Ska3 C-terminus binds to the Ndc80 coiled-coil regions. Consistent with that model, mass-spectrometry assays mapped the phosphorylated and unphosphorylated Ska3 C-terminus to be in close proximity to the Ndc80 complex coiled-coil regions (Helgeson, et al, 2018). Further, single particle *in vitro* EM showed that phosphorylated Ska (labelled with the streptavidin:treptavidin particle) appears to float around the Ndc80 coiled-regions and N-terminal tail. However, this model does not explain why *in vitro* Ndc80 ‘Bonsai’ that lacks most of the Ndc80 coiled-coil regions and the Ndc80 loop, can still bind Ska (Janczyk et al., 2017; Ciferri et al., 2016).

Another study implicated the Ndc80 loop as the Ska interaction site. Deletion of the Ndc80 loop region, or its replacement with the reverse sequence, reduced kinetochore Ska levels to different degrees (Zhang et al., 2012). However, in both cases the Ndc80 complex failed to form end-on attachments and reduction in other kinetochore protein levels was also observed (Zhang et al., 2012). Therefore, the observed effect may be indirect and stem from perturbations in the system.

Yet another set of studies implicated the Ndc80 N-terminal tail into Ska kinetochore targeting. In mass-spectrometry studies the Ska3 C-terminus also cross links with the Ndc80 N-terminal tail which suggests proximity of the two protein regions (Huis In’t Veld et al., 2019). Further, mutagenesis studies showed that charge mutations in the Ndc80 tail can affect Ska kinetochore localisation (Janczyk et al., 2017). Janczyk and colleagues mutated the C-terminal part of the Ndc80 tail region (Ndc80 +4CT, Ndc80^{K(42,47,53,59)A,R(52,60)A}). *In vivo*, expression of Ndc80 +4CT led to 50% reduction in Ska kinetochore levels and, consistent with loss of Ska, the cells displayed increased occurrence of unaligned kinetochores and profound metaphase arrest (Janczyk et al., 2017, Auckland et al., 2017; Hanisch et al., 2006; Daum et al., 2009; Gaitanos et al., 2009; Theis et al., 2009; Welburn et al., 2009; Jeyaprakash et

al., 2012; Schmidt et al., 2012; Abad et al., 2014; Makiejowski et al., 2017; Cheerambathur et al., 2017). Furthermore, Ndc80 ‘Bonsai’ +4CT did not enrich the microtubule bound population of Ska in electron tomography assay in contrast to wild type Ndc80 ‘Bonsai’ (Janczyk et al., 2017). These data suggested that Ndc80 +4CT is unable to bind Ska as efficiently. Furthermore, Ndc80 +4CT did not affect kinetochore Ska levels due to abrogated microtubule binding as: (1) Ndc80 +4CT did not display change in microtubule binding affinity *in vitro*, (2) formed end-on attachments *in vivo* and (3) in absence of microtubules, the Ndc80 +4CT mutant displayed 50% reduction in kinetochore Ska levels as compared to Ndc80 wild type in the same condition. In addition, Janczyk and colleagues showed that *in vitro* the Ndc80 +4CT does not oligomerise similar to when the Ndc80 N-terminal tail is deleted. Therefore, the only changes in Ndc80 +4CT behaviour detected were its inability to oligomerise *in vitro* and its reduced ability to load Ska *in vivo* (Janczyk et al., 2017). These data suggested that ~50% of Ska kinetochore accumulation may depend on Ndc80 oligomerisation. Alternatively, the N-terminal tail of Ndc80 may be involved in direct binding of Ska and the mutation may be abolishing one pool of kinetochore-bound Ska. This study also assayed the effects of mutations in the N-terminal part of the Ndc80 N-terminal tail (Ndc80 +4N, Ndc80^{K(2,26,35)A,R(3,13,20)A}) (Janczyk et al., 2017). Ndc80 +4N was deficient in kinetochore alignment and could not form end-on attachments. Strikingly, the mutant recruited Ska to kinetochores with efficiency comparable to Ndc80 wild type in late prometaphase cells. Therefore, charge reversal in the Ndc80 N-terminal tail could facilitate Ska recruitment. However, a caution is required because recent study performed in two types of human cells (HeLa and RPE1) showed that the Ndc80 N-terminal tail is not required for Ska localisation to kinetochores per se as deletion of the region did not abrogate Ska kinetochore localisation (Wimbish et al., 2020). This is in contrast to the study by Janczyk and colleagues, where deletion of the tail abolished Ska kinetochore localisation. Therefore, whether the Ndc80 N-terminal tail plays a role in Ska recruitment remains questionable.

In summary, Ska kinetochore localisation is dependent on Ndc80, Ska and Ndc80 binding to microtubules, and phosphorylation of Ska3 by Cdk1. Multiple sites of Ska and Ndc80 have been implicated in the interaction, with the favoured ones being the Ska3 C-terminus and the Ndc80 coiled region. However, further evidence

is required to understand how Ska and Ndc80 bind in cells and how is Ska loaded to kinetochores.

Roles of Ska in force generation in congression

In yeast, the force of curving microtubule protofilaments is utilized for congression by the Dam1 complex. Dam1 forms ring-shaped assemblies around the microtubule that slide as protofilaments peel off in ‘rams horn’ conformation at the depolymerising microtubule + end (Grishchuk et al., 2008; Miranda et al., 2005; Umbreit et al., 2014; Westermann et al., 2005; Tong Ng et al., 2019). Furthermore, Dam1 is recruited to kinetochores by binding to the Ndc80 complex and is required for stable kinetochore-microtubule attachment *in vivo* (Cheesman et al., 2001; Umbreit et al., 2014; Maure et al., 2011; Nogales and Ramey, 2009). However, no orthologue of Dam1 is found in mammalian cells. Several lines of experimental evidence suggest that the Ska complex is the functional Dam1 homologue in mammalian cells. Firstly, Ska can track with depolymerising microtubule +ends *in vitro* (Schmidt et al., 2012; Welburn et al., 2009). Ska has been shown to transduce the force of depolymerising microtubule +ends to a Ska-coated bead under load *in vitro* (Welburn et al., 2009) and *in vivo* depletion of the Ska complex causes congression defects (Abad et al., 2014; Hanisch et al., 2006; Jeyaprakash et al., 2012; Chan et al., 2012; Gaitanos et al., 2009; Schmidt et al., 2012; Welburn et al., 2009). More specifically Ska depletion causes detachment of the P kinetochore under high load in congression (Auckland et al., 2017). Ska recruitment is dependent on Ndc80-C similar to Dam1 in yeast, (Zhang et al., 2012; Maure et al., 2011), and two studies show that Ska could assist the Ndc80-C in forming stable attachments to depolymerising microtubule +ends *in vitro*. Ska binds straight and curved protofilaments with equal preference and does not display biased diffusion like Ndc80-C (Schmidt et al., 2012). Therefore, Ska could track with depolymerising microtubule +ends by stable association with the tip or by formation of a force-coupling ring as Dam1. In support of the later, the Ska complex has been shown to self-oligomerise *in vitro* (Welburn et al., 2009). Therefore there is mounting evidence that Ska may represent the mammalian orthologue of Dam1.

The Ska complex was further established as an essential force-coupling molecule in congression via *in vivo* studies. In early studies, abrogation of the Ska complex *in*

in vivo has been found to cause metaphase arrest, and ‘escaping’ of chromosomes from the metaphase plate (Hanisch et al., 2006; Daum et al., 2009; Gaitanos et al., 2009; Theis et al., 2009; Welburn et al., 2009; Jeyaprakash et al., 2012; Schmidt et al., 2012; Abad et al., 2014). However, the severity of congression defects reported by these studies was very variable, probably due to low temporal resolution imaging of labelled DNA and varying efficiency of Ska depletion by RNAi. Also, one study reported loose chromatid cohesion in fixed cell assay of Ska depleted cells (Daum et al., 2009). However, later study found that the prolonged metaphase arrest causes cohesion fatigue that has been initially misidentified by Daum and colleagues as Ska-depletion phenotype (Daum et al., 2011). Recently, a more detailed approach was taken by Auckland and colleagues where bi-oriented kinetochore pairs were followed in congression in wild type and Ska depleted HeLa cells (Auckland et al., 2017). The results of this study were also confirmed with transient CRISPR/Cas9 Ska knock-out, and thus provided a reliable read-out of the *in vivo* functions of Ska. The authors described an event, named flipping, that is particularly enhanced in Ska depleted cells but has been overlooked in previous studies due to the less detailed imaging. In this event, as the congressing bi-oriented kinetochore pair approached the plate, the P kinetochore rotated 90 degrees and simultaneously the inter-sister distance dropped to distance observed at unattached kinetochore pairs. Flipping can be explained by the P kinetochore suddenly losing grip of the depolymerising k-fibre tip that is pulling it. The loss of attachment virtually always occurred at the P kinetochore (Auckland et al., 2017). The P kinetochore powers the motion of the kinetochore pair and is bound to more depolymerising microtubule +ends than the AP kinetochore, and thus the P kinetochore is likely to be subjected to higher force than the AP kinetochore. Therefore, flip events have been suggested to occur if the kinetochore experiences a pulling force that is too high for it to sustain. This hypothesis was further confirmed by observations that reduced force at kinetochores alleviated the frequency of flip events. The increased frequency of flip events in Ska depleted cells suggests that in absence of Ska, kinetochores can sustain less force, and thus more frequently detach under load. Here it needs to be noted that all kinetochores eventually congressed, probably by utilizing another force-coupling protein and DCP, or by lateral sliding (Auckland et al., 2017). Interestingly, the flipped kinetochores in absence of Ska underwent series of flip-rebinding cycles and did not congress within 5 mins (Auckland et al., 2017). Therefore, kinetochores

lacking Ska could not form a load-bearing attachment after repeated trials. In contrast, flipped kinetochores in wild type cells rebound and successfully congressed. Therefore, the initially formed attachment was mechanically unstable under high load but it was ‘corrected’ after the flip.

A possible explanation of what in first place causes kinetochore flip in control cells comes from the observation that kinetochores progressively accumulate both Ska and microtubules as they congress by DCP, and thus mature (Figure 1.8; Auckland et al., 2017). Therefore, imbalance of these two events may create unstable attachments and cause flipping. In this respect, flip events could serve as a mechanical self-check to ensure that mature attachments are formed prior to anaphase onset.

However, this model needs further investigation: Is Ska recruitment to kinetochore progressive? As discussed, Ska is loaded to higher extent at aligned as compared to unaligned kinetochores. However, the dynamics of the Ska kinetochore-loading process remain unknown. Therefore, a future live-cell study Ska kinetochore accumulation with high spatio-temporal resolution is required to understand as to whether Ska is loaded to kinetochores progressively, and as to whether Ska recruitment correlates with kinetochore maturation. If such correlation is observed, the next critical questions will be: Is kinetochore maturation a prerequisite for Ska loading or is Ska loading a prerequisite for Ska maturation? Therefore, understanding of the dynamics of Ska kinetochore loading has critical implication in understanding how kinetochores mature and form stable attachments that are compatible with anaphase onset.

1.3.4 Knl1

Knl1 (kinetochore scaffold protein 1) serves as a platform for the assembly of the spindle assembly checkpoint signalling proteins. In this section I will outline the structural and functional domains of Knl1 while its functions in SAC assembly and silencing will be discussed in the next chapter.

Knl1 is 2342 amino acid protein with low structural complexity which is unsurprising given its role as a scaffold protein (Ghongane et al., 2014). The only defined structure in Knl1 is the C-terminus which forms a RWD domain followed by alpha helix region (Petrovic et al., 2010). The RWD domain of Knl1 interacts with the NSL1

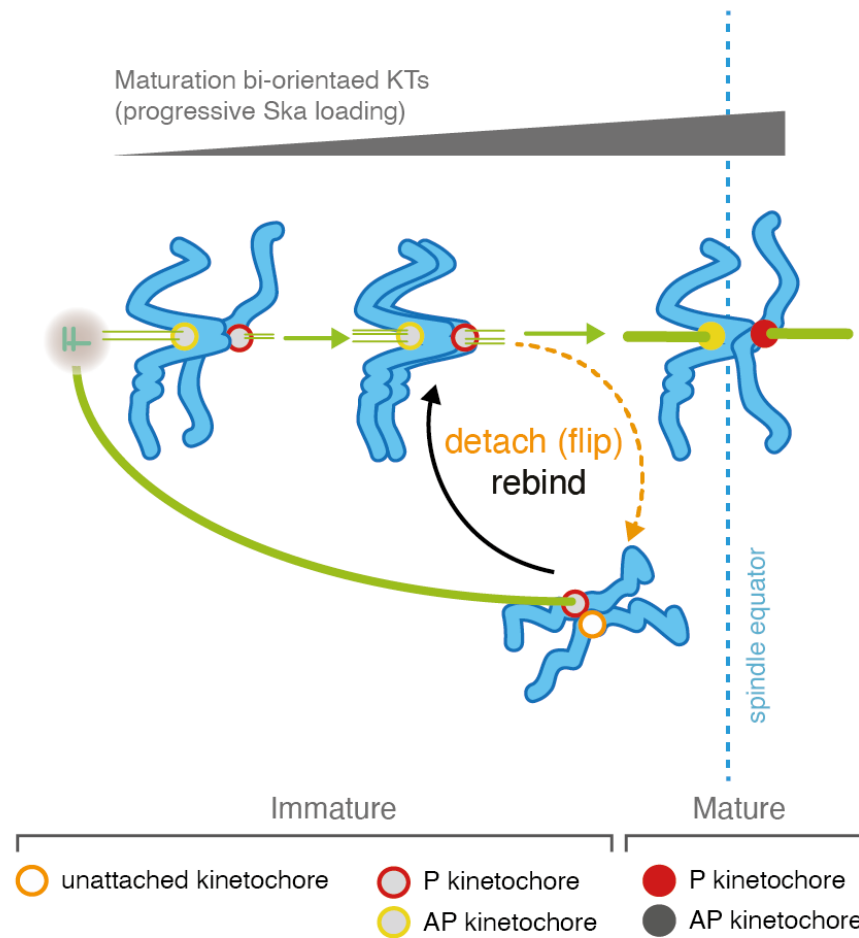


Figure 1.8: Model for Ska kinetochore loading dynamics and function at kinetochores Kinetochores progressively accumulate microtubule attachments as they congress to the spindle equator in prometaphase. As kinetochores congress, kinetochores also load Ska to stabilise the kinetochore-microtubule attachments. The process of progressive microtubule attachment and Ska accumulation is suggested to be the long-suspected process of kinetochore maturation. If there is an imbalance in the process such that the kinetochore accumulates microtubule attachments too fast or does not load sufficient amount of Ska, the microtubule attachment cannot be sustained. Consequently, the P kinetochore detaches, an event detected as kinetochore "flip", and attempts again to form a mature attachment. Auckland et al., 2017.

protein of the Mis12 complex and targets Knl1 to kinetochores (Petrovic et al., 2010, Petrovic et al., 2014, Cheeseman et al., 2006; Kiyomitsu et al., 2007; Petrovic et al., 2016, Cifferi et al., 2008;). The Knl1 C-terminus also recruits Zwilch to kinetochores (Petrovic et al., 2010). Following the Knl1 C-terminus, the protein is mainly unstructured. In the unstructured region five functional motifs have been identified: (1) MELT and MELT-like motifs, (2) KI motifs, (3) SILK, (4) RVSF, and (5) $\phi\phi$ motifs (Figure 1.9).

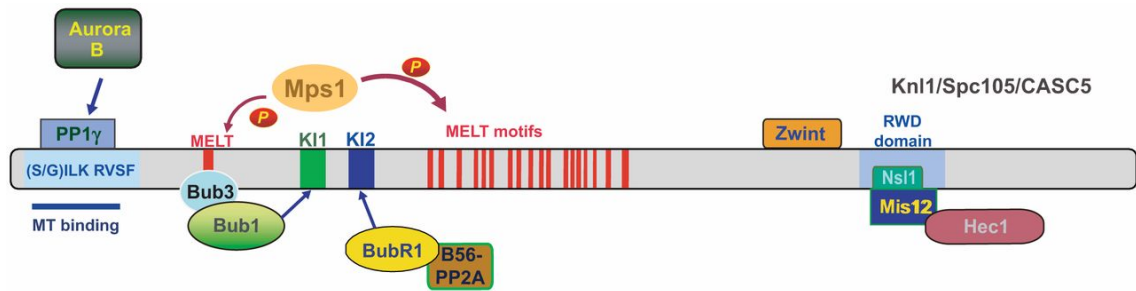


Figure 1.9: Functional organisation of Knl1. Schematic indicating the relative position of the identified Knl1 functional domains: SILK/RVSF (light blue), MELT (red) repeats, KI1 (green), KI2 (dark blue), RWD domain (navy blue). The SILK and RVSF domain of Knl1 bind competitively to PP1 and microtubules. The Knl1 MELT motifs bind to Bub3:Bub1 upon phosphorylation by Mps1. That further enables the Knl1 KI1 and KI2 regions to bind to Bub1 and BubR1. The Knl1 C-terminus contains a RWD domain that interacts with Mis12, and thus targets Knl1 to kinetochores. Ghongane et al., 2014

MELT and MELT-like motifs

The Knl1 MELT and MELT-Like motifs (consensus sequence (M/I/L/V)-(E/D)-(L/M/I/V)-(T/S)) are distributed along the Knl1 N-terminus and have been shown to be required for Bub1/Bub3 complex recruitment to kinetochores. The recruitment of Bub1/Bub3 to kinetochores was further shown to be dependent on phosphorylation of the threonine at position 4 in the MELT by the master SAC kinase Mps1 (London et al., 2012; Primorac et al., 2013; Shepperd et al., 2012; Yamagishi et al., 2012). The human Knl1 N-terminus contains 19 MELT motifs that can contribute to different extents in recruitment of Bub1/Bub3. For example, mutagenesis studies showed that 6 repeats of MELT17 are sufficient for functional SAC signaling, while 6 repeats of MELT2 do not support the SAC function (Vleugel et al., 2015). Therefore, the MELT motifs harbour different affinity for Bub1/Bub3 or suitability for phosphorylation by Mps1 (Primorac et al., 2013; Zhang et al., 2014; Vleugel et al., 2015). The different contributions of the MELTs were first suggested to be redundant as the number of MELT motifs highly varies between species (Ghongane et al., 2014). Another hypothesis is that the high number of MELT repeats is evolutionary trait that allows Knl1 to fine tune the SAC signaling (Ghongane et al., 2014). Based on that hypothesis, the variety in MELT affinity for Bub1/Bub3 can allow Knl1 to incorporate a number of mechanical and chemical stimuli and alter the SAC signaling in accordance.

KI motifs

Knl1 contains two KI (Lysine-isoleucine) motifs with consensus sequence of KI(D/N) FxxF (L/I)xRL. The two KI motifs are located at the Knl1 N-terminus and are flanked by MELT motifs. The Knl1 KI motifs also act in the recruitment of SAC signalling proteins to kinetochores. In specific, KI1 recruits Bub3 and KI2 recruits BubR1 to kinetochores (Kiyomitsu et al., 2007; Kiyomitsu et al., 2011). However, mutagenesis studies showed that neither KI1 nor KI2 is required for recruitment of Bub1 and BubR1 to kinetochores (Krenn et al., 2012; Yamagishi et al., 2012). In addition, the KI motifs were shown to require at least one MELT motif to interact with the SAC proteins (Krenn et al., 2012; Vleugel et al., 2015, Primorac et al., 2013). One hypothesis is that the MELT motifs provide large unstructured surface around the KI motifs and thus attract Bub1 and BubR1 to the KI motifs, that then serve as facilitators for the SAC signaling establishment (Ghongane et al., 2014).

RVSF, SILK and $\phi\phi$ motifs

The SILK (consensus sequence), RVSF (consensus sequence) and $\phi\phi$ (consensus sequence) motifs are located at the far N-terminus of Knl1 and bind to the SAC silencing phosphatase PP1 (Bajaj et al., 2018, Liu et al., 2010; Rosenberg et al., 2011). These motifs have also been shown to be phosphorylated by the Aurora B kinase which downregulates the ability of SILK and RVSF to bind PP1 (Liu et al., 2010). A main role of the Knl1-bound PP1 pool is also to dephosphorylate Aurora B targets and silence the SAC (Lesage et al., 2011; Espeut et al., 2012). Therefore a negative feedback loop is formed where PP1 binds the N-terminus of Knl1 and counteracts Aurora B activity, while Aurora B phosphorylation of the Knl1 N-terminus negatively affects PP1 binding to Knl1. Interestingly, the Knl1 N-terminus has been found to also be required for Aurora B function, as its deletion abolishes Aurora B target phosphorylation (Caldas et al., 2013). In addition the most N-terminus of Knl1 (residues 17-24), and the SILK and $\phi\phi$ motifs interact directly with microtubules (Bajaj et al., 2018). Albeit all of the three regions are involved in the Knl1-microtubule interaction, only the most N-terminus of Knl1 is required for Knl1-microtubule binding. Further, co-sedimentation studies showed that the Knl1 N-terminal region (Knl1¹⁻⁸⁰) has higher affinity for PP1 as compared to microtubules *in vitro*. After incubation of Knl1¹⁻⁸⁰ with PP1 and microtubules, Knl1¹⁻⁸⁰ remained in the supernatant and, in contrast to when Knl1¹⁻⁸⁰ is incubated with microtubules only, did not pellet with the microtubules. Therefore, the binding of Knl1¹⁻⁸⁰ to PP1 and microtubules is mutually exclusive and Knl1¹⁻⁸⁰ harbours much stronger affinity for PP1 as compared to microtubules. Nevertheless, whether the overlapping of PP1 and microtubule binding sites in Knl1 can potentially serve as an important readout that connects the kinetochore attachment status and SAC silencing remains to be investigated.

1.4 The Spindle assembly checkpoint signaling

1.4.1 Overview

The Spindle assembly checkpoint (SAC) delays anaphase onset until all kinetochores have formed bi-oriented attachments to spindle microtubules. This is an essential pre-requisite for the equal segregation of the duplicated genomic material during

mitosis. Premature silencing of the SAC or SAC mis-function can lead to abnormal chromosome numbers in the daughter cells, a phenomenon known as aneuploidy. Aneuploidy is well established as a hallmark of cancer and relates to poor prognosis in patients (Bharadwaj and Yu, 2004). Therefore, elucidating the molecular basis of SAC signalling in mammalian cells is essential to understand how genome stability is ensured.

The Anaphase Promoting Complex/Cyclosome (APC/C) is a 15-subunit polyubiquitin ligase, whose robust inhibition and timely activation is essential for the correct progression of mitosis. APC/C is activated by phospho-dependent binding to its co-activator Cdc20 (Kramer et al., 2000; Hershko et al., 1999; Dawson et al., 1995). Once activated, the APC/C ubiquitinates target proteins for degradation (Hershko et al., 1999). These include securin, the protein that guards sister-chromatid centromere cohesion (Alberts et al., 2002). Once securin is degraded, the protein separase is able to cleave the cohesin link that binds the two sister-chromatids allowing their separation at anaphase onset.

The inhibition of the APC/C complex from beginning of mitosis until the kinetochores have formed mature bi-oriented attachments is therefore essential for correct chromosome segregation and timely anaphase onset (Kramer et al., 2000). The SAC machinery is responsible for inactivation of the APC/C during mitosis, and for sensing when all kinetochores have formed bi-oriented attachments such that it can quickly alleviate the inhibition and allow the cell to progress into anaphase. Therefore, next I will discuss (1) how the SAC assembles and acts to inactivate the APC/C, (2) how is the SAC silenced, and (3) how the SAC reads out the kinetochore-K-fibre attachment status.

1.4.2 SAC assembly

At the start of prometaphase, all kinetochores are initially unattached. Unattached kinetochores recruit checkpoint proteins required to catalyse the inhibitor of the APC/C, called the mitotic checkpoint complex (MCC). The exact mechanism of MCC assembly at kinetochores is still under debate but the fundamentals are well documented (Sudakin, Chan and Yen, 2001; Silio et al., 2015; Currie et al., 2018, Zhang et al., 2019). Briefly, MCC is composed of four proteins: BubR1, Bub3, Mad2 and the APC/C coactivator Cdc20. Its role is to sequester Cdc20 away from

APC/C to inhibit its ubiquitination function and keep the cell in mitosis.

A platform for Mad1:Mad2 recruitment to kinetochores is established by Bub1:Bub3, and Bub1:BubR1 bound to Knl1; the KBB pathway (Silio et al., 2015; Currie et al., 2018, Zhang et al., 2019). Here Mad1:Mad2 bind directly to Bub1. However, the Rod-Zwilch-Zw10 (RZZ) complex is thought to provide a second pathway for targeting of Mad1:Mad2 to unattached kinetochores in higher organisms (Silio et al., 2015, Zhang et al., 2019). The exact dynamics of SAC signalling in mammalian cells therefore remain unclear.

The KBB pathway: At the beginning of prometaphase, the Knl1 SILK and RSVF motifs are first phosphorylated by Aurora B (Nijenuis et al., 2014). Then, Mps1 is targeted to kinetochores via the Ndc80 N-terminus and phosphorylates the Knl1 MELT motifs (Stucke, Baumann and Nigg, 2004; London et al., 2012, Shepperd et al., 2012). The MELT motif phosphorylation and Mps1 activity is also sustained by Plk1 phosphorylation (Ikeda and Tanaka, 2017). Mps1 is further phosphorylated by Cdk1 and autophosphorylates itself in trans to reach full kinase activity (Kang et al., 2007; Morin et al., 2012). This possibly amplifies Mps1 activity such that it can rapidly establish SAC signalling. When the MELT motifs are phosphorylated Bub1 and Bub3 bind to Knl1 as a heterodimer (Bub1:Bub3), followed by BubR1:Bub3 (Shepperd et al., 2012; Mora-Santos et al., 2016). Mps1 further phosphorylates Bub1 and allows it to recruit Mad1:Mad2 to kinetochores (Mora-Santos et al., 2016, Ji et al., 2017). Mad1 is then further phosphorylated by Mps1 to stimulate MCC formation.

Mad2 can obtain two conformations: Open (O-Mad2) and Closed Mad2 (C-Mad2) (Luo et al., 2002, De Antoni et al., 2015). The default conformation of Mad2 is O-Mad2. Kinetochores-bound Mad1 binds to O-Mad2 and catalyses its conversion to C-Mad2, which can bind and sequester the APC/C activator, Cdc20. The Mad1:C-Mad2 complex catalyses the conversion of free cytosolic O-Mad2 into C-Mad2, allowing more Cdc20 to be sequestered and the SC signal to be amplified.

The RZZ pathway: A second pathway for the recruitment of Mad1:Mad2 to kinetochores is suggested to be via the Rod:Zwilch:Zw10 (RZZ) complex. Here, Zwint1 binds to Mis12:Knl1 and targets the RZZ to kinetochores (Kops et al, 2005). The targeting of Mad1:Mad2 to kinetochores via the RZZ has been shown to be

essential for SAC activation (Kops et al, 2005; Zhang et al., 2019). However, the exact mechanisms of SAC activation by RZZ are not that well understood, and the Mad1:Mad2 binding site remains unknown.

1.4.3 SAC silencing upon microtubule attachment

The clue that leads to satisfying of the SAC and subsequent SAC silencing is kinetochore-microtubule end-on attachment (Kuhn and Dumont, 2017, Etemad et al, 2018, Dudka et al., 2018). Firstly, once the kinetochore establishes microtubule attachment, the RZZ SAC pathway is silenced mechanically by "stripping" of the RZZ from kinetochores (Mosalaganti et al., 2017). This 'stripping' mechanism is mediated by the dynein adaptor Spindly, which is bound to ZW10 and dynein at unattached kinetochores (Gassmann et al, 2010, Kops et al., 2005). Once the kinetochore binds a microtubule, dynein is activated and initiates poleward transport along the microtubule towards the pole (Gassmann et al., 2010). As dynein carries the RZZ complex as cargo as it leaves the kinetochore (Mosalaganti et al., 2017). This way, dynein 'strips' the RZZ complex, and its pool of Mad1:Mad2 from kinetochores upon kinetochore-microtubule attachment and silences the RZZ SAC pathway.

The KBB pathway silencing depends on a fine balance of kinase and phosphatase activity at the kinetochore (Saurin, 2018). BubR1 recruits PP2A-B56 to kinetochores, which dephosphorylates the SILK and RVSF motifs in Knl1 . This allows recruitment of PP1 to the Knl1 N-terminus (Espert et al., 2014; Nijenhuis et al., 2014). PP2A-B56 and PP1 phosphatase activity can then counter-act Mps1 kinase activity by dephosphorylating the MELT motifs and other targets (Espert et al., 2014; Nijenhuis et al., 2014; London et al., 2012). Here, negative feedback loops regulate the cross-talk between PP1, PP2A-B56, Mps1, and Aurora B (Saurin, 2018). Briefly, Aurora B phosphorylation of Knl1 SILK and RVSF motifs allows Mps1 recruitment. Mps1-mediated phosphorylation of Knl1 MELT motifs allows BubR1:Bub3 kinetochore binding (Saurin et al., 2011, London et al., 2012, Shepperd et al., 2012). PP2A-B56 is subsequently recruited to the kinetochore through the interaction with BubR1 (Espert et al., 2014, Shepperd et al., 2012). PP2A-B56 can then dephosphorylate the SILK and RVSF motifs, allowing PP1 to be recruited to the N-terminus of Knl1 (Stucke, Baumann and Nigg, 2004, Nijenhuis et al., 2014). PP1 bound to Knl1 then dephosphorylates the Knl1 MELT motifs and counteracts

Mps1 kinase activity, causing checkpoint proteins, including BubR1, to be unloaded (London et al., 2012). The loss of BubR1:PP2A-B56 activity then causes removal of PP1 and allows Mps1 kinase activity, and SAC activation, to resume. Therefore, for the SAC to be silenced, the phosphatase activity needs to predominate over the kinase activity at Knl1. This allows checkpoint proteins to be unloaded and subsequently MCC production to be stopped (Saurin, 2018). The balance further needs to be tipped towards target dephosphorylation and SAC silencing only when kinetochores have formed stable K-fibre attachments. Here, a major clue of how the balance is tipped comes from the fact that the Ndc80 N-terminus competitively binds Mps1 and microtubules (Gui et al., 2020). Therefore, as Ndc80 complex molecules bind to microtubules, Mps1 is removed from kinetochores. This enhances PP1 and PP2A-B56 phosphatase activity to dephosphorylate the SAC targets, unload the MCC and silence the checkpoint.

The kinetochore can "count" the number of microtubules and silence the SAC once its sufficient

Early studies by Rieder and colleagues in 1994 asked the question of as to whether the SAC monitors microtubule attachment, and whether this can act as a signal for SAC silencing. This study used low Taxol treatment (below 3 nM taxol) to reduce the number of microtubules bound to the kinetochore. The treatment also caused a reduction in kinetochore-kinetochore sister (K-K) distance due to lower force applied across the kinetochore pairs. Interestingly, this low dose of taxol was still sufficient to activate the SAC. The authors concluded that "unless the kinetochore attachment checkpoint monitors the number of microtubules associated with each kinetochore, and that this number is reduced on univalents [chromosomes with single kinetochore] and in experimentally treated HeLa cells, it is doubtful that attachment of MTs [microtubules] at a kinetochore is the event monitored by the checkpoint" (Rieder et al., 1994).

About quarter of a century later, the kinetochore was shown to indeed be able to count the number of bound microtubules and satisfy the checkpoint prior to full kinetochore microtubule occupancy. Kuhn and Dumont showed that Mad2 is unloaded from kinetochores in a switch-like manner (2017). Further, the authors showed that K-K tension is established just prior to Mad2 un-loading signifying that kinetochore-microtubule attachment precedes Mad1 kinetochore unloading. Finally, the study

showed that end-on attachment is required for Mad1 kinetochore unloading, as lateral attachments failed to trigger Mad2 release from kinetochores. Next, Dudka and colleagues used the drug BAL27862 to reduce the amount of kinetochore-bound microtubules and detected SAC activation (2018). BAL27862 reduced the number of kinetochore-bound microtubules from ~ 20 per kinetochore to ~ 13.5 per kinetochore (65% reduction) and resulted in decrease in the K-K distances. Treatment with BAL27862 did not activate the SAC. Therefore the SAC is not activated by sub-maximal (65%) kinetochore microtubule occupancy, a decrease in K-K tension, or reduced force at kinetochores. Furthermore, a study by Etemad and colleagues showed that the SAC is silenced at $\sim 30\%$ kinetochore microtubule occupancy (2019). Here, the authors first monitored the unloading of SAC proteins relative to tubulin signal at kinetochores. The results showed that at $\sim 30\%$ maximum kinetochore-microtubule occupancy, Mad1 and Mad2 signals rapidly decreased. Further, by $\sim 50\%$ maximum kinetochore-microtubule occupancy the Mad1 and Mad2 signals were at very low to undetectable levels. This result was substantiated by expressing Ndc80 complexes with mutated N-terminal tail phosphorylation to fine tune microtubule binding properties: Cells with Ndc80 complexes mutated such that the resulting microtubule occupancy is at $\sim 45\%$ of the maximum in wild type signal succeeded in silencing the SAC. In contrast, below 30% microtubule occupancy failed to do so. Together, these data show that silencing of the SAC requires $\sim 30-50\%$ of the kinetochore attachment sites to be occupied. Furthermore, this work disproved the hypothesised model that K-K tension and force at the kinetochore serve as the critical stimuli for SAC silencing. It remains unclear how the kinetochore is able to "count" the number of bound microtubules? How does the kinetochore distinguish between lateral and end-on attachments to specifically silence the SAC when kinetochores are end-on attached?

1.5 Studies of kinetochore architecture in intact mammalian cells: Intra-kinetochore (Delta) measurement

The structural biology of single kinetochore proteins and complexes is beginning to emerge through single particle electron microscopy and x-ray crystallography,

with *in vitro* reconstitution providing insight into their biochemical and biophysical properties (see above). However, it remains poorly understood how these hundreds of molecules are organised within an intact kinetochore that is binding multiple microtubules.

For example, the human kinetochore binds ~ 20 microtubules via ~ 240 Ndc80 molecules (Suzuki et al., 2015). *in vitro* studies indicated that Ndc80 molecules function differently with respect to microtubule tip tracking when, (1) Ndc80 is incubated in absence of other molecules with microtubules (Schmidt et al., 2012; Helgeson et al., 2018), (2) three or four Ndc80 molecules are attached via their native linkers to a particle and incubated with microtubules (Huis In't Veld et al., 2016; Such organisation of Ndc80 allows for flexibility in the Ndc80 position and likely resembles better the spatial organisation of Ndc80 within kinetochores), (3) Ndc80 is incubated with Ska complex molecules and microtubules and thus can interact with a native binding partner (Schmidt et al., 2012; Helgeson et al., 2018). These studies of isolated molecules are critical for our initial understanding of kinetochore biology but they cannot fully recapitulate how kinetochore molecules function in their native numbers and molecular environment *in vivo*. It is therefore crucial to define the *in vivo* architecture of the kinetochore. How does the interplay between individual components of the kinetochore machinery cause kinetochore architecture re-arrangements? Does that architecture adapt to mechanical stimuli such as microtubule binding, and chemical stimuli such as protein phosphorylation? Can such kinetochore architecture adaptations and rearrangements serve as input for the SAC silencing?

Intra-kinetochore (Delta measurements) have been employed to directly study the average kinetochore protein-protein distances within the kinetochores from intact cells (*in vivo*), and map the kinetochore architecture. Here, two kinetochore components are fluorescently labelled and imaged via light microscopy (Figure 1.10). As a result, a fluorescent spot is observed for each labelled kinetochore component. The observed fluorescent spot represents the fluorescence of all of the labelled kinetochore component molecules, convolved with the point-spread function of the microscope. Therefore, the center of the fluorescent spot (the centroid) denotes the average position of all of the fluorescent molecules of the kinetochore component. Further, the distance between the centroids of the two kinetochore components (Delta) yields

a measurement of the relative position of two kinetochore components. In theory, Delta studies can be used to map the relative average positions of kinetochore components and, thus create a map of the *in vivo* kinetochore architecture.

The Salmon lab pioneered the Delta methodology by using the following steps: the authors imaged fluorescently labelled kinetochore components in HeLa cells, selected for analysis images where the two sister kinetochore spots of both markers were in the same or similar plane, measured the K-K distances between the two sister kinetochores for each marker, and measured the 1D Delta by subtracting the two K-K distances (Figure 1.10 A; Wan et al., 2009). Mapping of the relative position of sixteen kinetochore proteins via Delta rendered correct inner-outer kinetochore position of the elements as we now know.

Does microtubule force at the kinetochore leads to kinetochore architecture changes? To investigate this, the authors abolished microtubule dynamics and force at the kinetochore via taxol treatment. 1D Delta distances in cells treated with 10 μM taxol were reduced by 9 to 16 nm. The authors explained the small 1D Delta distance changes after taxol treatment with movement of the Ndc80 complex level arm towards the inner kinetochore. In untreated cells, the authors proposed that establishing K-K tension "stretches" the kinetochore, which "stretch" informs the SAC that the kinetochore is bound and triggers SAC silencing. However, the study lacked evidence that the kinetochore "stretch" informs the SAC.

A parallel 1D Delta study explored if the kinetochore architecture responds to K-K tension and tested whether kinetochore architecture changes relay the K-K tension information to the SAC (2009). This study was performed in *Drosophila melanogaster* cells. The authors measured the K-K tension and the SAC status in three conditions: control treatment, 20 nM taxol, and 1 μM taxol, and then measured the K-K distance. The K-K distance was reduced by 200 nm in cells treated with 20 nM taxol (740 ± 120), and by 180 nm 720 ± 110 nm in cells treated with 1 μM taxol as compared to control treated cells (940 ± 140 nm). Further, cells treated with 20 nM taxol silenced the SAC comparable to control cells, while cells treated with 1 μM taxol failed to do so. These data hinted that the 20 nm higher K-K distance after 20 nM taxol treatment enables the cells to silence the SAC. How can the changes in K-K tension be translated to the SAC? One hypothesis is that the Ndc80 lever arm responds to K-K tension and informs the SAC. To explore whether

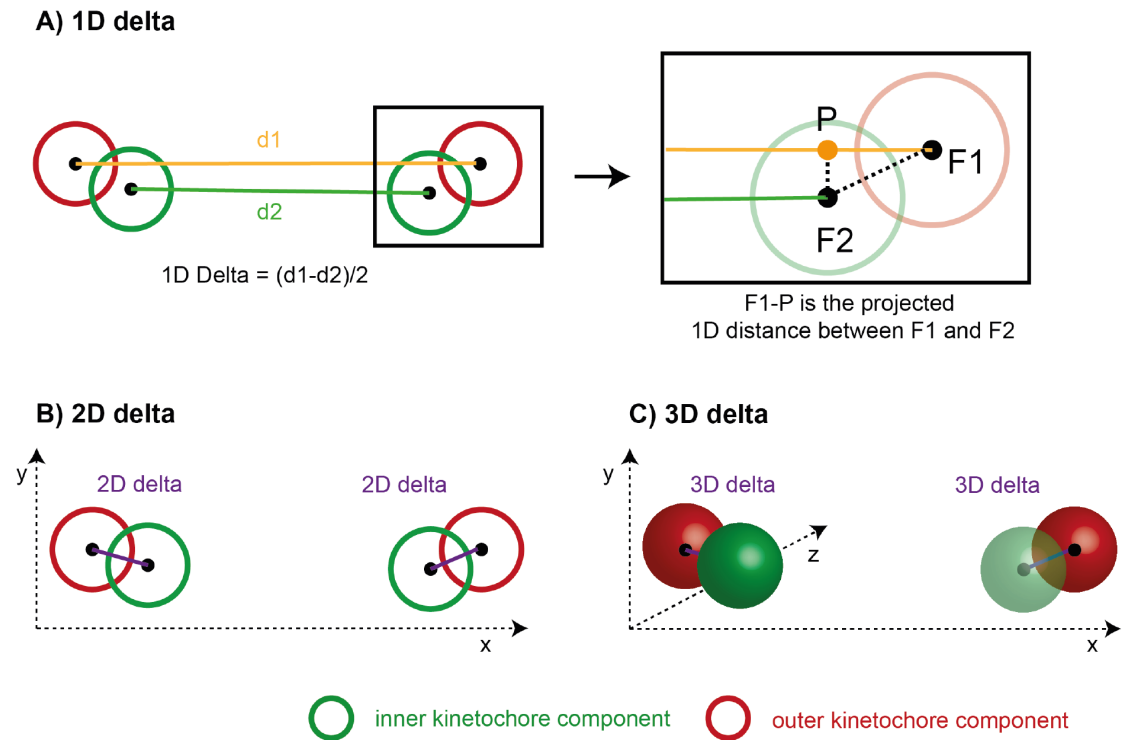


Figure 1.10: Kinetochores protein-protein distance measurements (Delta, Δ)

A) Right: 1D Delta measurements are performed by: (1) imaging of two fluorescently labelled kinetochores proteins via light microscopy. (2) detection of the center of the fluorescent spots (F1 represents the spot (red) centroid of one of the fluorescently labelled kinetochores markers and F2 represents the centroid of the other kinetochores marker spot (green)), (3) the distance between two kinetochores in a kinetochores pair is measured for each fluorescently labelled component (d1 and d2), (4) the distances are subtracted and the product is divided by two. Left: The measured 1D Delta distance is thus the 1D projection of the average kinetochores protein-protein distance. B) 2D Delta measurements are performed by measurement of the distance between the centroids of the two fluorescently labelled kinetochores markers within the same kinetochores. Here, only spots laying at the same z plane are analysed, or a projection in z is used. Therefore, the 2D Delta distance is measured only in the xy plane. C) 3D Delta measurements are also performed by measurement of the distance between the centroids of the two fluorescently labelled kinetochores markers within the same kinetochores. In difference to 2D Delta studies, in 3D Delta the distance is measured in x , y , and z and thus does not result in z projection of the distances or exclusion from analysis of kinetochores that do not lie on the same z -plane.

the NDC80 responds to K-K tension, the authors measured the 1D Delta distance between a centromere marker and Ndc80(N) in each condition. The 1D Delta distance was unchanged in cells treated with 20 nM taxol compared to control cells. In contrast, the 1D Delta distance was reduced by 32 nm in cells treated with 1 μ M taxol. Therefore, low tension at the kinetochore may increase the centromere-Ndc80(N) distance and "stretch" the kinetochore. The kinetochore "stretch" may in turn trigger SAC silencing. However, this study also lacked direct evidence that the K-K distance is informing the SAC and could not exclude other taxol effects.

Following study in 2016 combined electron microscopy of cells and 1D and 2D Delta measurements in taxol-treated cells to clarify whether a low-tension induced intra-kinetochore "stretch" informs the SAC (Magidson et al., 2016). Kintochores treated with 10 μ M taxol had reduced Delta as shown before but also suffered deformations. Therefore, the small Delta distance changes may result from kinetochore deformation rather than reduced K-K distance after taxol treatment. Further, treatment of cells with 10 μ M taxol led to detachment of detachment of a up to five kinetochores per cells. Detachached kinetochores activate the SAC. Therefore, the delay in SAC silencing after high dose taxol treatment likely results from a few unattached kinetochores rather than a low-tension induced intra-kinetochore "stretch". This study also highlighted that fixation could introduce small scale, \sim 20 nm, Delta changes. Therefore, the following open questions remained: does kinetochore tension plays a role in SAC silencing and can kinetochore architecture relay mechanical stimuli to the SAC? Further, a remaining uncharted territory is how the kinetochore architecture may respond to other stimuli such as microtubule binding and chemical stimuli.

Another set of studies explored if the kinetochore architecture is compliant to force, and which kinetochore components may act as tensile elements by comparing Delta distances at P and AP kinetochores. The P kinetochore generates a pulling force and is attached to an overall depolymerising K-fibre, while the AP kinetochore is suggested to follow the P kinetochore motions and to be bound to an overall polymerising K-fibre. Therefore, the P kinetochore is likely under higher force than the AP kinetochore. Therefore, if the kinetochore is compliant to force the kinetochore architecture would differ between the P and AP kinetochores. Metaphase kinetochores switch between P and AP states, and generate kinetochore oscillations

perpendicular to the metaphase plate. Detection of the kinetochore P and AP states requires following of the kinetochore motions, and thus, live-cell imaging. Dumont and colleagues developed a live-cell 2D Delta pipeline to detect the kinetochore P and AP state during kinetochore oscillations, and measure the 2D Delta distance between kinetochore components. In the live-cell 2D pipeline, Dumont and colleagues (1) label fluorescently two kinetochore components, (2) image the labelled components at oscillating metaphase kinetochores, (3) track the kinetochore oscillations, (4) find the kinetochore spot centers by 2D Gaussian fitting to the marker spots, (4) measure the distance between the kinetochore centroids in the two fluorescent channels, (4) fit a Gaussian distribution to the intra-kinetochore measurements distribution, and (5) calculate the mean of the intra-kinetochore measurement Gaussian, this is the 2D Delta distance (Figure 1.10 B; 2012). 2D Delta measurements at oscillating kinetochores showed that the Ndc80(N) is ~ 5 nm closer to CenpC at P kinetochores as compared with AP kinetochores. Therefore, the P kinetochore may be slightly compressed due to higher being under higher load. Further, differences on the scale of 5 nm suggested no large scale kinetochore re-organisation when kinetochores switch between P and AP states. However, 2D Delta distances suffer from projection in z. The projection in z can hinder any differences that involve rotation of the kinetochore in z. Therefore, remained unclear, whether in response to force kinetochores undergo re-arrangements that involve z kinetochore rotations.

To address this question, Smith and colleagues developed a method for 3D Delta measurements in live and fixed-cell studies (Figure 1.10 C) (2016). 3D Delta measurements of the CenpC-to-Ndc80 distance at oscillating metaphase kinetochores showed similar CenpC-to-Ndc80 distance at kinetochores treated with DMSO (control) and $1\mu\text{M}$ taxol. This result was in contrast to the 1D Delta distance measurements, which differ between control and taxol treated kinetochores, and showed that the observed 1D Delta changes likely reflect x/y and z projection effects. The authors also asked the question of does the kinetochore architecture change when kinetochores bind to microtubules. To address this question, they compared the 3D Delta distances at attached and unattached kinetochores. Unattached kinetochores displayed wide degree range of 3D rotations of the outer kinetochore relative to the inner kinetochore plate - an event termed swivel. In contrast, attached metaphase kinetochores had a narrow degree range of swivel. Therefore, the swivel was reduced

at attached kinetochores as compared with unattached kinetochores. One idea is that swivel at unattached kinetochores promotes microtubule capture by the kinetochore in prometaphase. These observations show that 3D Delta measurements are necessary to describe the kinetochore architecture as in 1D and 2D Delta measurements the outer kinetochore swivel was detected as large scale Delta distance decrease (~ 40 nm) due to projection effects, and thus misinterpreted. Finally, the authors explored whether the Ndc80(N) lever arm may respond to kinetochore attachment status. The authors compared the 3D Delta positioning of the Ndc80 N terminus at unattached and attached kinetochores and observed that the Ndc80(N) is ~ 13 nm closer to the inner kinetochore at unattached as compared to attached kinetochores. However, as to whether this change in Ndc80(N) positioning reflected Ndc80 conformational change and what may be its roles remained unclear.

The development of 3D Delta distance measurements was a milestone for the field. However, a later study by Suzuki and colleagues highlighted an innate problem with Delta distance measurements: Delta distance measurements are overestimates of the true distance due to the measurement error (Suzuki et al., 2018, Churchman et al., 2005). Further, smaller distance measurements suffer higher overestimation as they harbour higher measurement error. Therefore, the measured 1D, 2D and 3D raw Delta distances (herein termed inflation) are affected by overestimation in non-linear trend and that effect may hinder or exaggerate kinetochore architecture changes. The overestimation of the Delta distance can be mathematically corrected. The first distance measurement inflation correction method was put forward by Churchman and colleagues, and aimed to correct for overestimation of 2D (x/y) distance measurements between single molecules. In x/y the measurement error is isotropic, and thus maximum likelihood method could be applied. Suzuki and colleagues applied the 'Churchman' 2D inflation-correction algorithm to 2D Delta measurements at the kinetochore. The authors also show measurements termed as 3D inflation-corrected Delta measurements. However, the 'Churchman' algorithm is designed for measurements with isotropic error, i.e. 2D measurements, and the application of method to 3D measurements is inappropriate. Therefore, the measurements termed as 3D inflation-corrected Delta measurements in the paper remain questionable. The authors showed that the 2D and what is termed 3D inflation-corrected Delta measurements were reduced as compared with their raw Delta measurements

counterparts, thus demonstrating the inflation effects in kinetochore Delta measurements. Further, mapping of kinetochore components via this methodology rendered Delta distances similar to the structural distances measured *in vitro* for single kinetochore components. Therefore, the Suzuki study showed that correcting for the inflation in Delta distances is essential for accurate and reliable kinetochore architecture mapping, and called into question the previous conclusions based on raw Delta measurements. This study of 2D inflation-corrected Delta measurements thus set the scene for a next generation of experiments focused on: (1) development of a method for 3D inflation-correction, and (2) methodological investigation of how the kinetochore architecture may respond to stimuli via inflation-corrected 3D Delta measurements.

1.6 Rationale and Aims of Thesis

In this thesis we set to further develop an improved method for kinetochore Delta measurements, we incorporated: (i) gaussian-shape spot quality control, (ii) alignment of the kinetochore masses as a method for fine chromatic shift correction, and (iii) Bayesian MCMC framework for inflation correction, ultimately developing a method for 3D inflation-corrected Delta measurements with tight confidence intervals. Another issue in the field is the repetitive use of 1D Delta measurements (even in the last year), albeit their documented limitations. This has led to further confusion in the field, and a lack of reproducibility of the Delta measurements. The lack of integration of the latest methods in the field is likely due to the complexity of the methods and the requirement for a degree of computational know-how. To address this issue, we further developed a step-by-step guide on the use of our methodology for inflation-corrected 3D Delta measurements.

Further, as previous Delta methodologies were called into question, an important next task was to use the developed methodology for inflation-corrected 3D Delta measurements and reveal how the kinetochore architecture may respond to stimuli and whether kinetochore architecture changes may trigger SAC silencing. To do so we mapped the kinetochore architecture of attached, unattached and tensionless kinetochores in hTERT Retinal epithelial cells (Rpe)1 cells. The focus here is on the outer kinetochore Ndc80 complex, and we further investigated whether

conformational changes may serve as the SAC silencing trigger.

We next aimed to expand our work to the Ska complex which is the key binding partner for Ndc80 and together form the major microtubule attachment site. We sought to define the mechanisms and dynamics of Ska kinetochore recruitment and how Ska stabilises the kinetochore-K-fibre attachments potentially resulting in their maturation. To begin addressing these questions we created an endogenously fluorescently-labelled Ska cell line that would allow for live-cell imaging of Ska kinetochore recruitment dynamics. Further, we set to map the organisation of Ska at metaphase kinetochores. The endogenously labelled Ska cell line and the characterisation of Ska architecture in metaphase kinetochores together would lay the ground work for understanding the dynamic behaviour of Ska at *in vivo* kinetochores, and establish the basis for future investigation of how the Ska organisation may change as kinetochores congress and mature.

Chapter 2

Materials and methods

2.0.1 Cell culture and treatments

HeLa Kyoto (K) (MC009), eGFP-Ska1 HeLa K (MC177), 2xmNeonGreen-Ska1 HeLa-K (MC200) and Halo-tag-CENP-A 2xmNeonGreen-Ska1 HeLa K cells (MC206) were grown in Dulbecco's modified Eagle's media (DMEM), supplemented with 10% Foetal bovine serum, 100 $\mu\text{g}/\text{ml}$ penicillin and 100 $\mu\text{g}/\text{ml}$ streptomycin. Immortalized (hTERT) diploid human retinal pigment epithelial (RPE1) cells (MC133), RPE1 Ndc80-EGFP (MC191), and RPE1 Venus-Mad2 (MC112, Mad2L1 Venus/+; kind gift from Jonathan Pines) were grown in DMEM/F-12 medium containing 10% fetal bovine serum (FBS), 2 mM L-glutamine, 100 U/ml penicillin and 100 $\mu\text{g}/\text{ml}$ streptomycin. HeLa K cells cells stably expressing Halo-tag CENP-A were maintained in 300 $\mu\text{g}/\mu\text{l}$ G418. For screening of Ska1 knock-in clones on the Marianas Spinning disk microscope (3i), the media of the cells was changed to Leibovitz's L15 CO₂ independent media immediately prior to imaging.

The cells were maintained in a humidified incubator at 37 degrees C, 5% CO₂. Cells were fixed or imaged live at 75-85% confluence. Cells were seeded at least 24 hr prior to imaging as follows: (1) For overnight mitotic timing imaging, cells were seeded in 35mm Fluoro dish, four-compartment CELLview dish (627975, Greiner Bio-One Ltd.). (2) For screening of cell line clones, cell were seeded in in 35mm Fluoro dish, four-compartment CELLview dish (627975, Greiner Bio-One Ltd.) or in eight-compartment Nunc dish. (3) For fixed cell experiments cells were seeded on 22mm coverslips N.1.5 in six-well plate. (4) For genomic DNA extraction, cells

were seeded in 6-well plates. (5) For CRISPR/Cas9 plasmid and homology template transfection, cells were seeded in 10 cm plates. (6) For Lattice Light Sheet imaging, cells were seeded on 5 mm N.1 round cover slips (Thermo Scientific Menzel) in 6-well plates (Greiner Bio-One Ltd.).

For Lattice Light Sheet imaging, the Halo-tag CENP-A 2xmNeonGreen-Ska1 HeLa K cells were labelled with HaloTag TMR ligand (Promega UK LTD) according to manufacturer's instructions prior to imaging. For mitotic timing analysis, cells were incubated with 0.5 μ M sirDNA for 1 hr prior to imaging. In indirect immunofluorescence experiments, cells were treated with 3.3 μ M nocodazole (dissolved in DMSO) for 2 hrs, 1 μ M taxol for 15 min or 1:1000 DMSO dilution for 2hrs as control. In all immunofluorescence experiments where cells are not treated with nocodazole or taxol, cells were treated with DMSO to be comparable.

2.0.2 Indirect Immunofluorescence

Cells were fixed by 10 min incubation with PTEMF (10 mM EGTA, 1 mM MgCl₂, 20 mM PIPES pH 6.8, 0.2% Triton X-100, and 4% formaldehyde) at room temperature. The cells were then washed 3 times for 5 min in PBS. Next, non-specific antibody binding was blocked by 30 min incubation in PBS supplemented with 3% BSA. Then, cells were incubated with primary antibodies for 1 hr, and washed 3 times in PBS as above. The cells were then labelled by 30 min incubation with secondary antibodies. All of the antibody mixes were diluted in PBS + 3% BSA. Cells were washed 3 times in PBS before mounting in Vectashield (Vector laboratories Ltd). Cells were stained with DAPI either by addition of 1:1000 DAPI dilution with the secondary antibodies or by use of VectaShield supplemented with DAPI (Vector laboratories Ltd).

For experiments that were described as "pre-extracted" (HeLa K stained for CenpC, Nnf1 and 9G3; eGFP-Ska1 knock-in HeLa K cells stained for eGFP, Nnf1 and CenpC; and experiments where cells were stained for Ska3(M)), cells were incubated for 1 min with 10 mM EGTA, 1 mM MgCl₂, 20 mM PIPES pH 6.8, 0.2% Triton X-100 prior to fixation.

2.0.3 Antibodies

The following primary antibodies were used in this study: anti-GFP mouse monoclonal antibody (Rockland Immunochemicals, Inc., catalogue number: 600-201-315); anti-Ska3 B1 mouse monoclonal antibody (Santa Cruz Biotechnology, catalogue number: sc-390326); anti-Nfn1 rabbit polyclonal antibody (home made, McAinsh et al., 2006); anti-CenpC guinea pig polyclonal antibody (MBL, Catalogue number PD030); anti-Ndc80(N) mouse monoclonal antibody (9G3) (Abcam, catalogue number: ab3613).

The following secondary antibodies were used in this study: Goat anti-guinea pig AlexaFluor 647 (Invitrogen, catalogue number: A21450); Goat anti-guinea pig AlexaFluor 488 (Invitrogen, catalogue number: A11073); Goat anti-guinea pig AlexaFluor 568 (Invitrogen, catalogue number: A11075); Goat anti-mouse AlexaFluor 488 (Invitrogen, catalogue number: A32723); Goat anti-mouse AlexaFluor 647 (Invitrogen, catalogue number: A21235); Goat anti-mouse AlexaFluor 594 (Invitrogen, catalogue number: A11032); Goat anti-rabbit AlexaFluor 488 (Invitrogen, catalogue number: A11008); Goat anti-rabbit AlexaFluor 594 (Invitrogen; catalogue number: A11037).

2.0.4 DNA constructs and cloning

For CRISPR/Cas9 knock-in generation, Ska1 guide A (Auckland et al., 2017) was cloned into humanized SpCas9 vector that also encodes eGFP label (GFP_2A_Cas9 plasmid, Addgene, 44719) using Bbs1 according to protocol in Ran et al., 2013. The homology template for the eGFP-Ska1 knock-in generation has been previously designed by Phil Auckland and ordered from GeneArt. This homology template contains two 800 base pair homology regions that are complementary to the genomic DNA sequence before and after the start of exon1. The homology template for eGFP-Ska1 knock-in generation was prepared by Phil Auckland, who inserted eGFP tag and linker between the homology regions by EcoRI restriction digest cloning. A homology template with insert of Degron-eGFP-linker was also available from work by Phil AUckland.

The 2xmNeonGreen-Ska1 homology template was generated by replacing the Degron and eGFP tags in Degron-eGFP Ska1 homology template with mNeonGreen.

Firstly, the mNeonGreen sequence was amplified by PCR using the following EcoRI flanked primers 5' CT GAATTC atggtgagcaagggcgag 3' and 5' AA GAATTC cttgtacagctcgtccat 3', and Phusion DNA polymerase, reactions according to manufacturer protocol. The PCR temperature cycling is as follows: 1) 98°C 30s, 2) 98°C 10s, 3) 67°C 20s, 4) 72°C 15sec, 5) 72°C 15 min; with 34 cycles of steps 2 to 4. The resulting PCR product was isolated with QIAquick Gel-extraction Kit (QIAGEN), manufacturer protocol, after gel electrophoresis in 1% agarose gel. The PCR product and the Degron-GFP-Ska1 homology template plasmid were digested for 2hrs at 37°C with EcoRI enzyme. The digested vector and insert were isolated with QIAquick Gel-extraction Kit (QIAGEN), manufacturer protocol, after gel electrophoresis in 1% agarose gel. Ligation was performed with T4 DNA Ligase for 1hr at RT, manufacturer protocol. 10 ul of the ligation reaction was transformed in dH5a ultracompetent bacteria (homemade, Inoque protocol, Im, H. (2011).) and plated on Kanamycin resistant plates (the plasmid encodes Kanamycin resistance). DNA was isolated from single colonies with QIAprep Mini-prep Spin Kit (QIAGEN) according to manufacturer protocol and sequenced for successful generation of Degron-mNeonGreen-Ska1 homology template plasmid. Next, the procedure was repeated for replacing the Degron tag with mNeonGreen tag, with the following differences: the mNeonGreen PCR was done with 5' CT GGCGCGCC atggtgagcaagggcgag 3' and 5' CT GGCGCGCC C cttgtacagctcgtccat 3' primers and restriction digests were performed with AscI instead of EcoRI enzyme.

Up to a week prior to transfection, the Homology template was linearised by restriction digest with Sall, ran on 1% Agarose gel, and purified by QIAgen Gel Extraction kit.

2.0.5 Transient transfection

2xmNeonGreen-Ska1 knock-in (MC200) cells were transfected with Ndc80-tagRFP transgene by the following protocol: (1) 4 μ l Fugene6 (1:4, Fugene6:DNA ratio) was mixed with Optimem (up to 100 ul), (2) 5 min incubation at room temperature, (3) 1 μ g plasmid DNA was added to the mix, (4) 20 min incubation at room temperature, (5) 100 μ l of the reaction was added to the cells in 1.5 ml DMEM. The cells were imaged 24 hrs post transfection.

For CRISPR/Cas9 eGFP-Ska1 knock-in generation HeLa Kyoto cells were seeded

in 10cm plates 24 hrs prior to transfection. The cells were transfected with 1.5 μ g Ska1 Guide A plasmid DNA and 6.5 μ g linearised Homology template DNA, at 1:4 Fugene6 ratio using the protocol above.

For HeLa genomic DNA analysis control, HeLa K cells were transfected with SpCas9 plasmid (px330) that contained no guide as above.

For generation of MC200 cells with stable expression of Halo-tag CenpA, 250 ng Halo-tag CenpA containing plasmid was transfected in MC200 cells according to the above protocol (1:4, Fugene6:DNA ratio).

For transient transfection of Ndc80-tagRFP into MC200 cells, 1 μ g ng Ndc80-tagRFP containing plasmid was transfected in MC200 cells according to the above protocol (1:4, Fugene6:DNA ratio).

2.0.6 Genomic DNA PCR analysis

Genomic DNA was extracted from eGFP-Ska1 HeLa K (MC177) and 2xmNeonGreen-Ska1 HeLa K (MC200) cells, and from px330 transfected HeLa K cells using QIAmp DNA Blood Mini Kit according to manufacturer's protocol. For PCR amplification, the following primers were used: Forward primer - 5' CT TCTAGA TTAGACCCTCCCCTTCTCTCTC 3', Reverse primer - 5' AA TCTAGA CGCTTTTGTCA GAACACATCTC 3'. The primers are flanked by XbaI and AgeI restriction sites to allow for future cloning of the fragments into a plasmid and sequencing. The following mix was prepared for each genomic DNA reaction: 100 ng genomic DNA, 0.5ul each primer, 1ul dNTPs, 10ul Q5 reaction buffer, 0.5ul Q5 HF polymerase, ddH₂O to 50ul. The PCR temperature cycling is as following: 1) 98°C 30s, 2) 98°C 10s, 3) 65°C 20s, 4) 72°C 2 min, 5) 72°C 15 min; with 34 cycles of steps 2 to 4. The obtained PCR products were ran on 1% Agarose gel.

2.0.7 Genomic DNA PCR product preparation for sequencing

For eGFP-Ska1 cell line verification, the PCR product was sub-cloned as follows. The obtained PCR products were ran on 1% Agarose gel. DNA was purified with QIAmp Gel extraction Kit according to manufacturer spin protocol. Here, the different size bands were isolated in separate reactions. The PCR products and EGFP_N1

plasmid were digested with XhoI and AgeI HF (NEB, R0146S, R3552S) for 2hrs at 37°C, manufacturer protocol. The digest reactions were ran on 1% Agarose gel and isolated via QIAmp Gel extraction Kit according to manufacturer spin protocol. Ligation of the digested PCR products and EGFP_N1 vector was performed for 1hr at room temperature with T4 DNA Ligase (NEB, M0202S), standart protocol. 10 ul of the ligation reaction was transformed in dH5a competent bacteria and plated on Kanamycin resistant plates (EGFP_N1 encodes Kanamycin resistance). On the next day, 5ml LB supplemented with 50µg/ml Kanamycin was inoculated with single colony from the plate. 15 single colonies were picked for each PCR product. DNA was isolated from the overnight cultures with QIAprep Mini-prep Spin Kit according to manufacturer protocol. Plasmids were sequenced with 5' TTAGACCCTCCCCTTCTCTCTC 3' primer with Source Bioscience sequencing. Plasmid with successful inclusion of eGFP sequence, were also sequenced with primer 5' TTAACCTTCAAAGACATGTG 3' to ensure cover of the full Ska1 exon1. For eGFP-Ska1 HeLa K (MC177) sub-clone sequencing, the GFP insertion locus was PCR amplified and the DNA was extracted as above, and the PCR product was sent for sequencing via SourceBioscience. The following primers were used in addition to the 5' TTAGACCCTCCCCTTCTCTCTC 3' primer: 5' CCTAAGGCTCTAAGACAAGT 3' and 5' ACAATATTCAAATGACATT 3'. The two other primers bind the DNA sequence 200 prior and after the DNA locus cleaved by the CRISPR/Cas9.

For 2xmNeonGreen-Ska1 cell line verification, the PCR product was purified as above and send for sequencing via SorceBioscience.

2.0.8 Fluorescent In-situ Hybridisation (FISH)

Cells were fixed in 3:1 methanol to acetic acid solution for 10 min at room temperature and air-dried after. Slides were immersed in 2xSSC and then dehydrated in ethanol series (70%, 85% and 100%), each for 2 mins at room temperature. Next, cells were stained with centromeric probe for Chromosome 18: "Chromosome 18 Alpha Satellite Probe red" (CytoCell) according to manufacturer protocol. Samples were mounted with Vectashield supplemented with DAPI.

2.0.9 Fluorescence-activated cell sorting

FACS cell preparation: The media of the T75 FluorescentTag-Ska1 flask was carefully collected for preconditioned media. Cells were washed with 8ml PBS and trypsinised in 2ml trypsin. Cells were incubated at 37° in 5% CO₂ humidified incubator until detachment, and then collected in 8ml media in 50ml falcon tube. For control, the cells were washed with 5ml PBS, and trypsinised with 1ml trypsin. After detachment (as above), cells were collected with 3ml media and moved to 15ml falcon tube. Collected cells were spun for 5 min at 1200rpm, room temperature. The pellet was re-suspended in 1ml of the following media: 2% FBS, 1.5mM EDTA, DMEM. Then, cells were filtered through 50um filter into FACS tubes and placed on ice.

Media used for collecting the cells after FACS: The collected pre-conditioned media was spun for 5 min at 1200 rpm. The supernatant was transferred to clear 50ml falcon tube. After FACS, cells were collected in media composed of 30% pre-conditioned media supernatant, 10% FBS, and 60% media used for cell culture maintenance.

For generation of Ska1 knock-in cell lines, we enriched for the population of cells transfected with Ska1 GuideA_SpCas9_eGFP, and GFP-Ska1 or 2xmNeonGreen-Ska1 homology template by FACS sorting. First, 24 hrs post transfection with the Guide and Homology template, cells were sorted for signal in the 488 nm channel by Fluorescence activated cell sorting (ours - Muriel can you help here, cannot find it). Here, the population of cells with fluorescence in the 488 nm channel was sorted in a 50 ml falcon tube. Cells were then expanded to T75 and screened for positives. If the experiment was successful, second FACS was performed to enrich for the 488 nm fluorescent Ska1 signal. For eGFP-Ska1 knock-in generation, cells were sorted in the 488 nm channel on BD FACSAria™ Fusion (Birmingham imaging facility). Single cells with higher 488 nm signal as compared to negative control (un-transfected plain HeLa K cells) were isolated in 96-well plate and then expanded for screening. For 2xmNeonGreen-Ska1 knock-in generation, cells were sorted in the 488 nm channel on BD Melody FACS. The population of cells with higher 488 nm signal as compared to negative control (non-transfected plain HeLa K cells) was sorted in 5 ml tubes. Clonal lines were picked manually and then expanded for screening.

2.0.10 Generation of Halo-tag CenpA stable expression, Ska1 knock-in cell line (MC206)

24 hrs post transfection of MC200 with the Halo-tag CenpA plasmid, 50, 100 and 200 cells were transferred each to 10 cm dish with 15 ml DMEM supplemented with 10% FBS, 100 $\mu\text{g}/\text{ml}$ penicillin, 100 $\mu\text{g}/\text{ml}$ streptomycin and 300 $\mu\text{g}/\text{ml}$ G418. The media was changed to fresh one every 2-3 days. Once single clones could be observed, clones were manually picked and expanded for screening.

2.0.11 Fixed-cell imaging

For Delta experiments, image stacks were acquired using a confocal spinning-disk microscope (VOX UltraView; PerkinElmer, UK) equipped with a 100X / 1.4 NA oil-immersion objective and a Hamamatsu ORCA-R2 camera, controlled by Volocity 6.0 (PerkinElmer) running on a Windows 7 64-bit (Microsoft, Redmond, WA) PC (IBM, New Castle, NY). For the sample data sets, mitotic cells were imaged over 61 z-slices separated by 0.2 μm . For chromatic shift data sets interphase cells were imaged over 121 z-slices separated by 0.1mm. For acquisition of both types of data sets, we used 488, 561, 640 and 405 nm wavelength lasers. Exposure time and laser power were set such that the kinetochore signal is at least 50 units above the background signal.

For FISH experiments, image-stacks were acquired on Olympus DeltaVision microscope (Applied Precision, LLC) equipped with Photometrics CoolSNAP HQ (Roper Scientific) camera, and 40x/1.3 NA oil-immersion objective, using SoftWorX 6.0 software. 20 fields (1024 by 1024 pixels) with mitotic and interphase cells were captured over 55 z-slices, with 0.2 μm spacing, using SoftWorx point-visiting function and Experiment Set-up options. Number of centromere spots per cell was scored by eye.

For Structured illumination microscopy, microscopy slides with hTERT Rpe1 cells stained for CenpC, Nnf1 and Ndc80(N) were prepared by Emanuele Roscioli. The slides were imaged on DeltaVision OMX SR microscope equipped with 60x 1.42 NA Oil Immersion PSF objective, Standard filters for DAPICFPFITC/AF488YFP/AF568/Texas RedCy5/AF647, and sCMOS camera. Images were reconstructed with AcquireSR-softWoRx DeltaVision software.

2.0.12 Live-cell imaging

Live-cell imaging for knock-in cell line verification was done on Marianas Spinning disk confocal microscope (3i) equipped with Photometrics 95B Prime sCMOS camera, Quad - 446/523/600/677 filter, and 100X objective (Zeiss, NA 1.46, oil, alphaPInApo, effective pixel size $0.0892 \mu\text{m}$). During imaging the microscope chamber maintained temperature of 37°C . Mitotic cells were identified by eye in transillumination. Image-stacks of mitotic cells were captured via SlideBook 6 software at various z spacing and range, using 488 nm laser exposure of 500 ms to 1500 ms, and 30 - 50% laser power.

Live-cell imaging for mitotic timing analysis was done on Olympus DeltaVision microscopes (Applied Precision, LLC) equipped either with Photometrics CoolSNAP HQ (Roper Scientific) or Photometrics CoolSNAP HQ2 cameras (Roper Scientific) and 40X oil objective. During imaging the microscope chamber maintained temperature of 37°C and 5% CO_2 . 17 to 20 fields (1024 by 1024 pixels) were captured using the point-vision option in the SoftWorx software. Image stacks were captured with 7 z-slices, spaced by $2 \mu\text{m}$. Cells were imaged every 3 min for 12 hr using 10 or 32% ND filter, exposure time 0.05 or 0.01 s. The time of nuclear envelope break-down, metaphase alignment, and anaphase onset was scored by eye.

2.0.13 Lattice light sheet Microscopy

For live-cell Ska1 imaging, MC206 cells were imaged on Lattice Light Sheet Microscope (3i) equipped with 0.71 NA LWD WI (excitation) and 1.1NA WI (imaging) objectives, 2 Hamamatsu ORCA-Flash 4.0 v3 sCMOS cameras, 488 nm and 561 nm lasers. Cells were imaged every 15 s for 12.5 min over 60 z slices. The laser power and exposure were set to 2% and 100 ms, respectively, for each of the fluorescent channels.

2.0.14 Delta measurements and Statistical Analysis

Delta measurements were performed as described in Chapter 3 and Appendix B: Germanova et al., 2021 in revision. All significance tests were done using Mann-Whitney test of the medians, except for linear regression correlation analysis where we used rank correlation analysis. The calculation of Nematic order is defined in

Chapter 4.

Chapter 3

Protocol for Subcellular Euclidean distance measurements with Multicolour Fluorescence localization imaging

3.1 Background

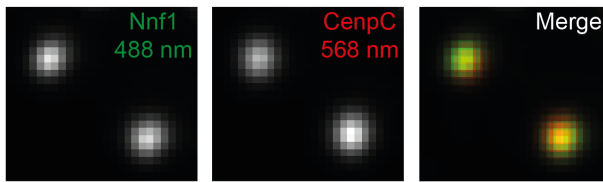
Previous studies have utilised intra-kinetochore distance measurements, termed Delta, to study the adaptability of the kinetochore architecture to stimuli. Most recent advances in the field have led to procedures for measuring the Delta distance between pairs of kinetochore components in 1D and 2D (Wan et al., 2009, Maresca and Salmon, 2009; Dumont et al., 2012; Magidson et al., 2016), and more recently in 3D (Smith et al., 2015; Suzuki et al., 2018). A major limitation of 1D and 2D methods is that they suffer from an underestimation of the true distance due to projection effects. To understand the effects of projection on 1D measurements consider a kinetochore where the sister-sister axes of the two examined fluorophores are parallel to each other (see Figure 3.1 A). To ease explanation I will call these fluorophores F1 and F2. To perform 1D Delta measurements, we effectively draw a line that connects the two sister-sister axes at the point of F2 at 90 degrees angle, thus creating a point that I will call "P". Therefore, we have created a right angled triangle between points F1, F2 and P. In that triangle F1-F2 is the hypotenuse and

the distance we want to measure. However, in 1D measurements we effectively measure the triangle side F1-P. By Pythagoras's theorem, the two sides adjacent to the hypotenuse are smaller than the hypotenuse. In our case, that means that the measured F1-P distance will always be smaller than the true F1-F2 distance. Therefore, 1D Delta distances are always underestimates of the true Delta distance. Later, 1D measurements were advanced to 2D measurements (Dumont et al., 2012). Here, the F1 to F2 distance is directly measured (Figure 3.1 B). Therefore, the 2D Delta measurement is not affected by underestimation due to subtraction of distances. However, the measurements still suffered from projection in Z or limitation of the analysis to only kinetochores on the same Z plane. In addition, the progress to 2D measurements imposed the problem of chromatic shift in the spot positions. Here, the distance F1 to F2 is measured between different fluorescent channels. Therefore, any un-alignment between fluorescent channels will affect the distance. In addition, different light wavelengths are not refracted the same by optics and objects. These two factors create a phenomenon termed chromatic shift. The chromatic shift in 2D measurements was roughly corrected by averaging over the Delta measurements of the two sister-kinetochores. Here, the assumption is that the axes are anti-parallel and thus will compensate each other. However, such correction can hinder variability in a kinetochore pair, and also fails when the two axes are not anti-parallel.

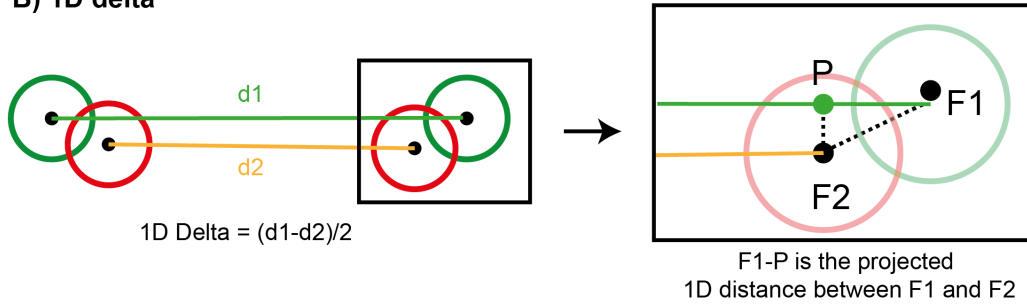
To improve the 2D Delta measurements, Smith and colleagues developed a 3D Delta measurement workflow using data from live cell imaging (2015). For this a Gaussian mixture model fitting routine was implemented in order to detect the centroid of the kinetochore signal in 3D (Figure 3.1 C). The two positions were then subtracted from each other, effectively resulting in a 3D F1-F2 distance measurement. This does not suffer from projection artifacts. The chromatic shift here was estimated in a separate sample as follows: interphase cells that stably express CenpA labelled fluorescently to emit in the 488 nm and 561 nm channels were imaged live or in fixed assays (Smith et al., 2015). The centers of fluorescent emission of CenpA at each kinetochore, i.e. the CenpA spot centers, in the different wavelengths are expected to co-localise with the only differences occurring due to the shape of the PSF. Any miss-match between spot localisations can thus be used to calculate and correct the chromatic shift error. In summary, here we reached a method that can measure the F1-F2 distance in 3D (no projections) and correct for most of the chromatic shift in

the sample.

A) Fluorescently labelled kinetochore sister-sister pair



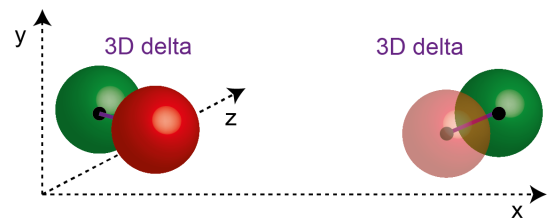
B) 1D delta



C) 2D delta



D) 3D delta



○ inner kinetochore component ○ outer kinetochore component

E) Inflation (overestimation) of distance measurements.

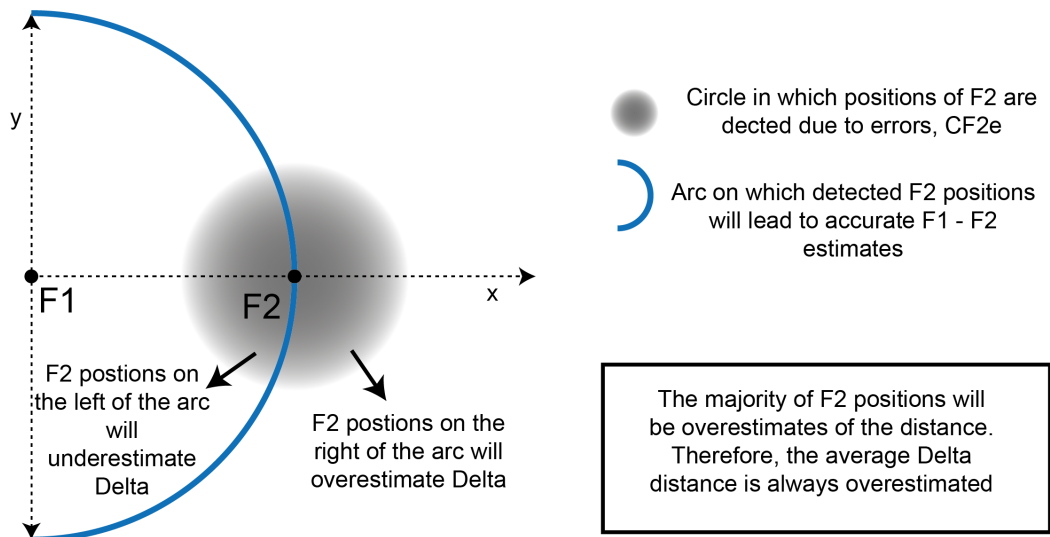


Figure 3.1: Kinetochores protein-protein distance measurements (Delta, Δ)

A) Representative image of a kinetochore sister-sister pair fixed with 4% paraformaldehyde and stained with rabbit anti-Nnf1 and guinea pig anti-CenpC primary antibodies, and anti-rabbit IgG AlexaFluor 488, and anti-guinea pig IgG AlexaFluor 568 secondary antibodies. B) Right: 1D Delta measurements are performed by: (1) imaging of two fluorescently labelled kinetochore proteins via light microscopy. (2) detection of the center of the fluorescent spots (F1 represents the spot (red) centroid of one of the fluorescently labelled kinetochore markers and F2 represents the centroid of the other kinetochore marker spot (green)), (3) the distance between two kinetochores in a kinetochore pair is measured for each fluorescently labelled component (d1 and d2), (4) the distances are subtracted and the product is divided by two. Left: The measured 1D Delta distance is thus the 1D projection of the average kinetochore protein-protein distance. C) 2D Delta measurements are performed by measurement of the distance between the centroids of the two fluorescently labelled kinetochore markers within the same kinetochore. Here, only spots laying at the same z plane are analysed, or a projection in z is used. Therefore, the 2D Delta distance is measured only in the xy plane. D) 3D Delta measurements are also performed by measurement of the distance between the centroids of the two fluorescently labelled kinetochore markers within the same kinetochore. In difference to 2D Delta studies, in 3D Delta the distance is measured in x, y, and z and thus does not result in z projection of the distances or exclusion from analysis of kinetochores that do not lie on the same z-plane. E) Schematic illustrating why Delta distance measurements suffer from overestimation (inflation). The schematic pictures a hypothetical scenario where the Delta distance is to be measured between the F1 and F2 centroids. To simplify the scenario, we assume we know the true position of F1 and look only at how errors in the position of F2 affect Delta. The grey sphere shows the positions of F2 that are detected due to error. Distances between F1 and F2 that lie on the blue arc will have accurate F1-F2 distance. The detected positions of F2 that lie on the left of the arc will result in F1-F2 distance underestimation. The detected distance on the right of the arc will result in F1-F2 distance overestimation. The positions of F2 detected on the right of the arc are more than the positions detected on the left of the arc. Therefore, the F1-F2 distance measured on average will be an overestimated of the true distance.

One limitation of the above discussed Delta measurements in 1D, 2D and 3D is overestimation of the mean, termed inflation, due to errors in the fluorophore detection. The problem has been discussed for distance measurements in single molecule

microscopy (Churchman et al., 2005) and was shown to also apply for Delta kinetochore ensemble measurements (Suzuki et al., 2018). To understand the concept, let us imagine that we can pin point the position of the first fluorophore (F1) and focus on the effects of the error in fluorophore two (F2) position. Here, we will center the x and y axes at F1. The explanation is in 2D to facilitate understanding. The error in the F2 position will result into measurements deviating from the true position. As the error is gaussian, the positions of F2 will be detected in a circle around the true position of F2 (circle of F2 position with error, CF2e). Now let us draw a circle with origin F1, and radius F1-F2. Any measurement on that circle will give us the true F1-F2 position (circle of true measurements, CT). Any measurement that stand on the left of the cross-section of the CT and CF2e are underestimates of Delta. Any measurement that stand on the right of the cross-section of the CT and CF2e are overestimates of Delta. As visible from figure 3.1 D, the region of overestimated values is larger than the region of underestimated values. Therefore, the F1-F2 measurement will always be overestimated. In addition the measurement overestimation will increase with increase in the error of the F1 and F2 positions. The error in the positions of F1 and F2 is larger with smaller distances as the distance becomes harder to resolve. Therefore, smaller distances will suffer from higher inflation than larger distances. Overall, the comparison of inflated distances of different size then becomes untrue. In summary, Delta distances are always overestimated (inflated), and smaller true distances suffer from higher overestimation. Therefore, to carry out a meaningful mapping of the kinetochore architecture (and any dynamics) we require a method for reliable inflation correction. The first method, the "Churchman" method was designed for single molecule 2D distance inflation correction (Churchman et al., 2005). Next, Suzuki and colleagues used the "Churchman" method to correct the inflation in 2D Delta measurements (2018). Furthermore, the authors attempted to correct the inflation in 3D Delta measurements. However, as to whether the presented 3D measurements were truly 3D is arguable as the authors "correct" for the Z offset and thus create a 2D projection. Further, if these are truly 3D Delta measurements, how the authors applied the "Churchman" 2D correction algorithm to 3D Delta measurements remains unclear. Here, it needs to be explained that the PSF is isotropic, i.e. Gaussian, in x and y . Due to the nature of light microscopy measurements, the PSF in the Z-direction is anisotropic, i.e. non-gaussian. Therefore, the error associated with the x/y will dif-

fer from the one in z. The "Churchman" method corrects for the isotropic inflation in x/y. However, there is no current method to correct for the anisotropic inflation in the Z direction. Therefore, there is no method for determination of reliable 3D Delta distances corrected for inflation (overestimation).

Furthermore, a main problem in the field remains unavailability of detailed methods and protocols for the used inflation-correction algorithms and procedures for Delta measurements. In contrast to the simplest 1D measurement, the current advanced Delta methodologies pose the requirements for (1) automated detection of spot coordinates in 3D, (2) estimation of displacement between fluorescent channels for chromatic shift correction, and (3) application of mathematical methods and computational algorithms for inflation correction. With the increased complexity, unfortunately, full descriptions of the methods have become scarce. Therefore, Delta measurements with the latest developments have become virtually impossible for a novice user, or a user that has not participated in the method development. Therefore, the data cannot be easily reproduced. In addition, methods that took years to develop cannot be used by others, a fundamental problem with complex scientific approaches. Another aspect of computational approaches is that broad availability of the method can lead to its improvement (the concept of open source code), as it can be adapted by users to perform additional tasks. This is in contrast to the requirement for each lab to start from ground zero when the methods are not accessible. Here, the most accessible method remains 1D Delta, and thus labs continue to use 1D Delta instead of the most recent state-of-the-art Delta measurement methods. Therefore, a future effort into making the Delta methodologies accessible and user friendly is required.

In summary, the Delta studies up to now have posed the following issues: (1) no available methods for correction of the inflation in 3D Delta measurements, that leads to no reliable protocol for 3D Delta measurements, (2) no available methods for fine chromatic shift correction at the level required for 3D Delta measurements, and (3) lack of detailed protocols to enable the use of developed Delta measurement methods.

3.2 Results

To address the above set of issues the development of new computational biology tools is required. The development of such methods requires a collaboration between researchers with expert knowledge in mathematics, computing and cell biology: Here, expert knowledge in mathematics and computing is essential for the development of the algorithms applied to biology. Further, expert cell biology input is essential to provide data for the implementation of algorithms and to ensure the biological phenomenon is captured appropriately. This process is iterative, thus slowly building the workflow based on a cycle of testing, refining and developing. Therefore, we established a collaboration with the Burroughs lab in the Warwick Mathematics Institute to develop an advanced method for inflation-corrected 3D Delta measurements. Here, I contributed with cell biology knowledge, provided a proportion of the data used for algorithm testing, tested the algorithm for troubleshooting, and contributed with ideas on problem solutions. In addition, I helped bridge the communication between other cell biology experts in our lab and our mathematics collaborators.

3.2.1 Inflation correction of 3D Delta distances

We first sought to address the issue of a lack of available methods for inflation correction in 3D. Here, our collaborator Nigel Burroughs wrote a sampling (Bayesian methodology) algorithm, termed Bayesian Euclidian Distance Correction Algorithm (BEDCA). The algorithm samples the 3D Delta distribution, and constructs the posterior corrected (Delta Euclidian corrected, ΔEC) distribution for the mean Delta value using a Markov chain Monte Carlo (MCMC) algorithm such that the samples are dependent. Therefore, the sampling algorithm needs to converge before samples can be used to construct the posterior distribution. Convergence was tested using a Gelman Rubin statistics (Gelman and Rubin, 1992). Parameter estimates and confidence intervals can then be calculated from the posterior as required. For example, the analysis pipeline outputs the constructed distribution of the mean corrected Delta Euclidian distance (μ), the mean value of this distribution (m_n), and the standard deviation of this distribution (sd). The use of Bayesian methodology also allows for prior information to be included if desired. The inclusion of prior

information (priors) can reduce the confidence intervals for the parameter estimates. Therefore, BEDCA uses weak or un-informative priors where possible. In some circumstances, in particular for small "true" distances (below 40 nm), weak priors are insufficient due to the weak information in the data. Therefore, here additional information in the form of priors needs to be provided, that BEDCA then integrates with the data. Prior information on the spot centre error was found to be sufficient to inform BEDCA in that case. We found that the spot centre error is consistent for a fluorophore between experiments. Therefore, we integrated that data as the a prior in BEDCA (for more information see Appendix B: Germanova et al., 2021 in revision). Here, with larger a BEDCA becomes more constricted to the prior. We use $a=10$ throughout for consistency, albeit smaller a could be used on many data sets (Figure 3.2). The effect of a was tested on these data sets, and $a=10$ was found not to affect the results significantly as compared to smaller a . In that case, the information in the data was strong enough such that the additional information supplied through the larger a prior was not needed.

BEDCA constructs the posterior distribution based on sampling of the measured inflated 3D Delta distribution. Therefore, the data on inflated 3D Delta measurements input into BEDCA needs to be high quality. We previously developed kinetochore tracking (KiT) algorithm for detection of spots through time (Smith et al., 2016). However, BEDCA is developed for fixed cell data and thus there is no time component to refine the spot selection. Therefore, we next sought to optimise the KiT algorithm such that spots can be identified in single time frame and the selection can be refined manually. Here, we also tested if fixation protocols affected Delta to re-assure ourselves that the algorithm performs robustly. Further, BEDCA assumes that spots have a Gaussian shape. Inclusion of miss-shaped spots distorted the analysis in BEDCA. Therefore, we developed KiT such that mis-shaped spots can be excluded from the analysis.

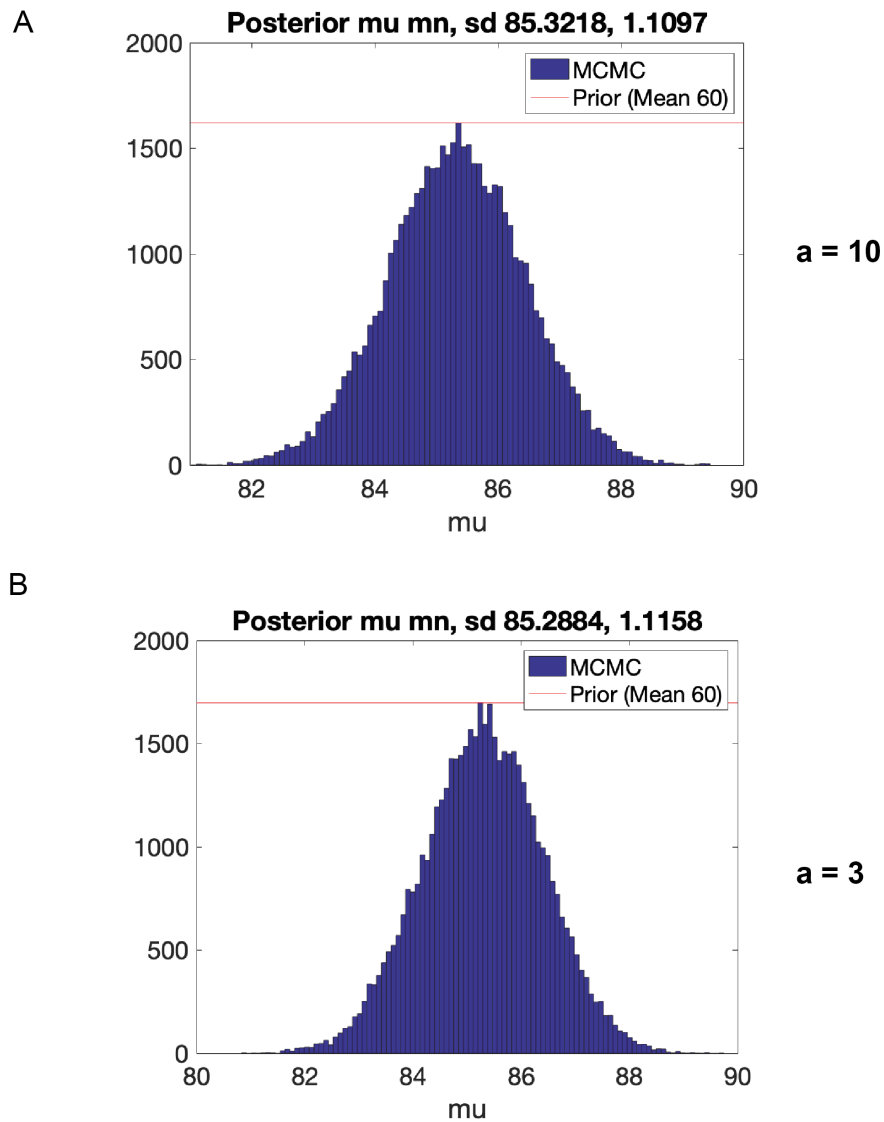


Figure 3.2: Posterior distributions of the mean ΔEC distance (μ parameter) between CenpC and Ndc80(N) after BEDCA correction with parameter a set to 10 and 3. A) Histogram of the posterior distribution of the mean (μ) CenpC-to-Ndc80(N) Delta distance after correction in BEDCA with $a=10$. The mean (mn) and standard deviation (sd) of the μ distribution are shown on top in that relative order, and in nm units. B) Histogram of the posterior distribution of the mean (μ) CenpC-to-Ndc80(N) Delta distance after correction in BEDCA with $a=3$. The mean (mn) and standard deviation (sd) of the μ distribution are shown on top in that relative order, and in nm units.

3.2.2 Sample preparation

High quality data on the position of kinetochores is essential for 3D Delta distance measurements. One of the data sets that we used for data quality testing is hTERT Rpe1 cells stained with anti-CenpC, anti-Nnf1, and anti-Ndc80(N) primary antibodies and A-488 nm, A-561 nm, and A-647 nm secondary antibodies, respectively. Here, I will show plots of that data set to demonstrate the data quality control process. However, the reader should note that the algorithm was tested on more than 10 other data sets (data not shown).

The first step in obtaining high quality data is sample imaging. Here, the sample was imaged on a spinning disk confocal microscope with 100x objective and camera such that the pixel size was $0.0694 \mu\text{m}$. That provided high resolution in the x/y image direction (Figure 3.3). The z-step was set to 200 nm such that the spot information can be captured in z. Here, we obtained a dataset of 20 cells to capture the biological variability in the sample. In addition, we collected a data set with interphase cells to provide an approximate chromatic shift correction, similar to the one used by Smith and colleagues (2016). For approximate chromatic shift correction, we cultured and fixed the cells in the same manner as the sample, and then stained a single kinetochore marker (CenpC or CenpA) with primary antibody and an equal mixture of three fluorescent AlexaFluor secondary antibodies emitting in green, red, and far red. We expect the center of fluorescence of the three secondary antibodies to overlap as: (1) the antibodies have similar affinities for the primary antibody, and (2) many secondary antibodies bind to each primary antibody, thus creating a floret mix with the true primary antibody position in the middle. In result, the same protein is labelled in three colours, and the distances between the centers of fluorescence are theoretically 0 nm. Therefore, the sample can serve for approximate estimation and correction of the chromatic shift between the fluorescent channels. In addition, using interphase cells for chromatic shift correction accounts for the refractive index in the cell and has been shown previously to give better chromatic shift estimate than fluorescent beads (Smith 2016).

In summary, at the end of the sample preparation step we had acquired image stacks of two or three fluorescently labelled kinetochore components in mitotic cells for Delta measurements, and, in parallel, image stacks of a single kinetochore marker

labelled in three fluorescent channels to serve for approximate chromatic shift correction.

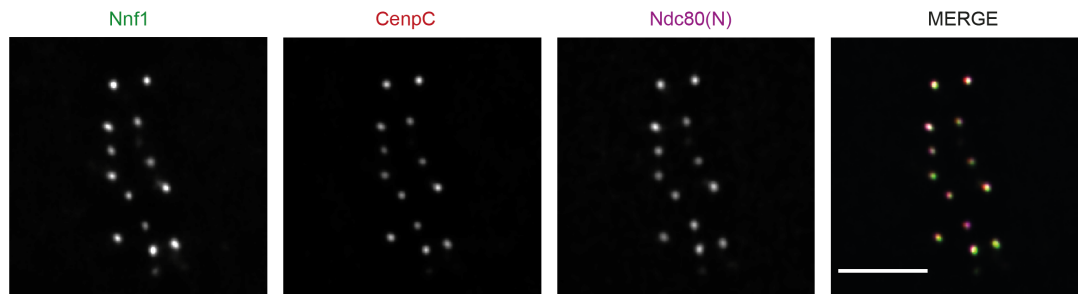


Figure 3.3: Representative images of the fluorescent signal in cells used for Delta measurements. Representative images of hTERT Rpe1 cells stained for Nnf1, CenpC and Ndc80(N). Scale bar 5 μm .

3.2.3 Kinetochore spot detection

Next, we sought to detect the kinetochore spot coordinates. Here, as for tracking data, the images were entered in KiT and spot detection was performed based on a histogram cut-off method. We term this method "Histogram" detection. In essence, KiT computes a histogram of all intensities in the fluorescent channel and based on the amount of spots expected in the sample, thresholds the spot versus background intensity. The default parameter in KiT specifies that between 20 and 100 kinetochore spots are expected, based on 92 kinetochore spots expected in metaphase cells. The potential spots are then filtered with Gaussian mixture model fitting, i.e. based on as to whether their shape resembles one or more Gaussian spots.

Here, we observed instances where more than 92 spots were detected as kinetochores suggesting that the background signal was detected as kinetochore (See Table 3.1), fields indicated in red). Delta measurements require accurate kinetochore detection in both channels used for the measurement. Therefore, we wished to facilitate the proper detection of both kinetochore markers at the same kinetochore. To do so, we first checked which channel had detection most reminiscent of the expected 92 kinetochores. In the case of Nnf1/CenpC/Ndc80(N), that channel was CenpC (See Table 3.1). Then, we used the spot coordinates from the fluorescent channel with best detection (CenpC), termed coordinate system (CS) channel, to guide spot detection in the rest of the fluorescent channels, termed non-coordinate system

(NCS) channels. In specific, in the NCS channels, KiT started from the location of the spot in the CS channel, and searched in a mask for the NCS spot. The mask was set to be a circle or semi-circle with radius of 300 nm. Kinetochores are diffraction limited objects, i.e. with size below 250 nm, and thus 300 nm should be sufficient. We term this method "Neighbour" detection. As seen in Table 3.1, the Neighbour method improved the detection and led to no cells with more than 96 detected kinetochore spots detected in difference to using Histogram method alone in the example data set. In other data sets, the "Neighbour" detection also improved the spot detection as compared to "Histogram" (data not shown). Therefore, from here on we used "Histogram" detection for the channel with best detection (the CS channel), and "Neighbour" detection in the rest of the fluorescent channels.

3.2.4 Approximate chromatic shift correction (ACS) and fine chromatic shift correction (centralisation)

The 'Neighbour' detection of fluorescent spots could be affected by large scale chromatic shift. If the chromatic shift is larger than the 300 nm mask, KiT would not detect the 'Neighbour' spot. Therefore, before performing "Neighbour" detection, we sought to align the coordinates in the CS and NCS channels. Here, we used the approximate chromatic shift (ACS) sample to detect the chromatic shift. Next, in the ACS sample, the centre of mass of all detected spots per channel was calculated in KiT. The difference between the centre of mass between fluorescent channels was then used for chromatic shift correction in the sample.

We further sought to correct the fine chromatic shift in the sample. Here, we utilised the fact that on average kinetochore sister pairs are symmetrical around the metaphase plate (Smith et al., 2015). Therefore, the center of mass of all analysed kinetochores should overlap between fluorescent channels. Chromatic shift on another hand would distort the expected overlap of kinetochore population center of mass between fluorescent channels. Therefore, we aligned the fluorescent channels based on the center of mass of the analysed kinetochores. From here on we term that alignment centralisation.

Up to now, we have therefore detected the spots in the CS channel, corrected for the chromatic shift in the sample, and detected the spot coordinates in the NCS

Cell	Nnf1-A488		CenpC-A568	Ndc80(N)-A647	
	Histogram Spot Detection	Neighbour Spot Detection	Histogram Spot Detection	Histogram Spot Detection	Neighbour Spot Detection
1	74	74	75	74	74
2	92	74	74	92	74
3	95	70	71	95	70
4	83	86	88	83	86
5	85	88	88	85	88
6	103	81	82	103	81
7	96	91	95	96	91
8	95	82	83	95	82
9	84	82	82	84	82
10	101	92	92	101	92
11	83	85	85	83	85
12	88	81	82	88	81
13	97	2	2	97	2
14	72	74	74	72	74
15	96	76	83	96	76
16	77	71	72	77	71
17	114	93	95	114	93
18	89	86	88	89	86
19	83	87	90	83	87
20	115	92	93	115	92

Table 3.1: Kinetochores spot detection improvement via "Neighbour" Spot detection method. Kinetochores spots in the CenpC channel are detected via a Histogram Intensity threshold method (Histogram spot detection). The number of detected kinetochores spots is indicated in respective column. Kinetochores spots are detected in the Nnf1 and Ndc80(N) channels via Histogram Intensity threshold and "Neighbour" Spot Detection methods for comparison. Fields where the number of detected spots exceeds 92 - the number of expected kinetochores in a cell, are highlighted in red.

channel via "Neighbour" spot detection.

3.2.5 Kinetochore spot quality control

We next sought to measure the 3D Delta and assess if the distances were realistic. We observed a small number of 3D Delta distances of more than 250 nm (Figure 3.4). Human kinetochores are diffraction-limited with size of less than 250 nm. Therefore, these measurements likely reflect instances where KiT failed to properly threshold the intensity and detected background instead of kinetochore spots.

Therefore, we sought to manually select kinetochore spots over background spots. We used the fact that kinetochores are in a pair in prometaphase and metaphase to clearly differentiate between background and kinetochore spots manually. Here, we developed the software such that it will display a graphic user interface (GUI) for manual kinetochore pairing. We typically perform the manual sister pairing in the CS channel as the CS channel spots inform on the spot detection in NCS channel spots. Therefore, appropriate kinetochore spot detection in the CS channel will result in most cases in corresponding appropriate kinetochore spot detection in the NCS channels. In addition, we implemented cell quality control. An example of where cell quality control is useful is when metaphase cells were analysed but my mistake a cell that has not reached that stage is captured.

Therefore, we developed a GUI for cell quality control and manual sister pairing. Here first a maximum intensity projection of the full cell is displayed and the user can decide whether to accept it for analysis. If the cell is accepted, the GUI proceeds to manual sister pairing of the kinetochores. In the manual kinetochore pairing GUI, a projection of the full cell over 5 z-slices is displayed on the left side (Figure 3.5). The center detection of the kinetochore to be paired is indicated on the full cell projection with a white cross. The kinetochore pair spot is expected to be less than 2.5 μm away from its sister from inter-kinetochore (K-K) distance measurements. Therefore, kinetochore spot centers detected within 2.5 μm of the kinetochore to be paired are indicated with a green cross. To facilitate visualisation, enlargement of the region containing the analysed kinetochore spot and the candidate sister spots is displayed in the GUI on the right. Here, the user is requested to identify by eye the kinetochore sister and click on it. If there is no clear sister, the user can skip the kinetochore spot and discard it from the analysis. Then, the next detected spot

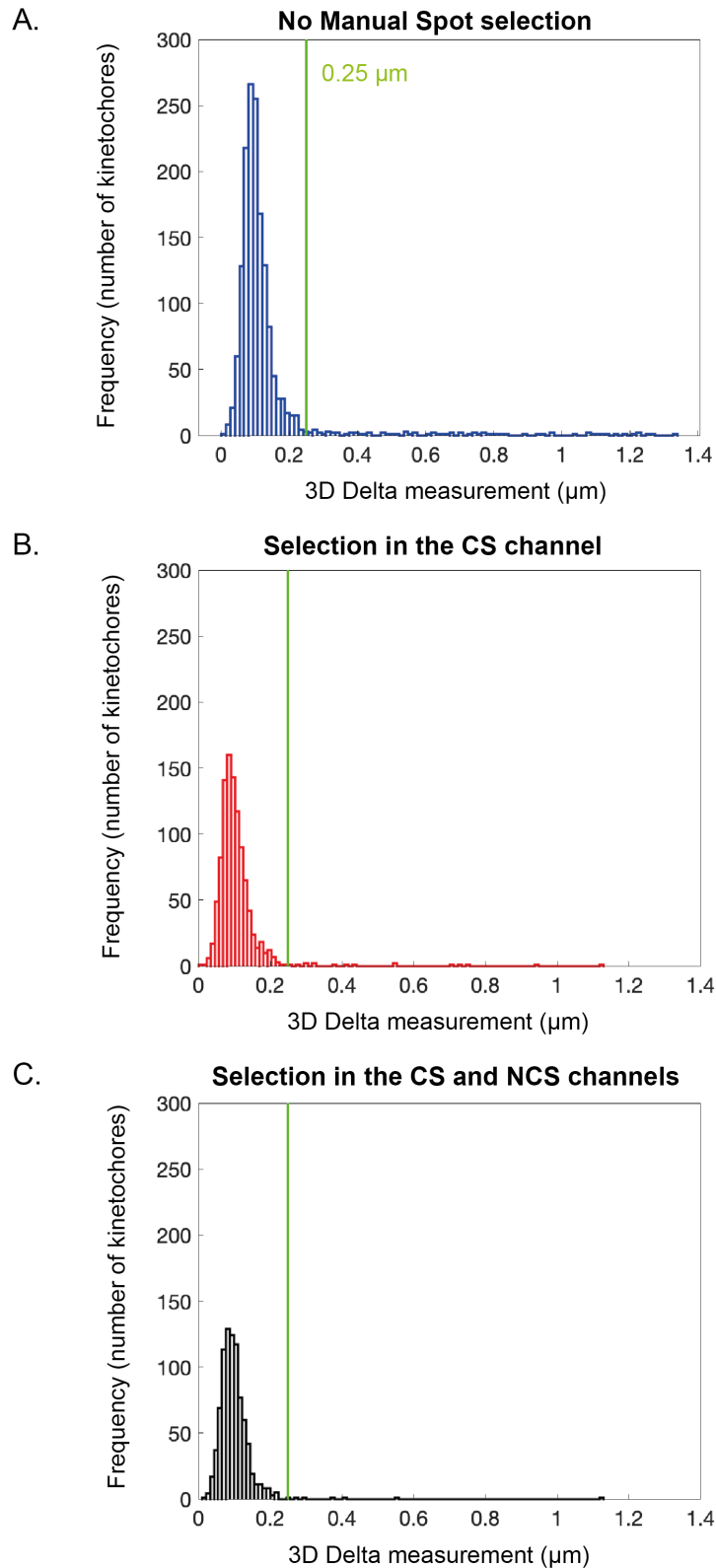
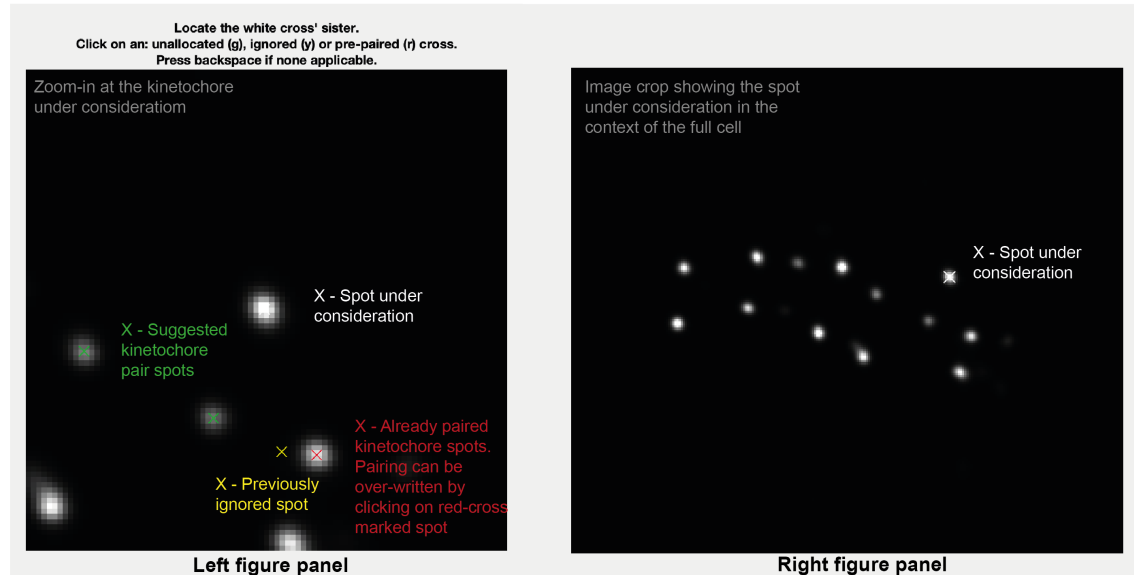


Figure 3.4: Spot quality control removes outlier 3D Delta distances. Intra-kinetochore distances are expected to be below $0.25 \mu\text{m}$ (green line) as kinetochores are observed to be 0.1 to $0.2 \mu\text{m}$ in size. Histogram of the measured 3D Delta CenpC-to-Ndc80(N) distances: A) without any spot quality control, B) after spot quality control in the Coordinate System (CS) channel, C) after spot quality control in the CS and non-coordinate system (NCS) channels.

A.



B.

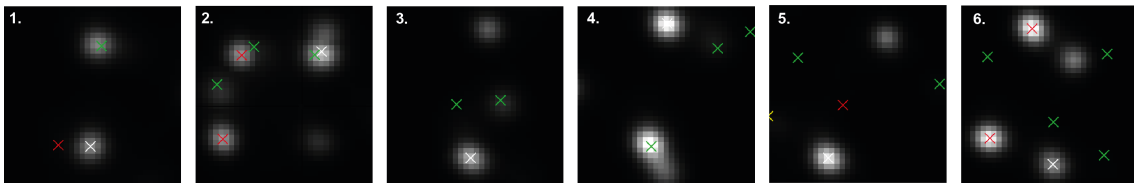


Figure 3.5: Quality control in the Coordinate system channel (CSC): kinetochore sister-sister pairing and spot quality control. A) Pairing of sister kinetochores. Left: zoom-in at the kinetochore spot under consideration (white cross) and spots within two microns that are suggested for pairing (green cross), already paired (red cross) or previously ignored for pairing (yellow cross). The image is projection of 5 z-slices around the spot under consideration. Right: image region of interest as set by the user in step 4, projection of 5 z-slices around the spot under consideration (white cross). B) Examples where the kinetochore spot under consideration should be excluded from analysis (ignored): the kinetochore spot under consideration or its sister kinetochore spot is distorted (2 and 4), the kinetochore spot center is not correctly detected (1), and the sister kinetochore spot is not detected (3, 5 and 6).

is displayed for pairing until all detected spots have been evaluated. In addition, if a spot is discarded but is a candidate for a following spot pair, the spot will be marked in yellow instead of in green. Here, to improve the data quality further we also ignored mis-shaped spots during kinetochore sister pairing. Mis-shaped spots can alter the detection of the spot center and thus are suspects for wrong center detection. Kinetochores that are close to overlapping with another kinetochore were also excluded as the signal overlap may confuse the detection. Therefore, up to now we have a refined spot position data set where background and suspect spots with possible poor center detection are discarded from the CS channel. The corresponding spots are also discarded from the NCS channels. However, we found that a small number of additional kinetochores are mis-shaped in the NCS channels only. This was further evident from remaining 3D Delta distance measurements higher than 250 nm. Such spots create outliers in the data and affect our measurements. Therefore, we sought to perform further quality control in the NCS channels.

The aim of quality control in the NCS channels is to discard mis-shaped spots and spots close to overlapping spots from the NCS channels. Therefore, we developed a GUI where all kinetochore spots and their detected centers from a cell will be displayed for assessment by the user (Figure 3.6). Spots that were discarded during the pairing in the CS channels are not analysed here, as they are already excluded from the analysis. The spot filtering GUI allows the user to create a list of the spots that they wish to accept for analysis. In two-colour Delta analysis, this step is performed in the one and only NCS channel. In three-colour pair-wise Delta analysis, there are two NCS channels. Therefore, NCS quality control is performed for each NCS channel, and a list with the intersection of good spots in both channels is generated.

In summary, now we have refined the spot detection data set such that (1) cells not fitting the analysis are excluded, (2) kinetochores are paired in the CS channel and thus background spots detected as kinetochores are excluded, (3) spots with suspected wrong center detection in the CS channel are excluded, and (4) spots with suspected wrong center detection in the NCS channel are excluded.

Here, we measured the 3D Delta again to see if we have remove the unrealistic distance of >250 nm. The 3D Delta distance histogram showed that only a few Delta distances of >250 nm remained. In the specific case of the Nnf1/CenpC/Ndc80(N)

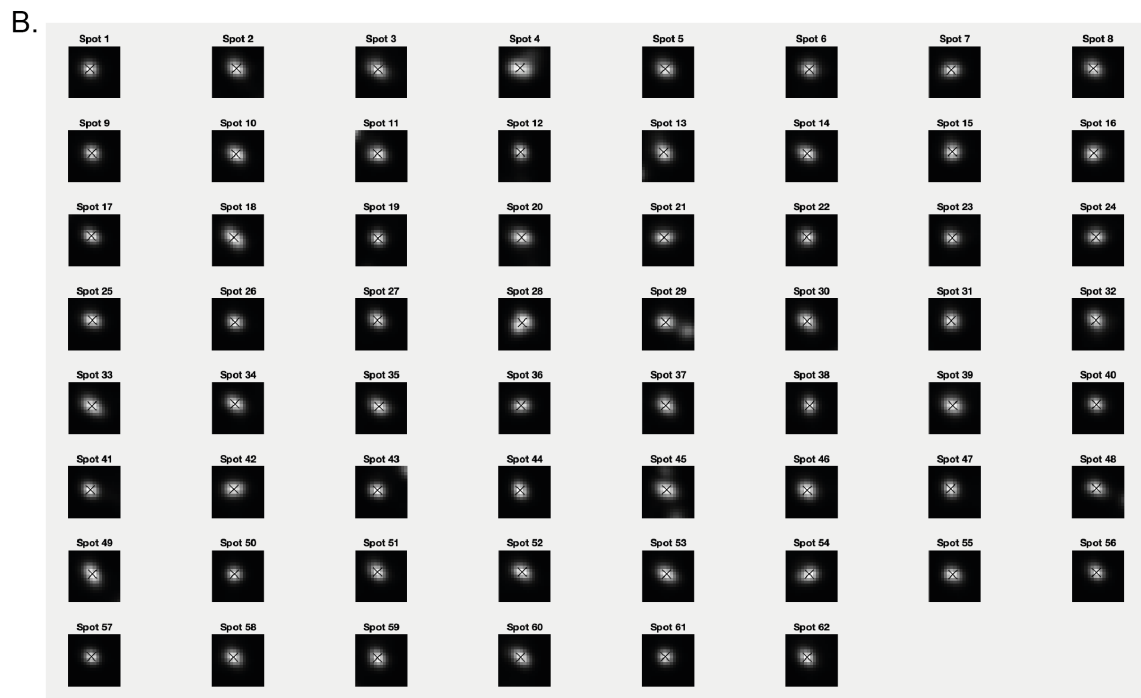


Figure 3.6: Kinetochores spot quality control in the non-coordinate system (NCS) channels. A. and B. show examples of spot selection GUI in two hTERT Rpe1 cells stained for Nnf1, CenpC and Ndc80(N). The spot selection is performed here in the Nnf1 channel. The user is required to evaluate the spot shape and center detection, and to discard non-gaussian shaped asymmetric spots (distorted spots) and spots with wrong center detection. In A), spot 1 is distorted, and Spots 31, 40 and 47 are too close to a neighbouring spot and their center may not be detected appropriately. Therefore, this spots should be excluded from analysis. In B), spots 4, 18, 28, 33 and 49 are distorted, and should be excluded from the analysis.

triangle, six distances were found to be larger than 250 nm. To eliminate the effect of those remaining outliers we set a threshold of 250 nm and excluded the distances.

The remaining step was to measure the 3D Delta and perform inflation correction in BEDCA. Here, we found the inflation-corrected 3D Delta (ΔEC) distance between CenpC and Ndc80(N) to be 85.4 ± 1.1 nm (847 kinetochores). The ΔEC distance between CenpC and Nnf1 was found to be 37.7 ± 0.8 nm (859 kinetochores). Finally, the ΔEC distance between Nnf1 and Ndc80(N) was found to be 57.5 ± 1.2 nm (848 kinetochores). This data represents a single experiment. For the pool of three performed experiments the reader is advised to see the complete work in Roscioli et al., provided in Appendix A. These distances, however, are not truly known in *in vivo* kinetochores. Therefore, we sought to test the protocol on a known true distance as a control. To do so, we stained cells with a-CenpC primary antibody and a mixture of A-488, A-568 and A647 secondary antibodies. Here, a single protein is labelled in three colours and thus the true distance is 0 nm. We analysed the data set via the methodology described above. The CenpC-CenpC measurement result showed 2.2 ± 1.5 nm between A-488 nm and A-561 nm (2303 kinetochores), 4.3 ± 2.7 nm between A-488 nm and A-647 nm (1437 kinetochores), and 4.5 ± 2.8 nm between A-561 nm and A-647 nm (1452 kinetochores). Therefore, we have achieved confidence of ~ 10 nm in our inflation-corrected 3D Delta distances. Further, the measured ΔEC distances has tight confidence intervals as compared to 3D Delta distance measurements as can be seen in Figure 3.7.

3.2.6 3D Delta measurements at kinetochore categories

In the study of kinetochore architecture we sought to investigate how the Spindle Assembly checkpoint may correlate with changes in the kinetochore architecture at unattached vs bi-oriented kinetochores. Therefore, we required a method to measure Delta distance at kinetochores with active and silenced SAC. One marker for SAC activity is Mad2. Therefore, we wished to (1) categorise kinetochores by eye into Mad2 positive and Mad2 negative, and (2) measure Delta distances at each sub-category. Earlier we developed a GUI that allows the user to view all spots detected in a cell and make a list of the accepted spots. Here, we decided to utilise that GUI for spot categorisation. All detected spots - real and background, were displayed in the GUI. The spots that had gaussian shape and resembled kinetochore spots were

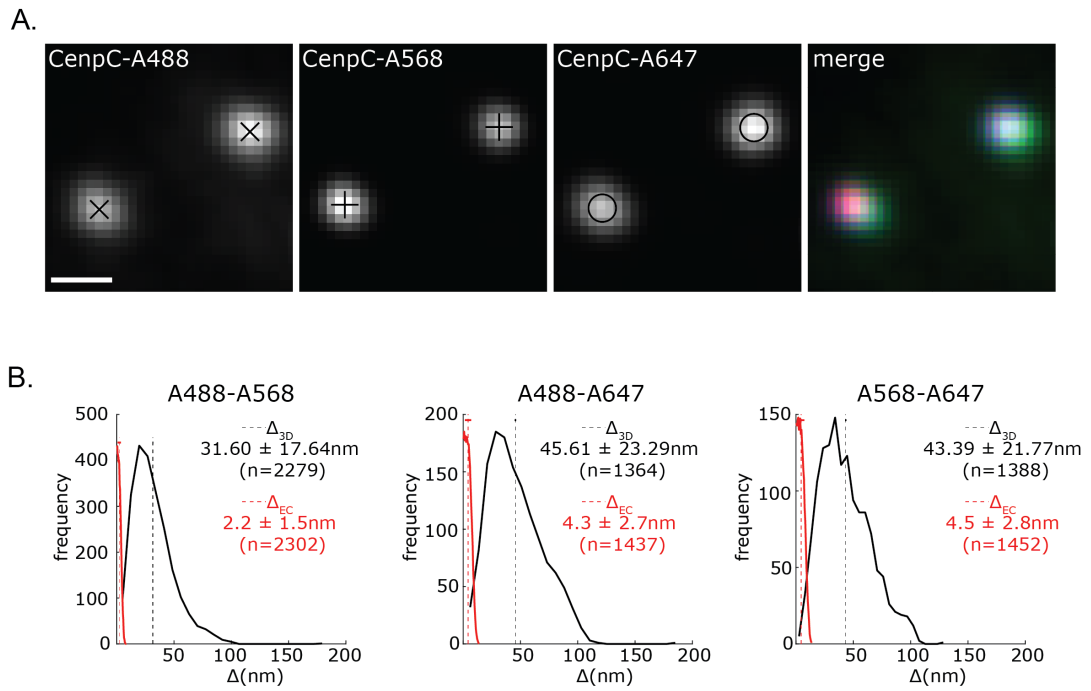


Figure 3.7: Accuracy of the Δ_{EC} measurement at 0 nm true intra-kinetochore distance. A) Representative images of a kinetochore pair in hTERT Rpe1 cells stained with anti-CenpC primary antibody and a mixture of A-488, A-568, and A-647 secondary antibodies. The centroid detection of the spots is denoted by a cross or a circle. Scale bar 500 nm. B) Histograms of the Δ_{3D} (black) and Δ_{EC} (red) measurements of the CenpC-to-CenpC distance. The CenpC secondary antibody labels between which the distance is measured is annotated above, the mean, standard deviation and number of kinetochores for each measurement is denoted on the right.

identified by eye were accepted in a list of "Mad2PositiveSelection". Similarly, non-gaussian background-like spots were classified as background and accepted in a list of "Mad2NegativeSelection". The 3D Delta was then measured in each sub-category. This method is not ideal as it qualitative but not quantitative. Nevertheless, it gave us initial insight into whether the SAC and kinetochore architecture interplay (see Chapter 4).

3.2.7 Protocol for inflation-corrected 3D Delta measurements

Here, we developed the first method for inflation-corrected 3D measurements. However, the method is complex due to the nature of the problem. That complexity and the combination of cell biology and computational knowledge required to run the algorithms with no direction would prevent the use of the method outside of our laboratory. In the same manner, previous Delta measurement methods are too complex for a novice to use. Therefore, we wished to make the methodology widely available and in that manner stimulated the progress and usability of Delta measurements. To do so, we first collaborated with Jonathan Harrison to improve the GUI in the software and make it more user friendly. Further, I described the full methodology in a detailed step-by-step guide. The guide is currently under revision in the STAR Protocols journal. Here, the aim is for the detail to be sufficient for even a novice Matlab user. This work is available in Appendix B.

3.3 Summary

To address the outstanding issues in the Delta measurement field, we made the following developments. Firstly, in collaboration with Nigel Burroughs, we developed a method for correction of the isotropic inflation in the X/Y axes and the anisotropic inflation in the Z-axis of 3D Delta measurements. We also improved our automatic spot detection to include manual cell and spot quality control components. Further, we implemented the previously discussed method for chromatic shift correction termed centralisation for fine correction of the chromatic shift. Finally, we described the method in a step-by-step guide (manuscript in revision, see Appendix B) such that even novice users can perform 3D inflation corrected measurements.

Chapter 4

Architecture and plasticity of the human kinetochore in non-transformed hTERT-Rpe1 cells

4.1 Background

In Chapter 3 we demonstrated the development and implementation of an image analysis pipeline and inflation correction algorithm that can accurately estimate the 3D euclidean distance (delta distances) between two kinetochore proteins labelled with different fluorophores (Germanova et al, in revision). The development of the methodology was a part of a larger effort in collaboration with E. Rosicoli to map the three dimensional architecture of the kinetochore in human non-transformed diploid cells (Rosicoli et al, 2020). These studies were motivated on two fronts:

(1) the rapidly emerging picture of kinetochore architecture based on *in vitro* reconstitution and structural biology studies using kinetochore proteins and complexes (Pesenti, Weir and Mussachio, 2016; Hamilton, Dimitrova and Davis, 2019). However, the link between these *in vitro* studies and how these proteins and complexes co-assemble *in vivo* is lacking. This is very important because we know that *in vivo* the human kinetochore provides binding sites for ~ 20 microtubules via ~ 8 Ndc80 complexes per microtubule (see Chapter 1 for details). Thus, unlike the single par-

ticles that are accessible to structural biology, the actual kinetochore is an ensemble of molecules forming a super-structure with a mass in the range of multiple megadaltons. The *in vivo* kinetochore architecture was first investigated in pioneering work by Wan and colleagues, who used 1D Delta measurements to identify the relative order of 16 kinetochore proteins (2009). An order that now we know to be broadly correct. However, as discussed in Chapters 1 and 3, 1D measurements suffer from projection and inflation effects and the exact measurements are not reliable. The *in vivo* kinetochore architecture was also investigated in 3D Delta study by Smith and colleagues. However, that also suffered from measurement inflation, and thus is unreliable. Therefore, detailed reliable map of the *in vivo* kinetochore architecture is lacking.

(2) Kinetochores are subjected to varying chemical and mechanical stimuli such as phosphorylation, force and microtubule binding. Determination of how these factors can influence kinetochore architecture *in vivo* will be an essential step towards understanding how kinetochores interpret inputs and alter their functional output to control chromosome segregation (Long et al., 2019).

This is particularly important with regard to how the spindle assembly checkpoint (SAC) and error correction processes operate. The SAC functions to prevent anaphase onset until all kinetochores have formed stable bi-oriented microtubule attachments. However, how the SAC detects such attachments remains unclear. There has been much debate as to whether the SAC detects and responds to kinetochore sister-sister (K-K) tension, to tension within the kinetochore (intra-kinetochore tension), or to the level of kinetochore microtubule occupancy. Early biophysics experiments showed that force applied to the kinetochore stabilises the kinetochore-microtubule attachment and correlates with changes in kinetochore phosphorylation (Nicklas and Koch, 1969; Nicklas et al., 1995). Therefore, tension was proposed to be one of the stimuli governing the kinetochore behaviour. In later studies, intra-kinetochore tension was suggested to lead to re-arrangement in the kinetochore architecture based on 1D Delta studies (Wan et al., 2009), and further raised the question of as to whether kinetochore architecture re-arrangements serve as an input for SAC silencing. To address that question, intra-kinetochore tension was investigated as an input for SAC silencing. Firstly, the kinetochore architecture was found to be affected by doses of taxol that prevent SAC silencing as detected by reduced

1D Delta distance, but not by doses that allow for mitotic progression (Maresca et al., 2009). Therefore, the authors suggested that the formation of stable bi-oriented attachments leads to intra-kinetochore stretch, which is further detected by the SAC and triggers SAC silencing at the kinetochore. However, in this study no direct evidence were presented that the intra-kinetochore stretch is the cause of SAC silencing. Attempting to address this question, a following study found that the observed mitotic arrest in taxol may be due to a small number of unattached kinetochores rather than the overall kinetochore conformation (Magidson et al., 2016). Overall, the conflicting data in the three studies, the different Delta methodologies utilised and the methodologies issues (see Chapter 3) led to confusion in the field and the following critical questions remained: are intra-kinetochore tension and kinetochore re-arrangements involved in SAC silencing?

A more recent set of studies investigated the question of as to whether the kinetochore detects kinetochore occupancy as a signal for SAC silencing. Here, SAC silencing at the kinetochore level was observed to occur at $\sim 50\%$ kinetochore-microtubule occupancy (Kuhn and Dumont, 2017; Dudka et al., 2018; Etemad et al., 2019). Therefore, the kinetochore appeared to "count" the number of microtubules. Further, kinetochore lateral attachments did not silence the SAC, albeit they resulted in K-K tension increase (Kuhn and Dumont, 2017; Dudka et al., 2018). That lead to two conclusions: (1) K-K tension is not the determinant of SAC silencing, and (2) end-on attachments provide unique interface that is the trigger for SAC silencing. However, the basis of that unique interface of the end-on kinetochore-microtubule attachment remains unclear. One hypothesis is that kinetochore architecture re-arrangements in response to end-on microtubule attachment provide that unique interface. Therefore, a crucial next step is to investigate how the kinetochore architecture responds to mechanical and chemical stimuli *in vivo* with reliable methods. Further, how the intra-kinetochore architecture and Delta may respond to microtubule occupancy and tension remains unclear and requires further investigation.

In this chapter, I will first summarize the main findings of the Roscioli et al study in which we provide a first 3D map of a human kinetochore and reveal how the structure responds to changes in attachment and tension. My aim is not to present the results in detail as my contribution was largely related to data analysis and interpretation (I am listed as the second author on Roscioli et al, 2020). The interested

reader can find the full paper in Appendix B. The chapter will instead focus on experiments that build on this work (Figure 4.5 onward) and provide a deeper insight into how conformation changes in the Ndc80 complex relate to the attachment state of the kinetochore and how this information may be relayed to the spindle assembly checkpoint (SAC).

4.2 Results

4.2.1 3D mapping of the human kinetochore architecture via ΔEC measurements

To understand how the kinetochore can adapt to chemical and mechanical stimuli, we first sought to understand the kinetochore architecture at metaphase kinetochores, which most likely have already formed mature bi-orientated attachments. To do so we mapped 12 proteins in metaphase hTERT Rpe1 cells. Consistent with previous data on the structural organisation of kinetochores, we found CenpC to be located inward from the outer kinetochore proteins. Further, Mis12-Ndc80(C)-Ndc80(N) mapped sequentially outward of CenpC (see Figure 4.1). The Knl1 N-terminus further positioned close to the Mis12-Ndc80 complex. That is consistent with its targeting to kinetochores via the Mis12 complex.

Interestingly, CenpC appeared to be on offset from the outer kinetochore axis. Here, the distances in CenpC-Nnf1-Ndc80(N) and in CenpC-Ndc80(C)-Ndc80(N) formed a triangle that is inconsistent with co-linear position of the proteins. That is in contrast to linearity observed for the Nnf1-Ndc80(C)-Ndc80(N) measurements. Structural studies have identified CenpC to be unstructured (see Chapter 1: Introduction). In comparison *in vitro* studies have shown that the Mis12-Ndc80 complex assembly appears as a mostly linear rod-like structure. Therefore, we hypothesised that flexibility in CenpC may result in small fluctuations in the CenpC position. These fluctuation could then result in CenpC appearing to be offset from the Mis12-Ndc80 axis in a population average measurement. It is important to note that while Delta measurements are a powerful method to probe kinetochore architecture, they only reflect the average conformation of an ensemble of protein complexes within a kinetochore, and the average of the structure within a population of kinetochores.

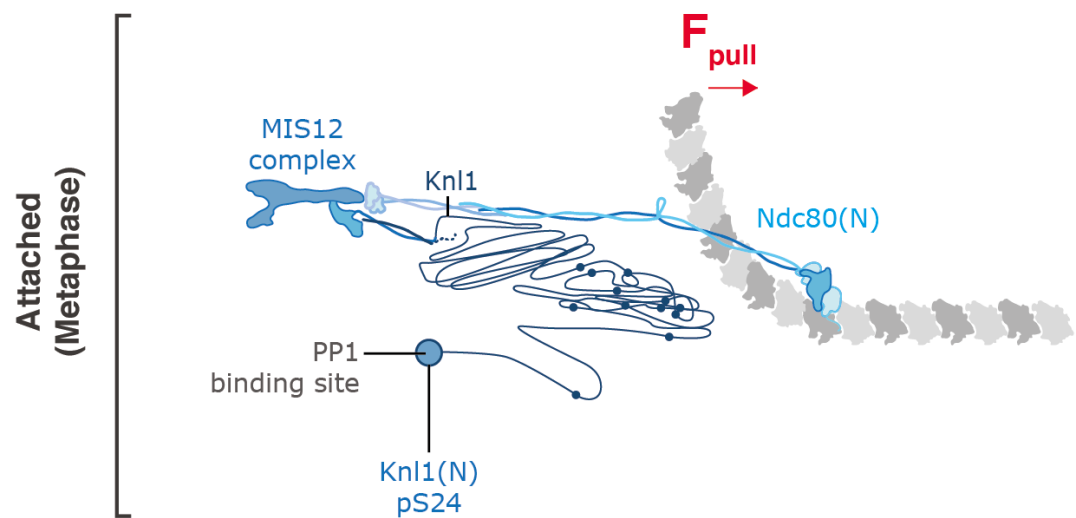


Figure 4.1: 3D Architecture of bi-oriented kinetochores. In Roscioli et al (2020), we mapped the organisation of the Mis12 complex (navy blue), Ndc80 complex (light blue), and Knl1 (dark blue) at metaphase kinetochores via 3D Δ EC population average measurements between the following proteins: Nnf1, Knl1 MELT 2, Knl1 pS24, Ndc80(C), and Ndc80(N). Based on the measurements and available structural information, we constructed the most likely configuration of a single kinetochore module at an attached kinetochore. The figure shows a cartoon representation of the predicted organisation. F pull arrow (red) denotes the direction of force generated by microtubule depolymerisation. Single microtubule protofilament is shown in grey.

i.e. it provides super-averaged distance and geometrical information. Therefore, we sought to visualise the CenpC offset in the context of known structural information via a computational simulation of the kinetochore ensemble. We built a simulation of a single kinetochore based on the following information from previous studies: (1) assembly order of the kinetochore, (2) structural biology of the Mis12 and Ndc80 complexes, (3) flexibility points in the Ndc80 complex, and (4) the numbers of molecules (see Table 4.1). The CenpC flexibility was visualised by fitting the distance of CenpC-to-Nnf1 (37.9 nm) and the focus point for CenpC molecules relative to the Nnf1-Ndc80N axis. The Mis12 and Ndc80 complexes, and the Ndc80 complex binding the K-fibre microtubule were constrained and modelled according to the information available in Table 4.1 and parameter fitting (for more information see Roscioli et al, 2020, Supplemental material). We mimicked making Δ EC distance measurements as follows: we performed super-averaging of 200 kinetochores and measured the distance between the centres of all molecules for every marker. In result we observed the mean marker positions of CenpC, Nnf1, Ndc80(C), and Ndc80(N) to form a triangle as expected from our Δ EC distance measurements. Therefore, the small random fluctuations in the CenpC position are sufficient to account for the non co-linear appearance of marker positions after Δ EC distance measurements (see Figure 4.2.).

The simulations revealed that indeed small fluctuation in CenpC position due to flexible linkage can explain the CenpC being offset from the Mis12-Ndc80 axis. Therefore, our ensemble average, combined with known structural information can be informative on the organisational properties of the kinetochore such as inherent flexibility. We next sought to further explore the organisation of the outer kinetochore by combining our Δ EC measurements on the Mis12 and Ndc80 complexes with known structural information. Here, we observed the Nnf1-to-Ndc80(N) and Ndc80(C)-to-Ndc80(N) Δ EC measurements to closely match available structural information (See Supplemental Table 2 from Roscioli et al., 2020). In an averaged ensemble measurement, if all molecules are aligned end to end, the individual molecule length will match the ensemble length (see Figure 4.3). On another hand, if the molecules are completely disorganised, the ensemble average length will be zero, and thus will not be representative of the length of single molecules. These phenomena of ensemble average length vs single molecule length can be described

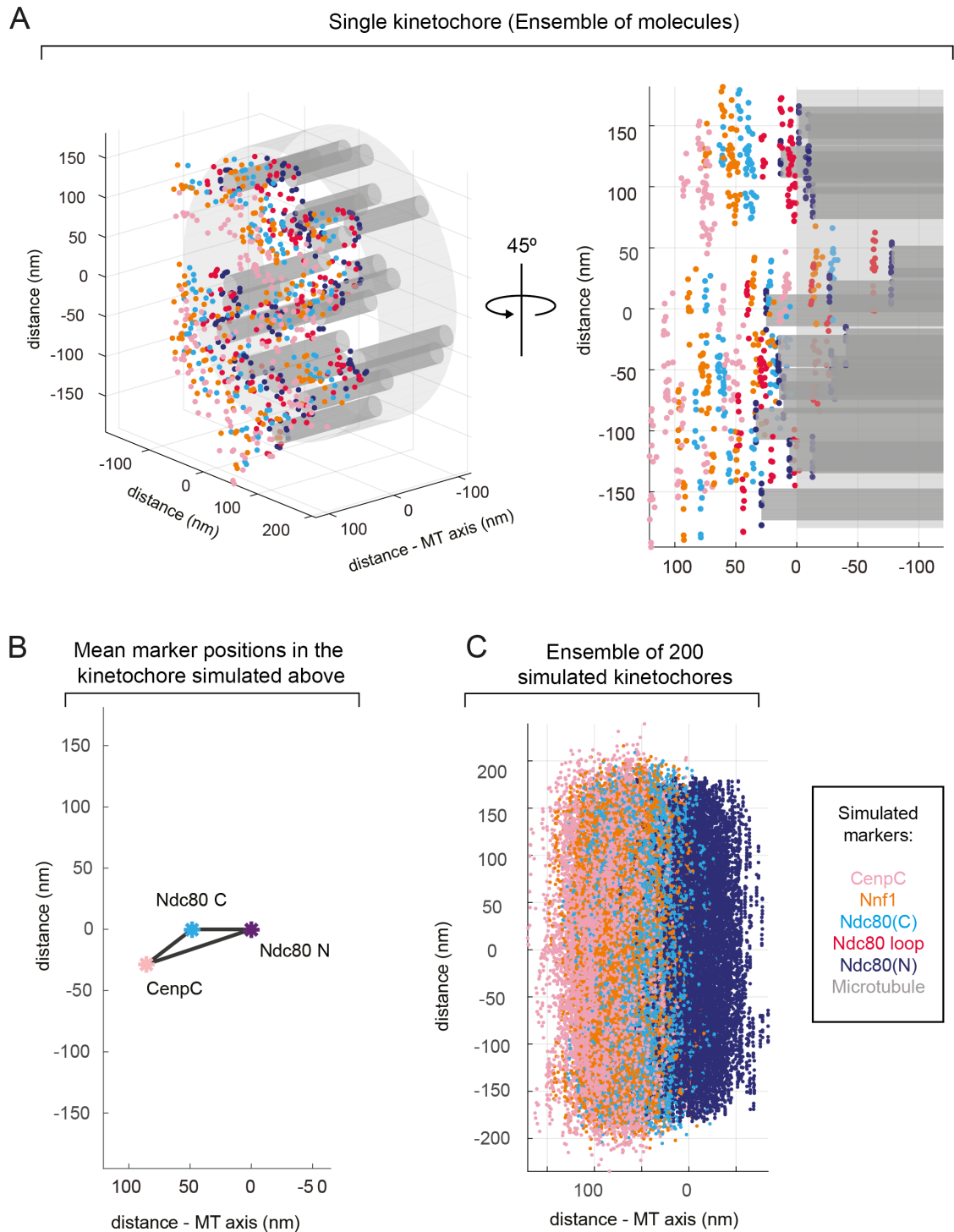


Figure 4.2: Simulations of bi-oriented kinetochore architecture. A) Two orientations of a simulated kinetochore. Each dot represents a marker at a single protein. Markers are denoted by colour. B) Distances between the mean positions of the CenpC, Ndc80(C), and Ndc80(N) markers in the simulated kinetochore, and their orientation relative to the microtubule axis. C) Ensemble of 200 simulated kinetochores. Kinetochores are aligned along the K-fibre axis and at the mean Ndc80(N) position.

Parameter	Value	Reference
Microtubule bundle (K-fibre)		
K-fibre cross-section area	0.1 μm^2	Nixon et al., 2015
Microtubule radius	13 nm	Ledbetter and Porter, 1963
Number of microtubules in a K-fibre	20	Booth et al., 2011
Ndc80 complex		
Number of Ndc80 complex molecules per microtubule	8	Joglekar et al., 2006
Ndc80 complex full length (along the complex)	60 nm	Huis in 't Veld et al., 2016; Wang et al., 2008; Wei et al., 2005;
Ndc80(C) to Ndc80(N)*	51 nm	estimated from: Huis in 't Veld et al., 2016; Wang et al., 2008;
Ndc80(C) to Ndc80 hinge	35 nm	estimated from: Huis in 't Veld et al., 2016
Ndc80 hinge to Ndc80(N)*	16 nm	Wang et al., 2008
Spc24/Spc25 RWD domains	4 nm	Cifferi et al., 2005
Ndc80(N)* to microtubule axis	4.25 nm	estimated from: Alushin et al., 2010
Mis12 complex		
Mis12 complex full length (along the complex)	20 nm	Huis in 't Veld et al., 2016; Petrovic et al., 2010
Nnf1** to Ndc80(C)	14 nm	estimated from: Huis in 't Veld et al., 2016; Petrovic et al., 2010;
Nnf1** to Ndc80(N)*	64 nm	estimated from: Petrovic et al., 2014; Screpanti et al., 2011;

Table 4.1: Parameters used for kinetochore ensemble simulations The Table uses the following annotations: *Ndc80(N) denotes the anti-Hec1 (9G3) antibody binding site (Ndc80 amino acids 200-215; DeLuca et al., 2006); ** The anti-Nnf1 antibody is assumed to bind in the middle of the MIS12 complex

by nematic order. Nematic order is the alignment of molecules along an internal axis with 1D orientation. Nematic order appropriately describes the kinetochore ensemble of molecules because kinetochores have intrinsic 1D orientation - kinetochore proteins assemble in a spatial directional sequence to create the inner and outer kinetochore layers and the protein sub-domains. Therefore, we calculated the nematic order of the kinetochore to assess the intra-kinetochore alignment of molecules. The nematic order can be calculated as the average length of the ensemble of molecules divided by the average length of the single molecule : $N = \frac{|\langle \vec{x} \rangle|}{\langle |\vec{x}| \rangle} = \frac{\Delta EC}{\Delta_{structural}}$ (see Figure 4.3). We estimated the Nnf1-to-Ndc80(N) single molecule distance to be 64 nm and the Ndc80(C)-to-Ndc80(N) single molecule distance to be 51 nm based on *in vitro* electron microscopy and crystallography studies (Huis in 't Veld et al., 2016; Wang et al., 2008; Wei et al., 2005; Petrovic et al., 2010; Ciferri et al., 2005; see Figure 4.3). For the estimation, we assumed that the Nnf1 antibody binds along the full Nnf1 protein, and thus renders a position in the middle of the Mis12 complex. Such estimation was necessary because the antibody is raised against the full-length Nnf1 protein and the antibody binding epitope is unidentified (see Roscioli et al for further details). Based on the estimated structural and the measured ΔEC lengths, we calculated the nematic order for the Nnf1-to-Ndc80(N), and Ndc80(C)-to-Ndc80(N) to be 0.95 ± 0.01 and 0.97 ± 0.06 , respectively. Such nematic order is close to 1, and thus shows that the outer kinetochore is highly ordered in hTERT Rpe1 cells.

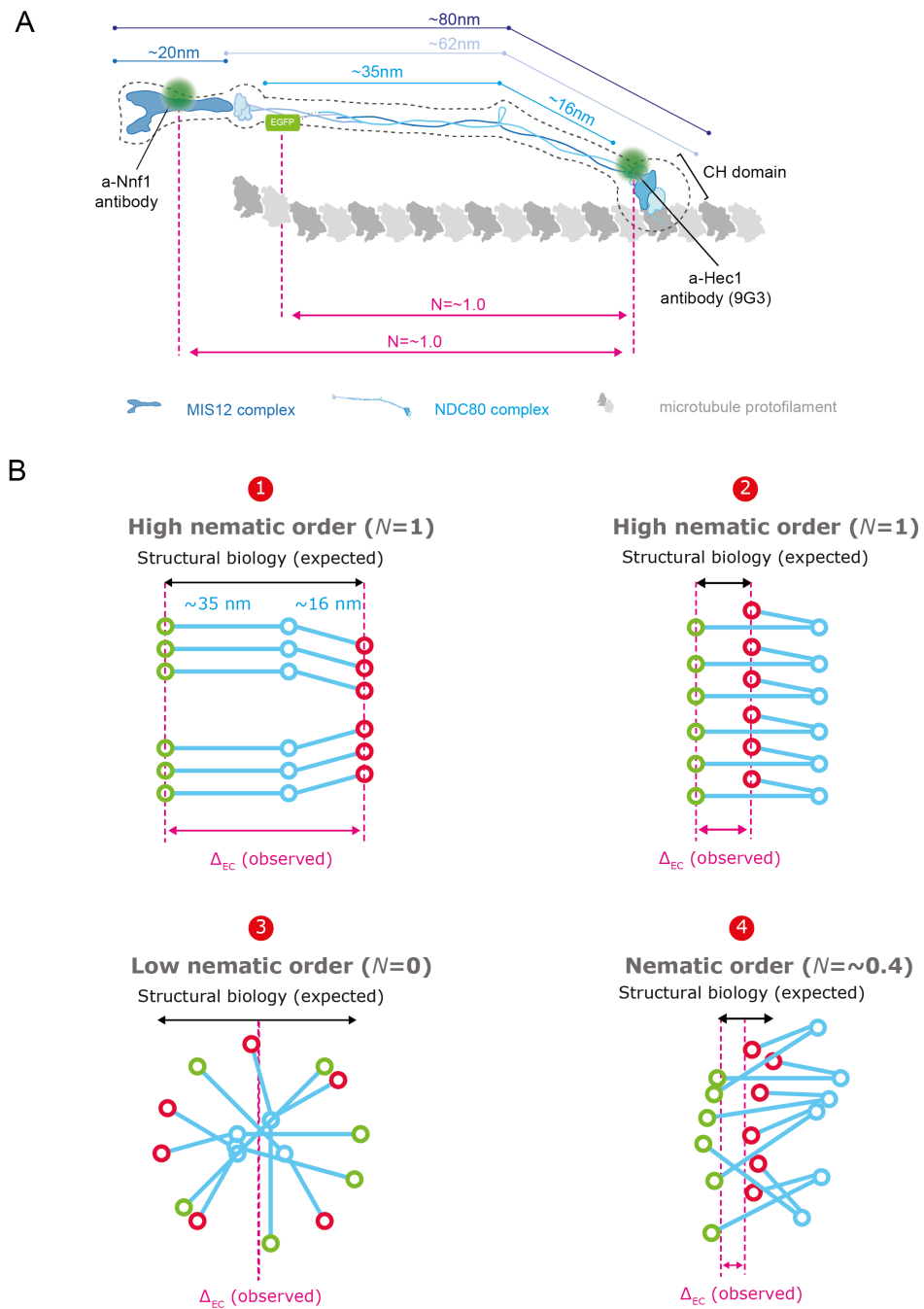


Figure 4.3: Nematic order of the outer kinetochore A) Schematic of the available structural information on Mis12 and Ndc80 complex organisation. The nematic order is indicated in pink. Positions of protein labelling are denoted by green shapes: estimated antibody epitopes (circles), and eGFP label (barrel). B) Schematic of the nematic order concept. To calculate the nematic order, the observed Δ_{EC} distance (pink) is divided by the expected distance from structural studies (black). If all molecules are perfectly aligned, the Δ_{EC} measurement will match the expected structural distance, i.e. high nematic order $N = \sim 1$ (1 and 2). If the molecules are unaligned, the Δ_{EC} measurement will be shorter than the expected structural distance, i.e. low nematic order, $N = \sim 0$ (3). The estimated $N = 0.4$ for Ndc80 at unattached kinetochores is visualised in (4)

4.2.2 Differential kinetochore architecture changes in response to loss of attachment and tension

We next sought to investigate how the kinetochore architecture may respond to microtubule attachment and imposition of forces. Here, we first utilised nocodazole treatment to depolymerise the microtubules in cells and recreate a state of the kinetochore where there is no microtubule attachment and, thus, also no K-K tension. After, mapping of 10 proteins we showed that the overall kinetochore architecture is retained. In specific, we showed that CenpC, Mis12 and the C-terminus of the Ndc80 protein do not respond to loss of attachment. In contrast, we showed that the Ndc80(C) to Ndc80(N) distance shortens by about 41 nm in nocodazole. Such measurement can reflect disorganisation of Ndc80 or change in the Ndc80 conformation. The Ndc80 loop situated between the Ndc80(C) and Ndc80(N) has been shown to allow for bending in Ndc80 *in vitro* (Wang et al., 2009). Therefore, we first hypothesised that the decrease in Ndc80(C)-to-Ndc80(N) distance is due to conformational change in the Ndc80 complex. To test that hypothesis we simulated as to whether bending of the Ndc80 complex at the Ndc80 loop can explain the distance decrease. Here, results showed that change in Ndc80 conformation alone is insufficient to explain the observed Delta distance reduction. Therefore, it is likely that in nocodazole, Ndc80 attains bent conformation (Ndc80 jack-knife) and becomes more disordered, i.e. the Ndc80 complex molecules are in preferred bent conformation and do not align along an internal axis (low nematic order). In addition to the changes in the Ndc80 complex, in nocodazole we observed the Knl1 unstructured N-terminus but not MELT domains to unravel outward of the inner kinetochore. Therefore, we identified two components that respond to microtubule attachment and/or imposition of force by the microtubules.

We next set to untangle as to whether Ndc80 and Knl1 sense lack of microtubule attachment or force in nocodazole. Here, we next used taxol to inhibit specifically the microtubule dynamics and, thus, imposition of force at the kinetochore. Ndc80 did not display jack-knifing and loss of alignment upon taxol treatment and thus did not respond to loss of tension alone. Therefore, Ndc80 specifically attains jack-knifed conformation and unaligned state at unattached kinetochores. In contrast, the Knl1 N-terminus unravelled outward upon taxol treatment, albeit not to the

same extend as upon nocodazole treatment. Therefore, Knl1 N-terminus unravels specifically at loss of K-K tension, and thus can sense changes in imposition of force at the kinetochore. In summary, here we uncovered Ndc80 and Knl1 to be distinct kinetochore sensors for microtubule attachment and force, respectively (see Figure 4.4).

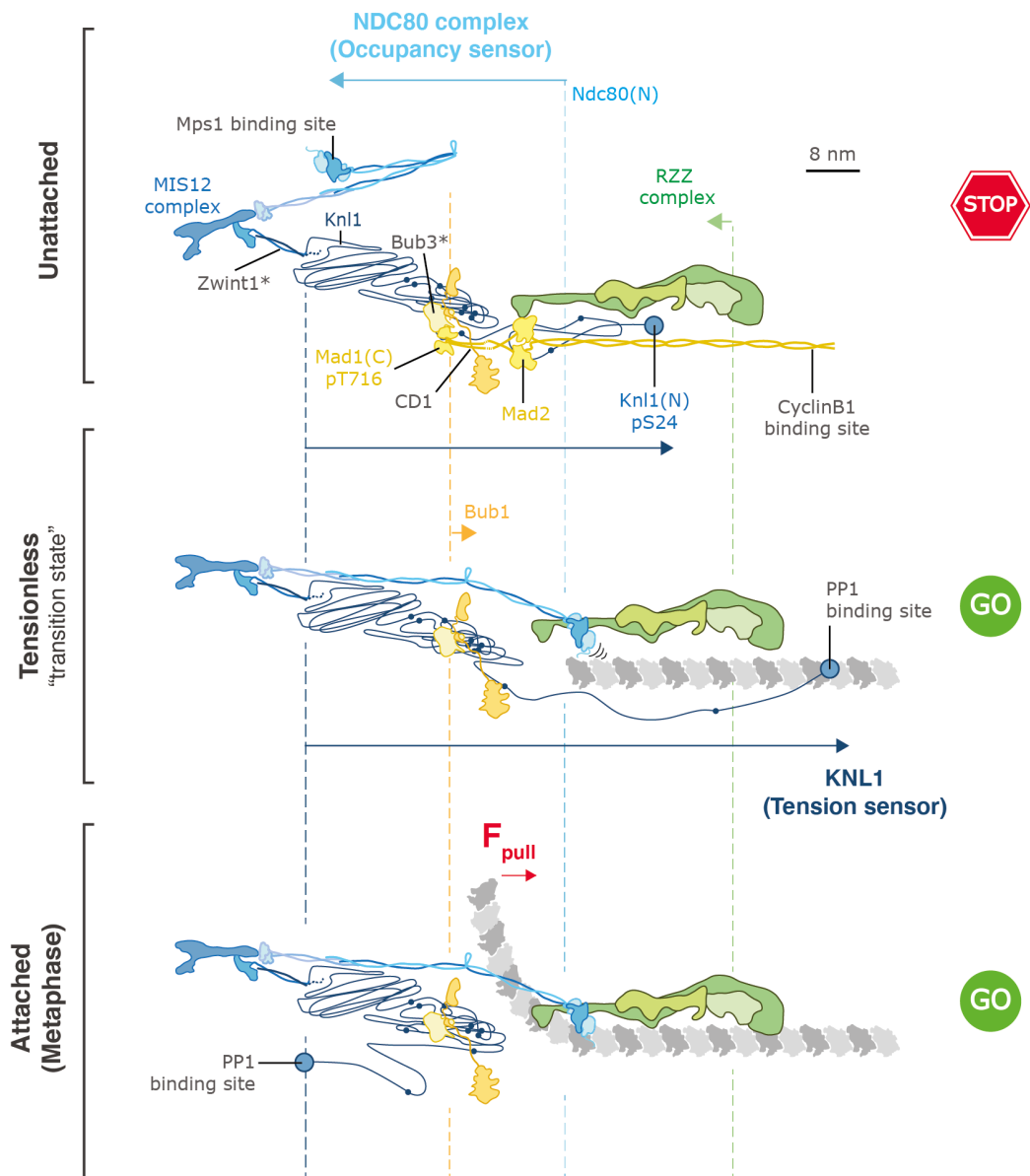


Figure 4.4: Ndc80 and Knl1 are distinct microtubule occupancy and tension sensors Schematic of the ensemble average organisation of the Mis12 complex (blue), Knl1 (dark blue), Ndc80 complex (light blue), Mad1:Mad2 (yellow), Bub1 (orange) and RZZ complex (green) at unattached (120 min nocodazole treatment), tension-less (15 min taxol treatment), and attached (unperturbed metaphase) kinetochores. The changes in Knl1 pS24 and Ndc80(N) positions are indicated with dark blue and light blue arrows, respectively.

4.2.3 Ndc80 jack-knifing correlates with Mad2 status

The sensor at kinetochores that senses kinetochore microtubule occupancy and triggers SAC silencing remains elusive. We uncovered that Ndc80 jack-knifes at loss of microtubule attachment. Therefore, we hypothesised that Ndc80 jack-knife and SAC activity are correlated. To test that hypothesis, we sought to measure the CenpC to Ndc80(N) distance at DMSO-treated kinetochores with active and silenced SAC separately. Here, we used Mad2 as a marker for kinetochore with active SAC (see Figure 4.5). We imaged metaphase hTERT Rpe1 cells expressing endogenous Mad2, and stained for CenpC and Ndc80(N). To uncover the Ndc80 conformation specifically on Mad2 positive kinetochores, we visually categorised the kinetochores as Mad2 "positive" and Mad2 "negative". To do the categorisation, we visually inspected the Mad2 signal at kinetochores in the KiD software, and categorised kinetochores with seemingly background-level Mad2 signal as Mad2 "negative", and kinetochores with spot- or crescent-like Mad2 signal as Mad2 "positive". Next, we performed Delta distance analysis on each category. The Mad2 "positive" kinetochores showed shorter CenpC-Ndc80(N) Δ EC distance as compared to Mad2 "negative" kinetochores (see Figure 4.5). The CenpC-to-Ndc80(N) Δ EC measurement in the pool of Mad2 "positive" and "negative" kinetochores was very similar to the one at Mad2 "negative" kinetochores only (see Figure 4.5). That result reflects on the fact that Delta is a population measurement where the average position of molecules is detected, i.e. Delta will reflect the most common kinetochore architecture.

Therefore, a small population of kinetochores with different architecture, such as the Mad2 "positive" kinetochores, will be masked by the prevalent kinetochore architecture, i.e. the Mad2 "negative" kinetochores. The pattern of decrease in the CenpC-to-Ndc80(N) distance at Mad2 positive kinetochores is consistent with the decrease in distance we observe at Mad2 "positive" unattached kinetochores in nocodazole. However, the exact distance at Mad2 "positive" kinetochores did not fully recapitulate the distances of nocodazole-treated kinetochores. That was probably due to the qualitative classification of kinetochores into Mad2 "positive" and "negative", and the small number of Mad2 "positive" kinetochores analysed. These results further suggested that Ndc80 jack-knifing and SAC activity are correlated. We further tested as to whether SAC activity is required for the Ndc80 jack-knifed state by artificial silencing of SAC (see Roscioli et al, Appendix B). The SAC was

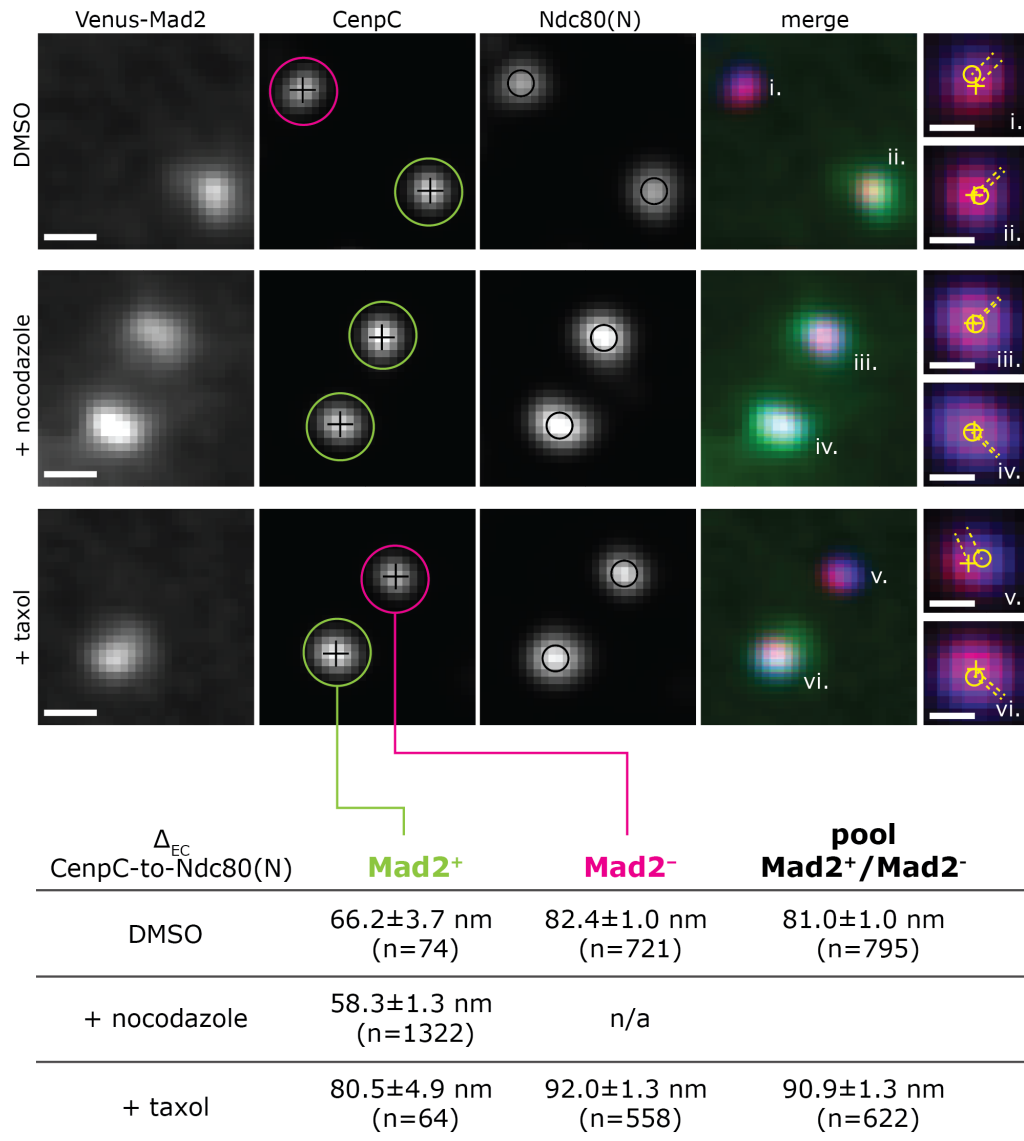


Figure 4.5: Ndc80 jack-knife correlates with Mad2 status Top: Representative images of kinetochores in hTERT Rpe1 cells expressing endogenous label Venus-Mad2, stained for CenpC and Ndc80(N) (9G3), treated for 120 min with 1:1000 DMSO or 3.3 μ M nocodazole, or for 15 min with 1 μ M Taxol. Kinetochores were categorised visually as Mad2 "negative" (purple) or Mad2 "positive" (green). Insets on the right show the centroid detection in the CenpC and Ndc80(N) channels, and the projected distance between the centroids. Bottom: The Δ_{EC} distance between CenpC and Ndc80(N) was measured in the kinetochore populations categorised as "positive" and "negative", and in the pool of all kinetochores for each treatment condition (n - number of kinetochores, two biological replicates, >30 cells per condition).

artificially silenced via Mps1 inhibition with reversine (Santaguida et al., 2010). Here, we showed that at unattached kinetochores even if the SAC is artificially silenced, Ndc80 remains in jack-knifed state. Therefore, the results suggested that the Ndc80 jack-knife conformation is not maintained by Mps1 and the transition of Ndc80 from jack-knife to straight conformation is not triggered by the inactivation of Mps1. However, the interplay between Ndc80 jack-knifing and SAC activity remained unclear.

4.2.4 Visual kinetochore categorisation vs Quantitative analysis of kinetochore Mad2 status

Here, I decided to further investigate the potential interplay between Ndc80 jack-knifing and SAC activity. In our previous investigation of the CenpC-to-Ndc80(N) distance relative to Mad2 status in physiological conditions, we imaged metaphase cells with at least one Mad2 positive kinetochore to enrich for the Mad2 "positive" kinetochore population. This selection, however, still resulted in a data set of only 74 Mad2 "positive" kinetochores out of 795 kinetochores total (see Figure 4.5, dataset discussed in sub-section above, 38 cells from two biological replicates). In our work in Roscioli et al, we obtained a larger dataset of Mad2 "positive" kinetochores via 120 min nocodazole treatment that depolymerises the mitotic spindle microtubules and renders kinetochores unattached. To advance our previous analysis, we first sought to improve our Mad2 "positive" sample size in physiological conditions rather than use nocodazole to create unattached kinetochores. Kinetochores with active SAC are primarily found in prometaphase cells. Therefore, to increase the number of Mad2 "positive" kinetochores, we imaged a mixture of prometaphase and metaphase cells. We imaged any cell that was in metaphase or prometaphase and thus the selection is random as far as is achievable. We estimate that about 38% of cells are in prometaphase in that selection by visual inspection of kinetochore alignment: cells classified as "prometaphase" had condensed chromosomes and one or more unaligned kinetochores. Such mixture of mitotic stages would also provide us with a sense of the full Venus-Mad2 signal variability in physiological conditions. We first repeated the workflow we used in the Roscioli et al study, and designated kinetochores to be Mad2 "positive" or Mad2 "negative" based on visual inspection. Here, the CenpC to Ndc80(N) distance was found to be 18.55 ± 10.32 nm in the

Mad2 "positive" kinetochore category (n=777 kinetochores, mean (mn) of the estimated mean ΔEC (μ) distribution \pm standard deviation (sd) of μ parameter, see Chapter 3 Figure 3.2) and 81.26 ± 1.69 nm in the Mad2 "negative" kinetochore category (n=1442 kinetochores, mean (mn) of the estimated mean ΔEC (μ) distribution \pm standard deviation (sd) of μ parameter, see Chapter 3 Figure 3.2). The CenpC-to-Ndc80(N) distance at Mad2 "negative kinetochores recapitulated our previous observation. The CenpC-to-Ndc80(N) distance at Mad2 "positive" kinetochores was much lower than we previously observed after 120 min of nocodazole treatment: 55.7 ± 3.2 nm (mean \pm sd). However, unpublished observations in our lab show that the duration of nocodazole treatment gives rise to different Delta values. In fact, at 15 min nocodazole treatment the CenpC-Ndc80(N) distance is ~ 30 nm. Therefore, there are two possibilities here: (1) the physiological distance may be shorter and reflect the configuration of unattached kinetochores where there is an intact spindle and (2) the visual categorisation of kinetochores into Mad2 "positive" and "negative" suffers from a kinetochore miss-assignment error that affects the results.

Kinetochore miss-assignment error is likely here because spots are visually inspected and assigned as "positive" or "negative". A further factor that potentially contributes to kinetochore miss-assignment is the auto-scaling of kinetochore intensities in KiD when images are displayed for visual spot inspection. In result, in each Mad2 category we may have a population of correctly assigned Mad2 "positive" kinetochores with short CenpC-to-Ndc80(N) distance and a population of incorrectly assigned kinetochores with longer CenpC-to-Ndc80(N) distance. Therefore, the resulting distribution of measurements may contain outlier measurements. As we described in Chapter 3, outliers affect the ability of BEDCA to correctly construct the non-inflated posterior Delta distribution. Therefore, the BEDCA measurement may be unreliable in this case due to outlier effects.

Therefore, I next sought to make quantitative measures of the Mad2 intensity and asses for kinetochore miss-classification. I measured the intensity of Venus-Mad2 on individual kinetochores as follows. The Mad2 intensity was measured in 300 nm radius from the CenpC centroid in KiD. The mammalian kinetochore has size of about 300 nm, and thus we do not expect Mad2 to be more than 300 nm apart from CenpC. Kinetochores with miss-shaped or overlapping CenpC or Ndc80(N)

signal were excluded from analysis. The background-subtracted Mad2 intensity measurement was then calculated for each of the analysed kinetochores. I first plotted a histogram of the Mad2 kinetochore measurements. The histogram showed Mad2 intensity distribution with a positive intensity tail as expected (see Figure 4.6).

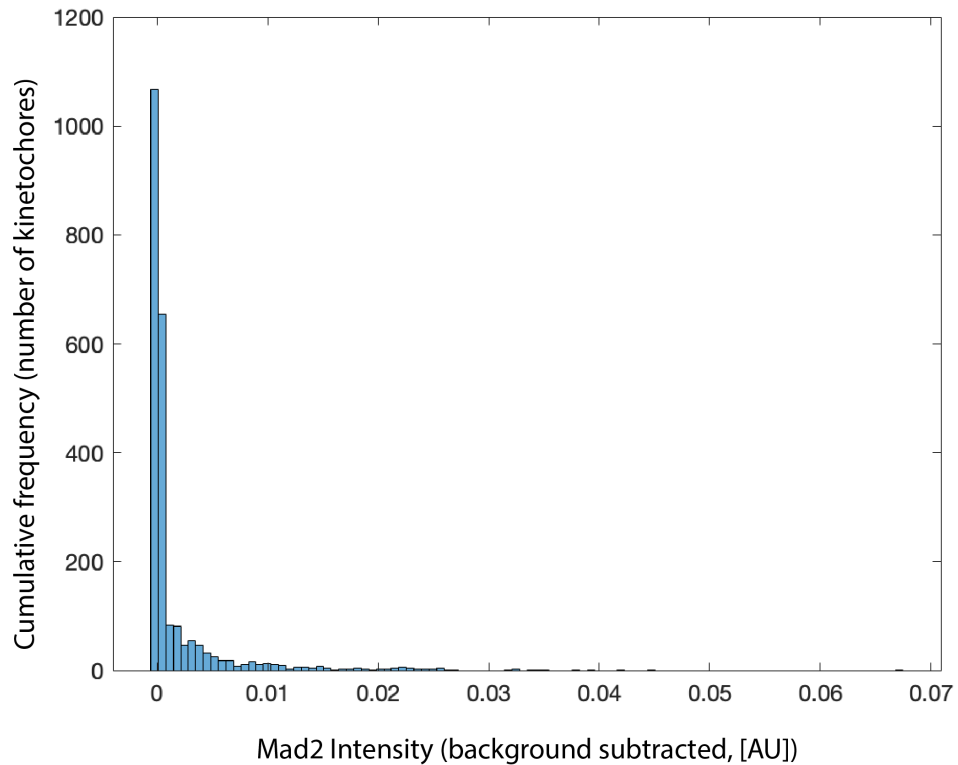


Figure 4.6: Quantification of Mad2 kinetochore intensity. Mad2 intensity was measured in a sphere with 300 nm radius, centered at the detected CenpC spot center. The figure shows a histogram of the measured background-subtracted kinetochore Mad2 intensities.

Finally, I tested the the visual categorisation against the qualitative analysis to understand if the visual categorisation is error prone. Specifically, I wanted to test to what extent the distribution of intensities overlap in the Mad2 "positive" and Mad2 "negative" categories. If the assignment is perfect, the intensity distributions of the two categories will show no overlap. Alternatively, a region of overlap would establish a sub-population of miss-assigned kinetochores. Plots of the cumulative intensity distribution of kinetochores assigned as "positive" (magenta) and "negative" (blue) showed a region of overlap (green) between the two categories (see Figure 4.7). Therefore, the plot confirmed that qualitative analysis is error-prone

and quantitative analysis should be used where possible.

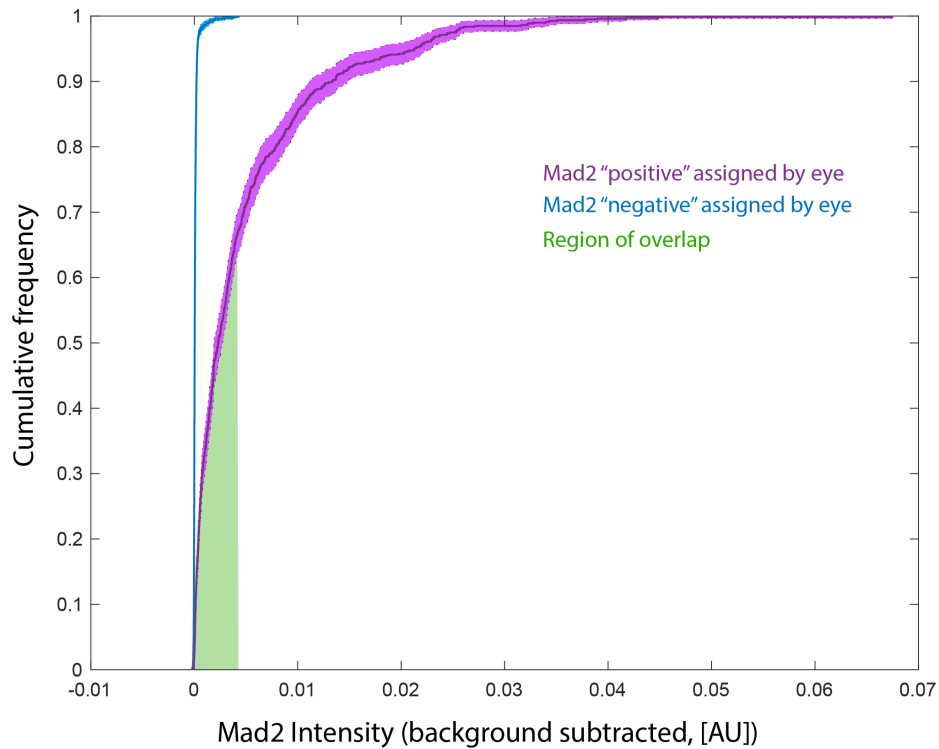


Figure 4.7: Miss-categorisation of kinetochores in qualitative Mad2 status analysis. Cumulative frequency distribution of the Mad2 intensities measured for kinetochores qualitatively assigned as "positive" (purple) and "negative" (blue). The Mad2 intensity overlap between the two qualitative categories is shown in green.

4.2.5 Mad2 unloading precedes the switch of Ndc80 into the ordered state

I next wanted to investigate the relation of ΔEC to the quantitatively measured Mad2 signal. What I would have liked to do is to measure the ΔEC on each kinetochore, and determine the correlation/association between the Mad2 intensity and ΔEC at each individual kinetochore. However, this is not possible because ΔEC cannot be measured at individual kinetochores due to insufficient accuracy in spot localisation. ΔEC distances can only be measured as a population average measurement because in this case the spot localisation error is reflected in the measurement distribution and is accounted for in the analysis pipeline. To circumvent the population measurement requirement issue I binned the kinetochores with respect to Mad2 intensity as follows: I ordered all kinetochores from lowest Mad2 intensity

to highest Mad2 intensity. Next I binned the kinetochores in bins of 100 from low towards high kinetochore Mad2 intensity, creating 23 bins. Here, bin 1 is with lowest Mad2 intensity and bin 23 is with highest Mad2 intensity. Next, we determined the CenpC-to-Ndc80(N) distance in each 100 kinetochore bin (See Table 4.2). We observed distances of below 50 nm in bins 23 to 18, and above 72 nm in bins 17 to 1. Therefore, in the six bins with highest Mad2 intensity, kinetochores had CenpC-to-Ndc80(N) distances of below 50 nm. In specific, the distances observed here for CenpC-to-Ndc80(N) are 37.6 ± 8.6 nm, 26.9 ± 10.2 nm, 33.2 ± 10.2 nm, 36.9 ± 9.1 nm, 29.2 ± 11 nm and 49.3 ± 6.7 nm, in bins 23 to 18, respectively (mean (mn) of the estimated mean ΔEC (μ) \pm standard deviation (sd) of μ parameter, see Chapter 3 Figure 3.2).

These distances are in the range of distances we observed after 15 to 120 min nocodazole treatment, i.e. 30 to 55 nm. This analysis avoids kinetochore miss-assignment due to qualitative analysis. Therefore, we can exclude effects of kinetochore miss-assignment and conclude that in physiological conditions the CenpC-to-Ndc80(N) distance is on average between 26.9 and 49.3 nm at unattached kinetochores.

Next, I wanted to visualise and explore how the Mad2 decays and how does the CenpC-to-Ndc80 distance behaves as Mad2 decays. In Figure 4.8, the 23 kinetochore bins are separated on the x-axis. The Mad2 intensity spread of each bin is shown on the primary y-axis. The CenpC-to-Ndc80(N) distance for each kinetochore bin is shown on the secondary y-axis. The plot showed that the Mad2 intensity decays exponentially from the highest Mad2 intensity bin 23 to the lowest Mad2 intensity bin 1. In contrast, the CenpC-to-Ndc80(N) distance did not follow this pattern. The CenpC-to-Ndc80(N) distance remained below 50 nm in bins 23 to 18. Next, the distance sharply increased as in bin 17 the CenpC-to-Ndc80(N) distance was found to be 75 nm. Finally, in bin 17 to bin 1, the CenpC-to-Ndc80(N) distance continued to increase but in linear fashion.

To observe directly the relation between Mad2 intensity and CenpC-to-Ndc80(N) ΔEC , I next plotted the median Mad2 intensity per bin vs the CenpC-to-Ndc80(N) distance in the bin (see Figure 4.9). To aid data visualisation in Figure 4.9, the plot is also shown with the Mad2 intensity displayed as percentage from the median of the bin with highest Mad2 intensity, i.e. normalised for the highest bin median to be 100% Mad2 intensity. That analysis revealed that the CenpC-to-Ndc80(N)

Mad2 intensity bin	CenpC-to-Ndc80(N) Euclidian corrected Delta distance (nm)	Standart deviation (nm)
1	95.522	4.2077
2	95.4676	3.671
3	90.4419	4.5754
4	95.1198	4.9509
5	85.262	5.4049
6	89.0053	5.2975
7	83.1466	4.5826
8	88.5154	4.1714
9	89.6207	4.0615
10	92.3961	4.3875
11	80.8646	5.579
12	83.3835	4.9705
13	80.1626	5.4222
14	81.6094	4.3815
15	73.7969	5.404
16	72.558	6.3609
17	75.5553	4.2397
18	49.3742	6.7332
19	29.2115	11.0695
20	36.8582	9.132
21	33.1793	10.1773
22	26.9421	10.2086
23	37.6044	8.6177

Table 4.2: CenpC-to-Ndc80(N) Δ EC distance at kinetochores binned based on Mad2 intensity Kinetochores were binned based on Mad2 kinetochore intensity in 23 bins of 100 kinetochores, where bin 23 has highest Mad2 intensity and bin 1 has lowest Mad2 intensity (column 1). The Δ EC distance between CenpC and Ndc80(N) was measured for each bin and mean (mn) of the estimated mean Δ EC (μ) distribution is shown in column 2. The standard deviation (sd) of the μ parameter distribution for each bin is shown in column 3.

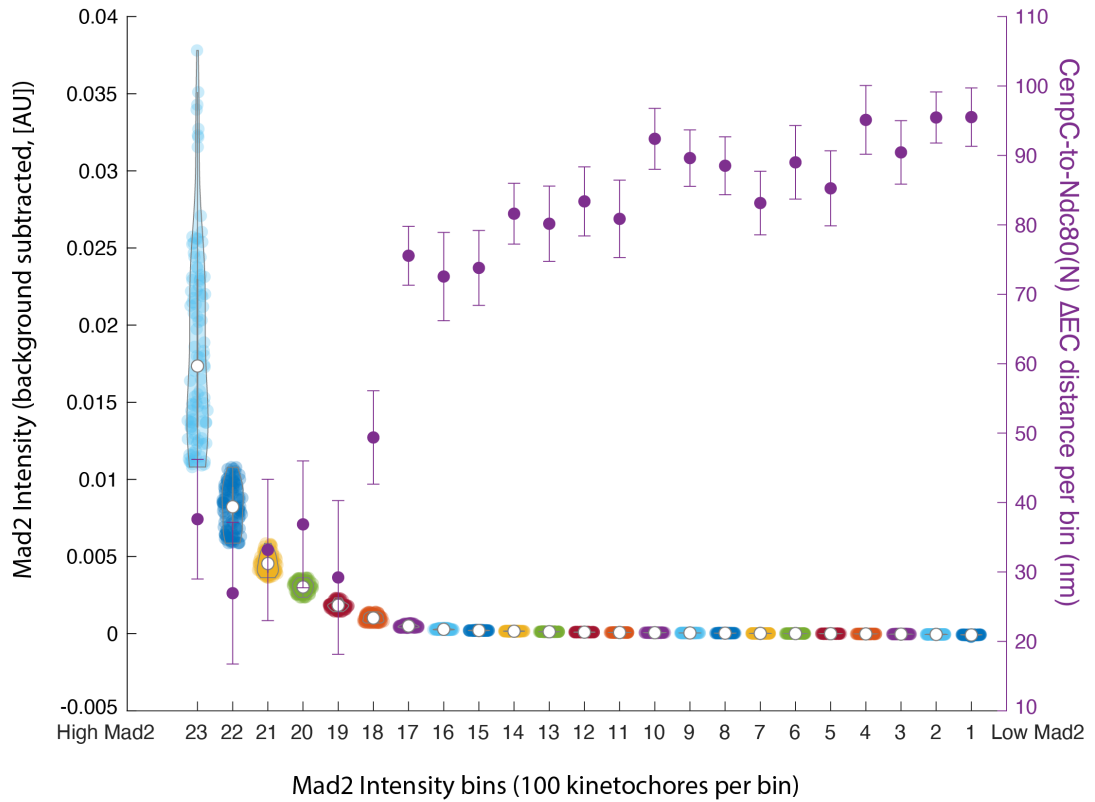


Figure 4.8: Ndc80 jack-knife to straight conformation transition relative to Mad2 unloading. Kinetochores were binned based on Mad2 kinetochore intensity in 23 bins of 100 kinetochores, where bin 23 has highest Mad2 intensity and bin 1 has lowest Mad2 intensity. The Mad2 intensity distribution in each bin is displayed as violin plot on the primary (black) y axis. The Δ EC distance between CenpC and Ndc80(N) was measured for each bin. The CenpC-to-Ndc80(N) Δ EC measurement per bin is displayed as scatter plot on the secondary (purple) y axis, where each bin measurement is denoted as purple dot. The standard deviation of each CenpC-to-Ndc80(N) Δ EC bin measurement is displayed as bar.

distance remains below 50 nm until 94% of the Mad2 is unloaded. This corresponds to the six bins with highest Mad2 intensity, i.e. 600 kinetochores. Once 94% of the Mad2 is unloaded from kinetochores, the CenpC to Ndc80N distance switches to 75 nm. This result clearly shows that Mad2 unloading precedes the Ndc80 transition from jack-knife to straight conformation. Moreover, this transition is not a gradual process suggesting that the majority of Ndc80 complexes change conformation in a coordinated fashion once the Mad2 falls beyond a (low) threshold.

Interestingly, we also observed that the CenpC-to-Ndc80(N) distance continued to increase from 75 nm to 95 nm as further Mad2 is unloaded from kinetochores (see Figure 4.10). Linear regression statistical analysis showed significance of the correlation (p) of 0.0001 and coefficient of determination (R^2) value of 0.66. These statistical analysis show significant correlation between the linear regressions of Mad2 unloading and ΔEC increase in bin 17 to 1. Further, the coefficient of determination suggests that 66% of the ΔEC trend in bins 1 to 17 can be explained by decrease in Mad2. Therefore, another factor may also be influencing the Ndc80 conformational changes at kinetochores with Mad2 below the threshold. Alternatively, the small sample size (17 bins) used for the analysis may be leading to noisier relation of the two trends and resulting in underestimation of the significance and the coefficient of determination.

The linear relationship between Venus-Mad2 and delta suggests a second process that eliminates the final Mad2 molecules from the kinetochore. Why this would result in further changes in Delta and what other factors contribute to that process are intriguing questions (see discussion for details).

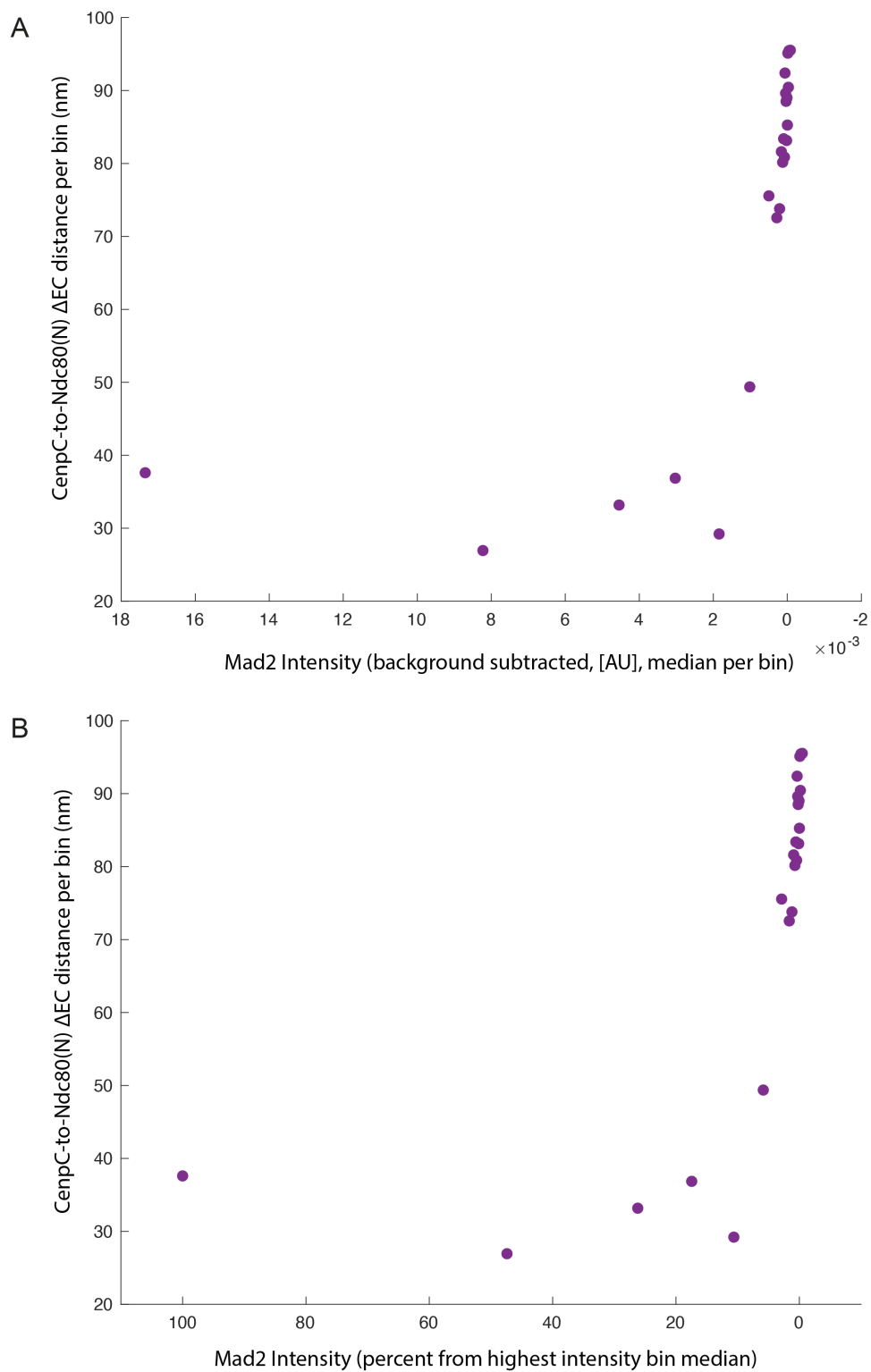


Figure 4.9: Ndc80 jack-knife to straight conformation transition relative to Mad2 unloading. A) Kinetochores are binned as in Figure 8, and the median Mad2 intensity and CenpC-to-Ndc80(N) Δ EC is calculated for each bin. The Mad2 bin median intensity is plotted relative to the CenpC-to-Ndc80(N) Δ EC bin measurement. B) The Mad2 median intensity measurement per bin is normalised to the bin with highest Mad2 intensity (bin 23, 100% Mad2 intensity). The % Mad2 intensity per bin is plotted relative to the CenpC-to-Ndc80(N) Δ EC bin measurement.

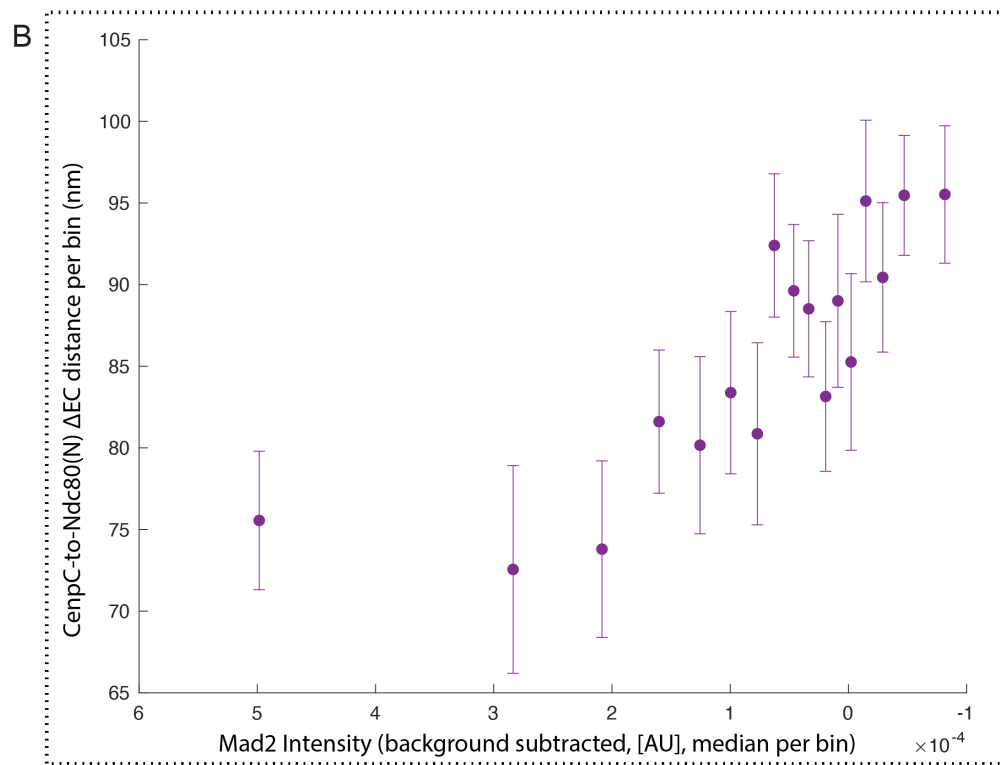
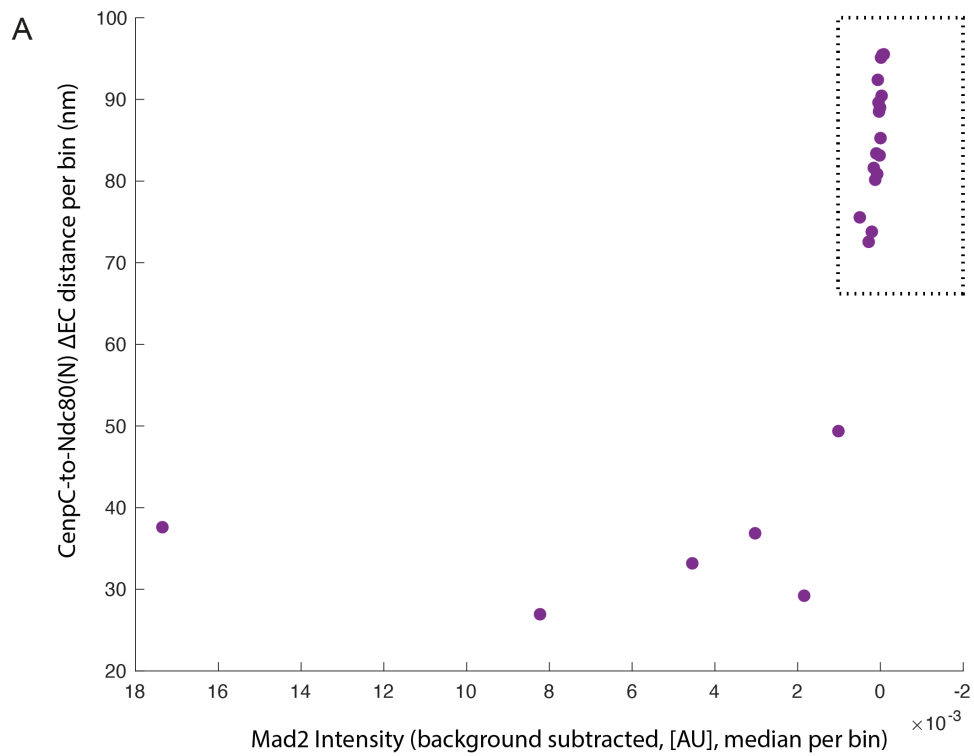


Figure 4.10: Relationship between Ndc80 conformation and Mad2 unloading.

A) The Mad2 bin median intensity is plotted relative to the CenpC-to-Ndc80(N) Δ EC bin measurement as in Fig. 4.9. The region of kinetochores that show linear regression CenpC-to-Ndc80(N) Δ EC increase is shown in box with dashed outline. B) Sub-plot of the kinetochores in the linear regression region annotated in A. Standard deviations of the Δ EC measurements are shown as horizontal bars.

4.2.6 Development of kinetochore state un-mixing algorithm

Previously we observed that a small sub-population (7%) of kinetochores that are positive for Mad2 and have Ndc80 in jack-knifed state is completely missed in the population average (see Figure 4.5, Roscioli et al). Therefore, small sub-populations of kinetochores with different conformation become hidden within the population average. This raises the question as to how different conformational states can be detected in a mixed population. One idea is to use the fully unattached state observed in nocodazole to as reference for the population of Ndc80 in jack-knifed state. Then we can potentially un-mix the sub-population of Ndc80 in jack-knifed state based on its fit to the reference. Ultimately, that will result in un-mixing of the Ndc80 jack-knifed sub-population from the overall kinetochore population. Here, Peter Embacher from the Burroughs lab built upon that idea and developed an algorithm that can un-mix Ndc80 in jack-knifed state from a mixed population (personal communication, manuscript in preparation). We first tested the algorithm on artificial data. Here, a known percentage of kinetochores with Ndc80 in jack-knifed state (nocodazole) was infused into the population of kinetochores with Ndc80 in straight conformation (DMSO, metaphase). The algorithm performed well in this setting and predicted the percentage with 2 to 8% error.

Ideally, next we would have liked to test that algorithm using the Mad2 staining as a proxy for Ndc80-jack-knifing. However, that triangle un-mixing algorithm requires data on the positions of three fluorophores. Therefore, we could not use the triangle un-mixing in cells expressing endogenous Venus-Mad2. Therefore, we sought to prepare two comparable data sets with respect to percentage of kinetochores with Ndc80 in jack-knifed state: (1) one where we can detect the percentage of kinetochores positive for Mad2 and with Ndc80 in jack-knifed conformation, and (2) one where we have three kinetochore markers, such as CenpC, Ndc80(C), and Ndc80(N), and we can un-mix the sub-population of kinetochores with Ndc80 in jack-knifed state. In the previous section, we performed an experiment where we imaged cells in prometaphase and metaphase, and showed that after quantitative analysis 600 out of 2300 kinetochores were Mad2 positive and had Ndc80 in jack-knifed state, i.e. 26% of the kinetochores. To generate a corresponding data set for Ndc80 jack-knife un-mixing, we again imaged randomly prometaphase and metaphase cells as before. However, here to accommodate the triangle in-mixing

algorithm requirements, we used hTERT Rpe1 cells expressing endogenous Ndc80-eGFP and stained for CenpC and Ndc80(N). We next wanted to make sure that the percentage of unattached kinetochores is roughly similar in the two data sets. To do so we visually assigned the cells as prometaphase or metaphase in each of the two data sets based on kinetochore alignment. Next, we counted the number of prometaphase and metaphase cells in each data set and calculated the percentage of prometaphase cells. The Venus-Mad2/CenpC/Ndc80(N) data set contained 51% prometaphase cells. The Ndc80-eGFP/CenpC/Ndc80(N) data set contained 38% prometaphase cells. Therefore, we concluded that the two data sets have not very different amounts of unattached and semi-attached kinetochores. The reader should note that data sets with even more corresponding percentages are currently under analysis. For the purpose of this study, we can predict the percentage of kinetochores with Ndc80 in jack-knifed state in the Ndc80-eGFP/CenpC/Ndc80(N) data to be approximately similar to the percentage of kinetochores with Ndc80 in jack-knifed state in the Venus-Mad2/CenpC/Ndc80(N) data set, i.e. $\sim 26\%$. Therefore, we next un-mixed the percentage of kinetochores with Ndc80 in jack-knifed state in the Ndc80-eGFP/CenpC/Ndc80(N) data to see if it fits the prediction. Here the algorithm found $13\% \pm 4$ (mean of the percentage of kinetochores estimate \pm standard deviation of the estimated percentage (absolute)) of the kinetochores in that data set to have Ndc80 in jack-knifed state. Therefore, the algorithm uncovered at least half of the sub-population of Ndc80 in jack-knifed state.

Finally, we sought to test the algorithm performance on a negative control, i.e. population with very little to zero Mad2 positive kinetochores. To do so we used metaphase cells, where the majority of kinetochores have mature attachments. To evaluate what percentage of kinetochores are "positive" for Mad2 we used hTERT Rpe1 cells expressing endogenous label Venus-Mad2 and stained them for CenpC and Ndc80(N). Due to the low number of Mad2 positives in this setting we could not use quantitative analysis. Therefore, we performed qualitative analysis, where we visually assigned the kinetochores as Mad2 "positive" or "negative". The qualitative analysis suggested about 3% of the metaphase kinetochores to be Mad2 "positive" and thus have Ndc80 in jack-knifed state. Next, we sought to investigate what percentage of kinetochores will the triangle un-mixing algorithm predict to be jack-knifed. To do so we used hTERT Rpe1 cells expressing endogenous label

Ndc80-eGFP, stained for CenpC and Ndc80(N). The metaphase cells were imaged and input in the algorithm for un-mixing. The algorithm predicted $4\% \pm 3$ (mean of the percentage of kinetochores estimate \pm standard deviation of the estimated percentage (absolute)) of the metaphase kinetochores to have Ndc80 in jack-knifed state. Therefore, even at such small sub-population of kinetochores with Ndc80 in jack-knifed state, the algorithm uncovered very similar percentage of Ndc80 jack-knifed kinetochores. The analysis of further data sets is under way.

In summary, we tested the algorithm for kinetochore state un-mixing developed by Peter Embacher and showed that its output accorded with expectations from Mad2 labelling. Therefore, the algorithm will be a very useful tool for future unravelling of the kinetochore architecture (see Discussion for possible applications).

4.3 Conclusions

Here, we utilised our method for ΔEC measurements to generate the first 3D *in vivo* map of human kinetochore architecture. We further showed that the kinetochore has distinct sensors for microtubule attachment and tension: the Ndc80 complex jack-knifes at kinetochores that lack microtubule attachment and the Knl1 protein unravels at loss of K-K tension. Further, we investigated how the Ndc80 jack-knife to straight conformation transition relates to the crucial mechanism of SAC silencing. We then employed quantitative measures of Mad2 intensity at single kinetochores and used these as a proxy for SAC activity. The results showed that the majority of Ndc80 molecules transition from jack-knife to straight conformation in a switch-like manner only when 94% of Mad2 is unloaded from kinetochores. Continued loss of residual Mad2 was then observed to be correlated with a linear increase in the CenpC-to-Ndc80(N) distance. This data suggested that additional Ndc80 molecules transition from jack-knifed to straight conformation as more Mad2 molecules are eliminated from the kinetochores. Finally, we tested a new algorithm for "un-mixing" of kinetochore states. We confirmed that the algorithm can successfully identify a sub-population of unattached kinetochores from a mixture with attached kinetochores - using delta measurements alone. This provides an important step towards using such algorithms in future investigations into mechanisms that control *in vivo* kinetochore architecture.

Chapter 5

Defining the sub-kinetochore position and organisational state of the Ska complex in human cells.

5.1 Background

During prometaphase, bi-orientated kinetochores congress chromosomes to the spindle equator by microtubule depolymerisation-coupled pulling (DCP) (Auckland and McAinsh, 2015). Here, the leading P (poleward) kinetochore is associated with a depolymerising K-fibre and generates a pulling force, while the trailing AP (anti-poleward) kinetochore sister is associated with a polymerising K-fibre and follows the leading kinetochore motions (and potentially contributes a pushing force, Armond et al., 2015). Successful congression by DCP requires that the two sister kinetochores form end-on attachments to microtubule plus ends, and then "hold on" to the depolymerising microtubule plus-ends, thus harnessing the energy of microtubule depolymerisation (Auckland and McAinsh, 2015). As discussed in Chapter 1, both experiments *in vivo* and *in vitro* have established the Spindle and kinetochore associated (Ska) complex as an essential kinetochore-microtubule attachment factor (see Chapter 1 Introduction).

Key experiments by Auckland and colleagues showed that depletion (or knock out) of Ska resulted in congression defects (as originally reported in Hanisch et al., 2006; Daum et al., 2009; Gaitanos et al., 2009; Theis et al., 2009; Welburn et al., 2009;

Jeyaprakash et al., 2012; Schmidt et al., 2012; Abad et al., 2014). This phenotype was shown to be the result of the following series of events: (1) the kinetochore pair bi-oriented, (2) congression was initiated via DCP and moves chromosomes close to the metaphase plate, (3) the leading kinetochore failed to sustain its microtubule attachment and detached, i.e. the inter-sister distance was reduced and the pair "flipped" so it is now oriented parallel to the metaphase plate, and (4) the kinetochore pair re-attached and re-attempted congression (Auckland et al., 2017). Here, it needs to be noted that kinetochores acquire microtubule attachments as they congress and thus the kinetochore can experience higher microtubule pulling force as it moves towards the equator. The current model is that as kinetochores experience more force towards the equator, Ska is required to maintain the attachment stability (Auckland et al., 2017).

How are Ska complexes recruited to kinetochores? The complex is a homodimer of the Ska1, Ska2 and Ska3 proteins that form a W-shaped molecule, from which the Ska1 and Ska3 C-termini protrude (Figure 5.1 A). The Ska1 C-terminus is a winged helix motif that can bind straight and curved microtubule protofilaments with equal affinity via three patches of positively charged amino acids (Abad et al., 2014; Schmidt et al., 2012). These multiple modes of Ska1 microtubule binding allow Ska to bind the flared dynamic microtubule tip and the lattice of the microtubule. The Ska3 C-terminus is relatively long (amino acids 101 - 412) and predicted to be disordered/unstructured (Abad et al., 2016, Figure 5.1 B). This region is required for recruitment of the Ska complex to kinetochores via physical interactions with the essential end-on attachment factor NDC80 complex (Ndc80/Nuf2/Spc24/Spc25) (Figure 5.1 C, Jeyaprakash et al., 2012; Helgeson et al., 2018; Huis In't Veld et al., 2019; Zhang et al., 2017; Zhang et al., 2020). The binding of Ska3 to Ndc80 is dependent on Ska3 C-terminus phosphorylation by Cdk1 (Zhang et al., 2019). Upon phosphorylation the Ska3 C-terminus is suggested to transition from globular structure in the non-phosphorylated protein to elongated unstructured shape in the phosphorylated protein (Huis In't Veld et al., 2019). The unstructured phosphorylated form of the Ska3 C-terminus is suggested to be the one responsible for Ndc80 binding and to provide flexible positioning of the core W-shaped Ska complex. The exact location of the binding site is unclear with studies implicating, (1) the Ndc80 coiled coil, (2) the Ndc80 N-terminal tail and (3) the Ndc80 loop region in kine-

tochore Ska loading. *In vitro* binding assays showed that phosphorylated Ska can bind truncated Ndc80 complex that lacks 34% of the middle coiled-coil region and the loop region (Ndc80 jubaea; Ndc80 aa 1-506, Nuf2 aa 1-351, Spc25 aa 54 - 224, Spc24 aa 59 - 197) (Huis In't Veld et al., 2019). Non-phosphorylated Ska was also shown to interact with Ndc80 that lacks 83% of the coiled-coil region and the loop (Ndc80 "Bonsai", Janczyk et al., 2017; Ciferri et al., 2016). Another set of experiments suggested that the Ndc80 loop is required for kinetochore recruitment of Ska *in vivo*. However, loss of the loop also leads to a failure in kinetochore microtubule attachment formation. Since Ska does not bind unattached kinetochores (Auckland et al., 2017) the role of the loop may be an indirect effect. The picture is further complicated because the Ndc80 unstructured N-terminal tail is also implicated in Ska recruitment (Janczyk et al., 2017) although more recent studies also call this into question (Wimbish et al., 2020). An open question is whether the Ska complex is actually located close to Ndc80 *in vivo*, and if so, which parts of Ndc80 and Ska are in close proximity.

The loading of Ska to kinetochores is also highly dynamic. Experiments in human HeLa cells and *C. elegans* show that Ska is absent from unattached kinetochores and then accumulates as kinetochores bi-orientate and congress (Auckland et al., 2017; Cheeseman and Desai, 2008). This progressive recruitment correlates with increased recruitment of microtubules to the kinetochore. This, together with the phenotypes associated with Ska depletion (see above) led to the model that kinetochores recruit microtubules and load Ska as they congress and that this provides an increase in the load bearing capacity of the kinetochore (Auckland et al., 2017). An imbalance between Ska loading and microtubule binding during this maturation leads to kinetochore-microtubule detachment and thus acts as a "mechanical self-check". A key prediction of this model is that low or poor Ska recruitment should be associated with subsequent attachment failure. Unfortunately, live cell studies of Ska dynamics during congression using overexpressed transgenes have been limited due to poor signal to noise ratio. The maximum temporal resolution achieved with that method was two time frames with arbitrary time resolution on the scale of minutes: one image stack was taken when a kinetochore pair was unaligned and one image stack was taken when the kinetochore pair aligned (Auckland et al., 2017). As described above many factors influence the loading of Ska to kinetochores, and

the process is phosphoregulated by Cdk1. Therefore, a crucial next step will be to generate tools that enable live-cell imaging of Ska dynamics in living cells.

In this chapter, I define the position of Ska relative to the KMN network at kinetochores in human hTERT Rpe1 intact cells. Further, I generate two endogenous Ska1 labelled HeLa K cell lines and utilise them to probe in detail the position of Ska relative to Ndc80. Finally, I show that high spatio-temporal resolution live-cell imaging of Ska in congression can be achieved via Lattice light sheet imaging of one of these cell lines.

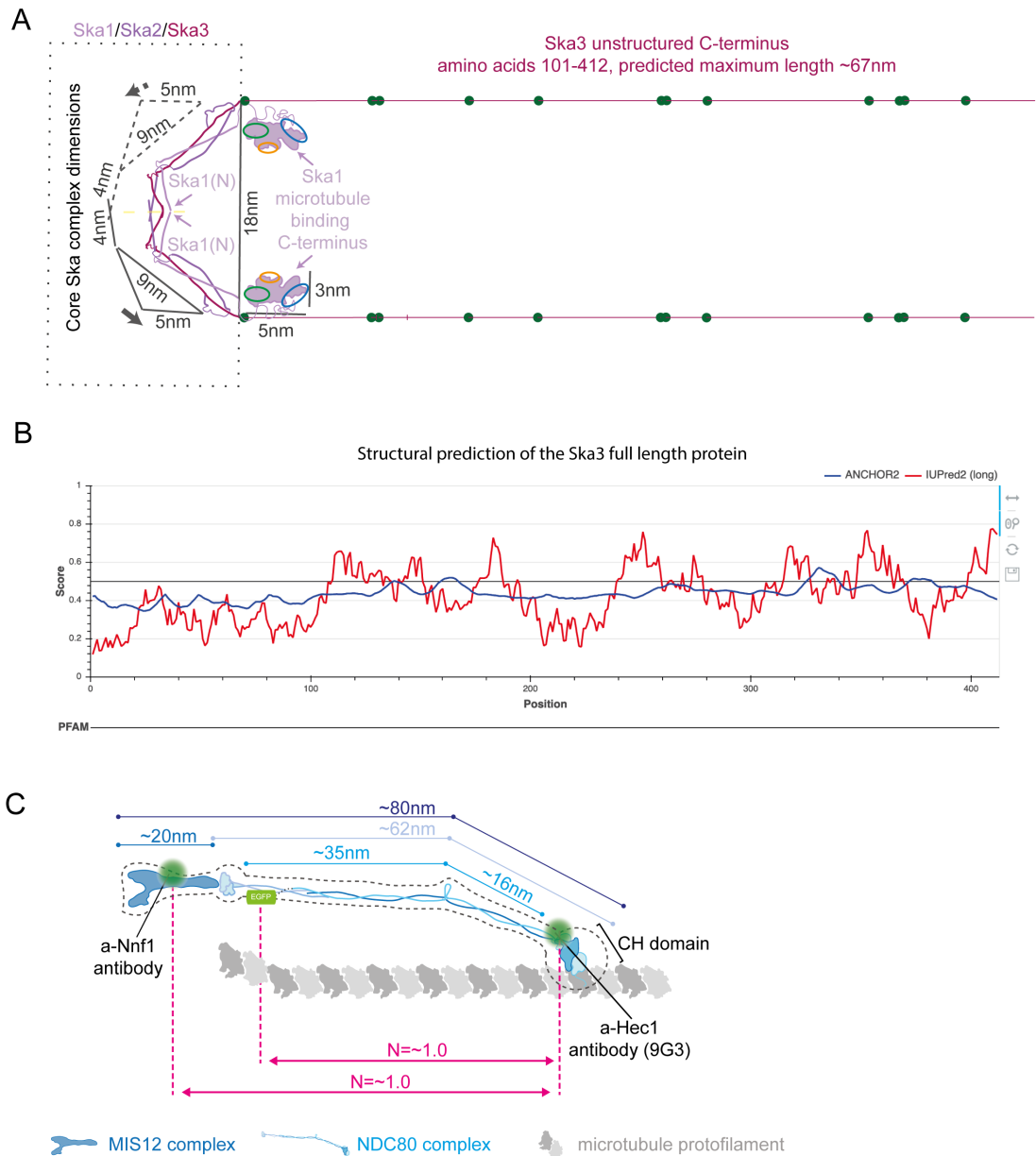


Figure 5.1: Structure of the Ska, Mis12 and Ndc80 complexes. A) Schematic of the available structural information on the Ska complex (Abad et al., 2014; Abad et al., 2016). Phosphorylation sites in the Ska3(C) are labelled with green dots (Huis In't Veld et al., 2019). Ska3 unstructured C-terminus length is estimated based on 0.214 nm distance between the residues of two amino acid. B) Structural prediction of the Ska3 full-length protein in IUPRED2A. Regions with score above the threshold (black) are predicted to be disordered. Position denotes the amino acid number. C) Schematic of the available structural information on Mis12 and Ndc80 complexes organisation. The nematic order is indicated in pink. Positions of protein labelling are denoted by green shapes: estimated antibody epitopes (circles), and eGFP label (barrel).

5.2 Results

5.2.1 Positioning of Ska complex within the architectural map of a human (Rpe1) kinetochore

To understand the *in vivo* organisation of Ska at human kinetochores we first sought to map the position of the Ska complex relative to the mapped positions of the NDC80 complex and CenpC in human nearly diploid Rpe1 cells (Roscioli et al., 2020). To do so we used a cell line with endogenous eGFP tag at the Ndc80 C-terminus (Ndc80(C)) (MC191 cell line), anti-CenpC antibody (amino acids 1-426) and anti-Ska3 antibody (amino acids 154 – 166, Ska3(M), predicted ≤ 11.34 nm from core Ska3: amino acids 1-101, Figure 5.2 A). We further used the methodology outlined in Chapter 3 that was previously used for generation of the Rpe1 kinetochore architecture map. Here, we first measured the CenpC to Ndc80(C) distance to be 39.2 ± 2.1 nm (mean \pm sd, $n=321$ kinetochores, cell number [cell n.] = 17, Figure 5.2 B). The measured distance is consistent with previous independent three-fluorophore experiment (Ndc80(C)-CenpC-Ndc80(N)) that measured the same distance to be 43.5 ± 2.3 (MC191, $n=247$ kinetochores, cell. n = 17, eff. cell n. = 13; Roscioli et al., 2020). Next, we measured the ΔEC distance between Ska3(M) and Ndc80(C) and found it to be 35.9 ± 12.4 nm ($n= 266$ kinetochores, cell n. = 17, eff. cell n. = 12.1, Figure 5.2 B). We further measured the Ska3(M)-to-CenpC ΔEC distance and found it to be 84.9 ± 3 nm ($n=265$ kinetochores, cell. n. = 16, Figure 5.2 B). Previously, we found the the Ndc80(C)-to-Ndc80(N) distance to be 48.4 ± 3.1 nm, and the CenpC-to-Ndc80(N) distance to be 81.9 ± 3.9 nm in hTERT Rpe1 cells. Therefore, the data altogether suggested that Ska3(M) is located close to the Ndc80(N). To determine whether the Ska complex and Ndc80(N) average positions co-localise (or are off-set from each other), we sought to directly measure the distance between the Ska complex and Ndc80(N). However, we were hampered in these efforts because the Ska3(M) antibody and the anti-Ndc80(N) antibody are raised in the same species and thus the experiment could not be conducted in this manner. This lack of high quality compatible antibodies (note that poor signal-to-noise is incompatible with accurate estimation of Delta distances - see Chapter 3), can be circumvented via endogenously labelled Ska complex cell line. Such cell line would also be essential for understanding of the dynamics of Ska kinetochore

loading in congression. Therefore, to probe the *in vivo* position and dynamics of Ska in detail, we sought to generate an endogenous label Ska cell line. Here, we first attempted to generate hTERT Rpe1 cell line with endogenous eGFP label at the Ska1 N-terminus. We chose that locus as there are available CRISPR/Cas9 Guides that efficiently cut at the beginning of *SKA1* exon 1 (Auckland et al., 2017, and unpublished data). However, multiple strategies and attempts were not successful.

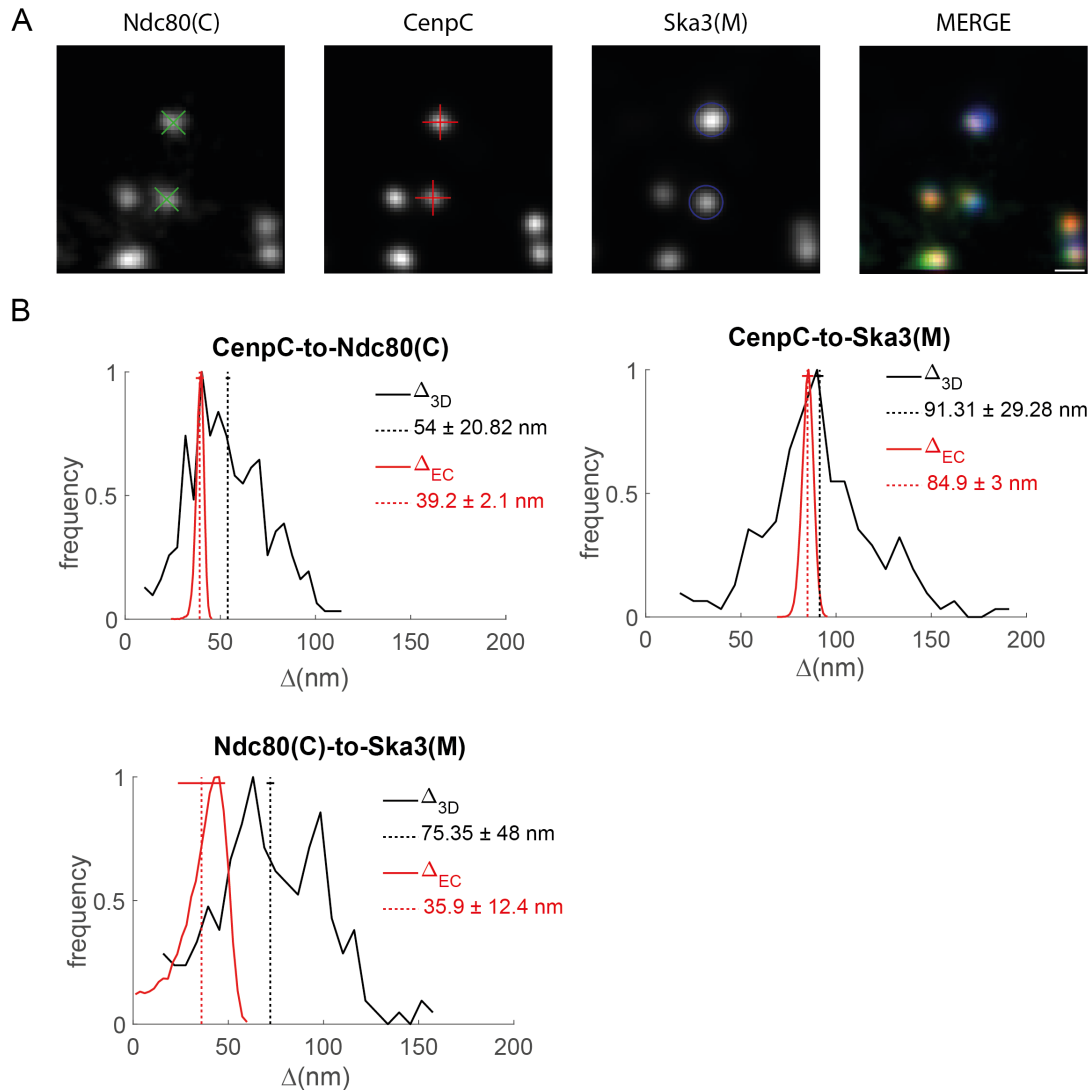


Figure 5.2: Position of Ska3(M) in hTERT Rpe1 cells. A) Representative images of kinetochores in hTERT Rpe1 cells expressing endogenous label Ndc80-eGFP and stained for CenpC and Ska3(M). Cells were treated for 2 hrs with 1:1000 DMSO prior to fixation. The centroid detection in KiD is marked by cross or circle over the kinetochore spot. B) Histogram of the measured Δ_{3D} (black) and Δ_{EC} (red) distances between: CenpC and Ndc80(C), CenpC and Ska3(M), and Ndc80(C) and Ska3(M). The median \pm sd of each measurement is denoted on the right. Δ measurements were performed as described in Chapter 3.

5.2.2 Generation of endogenously tagged Ska1 HeLa K cell lines by CRISPR/Cas9 genome editing

Given the experimental issues with investigating the Ska complex in hTERT Rpe1 cells we turned our attention to using human epithelial cancer HeLa cells. HeLa cells are more susceptible to manipulations and have been previously used to study Ska function *in vivo*, including work from our own lab (Auckland et al, 2017). One disadvantage of using HeLa cells is the relatively high frequency of chromosome miss-segregation as compared to hTERT Rpe1 cells. This can result in abnormal (and unstable) karyotypes and complicate gene targeting efforts if there are multiple alleles of a given gene. Therefore, we first sought to check if our HeLa Kyoto (k) cell clone has two copies of chromosome 18 which carries the SKA1 gene. *In situ* FISH hybridisation of the HeLa K cells with a probe for the Chromosome 18 centromere showed that 89.8% of the cells carry two copies of chromosome 18 (n=489 cells, Figure 5.3). We thus proceeded with generation of the endogenous label Ska HeLa K cell line.

To generate fluorescent-labelled Ska1 cell lines we used a small guide (sg) RNA (Ska1 Guide A) that targets SpCas9 to a PAM sequence at the beginning of *SKA1* exon 1 (Auckland et al, 2017). The guide sequence was cloned into an eGFP carrying SpCas9 vector to facilitate sorting of eGFP positive vector transfected cells. I then generated a double stranded linear homology DNA repair template to induce homology repair and insert eGFP at the amino-terminal end of the Ska1 protein (see methods for details). The homology repair template includes an 800 bp homologous region 5' from the start codon of *SKA1* exon1, followed by the eGFP gene sequence, a linker, and finally an 800 bp homologous region 3' of the start codon of *SKA1* exon1. HeLa K cells were co-transfected with the guide plasmid and the linearised homology template (see Methods for details). Transfected cells were enriched via 488 nm Fluorescence activated cell sorting (FACS) that would detect the eGFP in the SpCas9 vector and possibly any cells expressing eGFP-Ska1. In a following step, the population of cells that express eGFP-Ska1 was enriched by repeating the 488 nm FACS and sorting for single cells. Screening of the cells under spinning disk confocal microscope revealed a 488 nm signal resembling kinetochore signal in two clones out of ~30 (Figure 5.4 A). In this study we used only one of the clones, cell

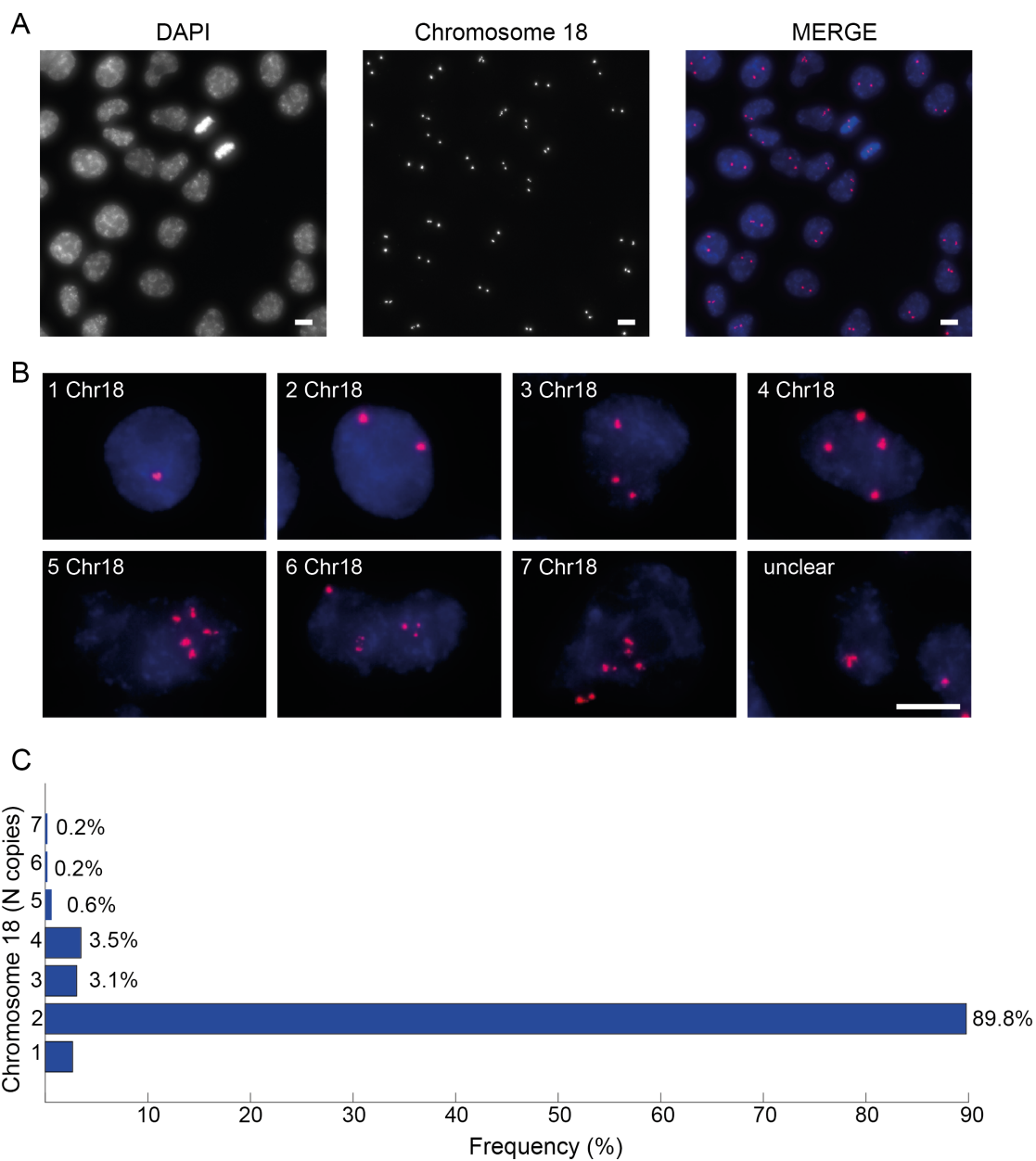


Figure 5.3: Chromosome 18 copy number in HeLa K cells. A) Example image of Fluorescent in-situ hybridisation (FISH) with fluorescent centromeric probe for Chromosome 18, and DAPI staining. Maximum Z-projection. Scale bar 10 microns. B) Examples of chromosome 18 counts. Maximum Z-projection. Scale bar 10 microns. C) Quantification of the number of Chromosome 18 copies (489 cells).

line MC177 and, therefore, only the characterisation of this clone will be described.

To validate that the signal is truly due to eGFP labelled endogenous Ska1, we amplified the 5' genomic region of *SKA1* by PCR. The resulting PCR products formed two bands on Agarose DNA gel: (1) one of the expected size of eGFP-Ska1, and (2) one of the size of the expected size of unlabelled Ska1 (See Supplemental Figure 1 in Appendix A). We then sub-cloned the higher and lower molecular weight products into plasmids and sequenced them. Sequencing of the higher molecular weight product showed *eGFP-SKA1* allele that does not contain mutations (Figure 5.4). Sequencing of plasmids with sub-cloned lower molecular weight PCR product identified a mixture of unlabelled Ska1 sequences in the population. Specifically, we identified three alleles: (1) 62% of the sequenced plasmids showed untagged *SKA1* allele with deletion of amino acids four and five, (2) 23% of the sequenced plasmids showed untagged *SKA1* allele that does not harbour mutations, and (3) 15% of the sequenced plasmids showed untagged *SKA1* allele with deletion of amino acids four and five, and mutation in the 5' UTR (Figure 5.4). This raised the question of whether the clone is impure or whether the cells contain more than two Ska1 alleles.

To understand that we manually subcloned the Ska1 population. All eleven of the subclones showed the same genotype of one eGFP-labelled non-mutated *SKA1* allele and one *SKA1* allele with deletion of amino acids four and five (Figure 5.4). Crucially, we observed that MC177 cells reproduced the mitotic timing of plain HeLa-K cells and thus the mutations appear to have no effect on Ska complex function (Figure 5.4). Finally, we tested the quality of the eGFP-Ska1 signal in immunofluorescence (data not shown). Unfortunately, the signal was not bright enough for reliable kinetochore detection without enhancement with anti-eGFP antibody. This is not ideal for follow on experiments and our ultimate goal to use live cell imaging. Moreover, the best tested anti-eGFP antibody is also raised in mouse and thus not compatible with making the Ska1(N) to Ndc80(N) (9G3; mouse) measurement. Although this MC177 cell line did prove useful for a subset of experiments that did not require Ndc80(N) terminus labelling (more details in section Mapping of the Ska complex position in HeLa cells, Figure 5.11). We therefore sought to generate a brighter endogenous labelled Ska1(N) cell line.

To improve the endogenous Ska1 fluorophore signal we sought to generate a tandem fluorophore Ska1(N) label and use the mNeonGreen fluorophore which benefits from

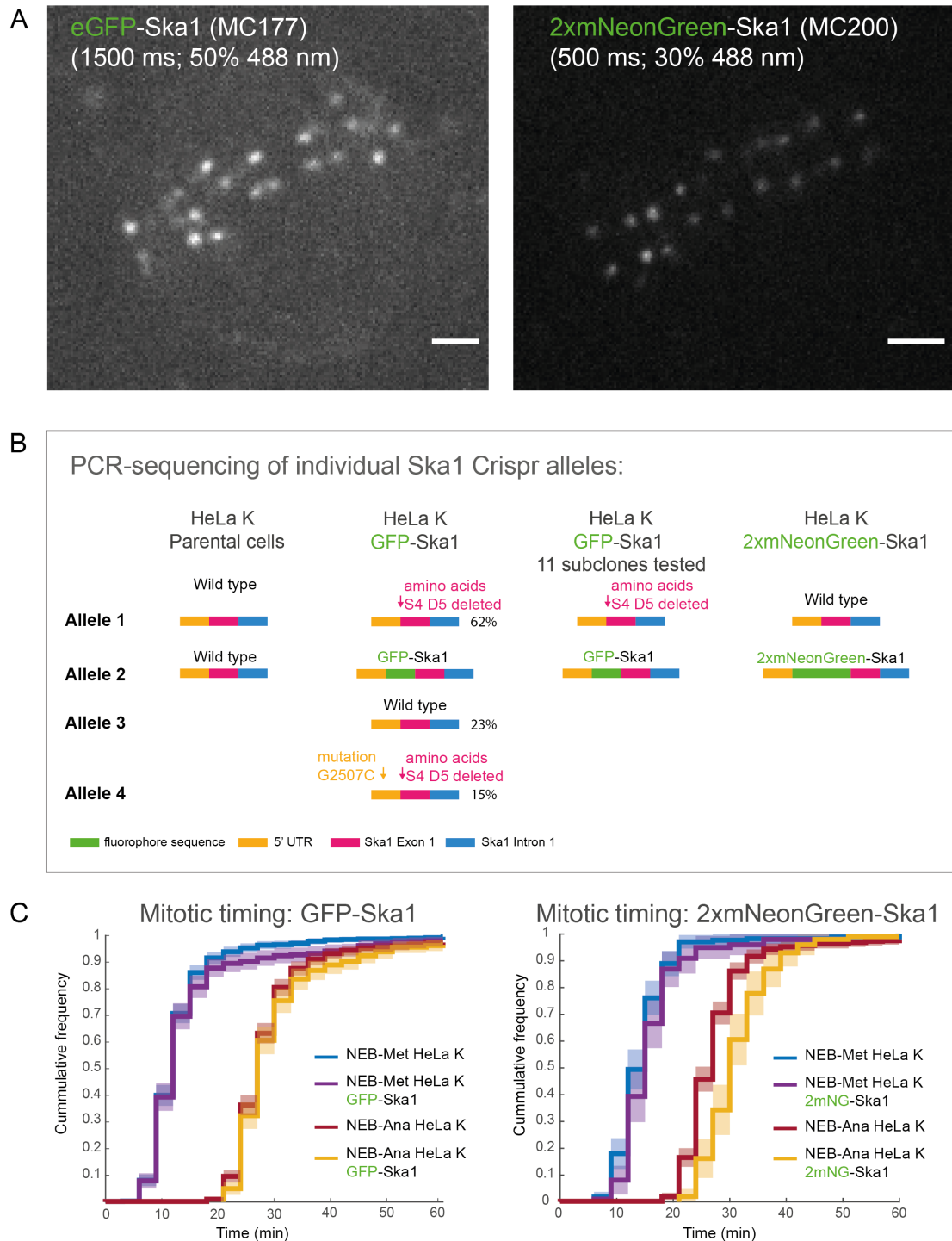


Figure 5.4: Characterisation of Ska1(N) endogenous fluorescent label cell lines. A) Representative images of eGFP-Ska1 (MC177) and the 2xmNeonGreen-Ska1 (MC200) cells. 488 nm laser power and exposure time are indicated. Scale bar 2 micron. B) Table showing the Ska1 alleles found in parental HeLa K , MC177 eGFP-Ska1 and MC200 2xmNeonGreen-Ska1 cells (see text for details). C) Cumulative frequency plots of the mitotic timings of the MC177 (n=343 cells) and MC200 (n=99 cells) cell lines as compared to parental HeLa K cells (left, n= 605 cells, right, n= 171 cells). The 95% confidence interval is shown as low opacity region, coloured as the respective measurement. Abbreviations: metaphase alignment (Meta), and anaphase onset (Ana).

improved brightness and photostability as compared to eGFP (Shaner et al., 2013). We replaced the linker and the eGFP with tandem mNeonGreen (see Chapter 2: Methods for more details) and repeated the workflow used for generation of MC177 eGFP-Ska1 (for details see Chapter 2 Methods). After FACS enrichment for cells with 488 nm signal, and confocal microscopy for kinetochores with 488 nm signal we identified one clone as a candidate for 2xmNeonGreen-Ska cell line (MC200, Figure 5.4 A.). Next we isolated genomic DNA, amplified the locus via PCR as above and ran the product in Agarose DNA gel. The gel showed two bands - the higher molecular weight band matched the expected size of 2xmNeonGreen-Ska1 and the low band matched the expected size of untagged Ska1 (See Supplemental Figure 1 in Appendix A). To ease the procedure we sequenced the DNA pool from each band. Sequencing of the higher molecular weight band revealed that there was one *SKA1* allele tagged with tandem mNeonGreen fluorophores. Sequencing of the low molecular band revealed one untagged (wild type) allele (Figure 5.4 B.). Both alleles were found to not harbour Ska1 mutations. Next, we tested the functionality of the Ska complex in MC200 by mitotic timing analysis and found that the cell line behaves as control cells (Figure 5.4 C.). Finally, we tested as to whether kinetochore Delta experiments can be performed with MC200 cells without signal enhancement. Here, we stained MC200 cells with anti-Nnf1 and anti-Ndc80(N) antibodies and ran the analysis in KiD. KiD successfully identified 2xmNeonGreen-Ska1 spots and the Delta was successfully measured (more details in section Mapping of the Ska complex position in HeLa cells, Figure 5.9). Having generated a Ska1(N) endogenous label cell line with sufficient signal quality, we next explored whether it recapitulates previous data on Ska1 kinetochore localisation in different conditions. We first confirmed that 2xmNeonGreen-Ska1 is loaded to a higher extent on attached kinetochores as compared to unattached, nocodazole-treated kinetochores (Figure 5.5 A, B and C). Further, we used transient transfection of Ndc80-tagRFP in 2xmNeonGreen-Ska1 cells and visually confirmed that Ska1 is loaded to higher extent on congressed kinetochores as compared to uncongressed ones (Figure 5.5 D).

In summary, here we generated two endogenous Ska1(N) knock-in cell lines with normal mitotic timing and no obvious phenotypes. The fluorescent Ska1(N) signal can be used for kinetochore localisation studies after eGFP-Ska1 signal enhancement with an antibody (MC177) or by the 2xmNeonGreen-Ska1 signal alone (MC200). In

addition, we showed that the endogenous label Ska1 protein recapitulates previous data on Ska1 kinetochore localisation in different conditions. Therefore, we next sought to (1) establish the map of CenpC-KMN network in HeLa cells, and (2) identify the position of the Ska complex in HeLa cells relative to the KMN network and CenpC.

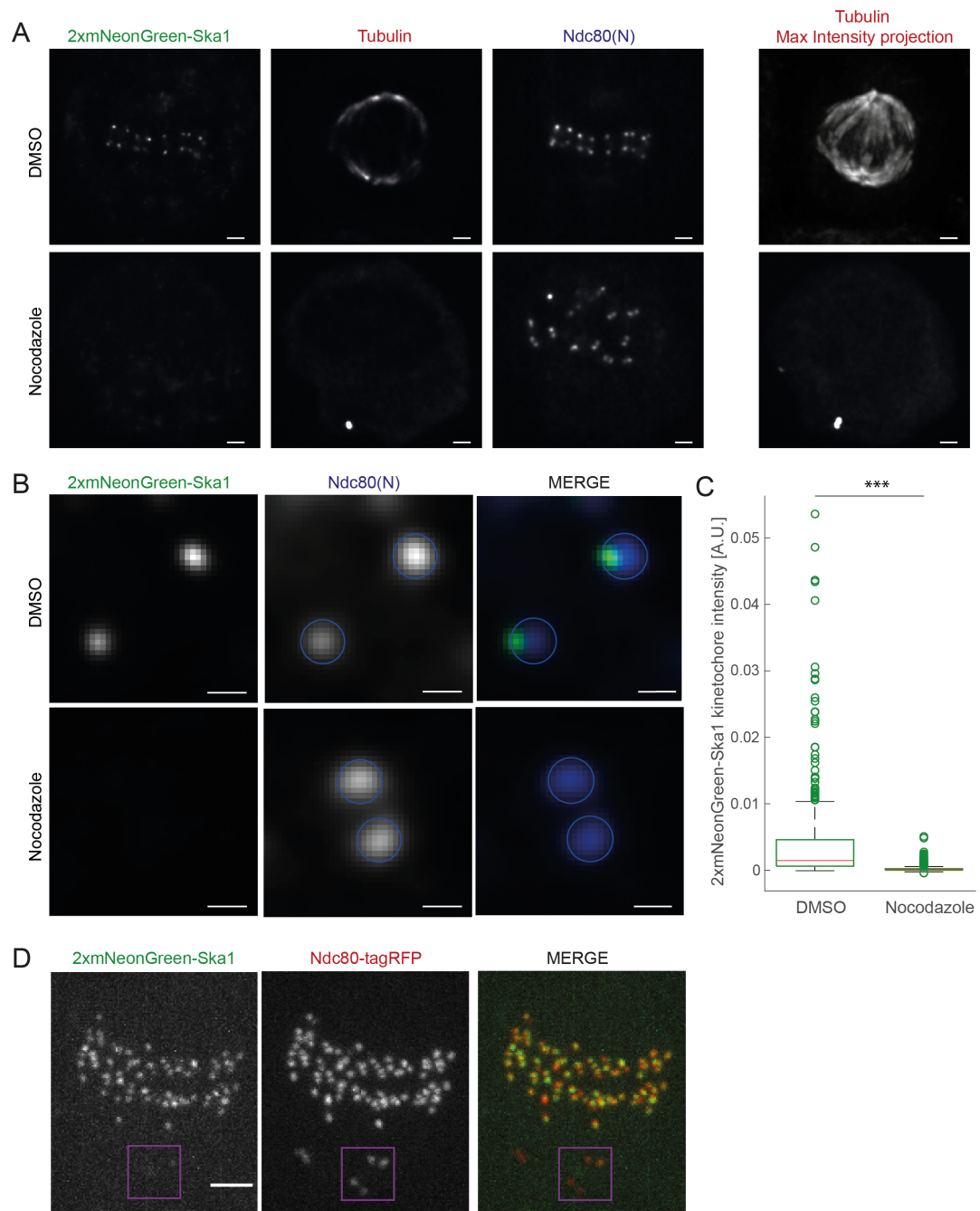


Figure 5.5: Kinetochore localisation of endogenous 2xmNeonGreen-Ska1 A) Left: Representative images of 2xmNeonGreen-Ska1 cells fixed and stained for Ndc80(N) and Tubulin. Cells were treated for 2 hours with 1:1000 DMSO or 3.3 μ M nocodazole. Right: Maximum intensity projection of the Tubulin signal in the 561 nm fluorescent channel. Scale bars 2 μ m. B) Representative images of kinetochore center detection in the Ndc80(N) channel. Intensity of 2xmNeonGreen-Ska1 was measured in 300 nm radius of the Ndc80(N) center (blue circle). Scale bars 500 nm. C) Quantification of the background-subtracted intensity measurements in (B), $p=1.0783e-90$. D) Representative images of 2xmNeonGreen-Ska1 cell transfected with Ndc80-tagRFP. Two uncongressed kinetochore pairs are highlighted by purple square. Scale bar 2 μ m.

5.2.3 Architecture of kinetochores in human HeLa cells

The endogenous fluorescent label Ska1 cell lines shown above are HeLa K cell lines. Since our previous map of the human kinetochore architecture is derived from Rpe1 cells it was important to first establish if the overall architecture is conserved in HeLa K cells. In the hTERT Rpe1 study we found that it is beneficial to obtain triangulation of the fluorophores and not rely on pair-wise distances alone, as triangulation can inform on axis offsets. Therefore, three-color experiments are beneficial especially to inform on possible flexibility in proteins. We therefore designed these experiments in HeLa K cells such that three fluorophores can be observed. Furthermore, recent developments in the McAinsh and Burroughs labs led to development of a correction algorithm that takes into account the positions of the three fluorophores simultaneously - triangle euclidean distance correction algorithm (TEDCA). The algorithm we used previously (BEDCA), corrects the inflation in pair-wise manner between the markers. In contrast, TEDCA utilizes the information on all three markers at the same time and results in higher confidence for distances at $\sim 30\text{nm}$ (Embacher et al., manuscript in preparation). We therefore used TEDCA for this study.

Here, we sought to first understand the kinetochore architecture in HeLa K cells. In particular, we sought to test as to whether the high alignment of outer kinetochore components in the KMN network is preserved in HeLa cells. To do so we imaged the inner kinetochore component CenpC, the Mis12 complex component Nnf1, and Ndc80(N) in cells fixed without pre-extraction and analysed the data in KiD and TEDCA. After analysis of the CenpC/Nnf1/Ndc80(N) data set, the ΔEC distance between Nnf1 and Ndc80(N) was found to be $75.08 \pm 1.2 \text{ nm}$ ($n = 476$ kinetochores, cell $n. = 16$, see Figure 5.6, and Table 5.1). The corresponding distance in hTERT Rpe1 cells was found to be $61.5 \pm 0.8 \text{ nm}$ and $66.4 \pm 1.5 \text{ nm}$ in two data sets. Therefore, the Nnf1 to Ndc80(N) distance in HeLa K cells is slightly higher than the one observed in hTERT Rpe1 cells. As will be discussed next, the Nnf1 to Ndc80(N) distance was slightly lower in the endogenously labelled Ska cell lines as compared to the parental HeLa K cell line, and was similar to the one observed in Rpe1 cells. Therefore, the kinetochore architecture can differ slightly between clonal cell lines, probably due to the kinetochore being adaptable to some level. However, the main feature of high nematic order of the outer kinetochore is observed for all cell lines.

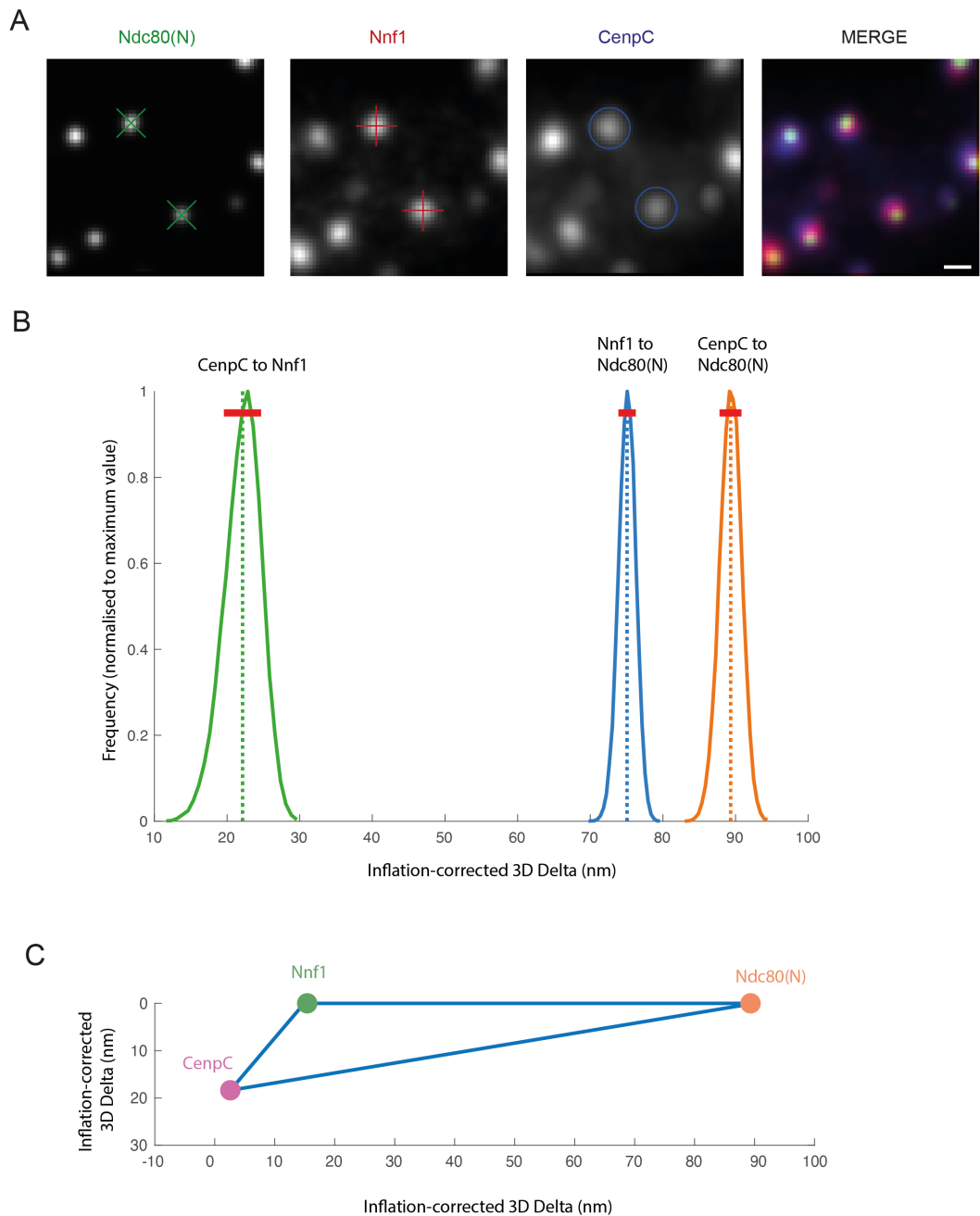


Figure 5.6: Δ EC positions of CenpC, Nnf1 and Ndc80(N) in HeLa K cells. A) Representative images of kinetochores in HeLa K cells stained for CenpC, Nnf1 and Ndc80(N) (“no pre-extraction” condition, see methods). Cells were treated for 2 hrs with 1:1000 DMSO prior to fixation. The centroid detection in KiD is marked by cross or circle over the kinetochore spot. B) Histograms of the measured Δ 3D distances. (see Table 5.1 for median \pm sd) Δ 3D measurements were performed as described in Chapter 3 and corrected in TEDCA. C) Plot showing the triangulation of the mean Δ EC distance measurements from B.

The Mis12 and Ndc80 complex together form assembly of ~ 80 nm length (Petrovic et al., 2010, Huis In't Veld, 2016). Therefore, the distance observed in plain HeLa K cells is even closer to the predicted structural length of the full Mis12-Ndc80 complex. That data suggests higher alignment of the Mis12-Ndc80 complexes along the outer kinetochore axis. Here, it needs to be noted that the 75nm distance between Nnf1 and 9G3 places the anti-Nnf1 antibody binding site at the Nnf1 N-terminal region, i.e. toward the inner kinetochore. The Nnf1 antibody is raised against the full protein and its exact antibody binding site is unknown. The structure of Nnf1 predicts that the majority of exposed Nnf1 protein is at the Nnf1 N-terminus. Work in our laboratory is undergoing to confirm, if possible, the region containing the Nnf1 binding site via biochemical assays. A colleague, Dr. Muriel Erent, has generated truncations of the Nnf1 protein and aims to test whether the Nnf1 antibody selectively binds to one of the generated Nnf1 regions. If we obtain the region of the Nnf1 binding site, we will update our nematic order calculations, albeit we do not expect the difference to affect our results as it will be at most 10 nm. For the purpose of calculating nematic order in this chapter, I will use the full Mis12-Ndc80 complex length under EM, 80 nm, as a structural distance. The nematic order is thus also recalculated for Rpe1 cells (Figure 5.7). Based on that calculations of nematic order, the nematic order of Nnf1 to Ndc80(N) is: 0.76 in non pre-extracted Rpe1 cells, and 0.94 in non pre-extracted HeLa cells. Therefore, in both cell lines the nematic order of Nnf1-Ndc80(N) is high even when the maximum Mis12-Ndc80(N) structural distance is used. All data on the Nnf1 to Ndc80(N) distance presented in this chapter is summarised in Figure 5.7. Here, I show that in all four cell lines used to measure this distance, and two fixation conditions (with and without pre-extraction), the nematic order remains high for the Mis12-Ndc80 complex molecules.

In the CenpC/Nnf1/Ndc80(N) experiment, we also analysed the position of CenpC. The ΔEC distance between Nnf1 and CenpC was found to be 22.13 ± 2.56 nm ($n = 476$ kinetochores, cell n. = 16, Figure 5.6). The ΔEC between CenpC and Ndc80(N) was found to be 89.31 ± 1.5 nm (MC009 plain HeLa K, $n = 476$ kinetochores, cell n. = 16, Figure 5.6). This measurement is similar to the corresponding measurement in hTERT Rpe1 cells of 85.8 ± 0.8 nm ($n = 1754$ kinetochores). Overall, the position of CenpC suggests triangle as compared to linear assembly: $22 + 75 \neq 89$ nm. In Rpe1 cells, the linear inequality is more pronounced: $34.9 + 61.5 \neq 85.8$. Therefore, the

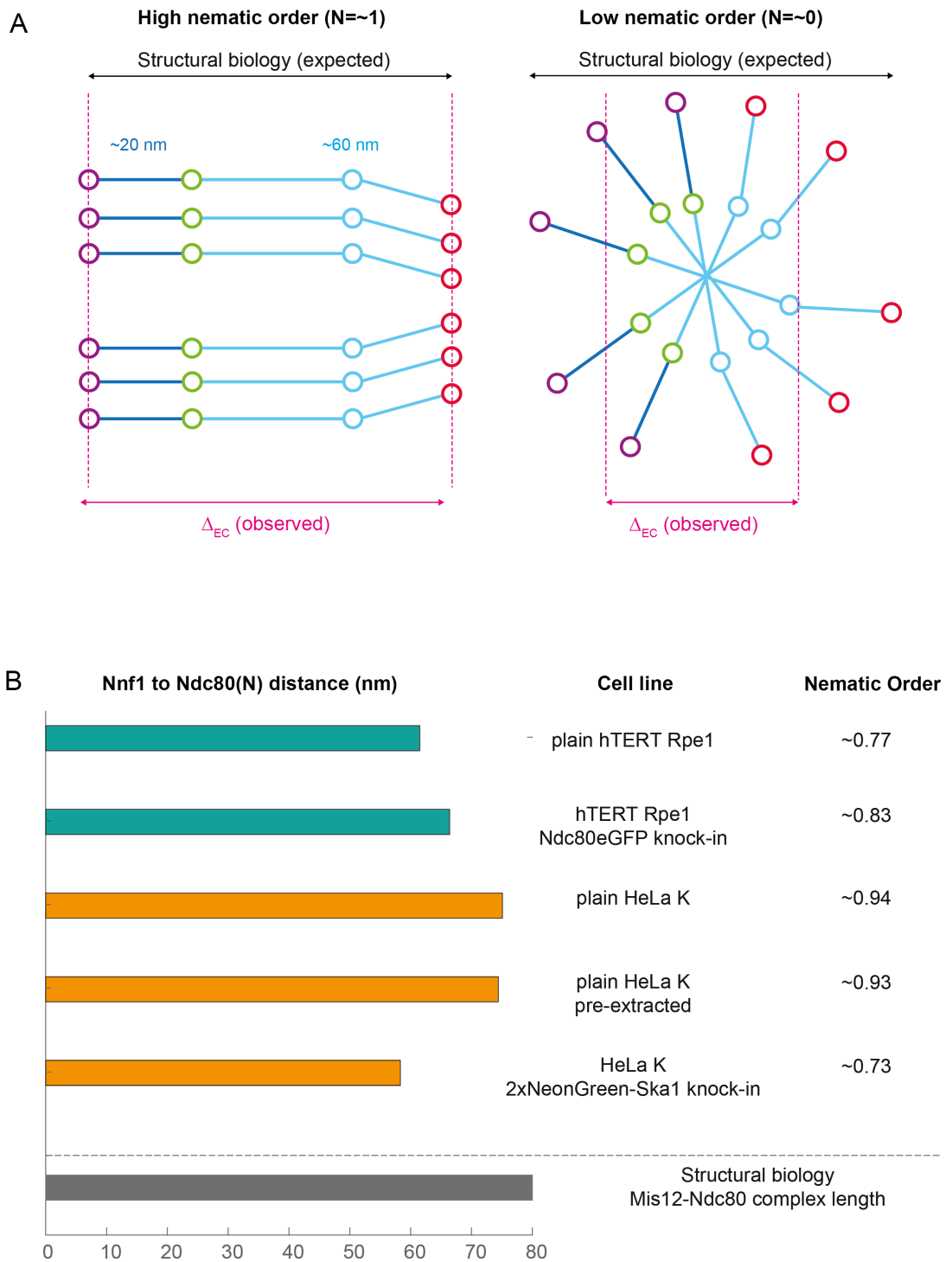
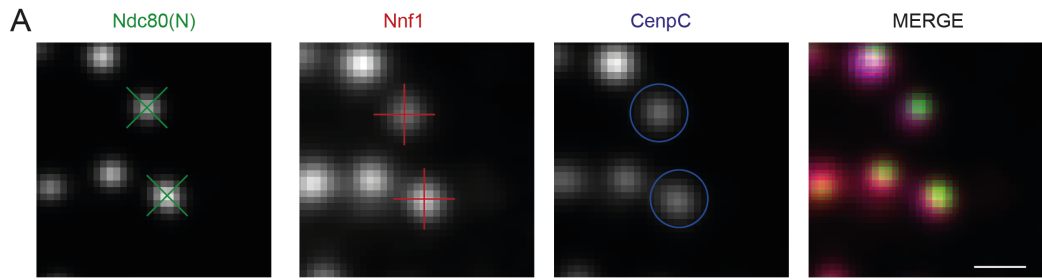
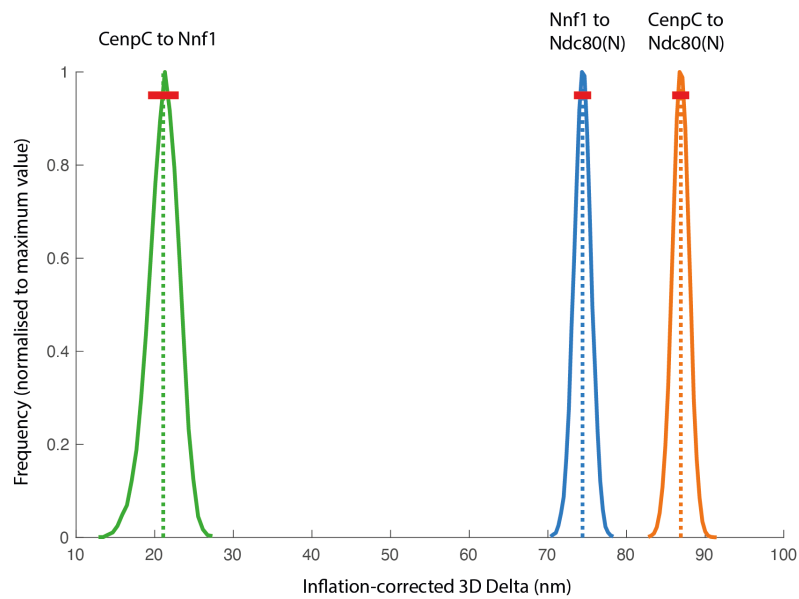


Figure 5.7: Nematic order of the outer kinetochore Mis12-Ndc80 complex molecules in hTERT Rpe1 and HeLa K cell lines A) Schematic of the nematic order concept. If all molecules are perfectly aligned, the Δ_{EC} measurement will match the expected structural distance, i.e. high nematic order $N = \sim 1$ (1 and 2). If the molecules are unaligned, the Δ_{EC} measurement will be shorter than the expected structural distance, i.e. low nematic order, $\sim N=0$. B) Bar plot of the calculated nematic orders in different cell lines and fixation conditions based on the Nfn1-Ndc80(N) Δ_{EC} measurement. The structural distance used as reference is the full length Mis12-Ndc80 complex (grey).

data suggests that CenpC is also off-axis in HeLa K cells, albeit to a lesser extent. The above HeLa K Delta experiments were performed without pre-extraction before fixation. However, in several of the following HeLa K Delta experiments a pre-extraction was required. In specific, for kinetochore detection in Ska3-labelled cells, and eGFP-Ska1 cells where the signal was enhanced with anti-eGFP antibody. Therefore, we wanted to test as to whether pre-extraction majorly affects HeLa K kinetochores. Here, we stained CenpC, Nnf1, and Ndc80(N) in pre-extracted HeLa K cells. The ΔEC distance between Nnf1 and Ndc80(N) was found to be 74.4 ± 1.1 nm ($n = 324$ kinetochores, cell n. = 14, Figure 5.8). This additionally confirms high nematic order of the outer kinetochore in HeLa cells: nematic order = 0.93 (Figure 5.7). The ΔEC distance between Nnf1 and CenpC was found to be 21.11 ± 1.94 nm ($n = 324$ kinetochores, cell n. = 14, Figure 5.8). The ΔEC distance between CenpC and Ndc80(N) was found to be 86.89 ± 1.08 nm ($n = 324$ kinetochores, cell n. = 14, Figure 5.8). The measurements in this pre-extracted condition, were therefore consistent to ~ 5 nm with the measurements in non pre-extracted condition. Therefore, we conclude that pre-extraction does not majorly affect the CenpC-Mis12-Ndc80 complex network in HeLa K cells.



B



C

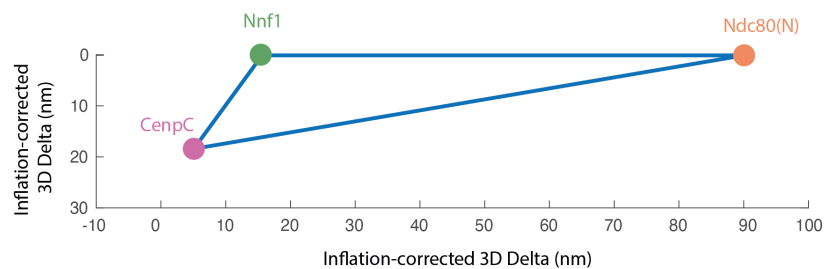


Figure 5.8: Δ EC positions of CenpC, Nnf1 and Ndc80(N) in HeLa K cells. Fixation with "pre-extraction" A) Representative images of kinetochores in HeLa K cells stained for CenpC, Nnf1 and Ndc80(N): "pre-extraction" condition (see methods). Cells were treated for 2 hrs with 1:1000 DMSO prior to fixation. The centroid detection in KiD is marked by cross or circle over the kinetochore spot. B) Histograms of the measured Δ 3D distances. (see Table 5.1 for median \pm sd) Δ 3D measurements were performed as described in Chapter 3 and corrected in TEDCA. C) Plot showing the triangulation of the mean Δ EC distance measurements from B.

5.2.4 Mapping of the Ska complex position in HeLa cells

To understand the intra-kinetochore position of Ska, we first sought to map Ska3(M) in HeLa cells and confirm that the measurements are consistent with Ska localisation in close proximity to Ndc80, as we saw in Rpe1 cells. To do so we measured the Δ EC distances in cell stained for Ska3(M), Nnf1, and CenpC. Here, we found CenpC to Nnf1 to be 23.68 ± 1.9 nm. That measurements is consistent with the CenpC-Nnf1 distance observed in the Ndc80(N)-Nnf1-CenpC triangle. Further, the CenpC to Ska3(M) distance was found to be 84.5 ± 1.5 . That distance is similar to the 86.89 ± 1.1 nm distance between CenpC and Ndc80(N) measured above in pre-extracted Rpe1 cells. Therefore, this measurement suggests close proximity between Ndc80 and Ska. Finally, the Nnf1 to Ska3(M) distance was found to be 65.46 ± 1.65 (MC009 plain HeLa K, n = 216 KT pairs, cell n. = 11, Figure 5.9). The Nnf1-Ska3 measurement is in line with the 74.4 ± 1.1 nm distance between Nnf1 and Ndc80N. Therefore, these distances are consistent with the model of Ska being in close proximity to Ndc80(N).

Next, to pinpoint the average position of Ska molecules in the kinetochore we utilised the Ska1(N) endogenous label cell lines. Here, we first utilised the 2xmNeonGreen-Ska1 cell line as it has cleaner genetic background. To map the position of Ska relative to KMN network, we stained MC200 cells for Nnf1 and Ndc80(N). The Δ EC distance between Nnf1 and Ndc80N was found to be 58.31 ± 2.02 nm (n = 164 kinetochores, cells n. = 18). That distance is somewhat shorter (by ~ 15 nm) than the one we observed in parental cells. That can represent effects of clonal selection or adaptation of the cells to the endogenous tag. We observed also small variation in this distance between non-modified HeLa K and Rpe1 cells. Therefore, the kinetochore likely has the ability to adapt to some level. Nevertheless, the cells show normal mitotic timing and thus Ska is functional in these cells. The high alignment of outer kinetochore Mis12-Ndc80 molecules is also retained in MC200 cells, with a nematic order = 0.73 (Figure 5.7). Further, the observed Nnf1 to Ndc80(N) distance in MC200 is close to the same distance in Rpe1 cells. Therefore, this further shows that the kinetochore architecture is adaptable and can attain small fluctuations that are still viable.

The Δ EC distance between Nnf1 and Ska1(N) was found to be 73.33 ± 4.6 nm (n =

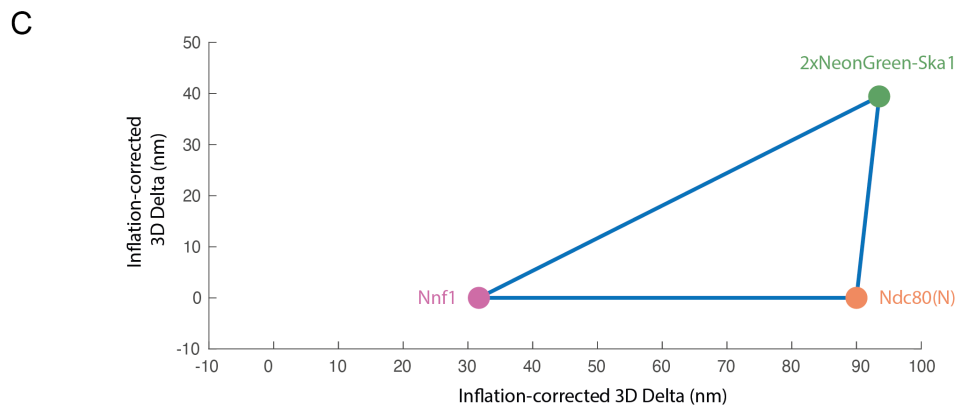
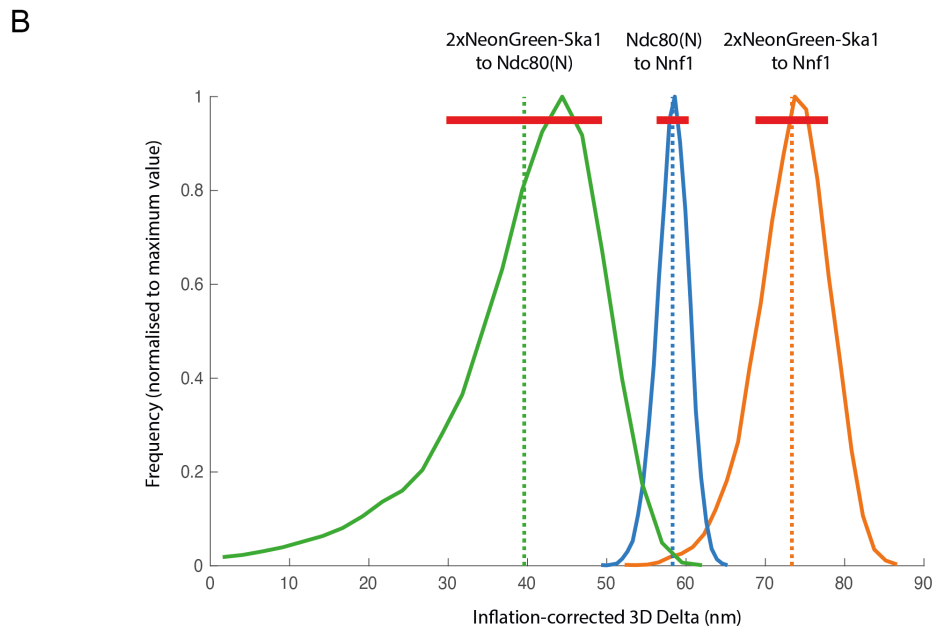
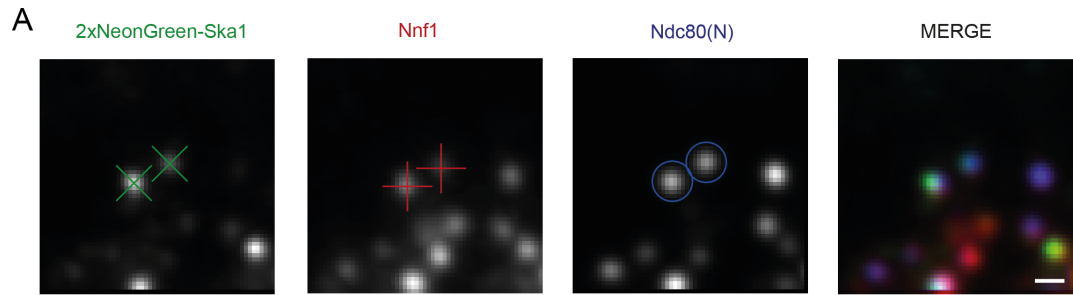


Figure 5.9: Δ EC positions of Ska1(N), Nnf1 and Ndc80(N) in HeLa K cells. MC200 cell line. A) Representative images of kinetochores in HeLa K cells expressing mNeonGreen tandem tag endogenous label Ska1(N) and stained for Nnf1 and Ndc80(N) ("no pre-extraction" condition, see methods). Cells were treated for 2 hrs with 1:1000 DMSO prior to fixation. The centroid detection in KiD is marked by cross or circle over the kinetochore spot. B) Histograms of the measured Δ 3D distances. (see Table 5.1 for median \pm sd) Δ 3D measurements were performed as described in Chapter 3 and corrected in TEDCA. C) Plot showing the triangulation of the mean Δ EC distance measurements from B.

164 kinetochores, cells n. = 18, Figure 5.9). This distance positions the average of the Ska molecules close to the Ndc80(N). Finally, the Ska1(N) to Ndc80(N) distance was found to be 39.59 ± 9.9 nm (n = 164 kinetochores, cells n. = 18, Figure 5.9). The distance of ~ 40 nm between Ska1(N) and Ndc80(N) in the context of the triangle measurements suggests that Ska1(N) is offset from the Mis12-Ndc80(N) axis as: $58.31 + 39.59 \neq 73.33$ nm (Figure 5.9). As we previously reported for CenpC, small fluctuations in the position of the molecule due to flexibility can give rise to such an offset.

We further, sought to confirm the Ska1(N) offset and position within the kinetochore by staining MC200 cells for Ndc80(N) and CenpC. Here, we observed the ΔEC distance between CenpC and Ndc80N to be 69.97 ± 2 nm (n = 254 kinetochores, cells n. = 14, Figure 5.10). Again there was a similar difference in the position of Ndc80(N) as compared to parental HeLa cells. The ΔEC distance between CenpC and Ska1(N) was found to be 73.32 ± 4.36 nm (n = 254 kinetochores, cells n. = 14, Figure 5.10). This result also positioned Ska1(N) close to the Ndc80(N), similar to previous results. Finally, the Ska1(N) to Ndc80(N) distance was found to be 40.65 ± 6.17 nm (n = 164 kinetochores, cells n. = 18, Figure 5.10). The distances in this experiment also violate linear assumption: $69.97 + 40.65 \neq 73.32$ nm. Therefore, two separate data sets confirm that Ska1(N) lies off-axis from the Mis12-Ndc80N assembly.

Finally, to confirm the position of Ska1(N) in a separate cell line, we utilised the eGFP-Ska1 MC177 cell line. Here we stained MC177 cells with anti-eGFP antibody to enhance the Ska signal, and anti-Nnf1 and anti-CenpC antibodies. The cells were also pre-extracted prior to staining. The ΔEC distance between Ska1(N) and CenpC was found to be 85.26 ± 2.8 nm (n = 212 kinetochores, cell n. = 10, Figure 5.11). The ΔEC distance between Ska1(N) and Nnf1 was found to be 66.55 ± 3.4 nm (n = 212 kinetochores, cell n. = 10, Figure 5.11). Finally, the ΔECt distance between CenpC to Nnf1 was found to be 23.4 ± 2.36 nm (n = 212 kinetochores, cell n. = 10, Figure 5.11). The Ska1(N)-Nnf1 distance shows a 7 nm difference between the MC200 and MC177 cell lines. The Ska1(N) to CenpC shows a difference of ~ 10 nm between the two cell lines. Therefore, we conclude that, albeit small measurement variations, the position of Ska1(N) close to the Ndc80N terminus on the inner-outer kinetochore axis is consistent between the two cell lines.

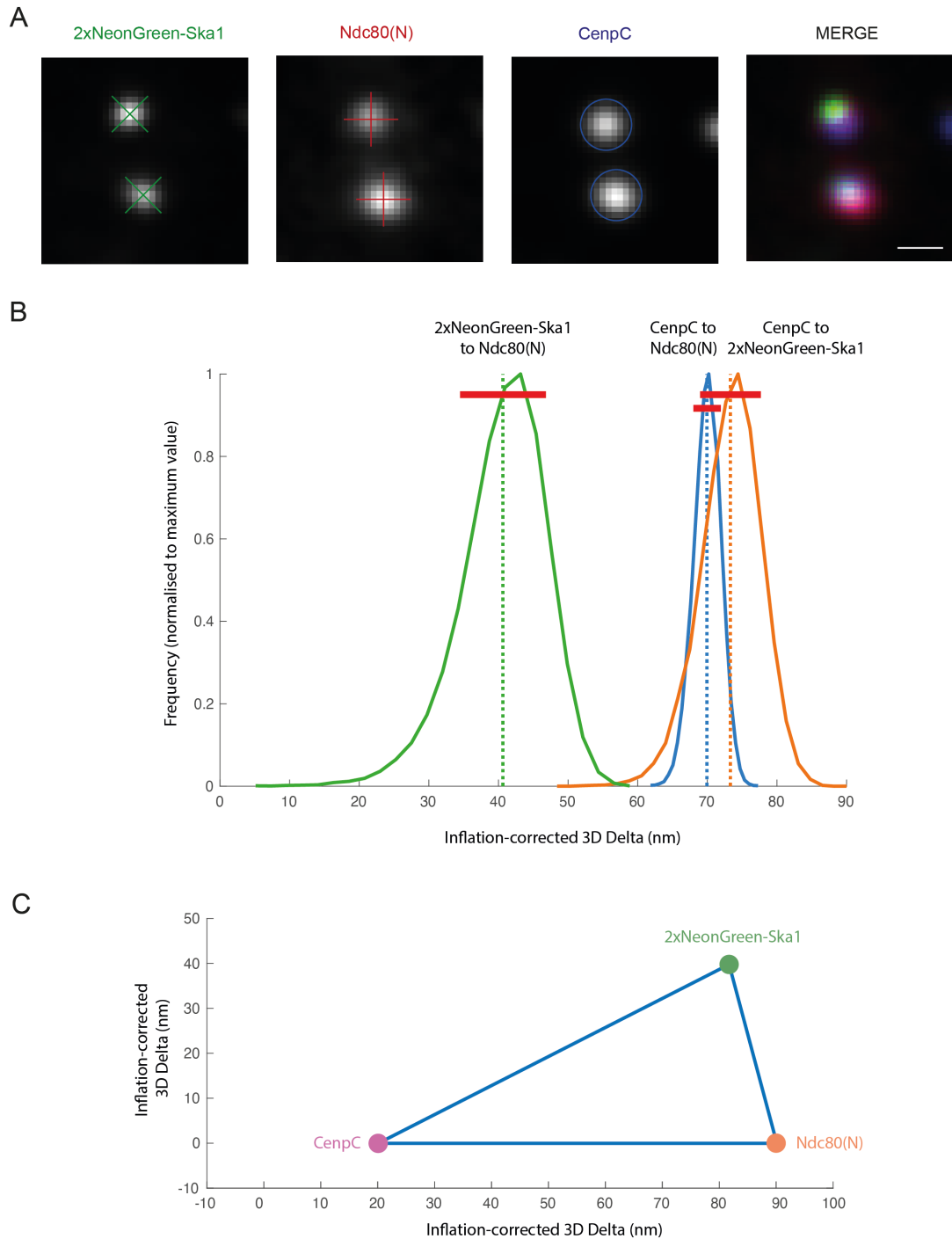


Figure 5.10: Δ EC positions of Ska1(N), CenpC and Ndc80(N) in HeLa K cells. MC200 cell line. A) Representative images of kinetochores in HeLa K cells expressing mNeonGreen tandem tag endogenous label Ska1(N) and stained for CenpC and Ndc80(N) (“no pre-extraction” condition, see methods). Cells were treated for 2 hrs with 1:1000 DMSO prior to fixation. The centroid detection in KiD is marked by cross or circle over the kinetochore spot. B) Histograms of the measured Δ 3D distances. (see Table 5.1 for median \pm sd) Δ 3D measurements were performed as described in Chapter 3 and corrected in TEDCA. C) Plot showing the triangulation of the mean Δ EC distance measurements from B.

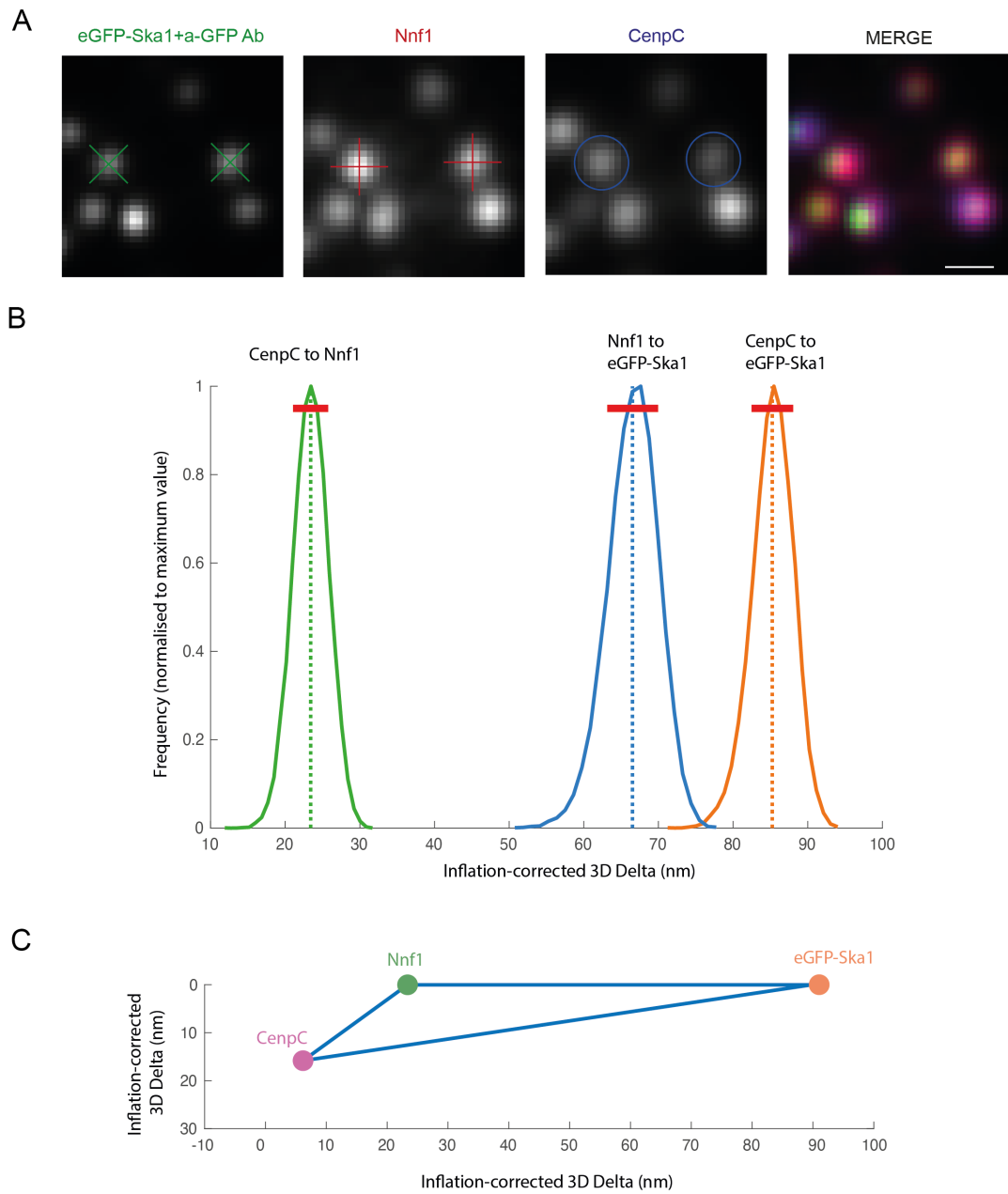


Figure 5.11: Δ EC positions of Ska1(N), CenpC and Nnf1 in HeLa K cells. Cell line MC177. A) Representative images of kinetochores in HeLa K cells expressing eGFP tag endogenous label Ska1(N) and stained for CenpC and Nnf1 ("pre-extraction" condition, see methods). Cells were treated for 2 hrs with 1:1000 DMSO prior to fixation. The centroid detection in KiD is marked by cross or circle over the kinetochore spot. B) Histograms of the measured Δ 3D distances. (see Table 5.1 for median \pm sd) Δ 3D measurements were performed as described in Chapter 3 and corrected in TEDCA. C) Plot showing the triangulation of the mean Δ EC distance measurements from B.

Distance		treatment	$\Delta 1D$ mean ¥	sd †	n	$\Delta 3D$ ¶	sd †	n	ΔEC mean	sd §	n	cell line
CenpC	Nnf1	DMSO	11.57	15.19	224	56.62	38.72	628	21.11	1.94	324	HeLa K
CenpC	Ndc80(N)		63.22	32.3	196	93.29	31.06	582	86.89	1.08	324	
Nnf1	Ndc80(N)		54.29	24.19	181	87.15	28.05	547	74.4	1.1	324	
CenpC	Nnf1*	DMSO	7.94	13.62	143	53.75	24.79	376	22.13	2.56	476	HeLa K
CenpC	Ndc80(N)*		65.31	30.13	159	92.3	33.8	404	89.31	1.50	476	
Nnf1	Ndc80(N)*		59.21	22.88	124	83.84	27.04	349	75.08	1.19	476	
Ska1(N)	Nnf1	DMSO	44.07	29.74	130	100.19	59.65	558	73.33	4.58	164	2xmNG-Ska1 HeLa K
Ska1(N)	Ndc80(N)		10.32	31.37	139	84.69	45.99	571	39.59	9.81	164	
Nnf1	Ndc80(N)		29.34	28.52	251	71.98	25.09	792	58.31	2.02	164	
Ska1(N)	Ndc80(N)**	DMSO	2.68	23.98	108	76.62	33.15	380	40.65	6.17	254	2xmNG-Ska1 HeLa K
Ska1(N)	CenpC**		44.18	32.37	91	96.12	35.19	350	73.32	4.36	254	
CenpC	Ndc80(N)**		40.66	33.74	129	81.99	24.52	439	69.97	1.98	254	
Ska1(N)	Ndc80(N)**	Taxol	0.86	24.25	72	79.93	53.25	283	45.88	5.21	156	2xmNG-Ska1 HeLa K
Ska1(N)	CenpC**		59.22	25.17	55	105.98	61.62	239	83.38	4.29	156	
CenpC	Ndc80(N)**		51.32	22.52	121	81.12	23.72	353	73.54	2.20	156	
CenpC	Nnf1*	DMSO	7.94	13.62	143	53.75	24.79	376	22.56	2.56	212	eGFP-Ska1 HeLa K
CenpC	Ska1(N)*		65.31	30.13	159	92.3	33.8	404	85.30	2.83	212	
Nnf1	Ska1(N)*		59.21	22.88	124	83.84	27.04	349	66.89	3.32	212	

Table 5.1: Ska architecture in HeLa kinetochores: ΔEC measurements in HeLa K cells, and their comparison to $\Delta 1D$ and $\Delta 3D$ measurements. The mean $\Delta 1D$, $\Delta 3D$, and ΔEC measurements, their standard deviations (sd), and the number of analysed kinetochores (n) are indicated for each pair of fluorophores in the six presented data sets (thick outline). Experiments where the samples were pre-extracted prior to fixation are indicated with one star (*). Experiments done in parallel, such that the treatments are comparable, are indicated with two stars (**). $\Delta 1D$ (¥) measurements were performed as in Smith *et al.*, 2016. $\Delta 3D$ measurements (¶) were performed as described in Chapter 3. For $\Delta 3D$ measurements, kinetochores with z-offset between the two markers of more than 100 nm were excluded from the analysis. For $\Delta 1D$ and $\Delta 3D$ measurements, the sd of the data set samples is indicated (†). ΔEC measurements were performed as described in Chapter 3, except the measurements were corrected in TEDCA. For ΔEC measurements, the sd of the posterior (estimated parameter) is indicated (§). Abbreviations: tandem mNeonGreen fluorophore label is abbreviated as "2xmNG". Treatment: cells were treated with either 1:1000 DMSO for 2 hrs or 1 μM Taxol for 15 min.

5.2.5 The Ska1(N) offset from the Mis12-Ndc80 complex axis is not dependent on microtubule dynamics

One hypothesis is that the offset of Ska1(N) relative to the Mis12-Ndc80 axis is due to Ska binding to the dynamic microtubule ends. Here, dynamics of the microtubules could induce small fluctuations in the Ska1(N) position which will result in Ska1(N) being offset. Therefore, we sought to test that hypothesis by inhibiting the microtubule dynamics in MC200 cells. Microtubule dynamics can be inhibited via treatment of the cells with 1 μ M taxol for 15 mins (Roscioli et al., 2020). Therefore, we treated MC200 cells with 1 μ M taxol for 15 min, and stained the cells for Ndc80(N) and CenpC. That experiment was done in parallel to the one presented in Figure 5.10 where MC200 cells were treated with DMSO and stained in the same manner. After taxol treatment, we observed CenpC to Ndc80N distance of 73.54 ± 2.2 nm ($n = 156$ kinetochores, cell n. = 10, Figure 5.12). That distance is similar to the one observed in DMSO-treated cells: 69.97 ± 2.0 nm. This data therefore shows that the Ndc80N terminus position is not affected by microtubule dynamics in HeLa K cells. We reached the same conclusion for Rpe1 cells in Chapter 4. Next we measured the CenpC to Ska1(N) distance and found it to be 83.38 ± 4.29 nm ($n = 156$ kinetochores, cell n. = 10, Figure 5.12). That distance is similar to the one observed in DMSO: 73.32 ± 4.36 nm. Therefore, in the absence of microtubule dynamics Ska does not drastically re-locate. Finally, we measured the Ska1(N) to Ndc80(N) distance and found it to be 45.88 ± 5.21 nm ($n = 156$ kinetochores, cell n. = 10, Figure 5.12). Therefore, the offset of Ska1(N) relative to the Mis12-Ndc80 does not depend on microtubule dynamics.

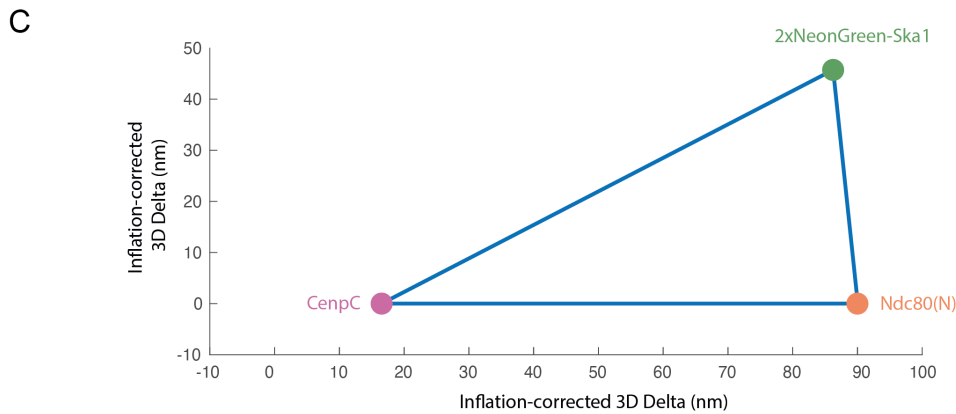
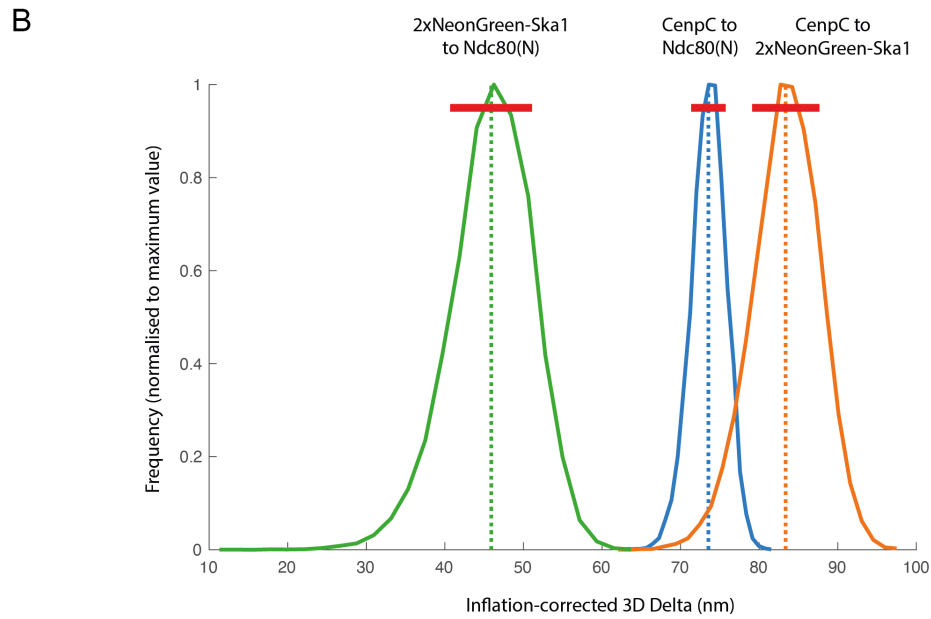
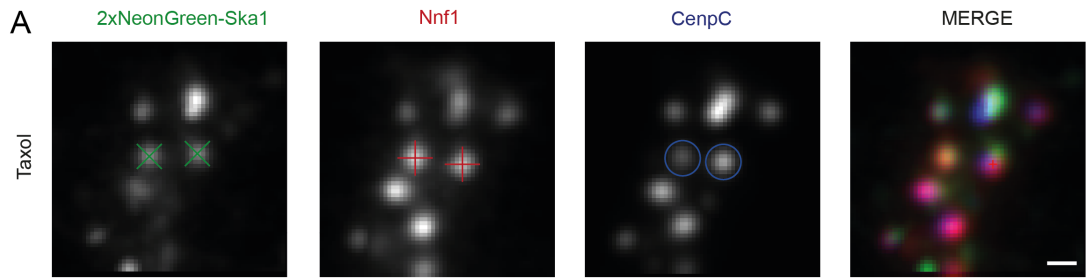


Figure 5.12: Δ EC positions of Ska1(N), CenpC and Nnf1 at tension-less kinetochores (taxol) in HeLa K cells. Cell line MC200. A) Representative images of kinetochores in HeLa K cells expressing eGFP tag endogenous label Ska1(N) and stained for CenpC and Nnf1 ("no pre-extraction" condition, see methods). Cells were treated for 15 min with 1 μ M taxol. The control for this experiment is presented in Figure 5.8. The centroid detection in KiD is marked by cross or circle over the kinetochore spot. B) Histograms of the measured Δ 3D distances. (see Table 5.1 for median \pm sd) Δ 3D measurements were performed as described in Chapter 3 and corrected in TEDCA. C) Plot showing the triangulation of the mean Δ EC distance measurements from B.

5.2.6 mNeonGreen-Ska1 as a tool for live-cell imaging of Ska dynamics

This study focused on the position of Ska in metaphase cells. An outstanding challenge is to understand the dynamic behaviour of Ska in prometaphase and during congression. In specific, the main role of Ska is to stabilise the kinetochore-microtubule attachment in congression. Further, Ska has been shown to be loaded to higher level at aligned as compared to unaligned kinetochores. However, there is no live-cell imaging of endogenous Ska up to date, and the dynamics of Ska localisation remain elusive. In this section I will show preliminary results that establish MC200 as a valuable tool for understanding the dynamics of Ska in congression. Here, I generated MC200 cell line stably expressing the kinetochore marker CenpA, labelled with Halo-tag (MC206) (see Chapter 1: Methods for details). Further, I imaged the MC206 cell line under the lattice light sheet microscope to obtain movies of prometaphase and metaphase cells with endogenous labelled Ska1 and Halo-CenpA. Figure 5.13 shows representative still images from a kinetochore congression movie where the Ska kinetochore levels can be detected. The time in this project was insufficient to study the dynamics of Ska localisation in congression. Nevertheless, here I have generated an endogenous Ska1 labelled cell line, with kinetochore marker that can be used for relatively high spatial and temporal resolution live-cell imaging of Ska loading dynamics in congression.

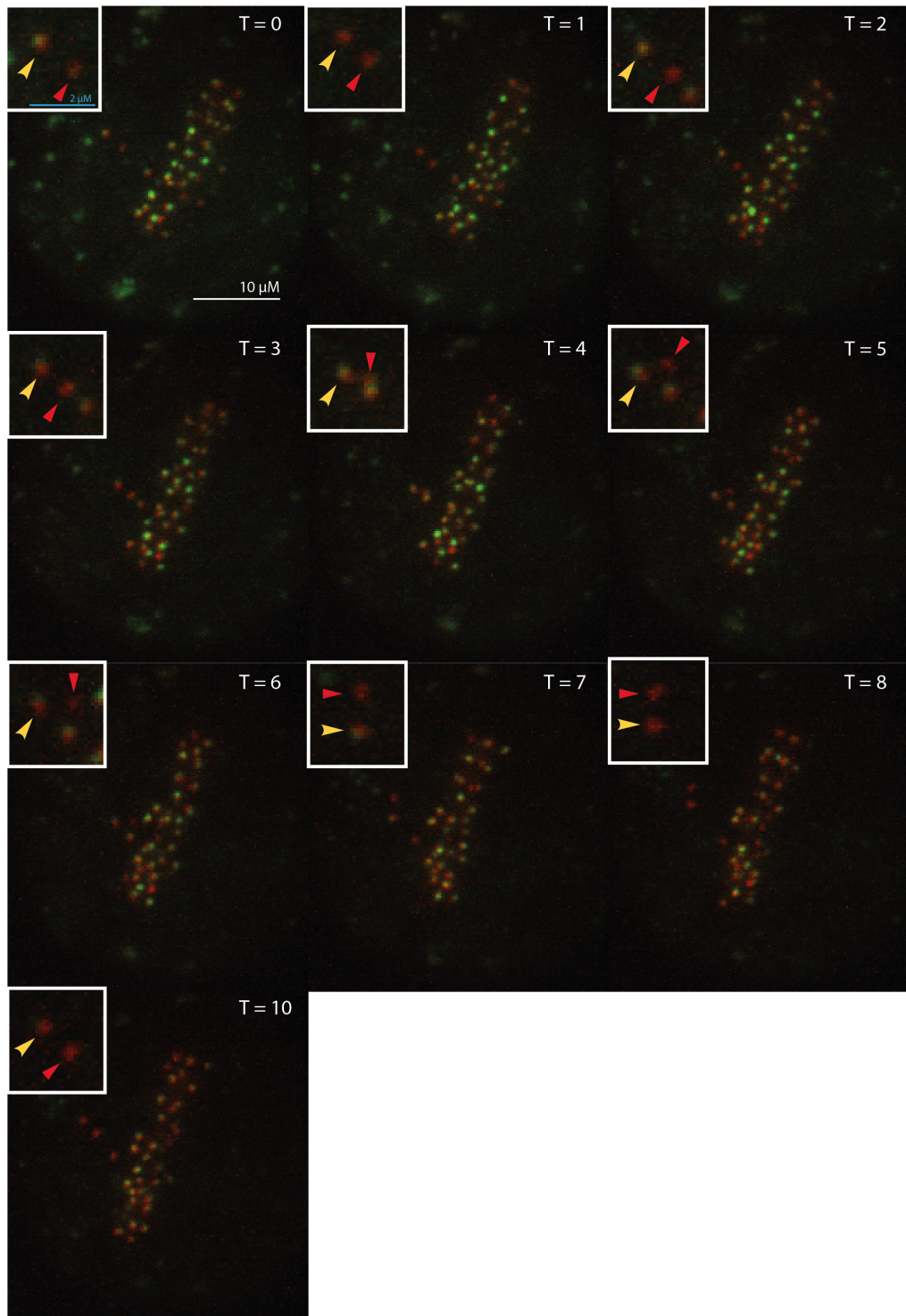


Figure 5.13: Live-cell imaging of endogenously labelled Ska1(N) (MC206 cell line) on Lattice Light Sheet microscope. Representative images of live-cell imaging of HeLa K cells that express endogenously labelled Ska1(N) with 2xmNeonGreen tag and Halo-tag-CenpA (stable expression). The Halo-CenpA tag was stained with TMR prior to imaging. Time step, 15 s. Scale bars: white, 10 μM ; blue, 2 μM . Inset on the top left shows zoom-in on the captured congressing kinetochore pair. Arrows annotate the Poleward (red) and Away-from-the-Pole (yellow) moving kinetochore. Images are not on the same intensity scale to aid visualisation.

5.3 Conclusions

In summary, HeLa kinetochores recapitulate the kinetochore architecture features observed in Rpe1 cells. In specific, in HeLa K kinetochores, the Mis12-Ndc80 complex assemblies are highly aligned and CenpC is offset from the Nnf1-Ndc80N axis. Further, use of a different cell line showed small differences in the Delta measurements and suggested that kinetochore architecture is adaptable to some extent. Second, we have shown that the Ska1 subunit lies in close proximity to Ndc80(N) in the inner-outer kinetochore axis. Furthermore, we show that Ska1(N) is offset from the Mis12-Ndc80 axis and that this is not related to microtubule dynamics. We propose that this offset can be created by the flexibility in the linkage of Ska to kinetochores. In Chapter 4, we discussed that the disorganised structure of CenpC could lead to position fluctuations, which in turn would be detected as offset in the ΔEC measurement. The Ska complex relies on the unstructured Ska3 C-terminus for kinetochore localisation. Therefore, we think that flexibility in the Ska3 C-terminus leads to small fluctuations in the position of the core Ska complex, and that these fluctuations are further detected in ΔEC mapping as offset of the Ska complex from the Nnf1-Ndc80(N) axis. This hypothesis also agrees with a recent *in vitro* study from the Mussachio lab, in which the authors observed fluctuations in Ska position relative to Ndc80 via electron microscopy of purified proteins (Huis In't Veld et al., 2019). Finally, we have shown how endogenous labelling now opens up the possibility to investigate the dynamics of Ska kinetochore binding and unbinding in living cells.

Chapter 6

Discussion

6.1 *In vivo* investigation of the 3D human kinetochore architecture

A key barrier to revealing the 3D geometry and architecture of the human kinetochore ensemble of molecules was the development of a method to reliably make inflation-corrected 3D measurements. Here, we developed such an algorithm that accounts for both the an-isotropic PSF in Z, and corrects the inflation in 3D image stacks (see Chapter 3). The algorithm thus surpasses the "Churchman" 2D inflation-correction algorithm and results in 3D Δ Euclidean corrected (EC) measurements with tight confidence intervals (Churchman et al., 2005).

Using this 3D Δ EC methodology we have made the first steps towards unravelling the full 3D geometry of kinetochores and how it responds to mechanical and chemical stimuli *in vivo*. We mapped 12 proteins from four major kinetochore complexes: Mis12 complex, Ndc80 complex, Ska complex, and RZZ complex (see Appendix B: Roscioli et al., 2020; and subsection 4.2.1). Previously, studies have used the Ndc80 complex as a molecular ruler to verify their measurements (Suzuki et al., 2018). We also measured the 3D Δ EC between the Ndc80(C) and Ndc80(N) and showed it to closely matched the structural length of the complex. However, we want to draw the attention of the reader to the fact that Δ EC measurements show the average position of all tagged molecules and do not report on the organisation and conformation of single molecules. The Δ EC measurements are also sensitive

to the alignment of molecules: (1) for molecules that are fully aligned end-to-end the ΔEC distance (average of all molecules) will match the structural distance of single molecule; Nematic order = 1. (2) for molecules that are completely unaligned, i.e. the molecules can be oriented in any direction relative to each other, the ΔEC average of all molecules will be shorter than the length of the single molecules; Nematic order = 0. Therefore, use of the Ndc80 structure as a "molecular ruler" is a flawed concept. Instead, the ΔEC measurements should really be discussed in terms of how the ensemble average measurement is built from the organisation of single molecules. To shed light on the 3D kinetochore ensemble architecture, we integrated available structural data with our 3D ΔEC measurements, and created a simulation of the kinetochore ensemble that represents the most likely organisation of the CenpC, Mis12 complex and Ndc80 complex molecules in a 3D kinetochore bound to a K-fibre. The simulation illustrated that, to obtain the observed 3D ΔEC measurements, the Mis12 and Ndc80 complex molecules need to be highly aligned along an internal axis. This high alignment of outer kinetochore molecules was recently confirmed by FRET proximity assays (Kukreja, Kavuri and Joglekar, 2020). Here, the authors observed that the Ndc80 complex molecules N-termini position in close proximity (below 10 nm), and also that the Ndc80 complex molecules C-termini are positioned in close proximity (below 10 nm). This result further solidifies the conclusion of high alignment of the Ndc80 molecules along an internal axis, and shows that the Ndc80 molecules are also staggered along that internal axis, and thus form a "cluster". We further found that the alignment of Mis12 and Ndc80 molecules is dependent on microtubule binding. A finding that was also consistent with FRET-based experiments (Kukreja, Kavuri and Joglekar, 2020). Therefore, the internal axis of alignment may be imposed by Ndc80 molecules binding the microtubule, and thus aligning along the microtubule axis.

Ndc80 has been shown to be mostly rigid with a point of flexibility approximately two-thirds between the Ndc80(C) and Ndc80(N): the Ndc80 loop (Wang et al., 2009; Huis In't Veld et al., 2016; Maiolica et al., 2007). The Ndc80 loop is suggested to allow for hinge-like bending of the complex (Wang et al., 2009). Further, in vitro FRET studies have suggested the Ndc80(N) to be "back-folded" towards the Ndc80(C) in absence of microtubules (Scarborough et al., 2019). This "back-fold" conformation was further suggested to represent auto-inhibition, albeit whether the

”back-fold” reflects a preferred conformation or true auto-inhibition remains unclear. Further, the ”back-fold” conformation was shown to be affected by Ndc80 microtubule binding, whereby after binding of the Ndc80 complex to microtubules abolished the close proximity of the Ndc80 complex N- and C-terminal domains (Scarborough et al., 2019). However, the following critical open questions remained: Does the ”back-fold” Ndc80 complex conformation occur *in vivo*? If so, does microtubule binding affect the conformation of the Ndc80 complex *in vivo*? What are the potential roles of the Ndc80 complex conformational changes in mitosis? Our data show that Ndc80 back-folding does occur *in vivo* and that it is also accompanied by a loss of order - for simplicity we term these changes the Ndc80 ”jack-knife” (see Appendix B: Roscioli et al., 2020; and subsection 4.2.2). In contrast, at attached kinetochores Ndc80 is in straight conformation and the Ndc80 molecules are highly aligned. Therefore, we next sought to test whether the Ndc80 complex molecules straighten and align in response to microtubule binding or in response to force exerted by the microtubules. We showed that the Ndc80 complex molecules are in straight conformation and are aligned at attached kinetochores not subjected to microtubule force (taxol treatment). Therefore, Ndc80 specifically senses microtubule attachment but not K-K tension. The identification of Ndc80 as microtubule-attachment kinetochore sensor can have important implications in how kinetochores ”count” microtubules to silence the SAC. Therefore, this topic will be discussed in the next section.

Furthermore, we found that Knl1 responds to changes in K-K tension: The Knl1 N-terminus moved ~ 93 nm outward relative to CenpC in the absence of tension (taxol) and ~ 65 nm in absence of tension and microtubule attachment (nocodazole) (see Appendix B, Roscioli et al., 2020; and subsection 4.2.2). Based on this we proposed that Knl1 is a K-K tension sensor. The ability of kinetochores to sense tension has been a long standing question. Early studies by Nicklas showed that kinetochores can stabilise their attachment when exposed to force (Nicklas and Koch, 1969; Nicklas et al., 1995). The search for such tensile elements in the kinetochore, however, has been largely unsuccessful up to now. Therefore, here we identify a long speculated tensile element in the kinetochore: Knl1. The observed rearrangements re-position the Knl1 N-terminus far from the outer kinetochore in absence of tension and close to the outer kinetochore when the K-K tension is high. Interestingly, the Knl1 N-terminus

binds the PP1 whose phosphatase activity counteracts Aurora B to stabilise the attachments. This provides a possible mechanism by which rearrangements of Knl1 link tension changes to functional outputs by altering the balance of phosphorylation within the inner-outer kinetochore.

We note that we did not detect other changes in the kinetochore organisation after taxol treatment. This is in contrast to previous 1D Delta studies that observed decrease in Delta distances upon taxol treatment (Wan et al., 2009). One hypothesis is that previous studies have detected artefacts from the projection and inflation of measurements. However, in our own 1D Delta measurements we don't see that effect either. Recent study suggested that the effects detected by Delta in these early studies are due to changes in kinetochore shape upon taxol treatment (Renda et al., 2020). Using 1D measurements this study proposed that kinetochore change their shape after taxol treatment, resulting in ~ 25 nm changes in delta. Therefore, the study questioned the reliability in using Delta distance measurements for understanding the kinetochore architecture. Here we show that our ΔEC measurements of taxol-treated kinetochores do not reflect the described by Renda and colleagues changes in kinetochore shape after taxol treatment as: (1) Apart from Knl1 N-terminus movement we do not detect other changes in kinetochore architecture: and thus our measurements are not significantly affected by changes in kinetochore shape, (2) the outward movement of Knl1(N) of ~ 93 nm and ~ 65 nm cannot be explained by ~ 25 nm change due to kinetochore shape change. (3) We excluded any "miss-shaped" spots from our analysis showing that distance changes cannot be due to shape effect alone. This also further shows the significance of performing data quality control for gaussian-shaped spots which likely excludes effects of kinetochore shape on Delta. Therefore, our ΔEC state-of-the-art measurements are a powerful tool to study the kinetochore architecture. Unfortunately, the out-dated 1D methodology remains the one widely used by the field (even within the last year, see: (Wimbish et al., 2020; Broad et al., 2020)). This likely stems from the lack of detailed guides and the complexity of the more recent methods. To tackle this issue we developed a step-by-step guide for our 3D ΔEC methodology that will enable wide use of the methodology (see Appendix B, Germanova et al., 2021 in revision). The hope is that the availability of the methodology will lead to its wide application and critically will lead to more coherent and conclusive information on

the kinetochore ensemble architecture.

Due to the ensemble average nature of the measurements, small population of molecules with distinct geometry can be hidden within the population average measurement. For example, in cells with all kinetochores aligned in a metaphase plate, we found a subset of kinetochores to be Mad2 "positive" and with Ndc80 in jack-knifed state, while the majority of kinetochores were Mad2 "negative" and had Ndc80 in straight conformation (see Chapter 4, sub-section 4.2.3). However, when we analysed the pool of kinetochores irrespective of their Mad2 status, we obtained ΔEC distance corresponding to Ndc80 in straight and aligned state. This is because the Mad2 "negative" population accounted for most of the kinetochore sample. Therefore, if there is a small population of kinetochores with Ndc80 in jack-knifed state (or in general small population of kinetochore in different state), these will not be detected in the ΔEC measurement. Such information is important to entangle the transition of kinetochores between states. Therefore, we are limited in our understanding of kinetochores in physiological conditions and how they transition between architectural states. Therefore, a critical next step is to be able to understand the varying stimuli that can govern the kinetochore transitions and what is the importance of these transitions. To understand the stimuli that trigger a kinetochore transition we need to un-mix the sub-population of kinetochores in a different state from the predominant kinetochore ensemble conformation, and ask how this sub-population varies in response to stimuli. Here, we presented and tested a new generation algorithm that can "un-mix" sub-populations of kinetochores with defined conformation from the overall kinetochore population (see subsection 4.2.6). We plan to use this approach to understand how Ndc80 jack-knife and Knl1 N-terminus unravelling respond to various stimuli and thus understand the roles of the sensors. For example, we can un-mix kinetochores with Knl1 N-terminus extended fully by ~ 93 nm and check what is the attachment status of these kinetochores by a separate marker. Further we wish to go a step further and develop the algorithm such that we can uncover three states simultaneously. That would help us in the case for example of Knl1 where we observed ~ 93 nm movement in tensionless and ~ 65 nm movement in unattached tensionless kinetochores. Understanding of how and where each of those movements occur in physiological condition is an important investigation given that the Knl1 N-terminus binds SAC phosphatase PP1 (Liu

et al., 2010). Therefore, "un-mixing" of the attached, tension-less, and un-attached states in physiological conditions can reveal how the Knl1 response to loss of tension can feed into the SAC and error-correction machinery. It may also become possible to model a hypothetical state of the kinetochore based on known structural data, predict how that state would reflect in Δ EC measurements and then un-mix - and provide evidence for this state *in vivo*. Development of such algorithm would allow us to validate kinetochore states observed only *in vitro* and to understand how they influence kinetochore function.

The next step will be to study kinetochores at even higher resolution and understand the re-organisations within the ensemble (including the shape effects mentioned above) *in vivo*. That would help us understand the phenomena we observe at the ensemble level, and the exact molecular mechanisms that govern them. Structured illumination microscopy has been previously used to obtain high resolution of kinetochores (Wynne and Funabiki, 2016). Using this methodology my own preliminary data shows that two kinetochore lobes (yellow arrow) can be observed at this higher resolution (see Figure 6.1). These "lobes" likely correspond to two kinetochore nucleation sites in the regional human centromere. Therefore, next it will be important to investigate as to whether the kinetochore molecule ensemble stems from discrete units, how these units respond to stimuli and as to whether they are co-dependent in their rearrangements. We can possibly address these question by applying 3D Δ EC measurements to SIM data. However, our current approach relies on center detection of Gaussian-shaped spots. As clear from the SIM kinetochore images, at higher resolution kinetochores are not Gaussian-shaped. Therefore, we will need to make further developments to segment the kinetochore shapes and then understand their relative positioning and movements at that higher resolution. Even higher, true single molecule, resolution can be obtained by STORM and PALM methods. The study of kinetochore architecture by STORM and PALM has been limited by the focal depth of the studies, their practical complexity and their 2D nature. However, recently a method for 3D STORM with Lattice Light Sheet microscopy has been developed (Waldchen et al., 2020). Therefore, the next big step in understanding the kinetochore organisation is to identify the 3D co-localisation of single kinetochore molecules using this approach. Such study would reveal how individual kinetochore molecules respond to chemical and mechanical stimuli. One view is that the kineto-

chore ”computes” the different stimuli and responds in a quantitative manner, which further informs the SAC and error-correction mechanisms. Therefore, integration of 3D STORM single molecule maps in a computational simulation would reveal as to whether and possibly how the kinetochore ”computes” stimuli and responds at the single molecule level.

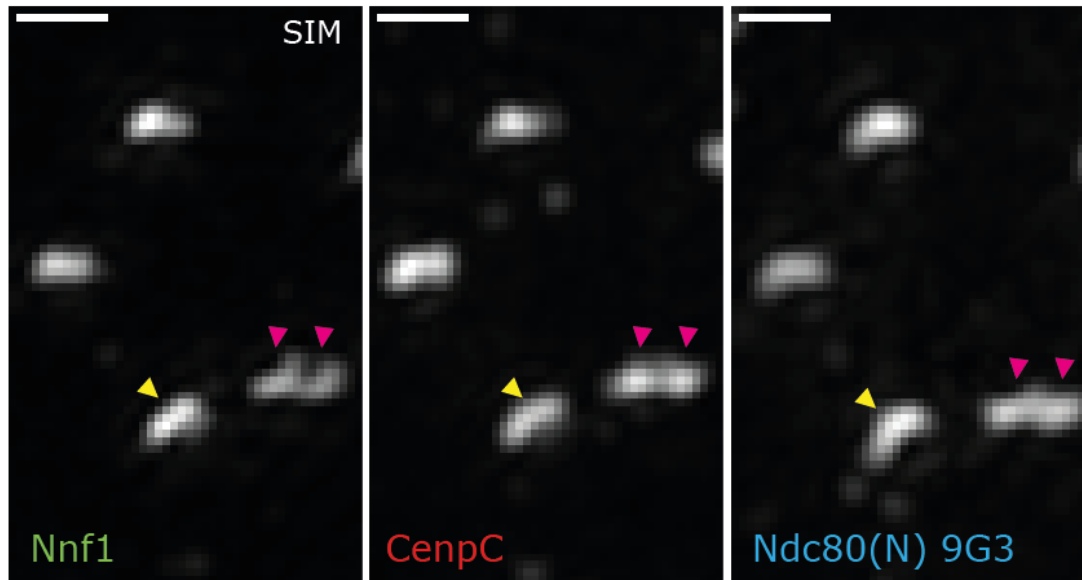


Figure 6.1: Structured illumination microscopy (SIM) of hTERT Rpe1 kinetochores Representative SIM images of hTERT Rpe1 kinetochores labelled for Nnf1 (green), CenpC (red) and Ndc80(N) (blue). Kinetochores can be observed to have single lobe (yellow arrow) or two-lobed architecture (pink arrow). Scale bar 500 nm.

6.2 Interplay between Ndc80 jack-knife and SAC activation-silencing

The spindle assembly checkpoint prevents anaphase onset until all kinetochores have formed mature bi-oriented attachments. SAC silencing has been shown to occur at 30-50% kinetochore-microtubule occupancy, specifically at end-on attached kinetochores (see subsection 1.4.3; Etemad et al., 2019; Dudka et al., 2018; Kuhn and Dumont, 2017). That led to the hypothesis that end-on attachments have a distinct interface that triggers SAC silencing. We found that Ndc80 undergoes conformational changes in response to microtubule binding and further hypothesised that these changes may serve as an input for SAC silencing. The prediction here

would be that Ndc80 transitions from jack-knifed into straight conformation first, and this event then triggers Mad2 unloading from kinetochores and silencing of the SAC. To test that hypothesis we used endogenous Venus-Mad2 as a reporter for SAC activity and monitored changes in the CenpC-to-Ndc80(N) Δ EC measurement (see subsection 4.2.5). Here we observed that Ndc80 displays three sequential distinct behaviours as Mad2 is lost from kinetochores: (I) until kinetochores unload $\sim 95\%$ of the Mad2 molecules, the vast majority of the Ndc80 molecules are in jack-knifed (unattached) conformation, (II) after kinetochores unload $\sim 95\%$ of the Mad2 molecules, a multitude of Ndc80 molecules switch from jack-knifed to straight conformation, and (III) as Mad2 molecules are further unloaded, i.e. beyond $\sim 95\%$, further Ndc80 molecules transition from jack-knifed to straight conformation in a trend co-linear with Mad2 loss from the kinetochore (see subsection 4.2.5 and Figure 4.8).

These data lead to several important conclusions on how the Ndc80 complex conformational and alignment changes relate with SAC signaling. 1) We can conclude that Ndc80 conformation and alignment indeed correlates with Mad2 signaling. 2) Based on the evidence that a multitude of Ndc80 molecules switch from jack-knifed to straight conformation only when $\sim 95\%$ of Mad2 is unloaded, we can conclude that the Ndc80 conformational change is likely not the trigger for SAC silencing. This further suggests our previous speculation to be incorrect. 3) Ndc80 not only correlates with SAC but displays distinct behaviours as Mad2 is unloaded from kinetochores. Therefore, the mechanisms that govern Ndc80 conformational changes may be influenced by SAC activity. Next, I will discuss each of the three distinct behaviours of Ndc80 ((I) to (III) above), what mechanisms may govern them and what are their potential roles.

I) Let us first look at the state of Ndc80 prior to $\sim 95\%$ Mad2 being unloaded. Here, we observed that the CenpC-to-Ndc80(N) distances to be below 50 nm. We previously observed that the CenpC-to-Ndc80(N) distance is 55 nm at unattached kinetochores (120 min nocodazole treatment) and 81 nm at attached metaphase kinetochores (DMSO). Therefore, prior to $\sim 95\%$ Mad2 un-loading most of the Ndc80 molecules are in "unattached" conformation, i.e. Ndc80 is jack-knifed and unaligned. One hypothesis here would be that kinetochores that have not yet unloaded $\sim 95\%$ of Mad2 are unattached or sub-maximally attached and thus have most of

the Ndc80 molecules in "un-attached" conformation. In agreement, previous studies have shown that Mad2 intensity is inversely proportional to kinetochore-microtubule attachment and is diminished after $\sim 30\%$ kinetochore-microtubule occupancy is reached (Etemad et al., 2019). To further background this hypothesis, let us estimate what would be the average number of Ndc80 molecules bound to microtubules at 30% microtubule occupancy. At maximum occupancy, kinetochores bind a ~ 20 microtubules via 240 Ndc80 molecules (Suzuki et al., 2015). Consequently, 30% kinetochore-microtubule occupancy would correspond to ~ 6 microtubules bound by ~ 72 Ndc80 molecules. Therefore, prior to $\sim 95\%$ unloading of Mad2 we can estimate maximum of 72 Ndc80 complexes to be bound to microtubules and a minimum of 168 Ndc80 complexes to be unbound (see Figure 6.2 A and B). This is consistent with our observation that prior to $\sim 95\%$ Mad2 unloading the majority of Ndc80 molecules are jack-knifed and unaligned, and thus are in unattached state.

Here, we also observed variability in the CenpC-to-Ndc80(N) distance from 26.9 ± 10.2 to 49.4 ± 6.7 nm. That raised the question of as to whether the variability is due to kinetochores binding microtubules anywhere in the range of 0 to 6. However, we did not observe the variability here to be correlated with Mad2 signal. Therefore, the variability may be due to error in our measurements as the confidence intervals of the measurements are ~ 10 nm. Measurements with tighter confidence intervals will be needed to determine how the number of jack-knifed Ndc80 molecules and their alignment varies at kinetochores below 30% microtubule occupancy.

Therefore, from Ndc80 behaviour (I) we can conclude that the majority of Ndc80 molecules are jack-knifed and not bound to microtubules until $\sim 95\%$ of Mad2 is unloaded and the SAC is silenced (see Figure 6.2 A and B).

II) Loss of $\sim 95\%$ of the Mad2 molecules from the kinetochore and SAC silencing correlate with a distinct Ndc80 switch where multitude of Ndc80 molecules transition from jack-knifed to straight conformation. Importantly, a detectable proportion of Ndc80 complex molecules switch conformation only when almost all Mad2 is unloaded from kinetochores and thus does not trigger the loss of Mad2. That further poses the question of as to whether SAC silencing alone triggers the Ndc80 transition from jack-knifed to straight conformation? We observed that SAC activity is not required for Ndc80 jack-knife maintenance in absence of microtubules (120 min nocodazole and Reversine treatment). Therefore, SAC silencing alone is insufficient

to trigger change in Ndc80 conformation.

Indeed, we showed previously that Ndc80 transition from jack-knifed to straight conformation relates to microtubule binding. Therefore, the switch in conformation at multitude of Ndc80 molecules may reflect a situation where SAC silencing causes more Ndc80 molecules to be microtubule-bound. Sudden increase in the number of microtubule-bound Ndc80 molecules can be achieved in two ways (1) rapid accumulation of microtubules at the kinetochore and (2) sudden increase in the number of Ndc80 molecules bound to a single microtubule. The key prediction of model (1) is that the kinetochore will rapidly accumulate microtubule attachments once the SAC is silenced. However, the binding of microtubules to the kinetochore is currently viewed as a gradual process based on EM evidence (Auckland et al., 2017). Therefore, rapid microtubule accumulation at kinetochores is likely not the trigger of switch in the conformation of multitude of Ndc80 molecules.

That makes model (1) unlikely and poses the question of how can SAC silencing lead to more Ndc80 molecules being bound to a single microtubule (model (2))? A key regulator of the Ndc80 complex behaviour in mitosis is the Aurora B kinase. Aurora B is active at unattached kinetochores and is essential for SAC activation. The Aurora B targets are further dephosphorylated by the phosphatases responsible for SAC silencing (DeLuca et al., 2011; Liu et al., 2010). Therefore, when the SAC is silenced the Aurora B targets will be dephosphorylated. Can de-phosphorylation of the Aurora B sites in Ndc80 cause multitude of Ndc80 molecules to bind to a microtubule and switch conformation? The Ndc80 complex is phosphorylated by Aurora B at nine sites in the N-terminal tail of the Ndc80 protein (DeLuca et al., 2011). Phosphorylation of the Ndc80 tail by Aurora B has been shown to decrease the affinity of Ndc80 to microtubules and to prevent clustering of the Ndc80 molecules (Umbreit et al., 2012; Jankzyk et al., 2017). Therefore, dephosphorylation of the Ndc80 N-terminal tail causes increased affinity of Ndc80 for microtubules and could lead to more Ndc80 molecules being bound to the microtubule. In addition, dephosphorylation of Ndc80 may induce clustering of Ndc80 molecules that would further induce more Ndc80 molecules to be bound to the microtubule. Therefore, dephosphorylation of the Ndc80 molecules may lead to rapid increase in the number of microtubule-bound Ndc80 molecules. That model would explain the rapid switch in conformation of a multitude of Ndc80 molecules. However, the model requires

further testing. Is Aurora B phosphorylation diminished rapidly when the SAC is silenced? We can answer this question by monitoring the levels of Aurora B target phosphorylation relative to Mad2 signal. If the above model is correct, we will observe a rapid decrease in Aurora B target phosphorylation as $\sim 95\%$ of Mad2 is unloaded from kinetochores.

Another question that the above model raises is whether SAC silencing is required for the rapid switch in conformation of multitude of Ndc80 molecules. We can investigate this question by artificially targeting Mps1 to kinetochores and thus not allowing for SAC silencing at attached kinetochores. If the model is correct the SAC activity will prevent rapid switch of the molecules and at most will allow only for gradual transition of Ndc80 molecules from jack-knifed to straight conformation.

A further endeavour will also be required to relate the Ndc80 behaviours we observe to other events in mitosis. For example: what are the local stimuli that the kinetochore experiences in terms of force and microtubule attachment? What is the kinetochore congression status, i.e. the kinetochore position in the spindle? Do cellular-level events affect the faith of the single kinetochore: for example, does the kinetochore transition to straight, highly aligned Ndc80 molecules state faster if the rest of the kinetochores are already aligned in the metaphase plate and mature? Such analysis will suggest the spatial and chemical clues that the kinetochore is experiencing when the Ndc80 molecules change their behaviour. Such notions are important to understand what may be the potential roles of that distinct Ndc80 behaviour in relation to Mad2 loss. One hypothesis is that the Mad2 threshold prevents stabilisation of incorrect attachments indirectly by preventing Aurora B target dephosphorylation. If this is the case Ndc80 molecules not susceptible to Aurora B phosphorylation (Ndc80 9A mutant, DeLuca et al., 2011) would lead to increase in kinetochore erroneous attachments. Therefore, such function can be tested by expressing Ndc80 9A mutant in cells and quantifying the number of formed syntelic attachments.

In summary, here we suggested that the observed switch of conformation in a multitude of Ndc80 molecules at SAC silencing may be mediated by Aurora B target dephosphorylation and likely occurs at $\sim 30\text{-}50\%$ kinetochore occupancy, and propose experiments for further testing of this hypothesis.

III) The next pending question is how do the remaining jack-knifed Ndc80 molecules at this sub-maximally attached kinetochore then transition to straight conformation at metaphase kinetochores? Kinetochores that have unloaded the majority of the Mad2 molecules have been suggested to further "mature" where they progressively bind microtubules to 100% kinetochore microtubule occupancy, unload the remaining of Mad2, and load Ska to stabilise the attachment (Auckland et al., 2017). Here, we observe gradual increase in Ndc80 molecules in straight conformation which may be due to gradual binding of microtubules to the kinetochore. That begs the question of as to whether the Ndc80 switch event gates maturation of the kinetochore-microtubule attachment. For example, Ndc80 conformational changes could gate the kinetochore loading of Ska. Previously, Ndc80 lacking the loop that allows for its flexibility in conformation has been shown to be unable to load Ska to kinetochores (Zhang et al., 2012). Therefore, Ska binding to Ndc80 may be dependent on Ndc80 being in straight microtubule-bound conformation. Further, Ska kinetochore loading has been shown to be inhibited by Aurora B phosphorylation of Ndc80 (Wimbish et al., 2020). Finally, Ska kinetochore loading has been suggested to be dependent on Ndc80 clustering based on *in vitro* evidence (Jankzyk et al., 2017). Therefore, one hypothesis is that the switch of the majority of Ndc80 molecules from jack-knifed to straight conformation allows Ndc80 to bind Ska, which then further stabilises the attachment. We plan to next test that model by monitoring Ska kinetochore loading and the CenpC-to-Ndc80(N) distance simultaneously. We plan to further test as to whether SAC silencing gates the Ska loading by monitoring the Ska intensity in relation to Mad2 kinetochore intensity. Such analysis may reveal the long hypothesised process of kinetochore attachment maturation process.

Nevertheless, a big open question remains: what triggers the switch of SAC silencing? The SAC master activator kinase Mps1 is targeted to kinetochores via Ndc80(N) (Stucke, Baumann and Nigg, 2004). Further, Ndc80(N) competitively binds Mps1 and microtubules (Gui et al., 2020). Therefore, one hypothesis here is that the binding of the first 7-10 microtubules leads to displacement of Mps1 from the Ndc80(N) and thus tips the balance of the kinase-phosphatase cross talk towards SAC silencing. Also, binding of a single microtubule has been shown to allow for dynein stripping of the RZZ complex from the kinetochore and Mad2 unloading. Therefore, the initiation of SAC inactivation at 30% microtubule occupancy

can be due to dynein stripping at the kinetochore. A further event that may be contributing to increase in phosphatase activity at the kinetochore, and thus SAC silencing, is the inward movement of the Knl1 N-terminus (see subsection 4.2.2). The Knl1 N-terminus binds to the PP1 phosphatase (Bajaj et al., 2018, Liu et al., 2010; Rosenberg et al., 2011). We showed that the Knl1 N-terminus is positioned ~ 65 nm inward at mature kinetochores as compared to unattached kinetochores, and responds specifically to K-K tension. Therefore, spatial re-positioning of PP1 closer to the Knl1 MELT motifs and SAC substrates when kinetochores bi-orient and come under tension may also facilitate the silencing of the SAC. However, the contributions of PP1 re-positioning and Mps1 displacement need further investigation.

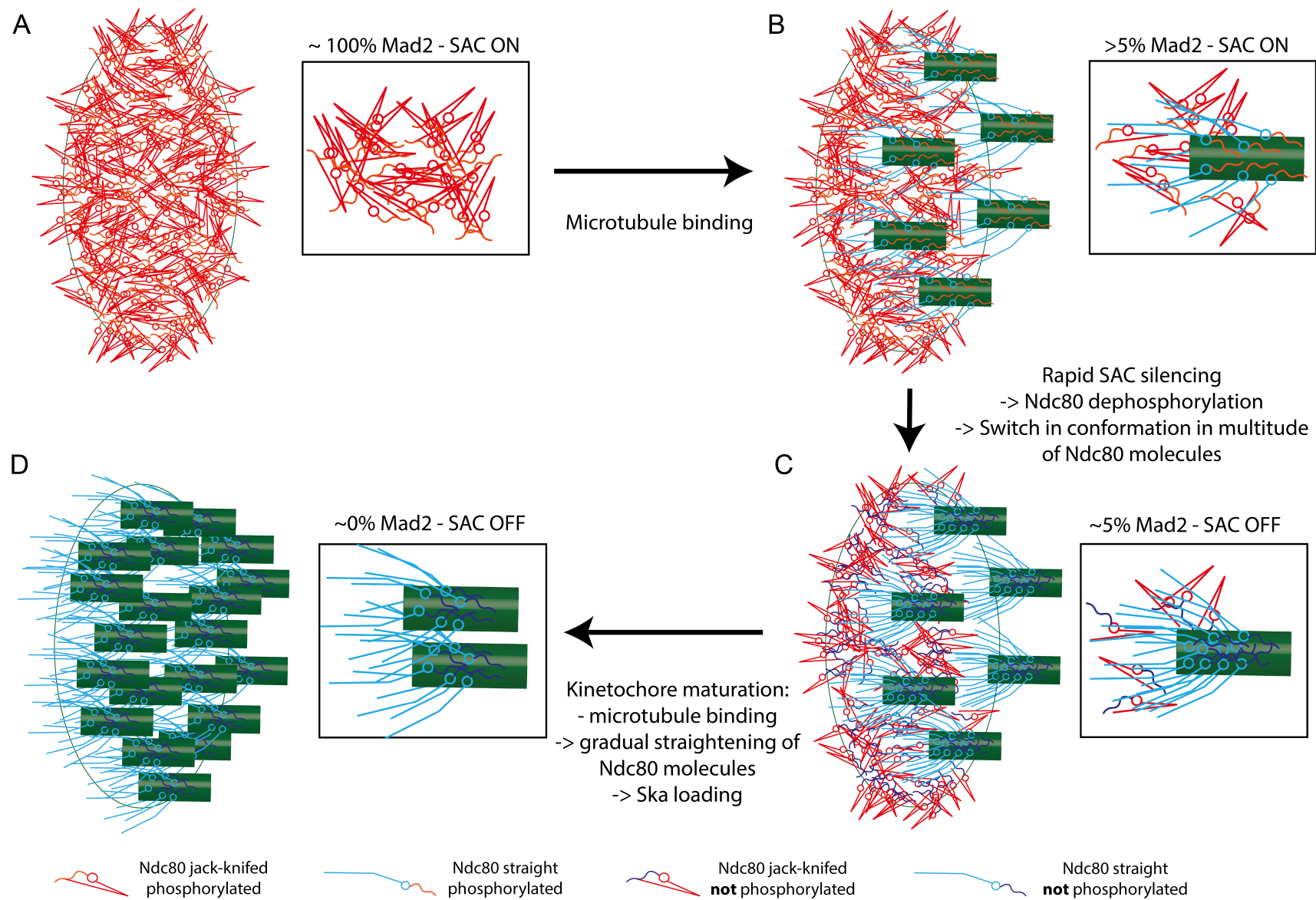


Figure 6.2: Schematic representing the distinct Ndc80 architecture changes as Mad2 is unloaded, and how they may integrate overall in the kinetochore bi-orientation and maturation processes A) At the beginning of prometaphase kinetochores are unattached and load high amount of Mad1:Mad2. The high amounts of Mad1:Mad2 maintain the SAC active until the kinetochore bi-orientates. In the unattached kinetochore, Ndc80 is not bound to microtubules and thus is unaligned and in jack-knifed conformation. Ndc80 is also phosphorylated by Aurora B in this condition. B) As the mitotic spindle forms, kinetochores bind microtubules, and progressively unload the Mad1:Mad2 complex. As the kinetochore binds microtubules, few of the Ndc80 complex molecules attach to the microtubules with low affinity. High affinity binding of Ndc80 to microtubules is prevented here by the phosphorylation of Ndc80 by Aurora B. C) When kinetochores reach ~30-50% microtubule occupancy, the kinetochores have unloaded ~95% of the Mad2 molecules and the SAC is rapidly silenced by phosphatase activity. The high phosphatase activity at the kinetochore also leads to dephosphorylation of Ndc80. The Ndc80 molecules now have high microtubule affinity and can cluster on the microtubule. Consequently, multitude of the Ndc80 complexes rapidly bind to the available microtubules and saturate the binding sites. The Ndc80 molecules for which there are no available binding sites remain jack-knifed. The clustered and "straightened" Ndc80 molecules also bind to Ska which increases the kinetochore-microtubule attachment stability. D) Kinetochores bind more microtubules until they reach ~100% microtubule occupancy and mature. In this process, the Ndc80 molecules straighten as microtubule binding sites become available and also some of the already bound Ndc80 molecules transfer to a nearby microtubule that is less crowded. Further, as the kinetochore binds microtubules and the Ndc80 molecules straighten, the remaining Mad2 is unloaded and Ska accumulates at the kinetochore. When the kinetochores reaches ~100% occupancy and the maturation process is complete, the kinetochore is ready for anaphase. When all kinetochores are ready, anaphase is initiated.

6.3 Ska Architecture at human kinetochores and its implications in Ska kinetochore recruitment mechanisms

The Ska complex is essential for maintenance of stable kinetochore-microtubule attachment and is recruited to kinetochores via the Ndc80 complex (Auckland et al.,

2017; Zhang et al., 2012). Further, microtubule binding, Ska phosphorylation, and potential Ndc80 clustering have been implicated as factors that gate Ska recruitment to kinetochores (Jeyaparakash et al., 2012; Zhang et al., 2017; Huis In't Veld et al., 2019; Jankzyk et al., 2017). However, the following open questions remain: what is the *in vivo* architecture of Ska, how these factors contribute to Ska loading, and what are the mechanisms responsible for Ska loading? To begin to tackle those questions we mapped the 3D average Ska geometry in metaphase cells by three-fluorophore Δ EC measurements (Δ EC) (see subsections 5.2.1 and 5.2.4). We created endogenous label Ska1 cell lines and utilised these cell lines and antibody staining to obtain the first mapping of the Ska complex 3D geometry at kinetochores. Our results showed that at metaphase kinetochores Ska is positioned close to the Ndc80(N) terminus in linear mapping. Further, we observed the core Ska complex (visualised by fluorescent tag Ska1(N)) to be on offset from the Mis12-Ndc80 complex axis. This result suggests that the core Ska is flexibly positioned around Ndc80 at metaphase kinetochores, and thus may provide a flexible linker between Ndc80 and microtubules. Such model has been previously proposed based on four pieces of evidence: (1) Ska lacking the Ska3 C-terminus cannot localise to kinetochores (Jeyaparakash et al., 2012) (2) mass spectrometry suggested that phosphorylation of the Ska3 C-terminus by Cdk1 leads to its unravelling into long unstructured conformation (Huis In't Veld et al., 2019), (3) Ska3 C-terminus phosphorylation by Cdk1 was shown to be essential for stable Ndc80:Ska complex assembly formation *in vitro* and for Ska kinetochore localisation *in vivo*, and (4) phosphorylated Ska was shown to have flexible positioning around Ndc80 via *in vitro* electron microscopy (Huis In't Veld et al., 2019). Therefore, the combination of our evidence and prior evidence suggest that at least at metaphase kinetochores Ska is flexibly linked to Ndc80 by the flexible and unravelled phosphorylated Ska3 C-terminus.

However, another set of evidence on Ska position *in vitro* suggest that more than one Ska architecture state may exist. *In vitro* evidence have shown that unphosphorylated Ska can also bind Ndc80 *in vitro* (Helgeson et al., 2018; Jankzyk et al., 2017; Schmidt et al., 2012). These *in vitro* studies demonstrated that unphosphorylated Ska complex confers depolymerising microtubule tip tracking ability to Ndc80 'Bonsai', increases the rupture force of the binding of full length Ndc80 complex to microtubules, and becomes enriched on microtubules if Ndc80 'Bonsai' is present.

Further, Ndc80 has been shown to orient unphosphorylated Ska on microtubules *in vitro*: in absence of Ndc80 Ska bound to microtubules with the core W-shaped complex erected perpendicular to the microtubule lattice (Jankzyk et al., 2017; see Figure 6.3). In presence of Ndc80, the Ska complex again bound to microtubules in the same manner but the height of the W-shaped core Ska was decreased. Further, this orientation of Ska was shown to be dependent on Ndc80 clustering *in vitro*, and Ska kinetochore localisation was suggested to dependent on Ndc80 clustering *in vivo*. These data suggest that another architectural state of Ska exists at least *in vitro*. How the two Ska architectures may interplay in mitosis?

One possibility is that Ndc80 orientating unphosphorylated Ska on microtubules is proto Ndc80:Ska assembly state which then is stabilised by Cdk1 phosphorylation to provide the functional form of Ska. This idea can further be exemplified in the following putative model (see Figure 6.3): When unbound to kinetochores Ska is in unphosphorylated compact conformation where the Ska3 C-terminus is folded into a globular domain. Such compact conformation of Ska prior to Ndc80 binding may be beneficial in the crowded mitotic spindle environment. The unphosphorylated Ska then encounters Ndc80 and transiently binds to it. In the transient Ndc80:Ska assembly, the Ndc80 complex orients Ska on the microtubule axis. Such orientation possibly positions the Ska3 C-termini such that the Ska-Ndc80 binding sites are in close proximity. Next, the Ndc80-Ska assembly is stabilised by Cdk1 phosphorylation. The phosphorylation of Ska can be imagined to require the transient binding of Ndc80:Ska to be sustained for long enough for Ska3 phosphorylation to take place. Two factors could increasing the duration of the transient assembly here: (1) Ndc80 clustering may provide more interaction sites for Ska. Ndc80 clustering facilitating Ska recruitment in this manner would explain the requirement of Ndc80 clustering for Ska kinetochore localisation. (2) Ska microtubule binding may prevent Ska from floating off and thus also increase the lifetime of the transient Ndc80:Ska assembly. That would explain why Ska that cannot bind to microtubules has highly reduced kinetochore localisation (Jeyaprakash et al., 2012; Auckland et al., 2017). Therefore, Ska microtubule binding and Ndc80 clustering may contribute to Ska kinetochore localisation by increasing the half-life of the transient Ndc80:Ska assembly, and thus allowing for Ska phosphorylation by Cdk1 before Ska detachment. When Ska is phosphorylated by Cdk1, the Ndc80:Ska assembly is be now stable, the

Ska3 C-termini unravel and lead to flexible positioning of Ska.

This model could explain the conflicting in first sight evidence in the field. However, an alternative hypothesis is that the Ska3 C-terminus is disordered in unphosphorylated Ska and becomes extended upon Ska phosphorylation. In such case, Ska orientation on microtubules by Ndc80 would be harder to explain (Jankzyk et al., 2017). However, this phenomenon has been observed only *in vitro*. In any case, the model requires further experimental testing. To do so, we plan to map the organisation of Ska at prometaphase kinetochores by ΔEC measurements. If the above model is correct, immature kinetochores will contain a mixture of (1) phosphorylated Ska flexibly positioned around Ndc80 and (2) unphosphorylated Ska oriented on the microtubule by Ndc80. We could un-mix the characterised here phosphorylated Ska state from the population by the kinetochore state un-mixing algorithm, and test as to whether a second state is present. That would further show as to whether the proposed second architecture of Ska occurs *in vivo*. Such analysis would greatly benefit of detection of the most C-terminus of Ska3 which would provide more direct evidence for Ska intra-molecular rearrangements. Therefore, next we plan to test commercial antibodies against the most C-terminal region of Ska3 and potentially homemade nanobodies against that region. If successful, we plan to investigate as to whether the most C-terminus of Ska3 changes its relative position with respect to the the core Ska complex using the un-mixing algorithm as described above. If our idea is correct, we will potentially observe the core Ska and the Ska3(C) to be closely positioned at immature kinetochores and to be far apart at mature kinetochores. Nevertheless, such analysis would only reveal snapshots of Ska kinetochore architecture in congression and metaphase. In contrast, Ska recruitment is suggested to be a dynamic process where Ska is loaded to kinetochores as they kinetochores congress (Auckland et al., 2017). An important next step would be to understand the dynamics of this process and whether these dynamics are important for kinetochore maturation. To allow for live-cell studies of Ska dynamics we generated endogenous labeled Ska cell lines (see subsection 5.2.2). The next step is to utilize these cell lines and Lattice Light Sheet live-cell imaging to study the dynamics of Ska binding and unbinding from kinetochores. We will follow Ska kinetochore recruitment as kinetochores congress and as the cell enters metaphase and anaphase. From this we anticipate deducing the proposed cross-talk between Ska loading and SAC silencing.

In addition, previous *in vivo* data showed that the Ska complex acts to prevent force-dependent detachments at the P (poleward moving) kinetochore (Auckland et al., 2017). That raised the question of as to whether Ska accumulation is biased between P and AP kinetochores. Lattice imaging should reveal whether Ska does predominantly associate with the P (or AP) kinetochore in living cells. Such analysis would be invaluable for broader investigations into how recruitment of Ska may be gated, and how Ska provides kinetochore-microtubule attachment stabilisation.

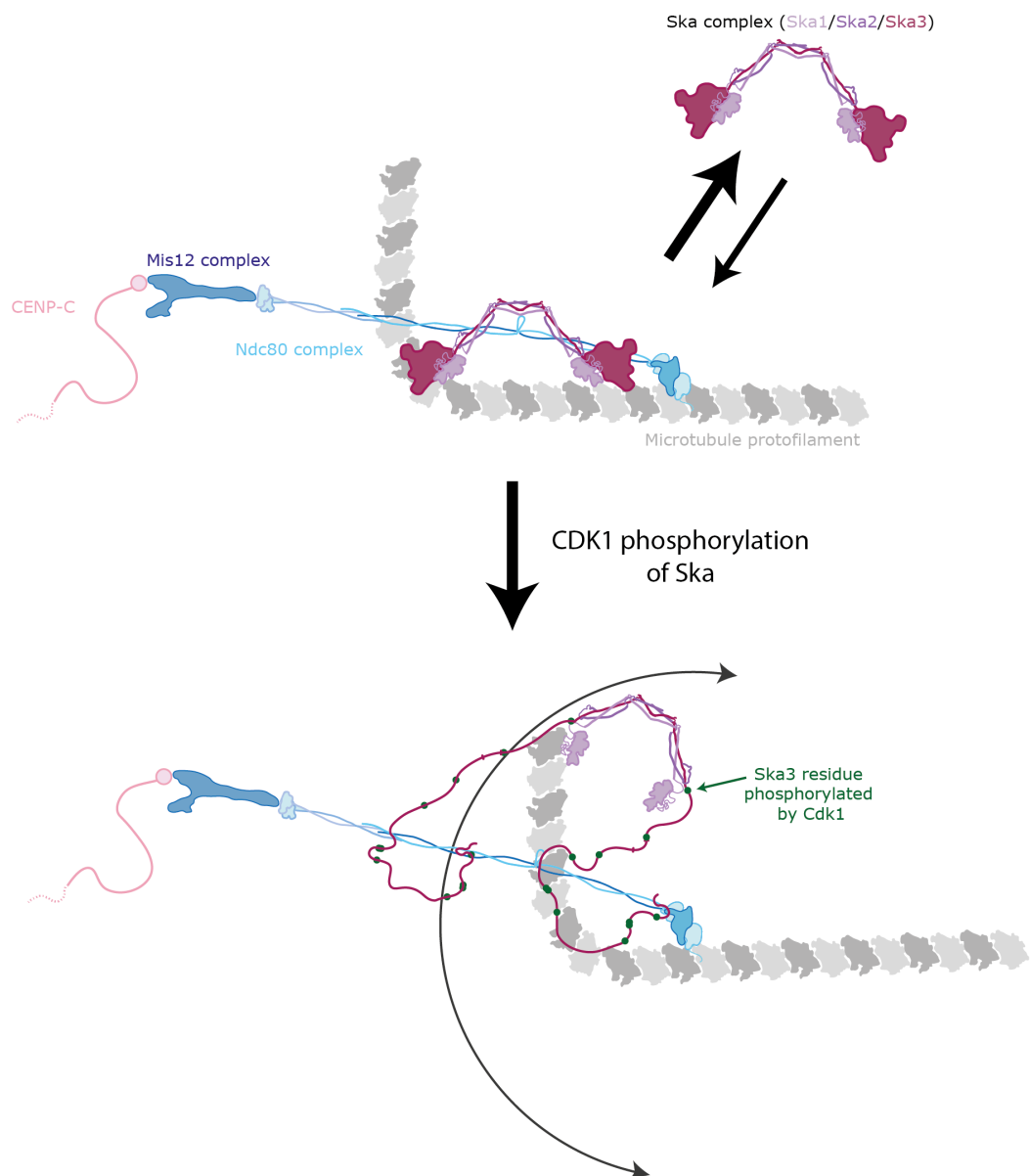


Figure 6.3: Schematic showing a putative model for Ska architectural changes in the process of Ska kinetochore recruitment Top: Cytosolic Ska is unphosphorylated and the Ska3 C-terminus is folded into a globular shaped domain. When Ska encounters Ndc80, the Ndc80 orients Ska on the microtubule (Jankzyk et al., 2017). That orientation further brings the Ska3 C-termini close to Ndc80 such that more Ndc80 and Ska3 bindings sites overlap. This Ndc80:Ska interaction is transient and thus prone to disassembly. Bottom: The Ska3 C-terminus is then phosphorylated by Cdk1. The phosphorylation stabilises the Ndc80:Ska assembly and leads to the unravelling of the long Ska3 C-terminus into unstructured conformation. The long flexible Ska3 C-terminus now provides a flexible link between the rest of the Ska molecule (the Core Ska and the Ska1 microtubule-binding domains) and Ndc80. This flexible link would allow for Ska to position flexibly around Ndc80 as supported by our *in vivo* data and *in vitro* data by Huis In't Veld and colleagues (2019).

Appendix A

Supplemental Figures

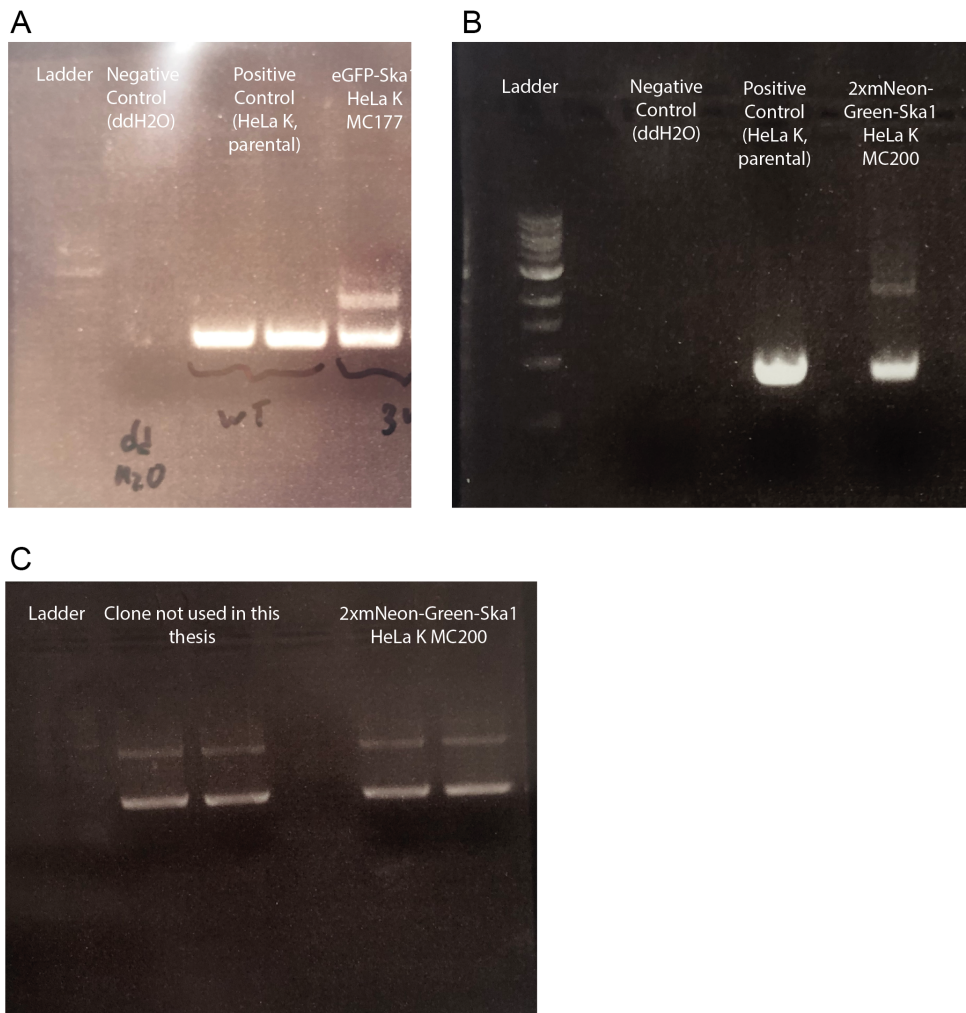


Figure A.1: PCR products of Ska1 N-terminal region amplification in MC177 and MC200 cell lines. The 5' region of the *SKA1* gene was amplified via PCR from MC200 and MC177 cell line genomic DNA. In parallel, the same PCR reaction was set up with double distilled water instead of DNA ("Negative Control"), and with genomic DNA from the parental plain HeLa K cell line ("Positive Control"). The PCR products were run on 1% Agarose Gel. 1 kB Ladder is used for band molecular weight estimation.

A) Products of the PCR amplification of the genomic DNA extracted from eGFP-Ska1 HeLa K MC177 cell line (column on the right), and the described controls. B) Products of the PCR amplification of the genomic DNA extracted from 2xmNeonGreen-Ska1 HeLa K MC200 cell line (column on the right), and the described controls. C) Repeat of the PCR amplification and agarose gel run done in B). The image is included as the bands are better resolved here.

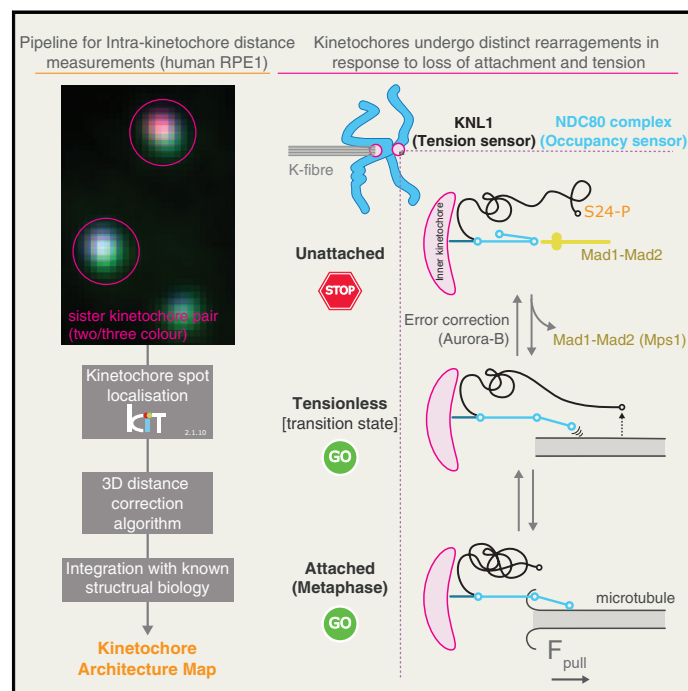
Appendix B

Manuscripts

B.1 Ensemble-Level Organization of Human Kinetochores and Evidence for Distinct Tension and Attachment Sensors

Ensemble-Level Organization of Human Kinetochores and Evidence for Distinct Tension and Attachment Sensors

Graphical Abstract



Authors

Emanuele Roscioli,
Tsvetelina E. Germanova,
Christopher A. Smith, ...,
Amelia I. Thompson, Nigel J. Burroughs,
Andrew D. McAinsh

Correspondence

n.j.burroughs@warwick.ac.uk (N.J.B.),
a.d.mcaish@warwick.ac.uk (A.D.M.)

In Brief

Roscioli et al. use subpixel imaging and computational methods to determine the ensemble-level 3D organization of the human kinetochore. They show how kinetochores undergo distinct rearrangements in response to the loss of attachment and tension.

Highlights

- 3D mapping of kinetochore architecture in human RPE1 cells
- Outer kinetochore (NDC80, Mad1, and RZZ) has high nematic order
- NDC80 jackknives and KNL1 unravels upon loss of attachment and tension, respectively
- Recruitment of Mad2 is only coupled to the occupancy sensor (NDC80)



Roscioli et al., 2020, Cell Reports 31, 107535
April 28, 2020 © 2020 The Author(s).
<https://doi.org/10.1016/j.celrep.2020.107535>



Article

Ensemble-Level Organization of Human Kinetochores and Evidence for Distinct Tension and Attachment Sensors

Emanuele Roscioli,^{1,2} Tsvetelina E. Germanova,^{1,2} Christopher A. Smith,^{1,2,4} Peter A. Embacher,^{1,3} Muriel Erent,^{1,2} Amelia I. Thompson,^{1,2} Nigel J. Burroughs,^{1,3,*} and Andrew D. McAinsh^{1,2,5,*}

¹Centre for Mechanochemical Cell Biology, University of Warwick, Coventry, UK

²Division of Biomedical Sciences, Warwick Medical School, University of Warwick, Coventry, UK

³Mathematics Institute, University of Warwick, Coventry, UK

⁴Present address: Metabolic Research Laboratories and MRC Metabolic Diseases Unit, Institute of Metabolic Science, Addenbrooke's Hospital, Cambridge, UK

⁵Lead Contact

*Correspondence: n.j.burroughs@warwick.ac.uk (N.J.B.), a.d.mcainsh@warwick.ac.uk (A.D.M.)

<https://doi.org/10.1016/j.celrep.2020.107535>

SUMMARY

Kinetochores are multi-protein machines that form dynamic attachments to microtubules and control chromosome segregation. High fidelity is ensured because kinetochores can monitor attachment status and tension, using this information to activate checkpoints and error-correction mechanisms. To explore how kinetochores achieve this, we used two- and three-color subpixel fluorescence localization to define how proteins from six major complexes (CCAN, MIS12, NDC80, KNL1, RZZ, and SKA) and the checkpoint proteins Bub1, Mad1, and Mad2 are organized in the human kinetochore. This reveals how the outer kinetochore has a high nematic order and is largely invariant to the loss of attachment or tension, except for two mechanical sensors. First, Knl1 unravels to relay tension, and second, NDC80 undergoes jackknifing and loss of nematic order under microtubule detachment, with only the latter wired up to the checkpoint signaling system. This provides insight into how kinetochores integrate mechanical signals to promote error-free chromosome segregation.

INTRODUCTION

Human kinetochores are multi-megadalton-sized protein machines that assemble on the centromeres of every sister chromatid and provide an attachment site for the tips of ~20 dynamic spindle microtubules (the kinetochore [K]-fiber). Kinetochores must coordinate microtubule dynamics within the K-fiber and maintain attachment during phases of growth and shrinkage, thus coupling the energy release from microtubule depolymerization to do work (Auckland and McAinsh, 2015; Rago and Cheeseman, 2013). These kinetochore-microtubule attachments are essential for the accurate segregation of chromosomes in all eukaryotes. However, there is limited understanding of how this machinery adapts to changes in microtubule occupancy and/or the imposition of pushing and pulling forces. These are important questions because a substantial body of work indicates that kinetochores must be able to sense changes in tension and occupancy (Long et al., 2019), sensors that underpin decision making and error correction of the kinetochore.

Classic biophysical experiments established how applying tension to a kinetochore stabilized the attachment to microtubules (Nicklas and Koch, 1969) and that this was coupled to changes in the chemical (phosphorylation) state of the kinetochore (Nicklas et al., 1995). Live cell imaging experiments further show that tension between sister kinetochores (as measured by

changes in inter-kinetochore [K-K] distance) can explain the oscillatory movements of bi-oriented kinetochores, being a determinant of directional switching (Burroughs et al., 2015; Wan et al., 2012). Changes in the K-K distance were also implicated in error-correction processes that destabilize improper kinetochore attachments and stabilize bi-orientation (Lampson and Cheeseman, 2011; Tanaka et al., 2005). Recent work has, however, shown that low K-K tension kinetochores do not necessarily trigger error correction (Dudka et al., 2018). Furthermore, the imposition of K-K tension does not appear to be required for silencing of the spindle assembly checkpoint (SAC). By correlating the number of kinetochore-bound microtubules with checkpoint protein recruitment, it appears that the crucial transition to SAC silencing occurs at approximately half-maximal occupancy (Dudka et al., 2018; Etemad et al., 2015, 2019; Kuhn and Dumont, 2017). Kinetochores thus appear to be able to “count” the number of bound microtubules.

Intra-kinetochore tension may generate key mechanical signals that are sensitive to changes in microtubule attachment and/or the imposition of force (for review, see Maresca and Salmon, 2010). Intra-kinetochore tension refers to the measurement of changes in distance between two components of the kinetochore labeled with different fluorophores (denoted by Δ). Initial pioneering experiments showed that increased Δ and not the K-K tension correlates with SAC silencing (Maresca and Salmon, 2009; Uchida et al.,





2009; Wan et al., 2009). However, there is also evidence that high Δ is not always necessary for SAC silencing (Etemad et al., 2015; Magidson et al., 2016; Tauchman et al., 2015). It thus remains uncertain how the kinetochore monitors change in occupancy and whether it can sense changes in tension at all. One idea is that there are kinetochore conformations or tensile elements that would function as tension and/or attachment sensors.

While X-ray crystallography and electron microscopy are beginning to provide a structural view of the kinetochore (Hamilton et al., 2019; Pesenti et al., 2016; Welburn and Cheeseman, 2008), this approach is limited to subsets of kinetochore components and does not allow the impact of microtubule binding and forces to be easily determined. Furthermore, these approaches are limited to single assemblies, while the human kinetochore in a living cell incorporates multiple microtubule attachment sites (~20) populated with multiple copies of each kinetochore complex (Huis In 't Veld et al., 2016; Johnston et al., 2010; Suzuki et al., 2011). Thus, the *in vivo* higher-order, ensemble-level organization of the human kinetochore remains out of reach.

RESULTS

Measurement of 3D Euclidian Distances between Kinetochore Proteins

To obtain insight into the 3-dimensional (3D) nanoscale architecture of the human kinetochore, we deployed an image acquisition and computational pipeline that outputs the 3D Euclidian distances (Δ_{3D}) between differentially labeled kinetochore proteins in near-diploid hTERT-RPE1 cells (referred to hereafter as RPE1; Smith et al., 2016). One limitation of this approach is the overestimation of mean distances (Suzuki et al., 2018). This is because Euclidian distances cannot be negative leading to a positive bias in the Δ_{3D} distribution; in other words, distances are overestimated (Figure 1A; Table S1; Methods S1). To correct for this bias, we developed an algorithm to infer the true Euclidian distance (Δ_{EC}) between two fluorophores. This algorithm goes beyond previous methods (Churchman et al., 2005; Suzuki et al., 2018) by taking into account the anisotropic point spread function in 3D datasets (see Methods S1 for details). To test the accuracy of this method, we fixed cells and stained them with an anti-CenpC antibody that recognizes the amino-terminal region of the protein (amino acids [aa] 1–426), binding to a site preceding the region binding CenpA nucleosomes. This primary antibody was then detected using a mixture of 3 different secondary antibodies (conjugated to Alexa Fluor 488, 568, and 647; Figure 1A). The Euclidean bias-corrected delta distances were 2.2 ± 1.5 nm (mean \pm standard deviation; $n = 2,302$; Alexa Fluor 488–568), 4.3 ± 2.7 nm ($n = 1,437$; Alexa Fluor 488–647), and 4.5 ± 2.8 nm ($n = 1,452$; Alexa Fluor 568–647), considerably smaller than the corresponding Δ_{3D} (Figure 1A; Table S1).

These data confirm that we can measure the 3D nanoscale distances between 3 different fluorophores within the human kinetochore with an accuracy on the scale of 2–4 nm. As a second test, the amino-terminal end of the Ndc80 subunit (of the NDC80 complex) was marked with the 9G3 monoclonal antibody that recognizes the N-terminal globular domain of Hec1 (aa 200–215; DeLuca et al., 2006; hereafter referred to as Ndc80(N)) and the carboxy-terminal end was marked with EGFP (Ndc80(C); Figures

1B and 1C). To label the Ndc80 C-terminal end, we inserted EGFP at the endogenous locus by CRISPR-Cas9 gene editing in RPE1 cells (cell line MC191; see Methods S1 and Figure S2 for details). The Δ_{EC} distance from Ndc80(C) to Ndc80(N) was 48.7 ± 1.2 nm ($n = 726$; Figure 1D; Table S1). Because there is substantial structural information describing the NDC80 complex *in vitro*, it has been used as a “molecular ruler” to validate 2 color fluorescence localization methods (Suzuki et al., 2018). Our Δ_{EC} measurements are close to the 51 nm distance estimated using negative stain electron microscopy (EM) (Huis In 't Veld et al., 2016; Wei et al., 2005; Figure 1B). As expected, the Δ_{3D} measurement is an overestimate (59.50 ± 20.52 nm, $n = 693$; Figure 1D; Table S1), while the Δ_{1D} is typically an underestimate (33.37 ± 14.48 nm, $n = 283$; Figure S1A; Table S1; Smith et al., 2016). We next measured the Δ_{EC} distance between the MIS12 complex subunit Nnf1 and Ndc80(N) (Figures 1B and 1C) and obtained a value of 66.4 ± 1.5 nm ($n = 724$; Figure 1D; Table S1). This is similar to the distance measured in parental cells that did not have EGFP knocked in to the *NDC80* locus (Δ_{EC} , 61.5 ± 0.8 nm, $n = 1,748$; Figure S1D; Table S1). Again, these distances are very close to the predicted distance (~65 nm) that can be estimated from EM studies (Petrovic et al., 2010; Screpanti et al., 2011). Finally, as expected from *in vitro* reconstitution experiments (Helgeson et al., 2018; Huis In 't Veld et al., 2019) the SKA complex (Ska3) was located proximal to the Ndc80 amino terminus (Table S1). Overall, these data confirm the accuracy of our method and the importance of correcting intra-kinetochore distance measurements.

The Inner Kinetochore Is Offset from the Outer Kinetochore

Concurrent with measuring the distance between Ndc80(C), Ndc80(N), and Nnf1, we also determined an inner kinetochore position using the CenpC antibody used in Figure 1A. We measured the distances from the amino- and carboxy-ends of Ndc80 to CenpC in a 3-fluorophores experiment and obtained a triangle with side lengths of 43.5 ± 2.3 nm ($n = 247$), 81.9 ± 2.9 nm ($n = 244$), and 48.4 ± 3.1 nm ($n = 247$; Figures 2A, 2B, and S1B; Table S1). These 3 distances are not compatible with collinearity ($p = 0.019$, $z = 2.07$; Figure 2B; Table S1). To further substantiate a lack of collinearity, we also measured the distances from Ndc80(N) and CenpC to Nnf1 in parental cells (Figure S1C). These measurements also indicate a lack of collinearity ($p = 6 \times 10^{-17}$, $z = 8.28$) with side lengths of 34.9 ± 0.6 nm ($n = 1,777$), 85.8 ± 0.8 nm ($n = 1,754$), and 61.5 ± 0.8 nm ($n = 1,748$; Figures 2A, 2B, and S1D; Table S1). This contrasts with distances between Nnf1-Ndc80(C)-Ndc80(N), which are collinear to our accuracy ($p = 0.07$, $z = 1.47$, distances 48.7 ± 1.2 nm [$n = 726$], 8.4 ± 6.0 nm [$n = 727$], and 66.4 ± 1.5 nm [$n = 724$]; Figures 1D, 2B, and S1A; Table S1). The CenpC position (inner kinetochore) must therefore be offset (on average) from the axis defined by the Nnf1-Ndc80(C)-Ndc80(N) axis.

Visualization of Kinetochore Ensemble Organization

Each kinetochore contains multiple copies of each protein per microtubule and multiple microtubule binding sites. Our experiments thus measure the ensemble average position of the tagged proteins and not the distance between single molecules. To understand the observed lack of collinearity and interpret our

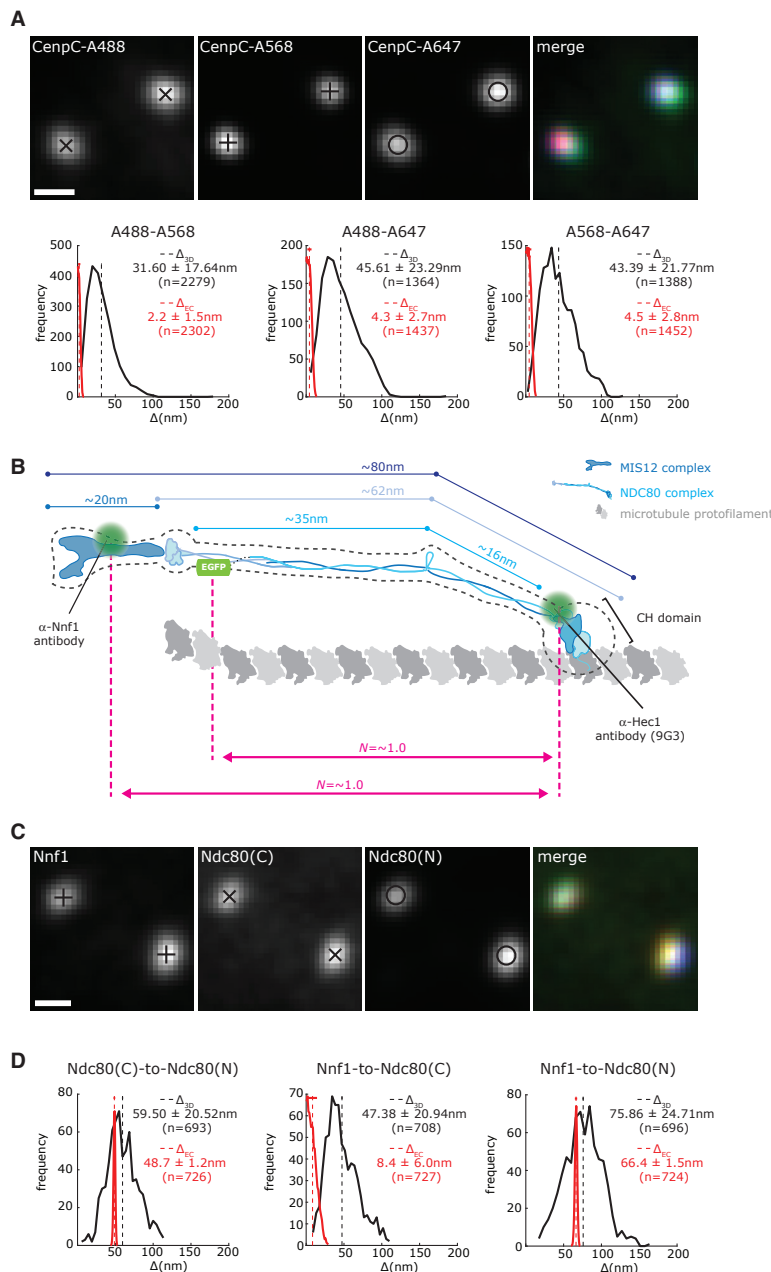


Figure 1. Δ_{3D} Measurements Overestimate the True Δ Distance

(A) Kinetochores stained with anti-CenpC primary antibody and a mixture of Alexa488 (A488), Alexa568 (A568), and Alexa647 (A647)-conjugated secondary antibodies. Histograms of Δ_{3D} (black) and inferred Δ_{EC} (red) distances between the indicated fluorophores, mean (dashed line), and SD (horizontal bar for Δ_{EC}) values are indicated at right.

(B) Schematic representation of MIS12 complex (dark blue) and NDC80 complex (light blue) bound to a microtubule protofilament (dark gray). Assembly organization and size are based on electron microscopy (black dotted line) and crystallography studies (see [Methods S1](#) for details). Approximate antibody binding sites (or EGFP tagging) are indicated with green dots. Distances used for nematic order (N) calculation are indicated in pink (see [Table S2](#)).

(C) Kinetochores stained with anti-Nnf1 and anti-Hec1(9G3) antibodies and RPE1 Ndc80-EGFP cells.

(D) Histograms of the Ndc80(C) to Ndc80(N), Nnf1 to Ndc80(C), and Nnf1 to Ndc80(N) Δ_{3D} and the Δ_{EC} distances measured in Ndc80-EGFP cells; means and SDs are displayed as in (A). Scale bars, 500 nm.

we fit the NDC80 complex hinge angle and the elevation of the NDC80 complex short arm (Ndc80(N)-to-Ndc80(hinge)) with the microtubule. Best fits are 203.5° and 22.4° , respectively ([Figure 2C](#); see [Methods S1](#)); hinge angles $>180^\circ$ have been observed ([Scarborough et al., 2019](#); [Wang et al., 2008](#)), while the latter is compatible with the range determined from EM and crystal structure studies ([Ciferri et al., 2008](#); [Wilson-Kubalek et al., 2008](#)). [Figure 2D](#) (left and center left panels) shows a simulation of a single kinetochore bound to a K-fiber (gray) with the simulated positions of CenpC (pink), Ndc80(C) (light blue), Ndc80 loop (red), Ndc80(N) (blue), and Nnf1 (orange) at single molecules. The center right panel displays the average of the simulated position of three markers showing the offset of CenpC with respect to the Ndc80 complex. Averaging across multiple simulated kinetochores reveals a multi-layered structure with tight localization and sequential ordering of kinetochore components along the K-fiber axis, and an extensive spread transverse to the axis that is suggestive of discs ([Figure 2D](#), right panel). Our simulations indicate that moderate levels of flexibility of the Ndc80 microtubule attachment angle and orientation can produce a lack of collinearity between the average positions of CenpC, Nnf1/Ndc80(C), and Ndc80(N). In addition, the broad transverse

distances in the context of known structural information, we built a computational simulation. Our simulations incorporate (1) known structural biology on NDC80-MIS12, (2) information from EM data of K-fiber and kinetochore organization, and (3) measurements of kinetochore protein numbers per microtubule. We optimized unknown parameters by fitting the simulations to our measured triangle CenpC-Ndc80(C)-Ndc80(N). Crucially,

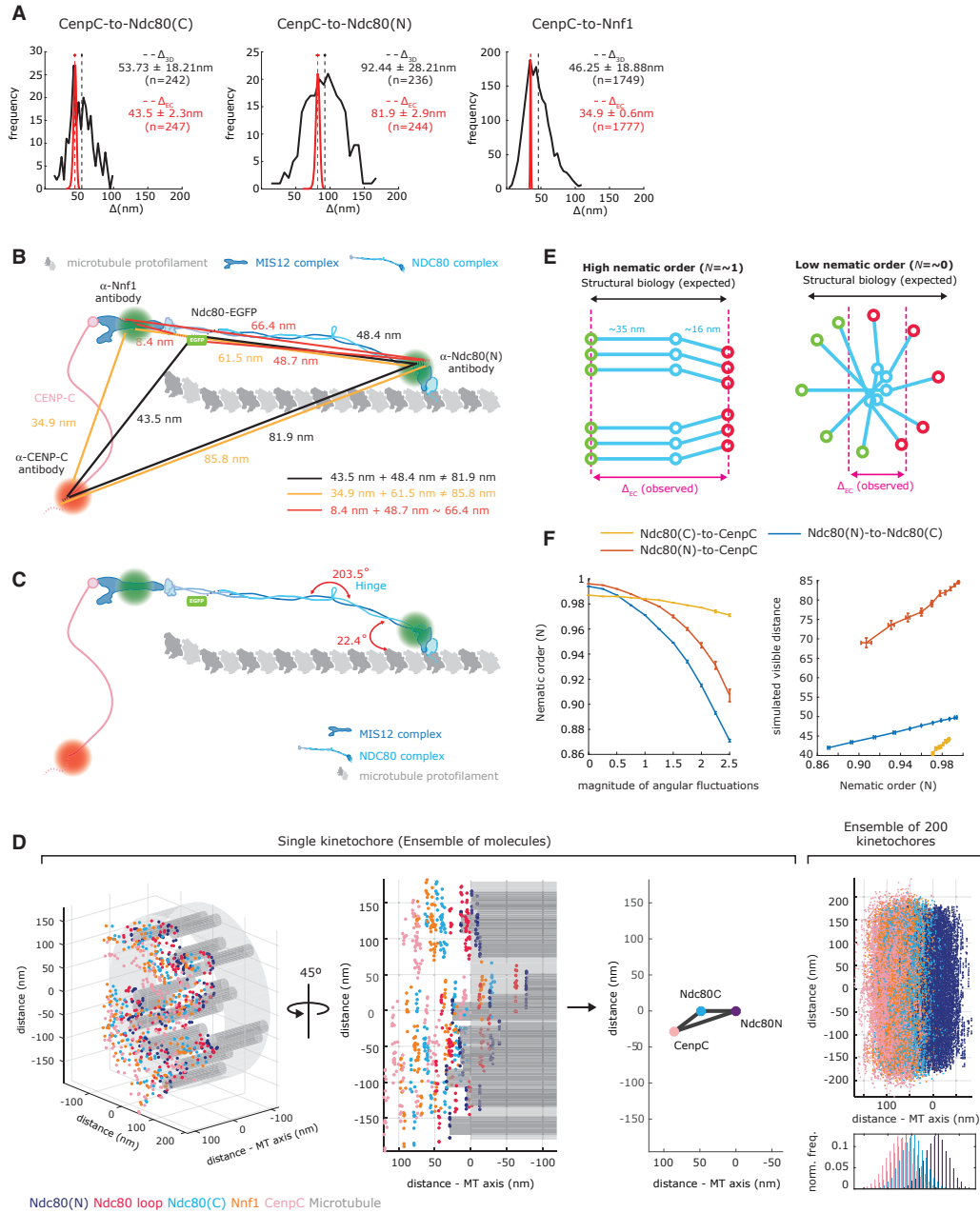


Figure 2. Simulations of the Architecture of a Bi-oriented Kinetochores

(A) Histograms of Δ_{3D} and Δ_{EC} distances for CenpC to Ndc80(C) and CenpC to Ndc80(N) (Ndc80-EGFP cells) and for CenpC to Nnf1, mean (dashed line), and SD (horizontal bar) values are indicated at right.

(B) Schematic showing the inferred architecture of CenpC-MIS12-NDC80. Approximate antibody binding sites (or EGFP tagging) are indicated with green dots. Lines indicate Δ_{EC} mean values (dotted lines show SDs) obtained in 3-fluorophore experiments: CenpC-Ndc80(C)-Ndc80(N) (black), CenpC-Nnf1-Ndc80(N) (orange), and Nnf1-Ndc80(C)-Ndc80(N) (red).

(C) Schematic of CenpC-MIS12-NDC80 showing best-fitted angles (red) from simulations; see [Methods S1](#).

(legend continued on next page)

dimension allows even small re-distributions of the CenpC population to give rise to an off-axis location. Thus, changes in the distribution of the CenpC marker, potentially due to CenpC's inherent flexibility, are sufficient to explain the lack of collinearity measured *in vivo*.

The simulations also revealed ordered alignment of kinetochore molecules along an internal axis. We sought to quantify the degree of alignment of individual NDC80 complexes. Because these complexes are rod-like with head-tail asymmetry, we can calculate the nematic order (N), which is a measure of the mean degree of filament alignment along a director (de Gennes and Prost, 1993; Doostmohammadi et al., 2018) and related to our distance measurements by $N = \Delta_{EC}/\Delta_{structural}$ (see Methods S1). Here, $N = \sim 0$ indicates no alignment (low nematic order), and $N = \sim 1$ is perfect parallel alignment of vectors (high nematic order; Figure 2E). At high alignment of the NDC80 complexes within the ensemble (i.e., high nematic order), the structural data and our *in vivo* distance measurements should match, while as nematic order decreases, the measured distance of the ensemble decreases (Figure 2E). We find that for both the Ndc80(C) to Ndc80(N) and Nnf1 to Ndc80(N) linkages, $N = \sim 1$ (Figure 1B; Table S2). This indicates that in the microtubule-attached state, the MIS12-NDC80 complex assemblies are highly ordered and that Δ_{EC} distances reflect the underlying molecular organization as implicitly assumed in using the NDC80 complex as a molecular ruler (Suzuki et al., 2018). We also investigated how increasing the fluctuations in the hinge angle and Ndc80 orientation decreased the nematic order (Figure 2F, left panel) and correspondingly decreased the average Δ_{EC} distance (Figure 2F, right panel). This further shows how the angular degrees of freedom, such as the NDC80 hinge (Methods S1) are in effect highly constrained to produce high alignment of the NDC80 complexes. Thus, our simulations and data indicate that at this resolution, the kinetochore is organized along an internal axis with high nematic order in the outer plate (Table S2).

Linking the Inner and Outer Kinetochores: CenpT and CenpC-Mis12 Linkages Both Position NDC80 in the Same Spatial Domain

It is well established that NDC80 complexes are not only targeted to kinetochores through CenpC-Mis12 linkages but also through CenpT (Gascoigne et al., 2011; Klare et al., 2015); each linker is responsible for recruiting $\sim 50\%$ of the Ndc80 molecules (Johnston et al., 2010). We determined the CenpT position using an antibody, which recognizes the non-histone fold region that extends and interacts with the NDC80 complex. This CenpT epitope was positioned close (5.7 ± 4.0 nm, $n = 894$) to the Ndc80 C terminus and 47.9 ± 1.6 nm ($n = 882$) from CenpC (Figure 3C; Table S1). This suggested that the NDC80

complexes tethered through CenpT or CenpC-MIS12 are not spatially separated within the kinetochore. To further investigate, we depleted each linker by RNAi. Depletion of CenpT resulted in the loss of $>93\%$ of the CenpT molecules from kinetochores and an increase in the number of CenpC molecules (Figures 3A and 3B). However, the distance between the remaining endogenous Ndc80-EGFP ($\sim 20\%$) and CenpC molecules increased by only 10.5 ± 7.0 nm compared to control cells (Figure 3C; Table S1). The reciprocal experiments (CenpC depleted by $>96\%$) resulted in the unbinding of CenpT (by $\sim 90\%$) and Ndc80-EGFP (by $\sim 75\%$; Figures 3A and 3B). The distance between the residual CenpT and Ndc80(C) also increased by 14.5 ± 9.9 nm (Figure 3C; Table S1). These data support the idea of a single NDC80 complex population and confirm that the linkers are required for normal kinetochore integrity and composition (Klare et al., 2015; Suzuki et al., 2014).

Jackknifing of NDC80 Complexes Follows Treatment with Nocodazole, but Not Taxol

We next investigated how the structural organization and geometry of the kinetochore respond to a loss of attachment or tension. To do this, we treated the RPE1 cell lines with either (1) $3.3 \mu\text{M}$ nocodazole for 2 h and confirmed by tubulin staining that all of the kinetochore-microtubule populations were eliminated and that the 3D K-K distance (CenpC to CenpC) was reduced ($0.93 \pm 0.005 \mu\text{m}$, $n = 2,537$, means \pm SEMs), or (2) $1 \mu\text{M}$ taxol for 15 min, which reduces the K-K distance to nearly rest length ($0.96 \pm 0.004 \mu\text{m}$, $n = 1,931$, means \pm SEMs), but leaves the majority of kinetochores associated with microtubules and aligned on the metaphase plate (Figure S3A). By measuring microtubule dynamics using photoactivatable PA-EGFP- α -tubulin, we also confirmed that $1 \mu\text{M}$ taxol largely eliminated microtubule dynamics (Amaro et al., 2010), consistent with the loss of tension (Figure S3).

We measured the geometry of the CenpC-MIS12-NDC80 assembly; the distances from CenpC to Ndc80(C) and Nnf1 were largely unchanged in nocodazole and taxol (Figures 4A, S4A, and S4B; Table S1). This is consistent with previous work reporting that the inner kinetochore does not collapse following microtubule detachment (Smith et al., 2016; Suzuki et al., 2018). However, the CenpC to Ndc80(N) distance was reduced by 25.3 ± 3.5 nm following treatment with nocodazole (Ndc80-EGFP cells; Figure 4A; similar to the reduction of 30.1 ± 3.3 nm observed in parental cells; Figure S4B; Table S1). Consistently, the Ndc80(C) to Ndc80(N) distance decreased by 41.1 ± 5.5 nm (85%) in unattached kinetochores (Figure 4A). We also measured the distances between Nnf1, Ndc80(C), and Ndc80(N) (Figure 4B). This triangulation confirms that there is a substantial reduction of 40.9 ± 5.1 nm (84%) in the Ndc80(C) to

(D) Simulated kinetochore organization. Left and center left: 2 perspectives of the same simulated kinetochore; each dot represents a single protein at the specified position (labeled by color). Center right: averages of the simulated position of each marker shown in the plane of the CenpC-Ndc80(N)-Ndc80(C) triangle. Right: an ensemble of 200 simulated kinetochores aligned along their microtubule axis and to the mean of their Ndc80(N) markers. Histogram of the marker density along K-fiber for the above plot.

(E) Schematic representation of NDC80 complexes under high ($N = \sim 1$) and low ($N = \sim 0$) nematic order. Circles represent Ndc80(C) (green), Ndc80 loop (blue), and Ndc80(N) (red).

(F) Left: change in the nematic order of the NDC80 complex population with respect to the magnitude of Ndc80 loop stochastic angular fluctuations. Right: average distance between the indicated molecular markers against the nematic order. Simulations based on 200 kinetochores.

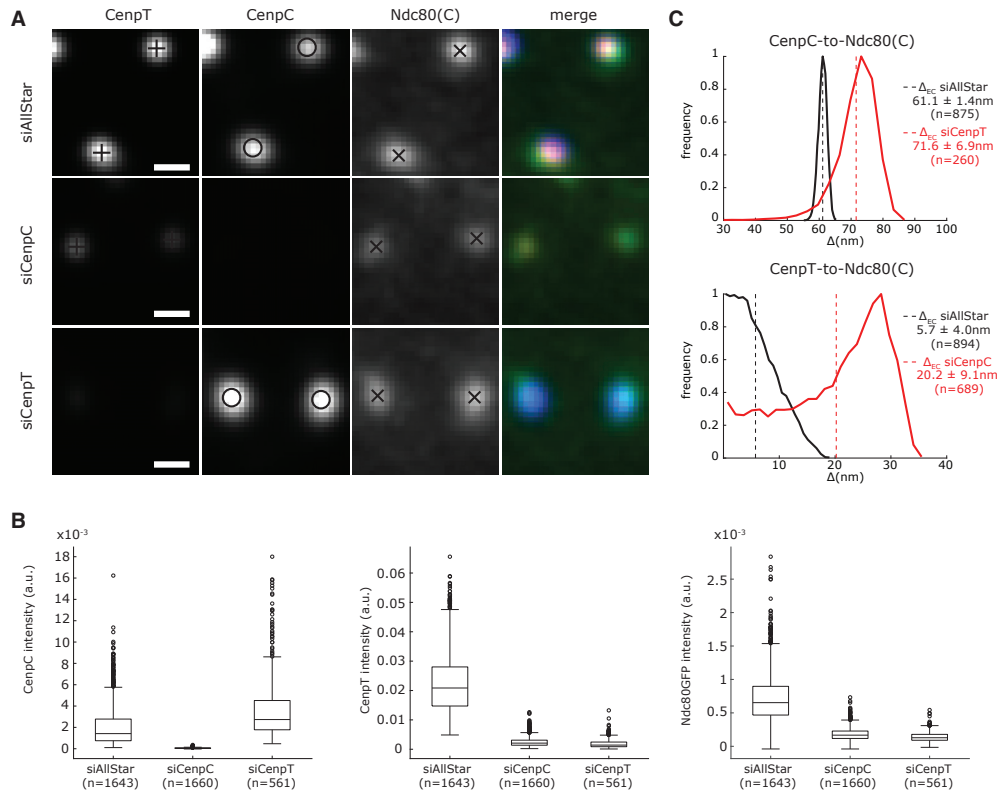


Figure 3. The CenpC and CenpT Linkers Contribute to a Single Spatial Population of NDC80 Complexes

(A) Kinetochores stained with anti-CenpT and anti-CenpC antibodies in Ndc80-EGFP cells transfected with small interfering AllStar (siAllStar) (control) and siRNA against CenpC and CenpT. Scale bar, 500 nm.

(B) Box and whiskers plots of CenpC, CenpT, and Ndc80-EGFP kinetochore intensity in the different RNAi conditions; signals are background subtracted.

(C) Histograms of CenpC to Ndc80(C) and CenpT to Ndc80(C) Δ_{EC} distances measured in Ndc80-EGFP cells treated as in (A); mean (dashed line) and SD values are indicated at right.

Ndc80(N) linkage under nocodazole treatment (Figure 4C; Table S1). In taxol, the Δ_{EC} between Ndc80(C) and Ndc80(N) remained the same as in the control (Figures 4A and 4C; Table S1). This suggests that the Ndc80 N terminus does not move inward following taxol treatment and the NDC80 complex remains in its straight configuration with a high nematic order, $N = \sim 1$ (Table S2). These data provide evidence that the kinetochore responds differentially to the loss of attachment and tension.

Next, we sought to investigate the underlying cause of the $\sim 85\%$ reduction in the distance between Ndc80 C and N termini observed under nocodazole treatment. Previous studies have suggested that the Ndc80 loop acts as a pivoting point and thus we asked whether the distance reduction can be explained by conformational change in the Ndc80 complex such that the Ndc80 N terminus is brought into close proximity to the C terminus (we call this jackknifing; Figure 4D, model 2). Ndc80 structural data suggest that the expected distance between Ndc80 C and N termini upon full closure of the N terminus is ~ 19 nm, and thus is insufficient to explain the measured 7.8 nm distance in nocodazole. Since the measurements reflect

kinetochore ensemble organization, the change could alternatively be explained by the disorganization of the Ndc80 molecules (i.e., loss of nematic order) or a combination of Ndc80 jackknifing and disorganization. Our analysis shows that in the absence of Ndc80 jackknifing (i.e., if Ndc80 maintains its straight conformation as in DMSO), a nematic order decrease from ~ 1 observed in DMSO (Figures 4D and 4E, model 1) to < 0.2 is required to explain the observed 7.8 nm distance between Ndc80 C and N termini (Figures 4D and 4E, model 3). Alternatively, if Ndc80 undergoes full jackknifing then a loss of order to 0.4 is still required to explain the measured 7.8 nm distance (Figures 4D and 4E, model 4). We favor this model (see Discussion for details) and hereafter refer to these changes in NDC80 organization as jackknifing.

NDC80 Jackknifing Marks Spindle Checkpoint Active Kinetochores

Does jackknifing within the outer kinetochore plate relate to checkpoint signaling from the kinetochore? For these experiments, we used cells in which Mad2 was labeled at its endogenous locus

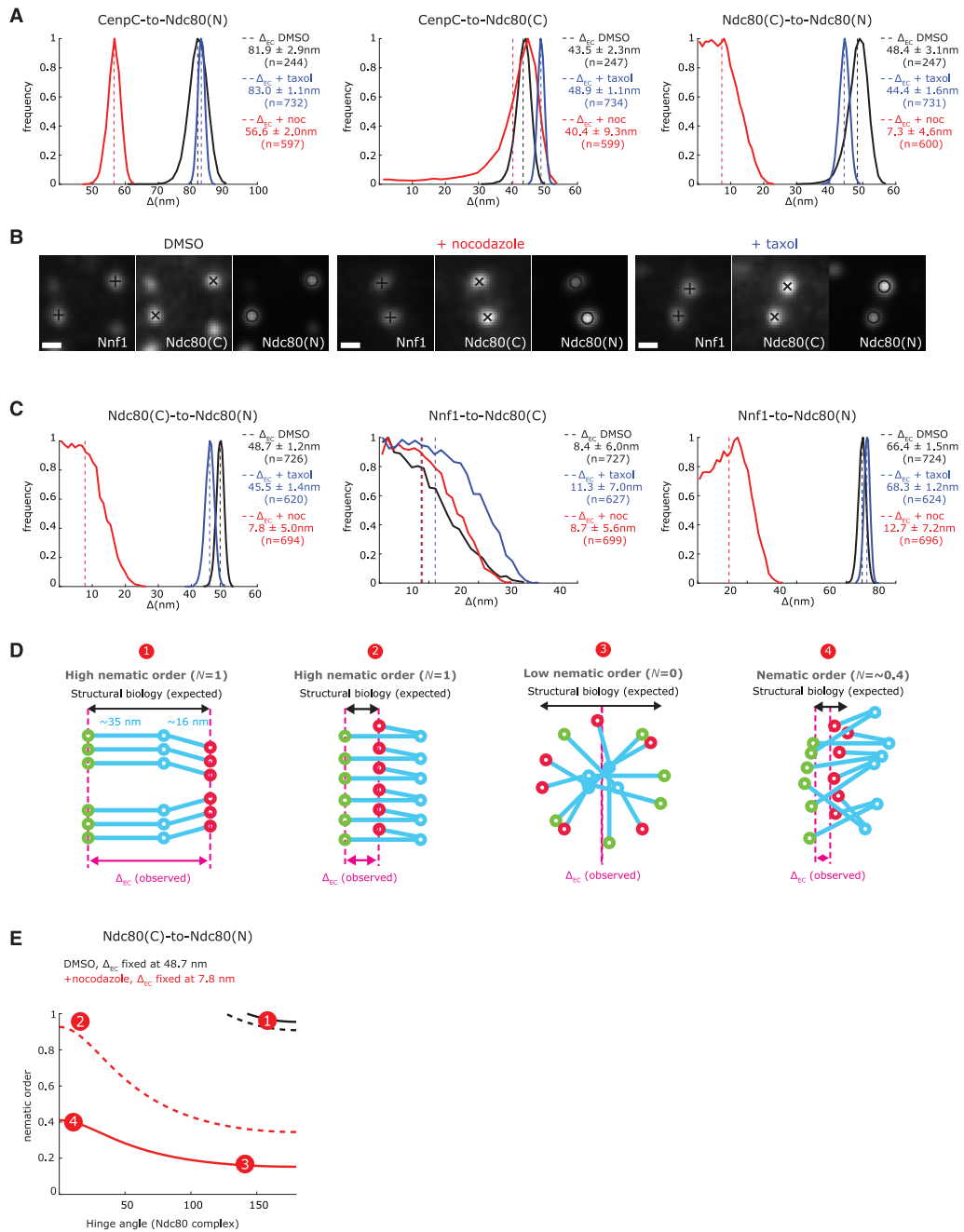


Figure 4. Loss of Microtubule Attachment and Stabilization of Microtubule Dynamics Induce Different Organization of Ndc80

(A) Histograms of CenpC to Ndc80(N), CenpC to Ndc80(C), and CenpC to Ndc80(N) Δ_{EC} distances in Ndc80-EGFP cells treated with 3.3 μ M nocodazole for 2 h, 1 μ M taxol for 15 min, or DMSO; mean (dashed line) and SD values are indicated at right.

(B) Kinetochores stained with anti-Nnf1 and anti-Hec1(9G3) antibodies and in Ndc80-EGFP cells treated as in (A). Scale bar, 500 nm.

(legend continued on next page)



with Venus (Collin et al., 2013). As expected, nocodazole treatment (unattached kinetochores) led to an increase in Venus-Mad2 and Bub1 kinetochore binding on most kinetochores, while after taxol treatment, the average levels of these proteins were similar (Figures 5A, 5B, and S5A). However, in taxol and DMSO, there were multiple outliers (Figure 5B), suggesting the presence of a Mad2-positive subpopulation, as previously reported (Magidson et al., 2016). In addition, we found that treatment with 1 μ M taxol prevents cells in metaphase from exiting mitosis unless 1 μ M reversine (Mps1 inhibitor) is added to the media to override the spindle checkpoint (Figures 5C and S5B). These experiments indicate that the spindle checkpoint is active following treatment with 1 μ M taxol and suggest that the few Mad2-signaling kinetochores may be responsible. To understand how the Ndc80 jackknifing relates to Mad2 recruitment, we separated our kinetochore spots into a Venus-Mad2-positive (Mad2⁺) and -negative (Mad2⁻) population, and then determined the distance from CenpC to Ndc80(N) (Figure 5D). The CenpC to Ndc80(N) distances were significantly different in these 2 populations ($p = 2.4 \times 10^{-5}$), with the distance in the Mad2⁺ population (66.2 ± 3.7 nm) nearly identical to that of nocodazole-treated cells (which were all Mad2⁺, $\Delta_{EC} = 58.3 \pm 1.3$ nm, $p = 0.044$). Furthermore, the 16.2 ± 3.8 nm difference in the CenpC to Ndc80(N) between Mad2⁻ and Mad2⁺ in DMSO (Figure 5D; Table S1) is consistent with the jackknifing of Ndc80 under the lack of attachment in Mad2⁺ (compare to the Δ_{EC} decrease of 25.3 ± 3.5 nm under nocodazole, $p = 0.039$), suggesting that there is a high correlation between Mad2⁺/Mad2⁻ and Ndc80 being in the jackknife or straight conformations (nocodazole versus DMSO, respectively). Under taxol, we could also detect an inward movement of 11.5 ± 5.1 nm of the Ndc80(N) in the Mad2⁺ versus Mad2⁻ subpopulations (Figure 5D). These correlations are likely imperfect because the Mad2⁺/Mad2⁻ populations are also heterogeneous with respect to attachment status and include partial jackknifing states as error correction proceeds.

These data indicate that we can detect the inward movement of Ndc80(N) at Mad2⁺ kinetochores in control metaphase cells, not just under nocodazole treatment. These data clearly demonstrate that checkpoint activation (in terms of Mad2 recruitment) occurs at kinetochores that are in the unattached conformation (Ndc80 jackknifed). Moreover, our data show how most kinetochores in 1 μ M taxol have a low K-K distance without triggering the recruitment of Mad2. We next reasoned that if the Ndc80 jackknifing is downstream of checkpoint activation, then it should not occur when Mps1 kinase activity is inhibited. The treatment of cells with 1 μ M reversine eliminated the Mad1-pT716 substrate signal (Allan et al., 2020), but had no effect on Ndc80(N) movement in the presence of nocodazole (and MG132 to prevent entry to anaphase; Figure S5C), suggesting that jackknifing is independent from Mps1 activity.

3D Mapping of the Key Checkpoint Protein Platforms Bub1 and RZZ

We next sought to establish where in the kinetochore the Mad1:Mad2 complex is recruited. While Bub1 is a bona fide kinetochore receptor for human Mad1:Mad2 complexes (Zhang et al., 2017), the RZZ complex is also implicated (Kops et al., 2005) and may even operate as a second receptor (Silió et al., 2015). To read out the position of Bub1, we used an antibody that recognizes the first 130 aa (referred to as Bub1(N); Figure 6B) and found it positioned 58.9 ± 1.1 nm ($n = 2,232$) from CenpC and therefore 26.9 ± 1.4 nm to the inside of the Ndc80 head domain (Figure 5C; Table S1). Using antibodies that recognize the carboxy-terminus of Rod (recombinant fragment aa 2,100–2,209, referred to as Rod(C)) and Zwlch (Figures 6A and 6B), we found that while Rod(C) is positioned 14.4 ± 2.1 nm inside Ndc80(N), Zwlch is 10.5 ± 1.3 nm to the outside (Figures 6B and 6C; Table S1). In addition, EGFP-Zw10 was positioned 11.5 ± 3.6 nm outside Rod(C) and 13.4 ± 3.3 nm inside Zwlch (Figures 6A and 6B; Table S1). This is broadly consistent with the arrangement of these subunits within the cryo-EM structure of the RZZ complex (Mosalaganti et al., 2017). These results indicate that most of the RZZ complex is located outside the Ndc80 head domain, and thus is spatially separated from Bub1. We can estimate the distance between Zwlch and Rod by subtracting the CenpC to Rod(C) from CenpC to Zwlch distances, giving 24.9 ± 2.1 nm (Figure 6C; Table S1). This distance is similar to that determined from the cryo-EM structure (Mosalaganti et al., 2017) and indicates high nematic order ($N = \sim 0.8$; Table S2). The high nematic order further justifies the assumption of the molecular ruler to organize components of the outer kinetochore/corona. These data also suggest that within an end-on attached kinetochore, the RZZ complex is not forming a head-to-tail dimer, as suggested by cryo-EM (Mosalaganti et al., 2017); this would have resulted in Rod(C) and Zwlch signals being coincident. These data thus provide the first 3D mapping of the key checkpoint protein platforms (Bub1 and RZZ) relative to the major microtubule attachment factor (NDC80 complex) in the human kinetochore.

Mad1:Mad2 Complex Can Occupy Two Distinct Positions within the Kinetochore

We next used the RZZ molecular ruler to map the positions of Mad2 and a phospho-epitope in the carboxy-terminus of Mad1(pT716) following treatment with nocodazole. As the corona/outer kinetochore begins expanding into crescent-shaped structures under these (unattached) conditions, we limited our analysis to non-expanded kinetochores (a “proto-corona”) to have accurate positional information (Figure 6D). The position of Bub1, Rod, and Zwlch (RZZ complex) remained largely unchanged (Figure 6C), showing that kinetochores do not simply

(C) Histograms of Ndc80(C) to Ndc80(N), Nnf1 to Ndc80(C), and Nnf1-to-Ndc80(N) Δ_{EC} distance in Ndc80-EGFP cells treated as in (A); mean (dashed line) and SD values are indicated at right.

(D) Four models of different structural and nematic organizations of NDC80. Circles represent Ndc80(C) (green), Ndc80 loop (blue), and Ndc80(N) (red). For each model, the nematic order (gray), the distance expected from structural information (black), and the expected Δ_{EC} (pink) are indicated.

(E) Data-constrained nematic order and hinge angle of the NDC80 complex. For each hinge angle, the nematic order is calculated that is consistent with the observed Δ_{EC} , 48.7 nm (DMSO) and 7.8 nm (nocodazole) for the Ndc80(C) to Ndc80(N) linkage. Dashed lines show 95% confidence intervals. Numbered circles annotate the approximate position of each model on the graph.

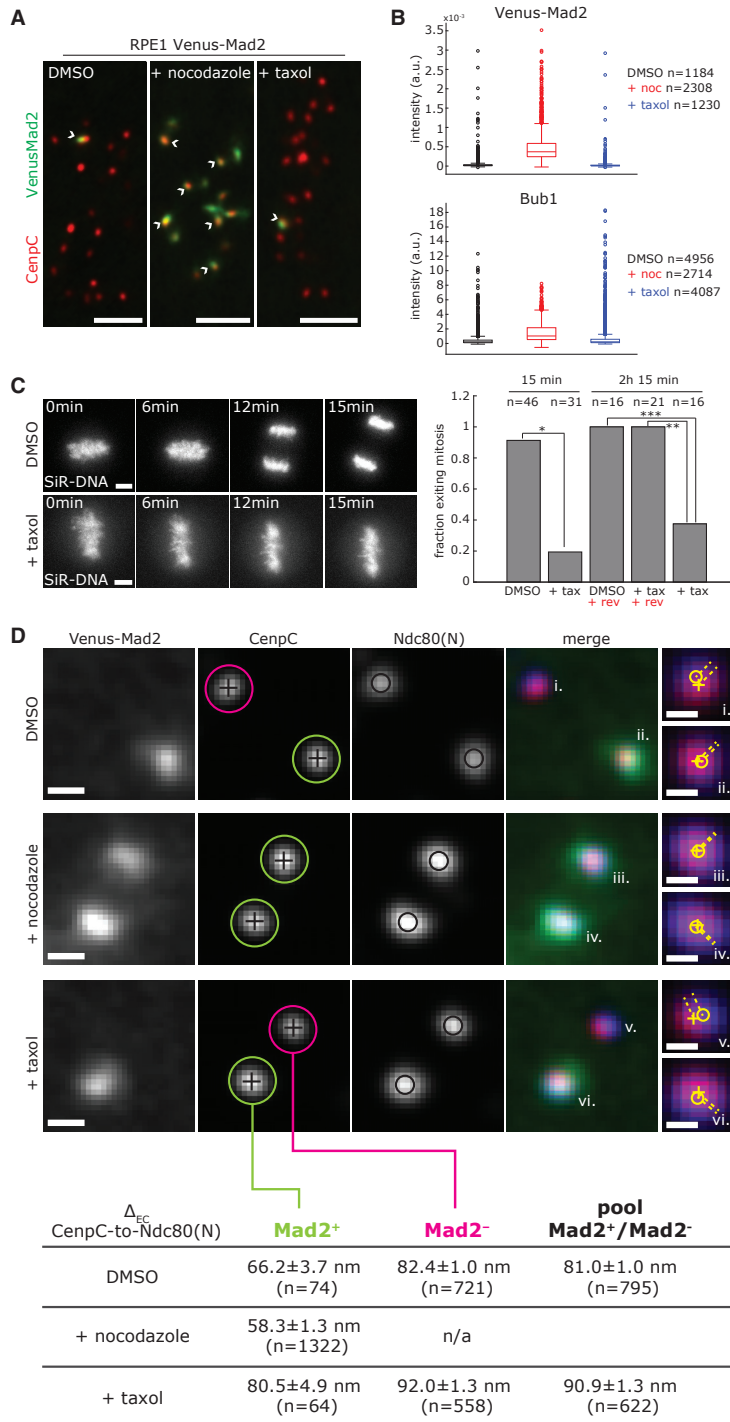


Figure 5. Activation of the Spindle Assembly Checkpoint Correlates with NDC80 Conformational Change

(A) Images of Venus-Mad2 cells stained with anti-CenpC antibody and treated with 3.3 μ M nocodazole for 2 h, 1 μ M taxol for 15 min, or DMSO. White arrows indicate Mad2⁺ kinetochores. Scale bar, 3 μ m.

(B) Box and whisker plots of Venus-Mad2 and Bub1 kinetochores intensity in cells treated as in (A). All of the intensities are background subtracted. The Bub1 signal is normalized to the CenpC signal.

(C) Images of cells treated with 1 μ M taxol and DMSO for 15 min and stained with SiR-DNA. Scale bars, 5 μ m. Bar chart indicates the fraction of cells exiting mitosis within the indicated imaging time, after DMSO, taxol (+tax), and 1 μ M reversine (+rev) treatment (Figure S5B; Method Details). Fisher's exact test indicates that the differences are significant with a 99% confidence interval: *p = 7.7 \times 10⁻¹², **p = 2.3 \times 10⁻⁵, ***p = 1.2 \times 10⁻⁴.

(D) Example images of kinetochores stained with anti-CenpC and anti-Hec1(9G3) antibodies in RPE1 Venus-Mad2 cells treated as in (A). Scale bar, 500 nm. Table S1 displays the Δ_{EC} (mean \pm SD) between CenpC and Ndc80(N) in Venus-Mad2⁺ (green circle), Venus-Mad2⁻ (pink circles) kinetochores, and pool samples in the 3 conditions. Insets (i-vi) show the distances (yellow dotted lines) between CenpC (+) and Ndc80 (○) in the indicated kinetochores on the XY plane. Scale bar in insets, 250 nm.

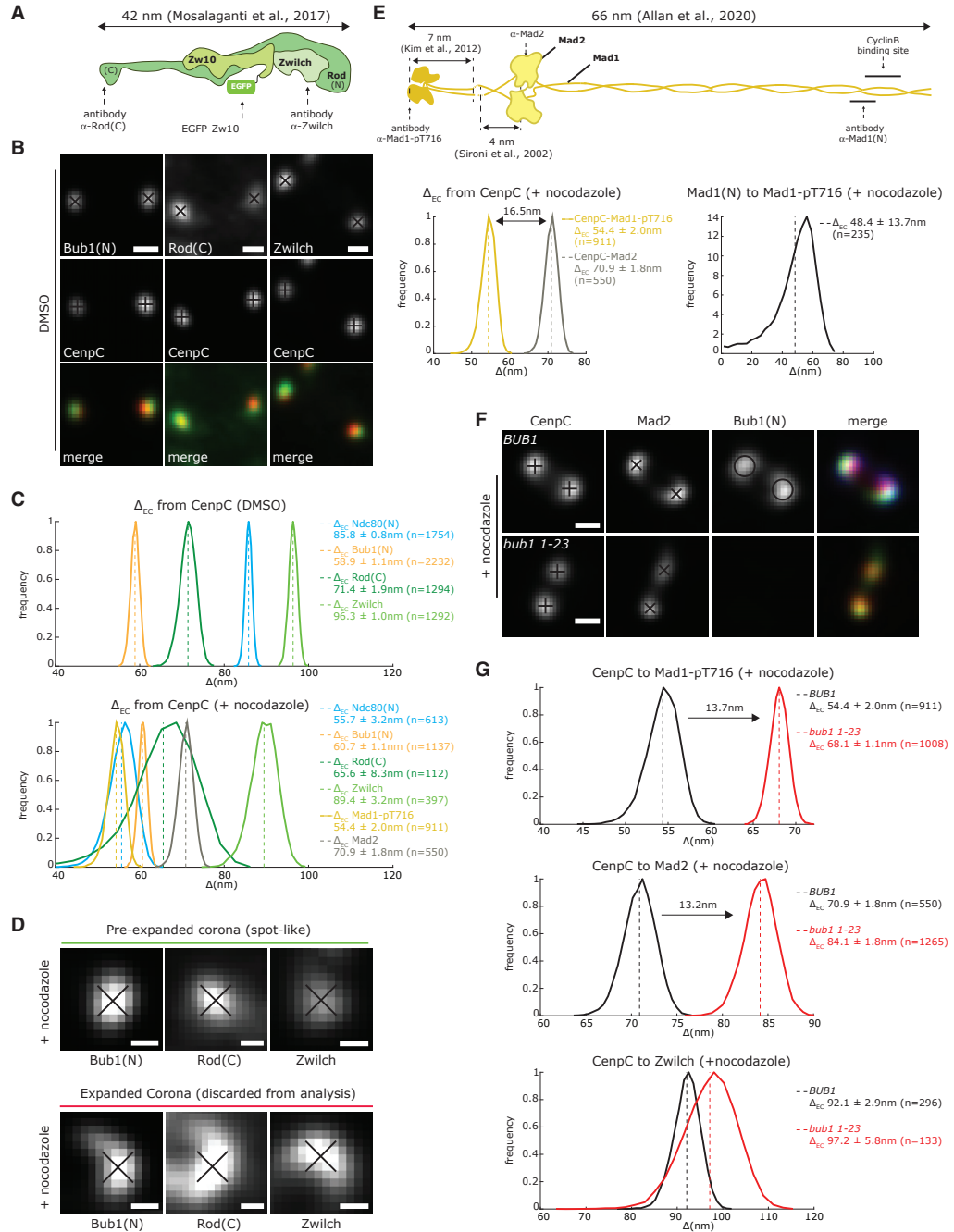


Figure 6. Mad1:Mad2 Binds Different Kinetochore Sites upon Activation of the Spindle Assembly Checkpoint

(A) Scale model of RZZ and approximate positions of anti-Rod(C) and anti-Zwilch antibodies and EGFP-Zw10.
 (B) Kinetochore pairs stained with anti-CenpC antibody in combination with anti-Bub1, anti-Rod, or anti-Zwilch antibodies in DMSO-treated cells. Scale bar, 500 nm.
 (C) Histograms of Δ_{EC} between CenpC and Ndc80(N), Bub1, Rod, and Zwilch in DMSO- and nocodazole-treated cells. Mad1-pT716 and Mad2 positions are shown for nocodazole only. Mean (dashed line) and SD values are indicated at right.

(legend continued on next page)

collapse when unattached. Mad1-pT716 was located 54.4 ± 2.0 nm ($n = 911$) from CenpC (close to its binding partner Bub1), while Mad2 was located 16.5 ± 2.7 nm further outward (Figures 6C and 6E; Table S1). This distance is consistent the Mad1:Mad2 complex structure (Figure 6E; Allan et al., 2020; Kim et al., 2012; Sironi et al., 2002). Moreover, the distance from Mad1-pT716 to an antibody that recognizes an epitope (aa 77–115) in the amino terminus, referred to as Mad1(N), was 48.4 ± 13.7 nm ($n = 235$) (Figures 6E and S6A), close to the predicted 57 nm from EM structure (Allan et al., 2020). Thus, Mad1 looks to be extended within the kinetochore and highly ordered (Table S2).

Mad1:Mad2 are proposed to bind to both Bub1 and a second RZZ-dependent receptor, recently identified as CyclinB (Allan et al., 2020; Silió et al., 2015). Our measurement of Mad1:Mad2 would thus reflect the average position of these proteins within a kinetochore. To test this idea, we measured the position of Mad1-pT716 and Mad2 in cells carrying a homozygous *bub1* 1-23 mutation (Figures 6F, S7A and S7B). In these cells, Bub1 levels are reduced to almost undetectable levels, but Mad1-pT716, Mad2, and Zwilch can still bind kinetochores and generate a checkpoint signal (Figures S7A, S7B, and S8A) (Currie et al., 2018; Zhang et al., 2019). Here, both Mad1-pT716 and Mad2 signals moved outward by 13.7 ± 2.3 nm and 13.2 ± 2.5 nm, respectively (Figure 6G). In contrast, we found that the Zwilch position from CenpC was 92.1 ± 2.9 nm ($n = 296$) in parental cells and 97.2 ± 5.8 nm ($n = 133$) in *bub1* 1-23 cells, suggesting that the RZZ complex was not affected by the loss of Bub1 (Figure 6G). These data are consistent with the model that there are two spatially distinct kinetochore receptors for Mad1:Mad2.

Kinetochores Adopt a Unique Conformation following the Loss of Tension

The absence of NDC80 jackknifing following taxol treatment raised the question of whether the loss of tension is detected at all. We first checked the position of Bub1 and RZZ subunits in taxol-treated cells and found no changes (Figures 7A and 7B). We then turned to Knl1, the third component of the KMN network (Cheeseman et al., 2006). Knl1 is a largely disordered protein that binds to the MIS12 complex through the carboxy-terminus with the remaining protein comprising multiple MELT sequences that operate as phospho-dependent binding sites for the Bub3-Bub1 checkpoint complexes (Figure 7C; London et al., 2012; Shepperd et al., 2012; Yamagishi et al., 2012). The extreme amino-terminal end of Knl1 contains a microtubule-binding site and a docking site for protein phosphatase 1 (PP1) (Figure 7C). The amino terminus of Knl1 (marked with a phospho-specific anti-

body that recognizes serine 24, referred to as Knl1-pS24; Figure 7C) was positioned 32.8 ± 12.5 nm from Bub1 (Figure 7B), whereas the second MELT (aa 300–350, referred to as Knl1(MELT2); Figure 7C) was only 6.5 ± 1.5 nm from Bub1, which is consistent with the role of the MELT motifs in recruiting Bub1 to the kinetochores (Figures 7B and 7E). These data suggest that the unstructured region of Knl1 (Figure 7C), which has a predicted path length of ~ 380 nm, must be “wrapped up” and occupy the space between the Ndc80 head domain and the CCAN (CenpC here). We next checked the position of the amino terminus of Knl1 (Knl1-pS24) following taxol treatment (Figure 7D) and found that it moved outward by 93.0 ± 12.8 nm (Figure 7B). There was minimal movement of the second MELT, indicating that the bulk of the MELT array is unchanged (Figures 7B and 7E; Table S1). This is consistent with our observation that the Bub1 position, which is a proxy for the MELTs, does not change. Because the predicted length of the disordered first 300 aa is ~ 64 nm and the distance from Knl1(MELT2) to Knl1-pS24 in taxol is 50.6 ± 3.3 nm, this region of Knl1 must switch into an almost straight configuration. Compared to the increase in nocodazole treatment, an increase was not detected in the phosphorylation of Knl1-pS24 (Figure 7D), which is a substrate for AuroraB (Welburn et al., 2010). Because nocodazole also causes a loss of tension, we checked the position of Knl1 (Figures 7D and 7E). Knl1 is again more extended, with the amino-terminal end located 91.7 ± 6.3 nm ($n = 472$) from CenpC (compared to 26.1 ± 12.5 nm, $n = 1,260$ in DMSO; Figure 7D; Table S1). We also detected an outward movement (17.1 ± 2.4 nm) of the MELT2 position (Figure 7E). These data provide evidence that the physical re-organization of Knl1 responds to the loss of tension.

DISCUSSION

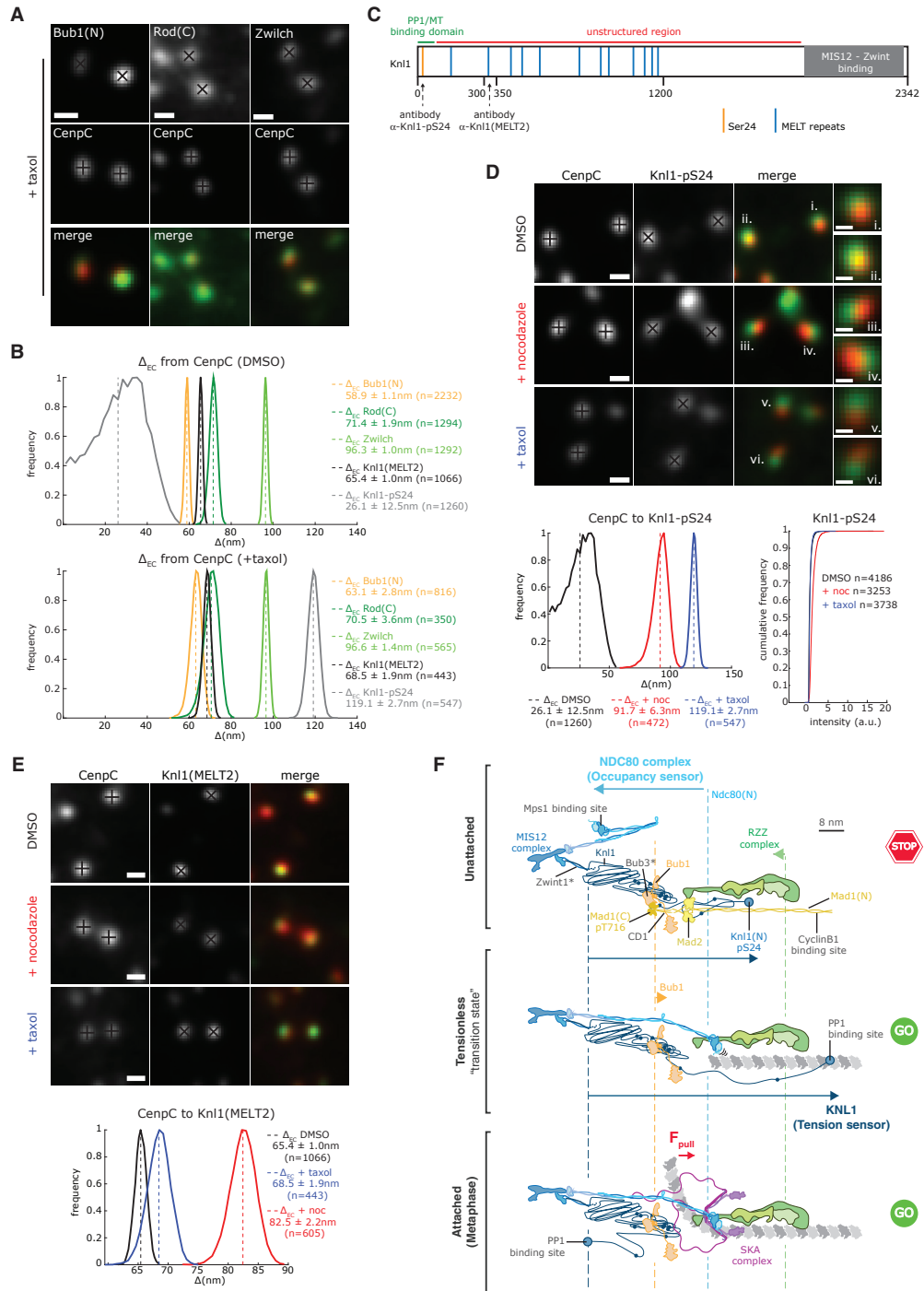
This work provides an initial architectural map of the human kinetochore by quantifying the relative position (to accuracy 1–10 nm) and movement of major complexes and subunits (see Figure 7F). Our intra-kinetochore distances are corrected for Euclidean distance inflation and interpreted within the context of a kinetochore ensemble of molecules and available structural data. Using a computational simulation, we generated a 3D visualization of a human kinetochore that produces plate-like structures for the outer (MIS12-NDC80) and inner (CenpC) kinetochores, which is reminiscent of that observed in electron micrographs (Brinkley et al., 1992). These data also demonstrate how the inner and outer plates are shifted relative to each other in the direction perpendicular to the microtubule axis. We propose here that the outer kinetochore is highly ordered with molecules aligned along an outer kinetochore axis, presumably parallel to

(D) Examples of spot-like and expanded kinetochores. Kinetochores are stained with anti-Bub1, anti-Rod, and anti-Zwilch antibodies in cells treated with $3.3 \mu\text{M}$ nocodazole. Scale bars, 250 nm.

(E) Top: schematic indicating the Mad1:Mad2 complex size and the approximate binding positions of anti-Mad1-pT716; anti-Mad1 directed against aa 77–115, referred to as Mad1(N); and anti-Mad2 antibodies used in this study. Bottom: histograms of the Δ_{EC} values between CenpC to Mad1-pT716 and CenpC to Mad2 (left), and Mad1(N) to Mad1-pT716 (right). Mean (dashed line) and SD values are indicated at right. The difference between Δ_{EC} mean values is indicated in black.

(F) Kinetochores stained with anti-CenpC, anti-Bub1, and anti-Mad2 antibodies in parental and *bub1* 1-23 cells treated with $3.3 \mu\text{M}$ nocodazole. Scale bars, 500 nm.

(G) Histograms of the Δ_{EC} distances between CenpC and Mad1-pT716, Mad2, and Zwilch in parental and *bub1* 1-23 cells treated as in (F). Mean (dashed line) and SD values are indicated at right. The difference between Δ_{EC} mean values is indicated in black.



the K-fiber axis. Within the outer plate, the NDC80 complex and the more distal RZZ complex must have a high nematic order, otherwise the ensemble average distances would not be consistent with distances from structural biology. It thus follows that our methods allow structural insights from cryo-EM and X-ray crystallography to be assessed within an *in vivo* context. They also provide a framework for understanding the higher-order ensemble organization of the kinetochore.

We have discovered that there is substantial re-organization of the kinetochore outer plate when microtubules detach (nocodazole). Our analysis shows that this can be explained through a combination of NDC80 jackknifing and loss of nematic order or through a loss of order alone. Two lines of evidence suggest that jackknifing is involved: (1) *in vitro* experiments have directly shown how the NDC80 complex does jackknife in the absence of microtubules around the loop (Scarborough et al., 2019), and (2) mutations in the Ndc80 loop that reduce the degree of jackknifing interfere with microtubule-kinetochore attachment (Zhang et al., 2012). We therefore favor a model in which the loss of attachment triggers NDC80 jackknifing. However, we note that an additional loss of nematic order within the NDC80 complexes is necessary to explain the measured distance changes. This hints at larger-scale reorganization in the outer kinetochore in the absence of microtubule binding. When kinetochores are attached, but no tension is generated, we find that the first 300 aa of Knl1 are unraveled, while NDC80 remains unchanged. What drives cycles of unraveling-raveling in the first 300 aa of Knl1 remains unknown. We also need to consider that taxol and nocodazole do not represent “physiological” conditions, and it will be important to develop assays to follow Knl1/Ndc80 re-organization during the prometaphase-to-metaphase transition.

The three kinetochore architectures defined in this work (attached, unattached, and tensionless) can be interpreted in terms of our present understanding of spindle checkpoint and er-

ror-correction mechanisms (see model in Figure 7F). The jackknifed NDC80 state is tightly correlated with the recruitment of Mad2 to kinetochores and activation of the spindle checkpoint, but it is not a downstream consequence, as the state exists when Mps1 is inhibited (Figure 7F, top). The formation of end-on attachment correlates with the NDC80 complexes straightening out and aligning. During this time, the Mps1 kinase is displaced from kinetochores because of the competition with microtubules for binding to the Ndc80 calponin homology domain (Figure 7F, center; Hiruma et al., 2015; Ji et al., 2015). One idea is that the auto-inhibited Ndc80 conformation gates the recruitment of Mad1:Mad2, perhaps by favoring Mps1 binding. This model is different from that presented in budding yeast, which proposes that attachment separates Mps1 from the Knl1 substrate, thus silencing the checkpoint (Aravamudhan et al., 2015). However, at bi-oriented human kinetochores, the Ndc80 head domain (which binds Mps1) and Knl1 MELTs (marked by the average position of Bub1) are only 26.9 ± 1.4 nm apart (Figure 7F, bottom). Nevertheless, conformational changes in Ndc80 appear to be a conserved feature of the mechanisms that monitor microtubule attachment.

Our data also suggest that the loss of tension (taxol) is not sufficient to activate the spindle checkpoint; the tensionless kinetochores do not jackknife NDC80 and have undetectable levels of Mad2 (Figure 7F, center). The detected mitotic delays during metaphase are likely due to a sub-population of unattached kinetochores (which do jackknife NDC80), as previously suggested (Magidson et al., 2016), although we cannot yet formally rule out weak checkpoint signals (without detectable Mad2 binding). We also propose that taxol-treated kinetochores reflect a “transition state” between the attached (and under tension) and unattached states (see model in Figure 7F for details). While the Aurora B site in the now-unraveled amino terminus of Knl1 is dephosphorylated, fluorescence lifetime imaging microscopy-Förster resonance energy transfer (FLIM/FRET) measurements

Figure 7. Knl1 1–300 Unravels upon the Loss of Kinetochore Tension

(A) Kinetochore pairs stained with anti-Bub1, anti-Rod, and anti-Zwisch antibodies in cells treated with 1 μ M taxol for 15 min. Scale bars, 500 nm.
 (B) Histograms of the Δ_{EC} distances from CenpC to Bub1, Rod, Zwisch, Knl1-MELT2, and pKnl1(S24) in DMSO and taxol. Mean (dashed line) and SD values are indicated at right.
 (C) Schematic map of Knl1 where the positions of Serine24 (Ser24, orange), MELT repeats (blue), and MIS12-Zwint-binding domain (gray) are shown. Lines indicate the PP1-microtubule binding site (green) and the unstructured region (red). Arrows indicate the binding sites of anti-Knl1-pS24 and anti-Knl1(MELT2) antibodies used in this study.
 (D) Top: kinetochores stained with anti-CenpC and anti-Knl1-pS24 antibodies in cells treated with 3.3 μ M nocodazole for 2 h, 1 μ M taxol for 15 min, or DMSO. Scale bar, 500 nm. Insets show enlargements for the indicated kinetochores. Scale bar, 250 nm. Bottom: histograms of the Δ_{EC} between CenpC and Knl1-pS24 in cells treated as above. Mean (dashed line) and SD values are indicated below. Cumulative frequency plots display the Knl1-pS24 intensity in DMSO-, nocodazole (+noc)-, and taxol-treated cells. The Knl1-pS24 signal is normalized to the CenpC signal. Signals are background subtracted.
 (E) Top: kinetochores stained with anti-CenpC and anti-Knl1(MELT2) antibodies and treated as in (D). Scale bars, 500 nm. Bottom: histograms of the Δ_{EC} distances between CenpC and Knl1 in DMSO-, nocodazole (+noc)-, and taxol-treated cells. Mean (dashed line) and SD values are indicated at right.
 (F) Schematics representing the ensemble average arrangement of MIS12 complex (dark blue), NDC80 complex (light blue), Bub1 (orange), RZZ complex (green), Mad1:Mad2 (yellow), Knl1 (black), and SKA (purple) in RPE1 cells treated with nocodazole (top), taxol (center), and DMSO (bottom). A single microtubule protofilament is shown in gray and dotted lines represent the position of the indicated complexes in control cells. The arrows indicate the change in position between different conditions. The positions of proteins marked with an asterisk are inferred from known biochemical data. These kinetochore organizational states can be integrated with known checkpoint and error-correction mechanisms as follows: at unattached kinetochores (top), NDC80 is disordered and in an auto-inhibited state, while the first 300 aa of Knl1 are in an extended conformation. Aurora B kinase activity dominates, kinetochore substrates (i.e., Ndc80 and Knl1) are phosphorylated, and Ndc80 is in a low-affinity microtubule-binding state. We note that Mad1 can bridge from the outer kinetochore to the corona, with interactions at either end necessary for stable binding and spindle checkpoint activation. When end-on attachment forms (center), but no tension is generated (e.g., monotelic attachments in which one sister is attached and the other is unattached), the checkpoint is silenced on the attached sister concomitantly with the straightening of Ndc80, which binds to the microtubule lattice. As force from the microtubule depolymerization generates tension (bottom), SKA complexes are recruited and the Knl1 amino terminus ravel. PP1 now fully binds, leading to kinetochore dephosphorylation (counteracting Aurora B) and increased microtubule binding affinity. This model can also explain error correction following the loss of tension at a bi-oriented kinetochore, which would switch the system into the transition (center panel) state (see Discussion for details).



in taxol-treated cells show that the affinity of NDC80 complexes for microtubules is reduced, an event associated with increased Aurora B recruitment (Yoo et al., 2018). This may be explained by the spatial separation between Knl-pS24 and Ndc80(N) that we observe under that condition. We also need to consider the impact of PP1 recruitment to the amino terminus of Knl1, which competes with microtubules (Bajaj et al., 2018). Understanding how changes in NDC80 microtubule-binding affinity and the spatial balance of phosphatase-kinase activity within the kinetochore are related to the unraveling of Knl1 (and other mechanical transitions) will be an important next step.

In conclusion, our data suggest that kinetochores are able to distinguish between changes in tension and microtubule occupancy using in-built occupancy (Ndc80) and tension (Knl1) sensors.

STAR★METHODS

Detailed methods are provided in the online version of this paper and include the following:

- KEY RESOURCES TABLE
- LEAD CONTACT AND MATERIALS AVAILABILITY
- EXPERIMENTAL MODEL AND SUBJECT DETAILS
- METHOD DETAILS
 - Construction and verification of cell lines
 - Drug treatments and siRNA transfection
 - Immunofluorescence microscopy
 - Delta distance and intensity measurements
 - Assay for spindle assembly checkpoint activity
 - Long term live-cell imaging
 - Photoactivation experiments
- QUANTIFICATION AND STATISTICAL ANALYSIS
- DATA AND CODE AVAILABILITY

SUPPLEMENTAL INFORMATION

Supplemental Information can be found online at <https://doi.org/10.1016/j.celrep.2020.107535>.

ACKNOWLEDGMENTS

We thank O. Sen for help validating the cell lines; A. Saurin, A. Musacchio, and I. Cheeseman for the antibodies; J. Pines for the cell lines; G. Chan for the EGFP-Zw10 construct; and V. Silió for construction of the stable EGFP-Zw10 RPE1 line. We also thank the CAMDU (Computing and Advanced Microscopy Unit) for support and J. Harrison for proofreading the manuscript. This work was supported by the Leverhulme Trust (RPG-2017-349 to A.D.M. and N.J.B.). Work in the A.D.M. lab was also supported by a Wellcome Trust Senior Investigator Award (106151/Z/14/Z) and a Royal Society Wolfson Research Merit Award (WM150020). T.E.G. and A.I.T. are funded by the Medical Research Council Doctoral Training Partnership grant MR/J003964/1.

AUTHOR CONTRIBUTIONS

A.D.M. and N.J.B. were responsible for the project conception, planning, and supervision. E.R. carried out the experiments, except for mapping the SKA position (T.E.G.) and the photoactivation experiments (A.I.T.). E.R. carried out the data analysis, with help from T.E.G., and M.E. generated the Ndc80-EGFP knockin cell lines. A.D.M., N.J.B., E.R., and T.E.G. interpreted the data. C.A.S. developed the kinetochore analysis code. N.J.B. developed the

Euclidean distance correction algorithm. P.A.E. built the visualizations of the kinetochore organization. A.D.M. and N.J.B. prepared the manuscript, with input from E.R. and T.E.G.

DECLARATION OF INTERESTS

The authors declare no competing interests.

Received: August 6, 2019

Revised: February 10, 2020

Accepted: March 27, 2020

Published: April 28, 2020

SUPPORTING CITATIONS

The following references appear in the Supplemental Information: Alushin et al. (2010); Booth et al. (2011); Churchman et al. (2006); Ciferri et al. (2005); Joglekar et al. (2006); Ledbetter and Porter (1963); Maiolica et al. (2007); Musacchio and Desai (2017); Petrovic et al. (2014); Craiu and Rosenthal, 2014; Nixon et al., 2015.

REFERENCES

- Allan, L.A., Camacho Reis, M., Ciossani, G., Huis in 't Veld, P.J., Wohlgemuth, S., Kops, G.J., Musacchio, A., and Saurin, A.T. (2020). Cyclin B1 scaffolds MAD1 at the kinetochore corona to activate the mitotic checkpoint. *EMBO J.*, e103180.
- Alushin, G.M., Ramey, V.H., Pasqualato, S., Ball, D.A., Grigorieff, N., Musacchio, A., and Nogales, E. (2010). The Ndc80 kinetochore complex forms oligomeric arrays along microtubules. *Nature* 467, 805–810.
- Amaro, A.C., Samora, C.P., Holtackers, R., Wang, E., Kingston, I.J., Alonso, M., Lampson, M., McAnish, A.D., and Meraldi, P. (2010). Molecular control of kinetochore-microtubule dynamics and chromosome oscillations. *Nat. Cell Biol.* 12, 319–329.
- Aravamudhan, P., Goldfarb, A.A., and Joglekar, A.P. (2015). The kinetochore encodes a mechanical switch to disrupt spindle assembly checkpoint signaling. *Nat. Cell Biol.* 17, 868–879.
- Auckland, P., and McAnish, A.D. (2015). Building an integrated model of chromosome congression. *J. Cell Sci.* 128, 3363–3374.
- Bajaj, R., Bollen, M., Peti, W., and Page, R. (2018). KNL1 Binding to PP1 and Microtubules Is Mutually Exclusive. *Structure* 26, 1327–1336.e4.
- Booth, D.G., Hood, F.E., Prior, I.A., and Royle, S.J. (2011). A TACC3/ch-TOG/clathrin complex stabilises kinetochore fibres by inter-microtubule bridging. *EMBO J.* 30, 906–919.
- Brinkley, B.R., Ouspenski, I., and Zinkowski, R.P. (1992). Structure and molecular organization of the centromere-kinetochore complex. *Trends Cell Biol.* 2, 15–21.
- Burroughs, N.J., Harry, E.F., and McAnish, A.D. (2015). Super-resolution kinetochore tracking reveals the mechanisms of human sister kinetochore directional switching. *eLife* 4, e09500.
- Cheeseman, I.M., Chappie, J.S., Wilson-Kubalek, E.M., and Desai, A. (2006). The conserved KMN network constitutes the core microtubule-binding site of the kinetochore. *Cell* 127, 983–997.
- Churchman, L.S., Okten, Z., Rock, R.S., Dawson, J.F., and Spudich, J.A. (2005). Single molecule high-resolution colocalization of Cy3 and Cy5 attached to macromolecules measures intramolecular distances through time. *Proc. Natl. Acad. Sci. USA* 102, 1419–1423.
- Churchman, L.S., Flyvbjerg, H., and Spudich, J.A. (2006). A non-Gaussian distribution quantifies distances measured with fluorescence localization techniques. *Biophys. J.* 90, 668–671.
- Ciferri, C., De Luca, J., Monzani, S., Ferrari, K.J., Ristic, D., Wyman, C., Stark, H., Kilmartin, J., Salmon, E.D., and Musacchio, A. (2005). Architecture of the human ndc80-hec1 complex, a critical constituent of the outer kinetochore. *J. Biol. Chem.* 280, 29088–29095.

- Ciferri, C., Pasqualato, S., Screpanti, E., Varetto, G., Santaguida, S., Dos Reis, G., Maiolica, A., Polka, J., De Luca, J.G., De Wulf, P., et al. (2008). Implications for kinetochore-microtubule attachment from the structure of an engineered Ndc80 complex. *Cell* 133, 427–439.
- Collin, P., Nashchekina, O., Walker, R., and Pines, J. (2013). The spindle assembly checkpoint works like a rheostat rather than a toggle switch. *Nat. Cell Biol.* 15, 1378–1385.
- Craiu, R.V., and Rosenthal, J.S. (2014). Bayesian Computation via Markov Chain Monte Carlo. *Annual Review of Statistics and Its Application* 7, 179–201.
- Currie, C.E., Mora-Santos, M., Smith, C.A., McAinsh, A.D., and Millar, J.B.A. (2018). Bub1 is not essential for the checkpoint response to unattached kinetochores in diploid human cells. *Curr. Biol.* 28, R929–R930.
- de Gennes, P.G., and Prost, J. (1993). *The Physics of Liquid Crystals*, Second Edition (Clarendon Press).
- DeLuca, J.G., Gall, W.E., Ciferri, C., Cimini, D., Musacchio, A., and Salmon, E.D. (2006). Kinetochore microtubule dynamics and attachment stability are regulated by Hec1. *Cell* 127, 969–982.
- Doostmohammadi, A., Ignés-Mulloi, J., Yeomans, J.M., and Sagués, F. (2018). Active nematics. *Nat. Commun.* 9, 3246.
- Dudka, D., Noatynska, A., Smith, C.A., Liaudet, N., McAinsh, A.D., and Meraldi, P. (2018). Complete microtubule-kinetochore occupancy favours the segregation of merotelic attachments. *Nat. Commun.* 9, 2042.
- Etemad, B., Kuijt, T.E., and Kops, G.J. (2015). Kinetochore-microtubule attachment is sufficient to satisfy the human spindle assembly checkpoint. *Nat. Commun.* 6, 8987.
- Etemad, B., Vertesy, A., Kuijt, T.E.F., Sacristan, C., van Oudenaarden, A., and Kops, G. (2019). Spindle checkpoint silencing at kinetochores with submaximal microtubule occupancy. *J. Cell Sci.* 132, jcs231589.
- Famulski, J.K., and Chan, G.K. (2007). Aurora B kinase-dependent recruitment of hZW10 and hROD to tensionless kinetochores. *Curr. Biol.* 17, 2143–2149.
- Gascoigne, K.E., Takeuchi, K., Suzuki, A., Hori, T., Fukagawa, T., and Cheeseman, I.M. (2011). Induced ectopic kinetochore assembly bypasses the requirement for CENP-A nucleosomes. *Cell* 145, 410–422.
- Hamilton, G., Dimitrova, Y., and Davis, T.N. (2019). Seeing is believing: our evolving view of kinetochore structure, composition, and assembly. *Curr. Opin. Cell Biol.* 60, 44–52.
- Helgeson, L.A., Zelter, A., Riffle, M., MacCoss, M.J., Asbury, C.L., and Davis, T.N. (2018). Human Ska complex and Ndc80 complex interact to form a load-bearing assembly that strengthens kinetochore-microtubule attachments. *Proc. Natl. Acad. Sci. USA* 115, 2740–2745.
- Hiruma, Y., Sacristan, C., Pachis, S.T., Adamopoulos, A., Kuijt, T., Ubbink, M., von Castelmur, E., Perrakis, A., and Kops, G.J. (2015). Competition between MPS1 and microtubules at kinetochores regulates spindle checkpoint signaling. *Science* 348, 1264–1267.
- Huis In 't Veld, P.J., Jeganathan, S., Petrovic, A., Singh, P., John, J., Krenn, V., Weissmann, F., Bange, T., and Musacchio, A. (2016). Molecular basis of outer kinetochore assembly on CENP-T. *eLife* 5, e21007.
- Huis In 't Veld, P.J., Volkov, V.A., Stender, I.D., Musacchio, A., and Dogterom, M. (2019). Molecular determinants of the Ska-Ndc80 interaction and their influence on microtubule tracking and force-coupling. *eLife* 8, e49539.
- Ji, Z., Gao, H., and Yu, H. (2015). CELL DIVISION CYCLE. Kinetochore attachment sensed by competitive Mps1 and microtubule binding to Ndc80C. *Science* 348, 1260–1264.
- Joglekar, A.P., Bouck, D.C., Molk, J.N., Bloom, K.S., and Salmon, E.D. (2006). Molecular architecture of a kinetochore-microtubule attachment site. *Nat. Cell Biol.* 8, 581–585.
- Johnston, K., Joglekar, A., Hori, T., Suzuki, A., Fukagawa, T., and Salmon, E.D. (2010). Vertebrate kinetochore protein architecture: protein copy number. *J. Cell Biol.* 189, 937–943.
- Kim, S., Sun, H., Tomchick, D.R., Yu, H., and Luo, X. (2012). Structure of human Mad1 C-terminal domain reveals its involvement in kinetochore targeting. *Proc. Natl. Acad. Sci. USA* 109, 6549–6554.
- Klare, K., Weir, J.R., Basilico, F., Zimniak, T., Massimiliano, L., Ludwigs, N., Herzog, F., and Musacchio, A. (2015). CENP-C is a blueprint for constitutive centromere-associated network assembly within human kinetochores. *J. Cell Biol.* 210, 11–22.
- Kops, G.J., Kim, Y., Weaver, B.A., Mao, Y., McLeod, I., Yates, J.R., 3rd, Tagaya, M., and Cleveland, D.W. (2005). ZW10 links mitotic checkpoint signaling to the structural kinetochore. *J. Cell Biol.* 169, 49–60.
- Kuhn, J., and Dumont, S. (2017). Spindle assembly checkpoint satisfaction occurs via end-on but not lateral attachments under tension. *J. Cell Biol.* 216, 1533–1542.
- Lampson, M.A., and Cheeseman, I.M. (2011). Sensing centromere tension: Aurora B and the regulation of kinetochore function. *Trends Cell Biol.* 21, 133–140.
- Ledbetter, M.C., and Porter, K.R. (1963). A “Microtubule” in Plant Cell Fine Structure. *J. Cell Biol.* 19, 239–250.
- London, N., Ceto, S., Ranish, J.A., and Biggins, S. (2012). Phosphoregulation of Spc105 by Mps1 and PP1 regulates Bub1 localization to kinetochores. *Curr. Biol.* 22, 900–906.
- Long, A.F., Kuhn, J., and Dumont, S. (2019). The mammalian kinetochore-microtubule interface: robust mechanics and computation with many microtubules. *Curr. Opin. Cell Biol.* 60, 60–67.
- Magidson, V., He, J., Ault, J.G., O’Connell, C.B., Yang, N., Tikhonenko, I., McEwen, B.F., Sui, H., and Khodjakov, A. (2016). Unattached kinetochores rather than intrakinetochore tension arrest mitosis in taxol-treated cells. *J. Cell Biol.* 212, 307–319.
- Maiolica, A., Cittaro, D., Borsotti, D., Sennels, L., Ciferri, C., Tarricone, C., Musacchio, A., and Rappsilber, J. (2007). Structural analysis of multiprotein complexes by cross-linking, mass spectrometry, and database searching. *Mol. Cell. Proteomics* 6, 2200–2211.
- Maresca, T.J., and Salmon, E.D. (2009). Intrakinetochore stretch is associated with changes in kinetochore phosphorylation and spindle assembly checkpoint activity. *J. Cell Biol.* 184, 373–381.
- Maresca, T.J., and Salmon, E.D. (2010). Welcome to a new kind of tension: translating kinetochore mechanics into a wait-anaphase signal. *J. Cell Sci.* 123, 825–835.
- McAinsh, A.D., Meraldi, P., Draviam, V.M., Toso, A., and Sorger, P.K. (2006). The human kinetochore proteins Nnf1R and Mcm21R are required for accurate chromosome segregation. *EMBO J.* 25, 4033–4049.
- Mosalaganti, S., Keller, J., Altenfeld, A., Winzler, M., Rombaut, P., Saur, M., Petrovic, A., Wehenkel, A., Wohlgemuth, S., Müller, F., et al. (2017). Structure of the RZZ complex and molecular basis of its interaction with Spindly. *J. Cell Biol.* 216, 961–981.
- Musacchio, A., and Desai, A. (2017). A Molecular View of Kinetochore Assembly and Function. *Biology (Basel)* 6, E5.
- Nicklas, R.B., and Koch, C.A. (1969). Chromosome micromanipulation. 3. Spindle fiber tension and the reorientation of mal-oriented chromosomes. *J. Cell Biol.* 43, 40–50.
- Nicklas, R.B., Ward, S.C., and Gorbsky, G.J. (1995). Kinetochore chemistry is sensitive to tension and may link mitotic forces to a cell cycle checkpoint. *J. Cell Biol.* 130, 929–939.
- Nixon, F.M., Gutiérrez-Caballero, C., Hood, F.E., Booth, D.G., Prior, I.A., and Royle, S.J. (2015). The mesh is a network of microtubule connectors that stabilizes individual kinetochore fibers of the mitotic spindle. *eLife* 4, e07635.
- Olziersky, A.M., Smith, C.A., Burroughs, N., McAinsh, A.D., and Meraldi, P. (2018). Mitotic live-cell imaging at different timescales. *Methods Cell Biol.* 145, 1–27.
- Pesenti, M.E., Weir, J.R., and Musacchio, A. (2016). Progress in the structural and functional characterization of kinetochores. *Curr. Opin. Struct. Biol.* 37, 152–163.
- Petrovic, A., Pasqualato, S., Dube, P., Krenn, V., Santaguida, S., Cittaro, D., Monzani, S., Massimiliano, L., Keller, J., Tarricone, A., et al. (2010). The MIS12 complex is a protein interaction hub for outer kinetochore assembly. *J. Cell Biol.* 190, 835–852.



- Petrovic, A., Moslaganti, S., Keller, J., Mattiuzzo, M., Overlack, K., Krenn, V., De Antoni, A., Wohlgemuth, S., Cecatiello, V., Pasqualato, S., et al. (2014). Modular assembly of RWD domains on the Mis12 complex underlies outer kinetochore organization. *Mol. Cell* 53, 591–605.
- Rago, F., and Cheeseman, I.M. (2013). Review series: the functions and consequences of force at kinetochores. *J. Cell Biol.* 200, 557–565.
- Ran, F.A., Hsu, P.D., Wright, J., Agarwala, V., Scott, D.A., and Zhang, F. (2013). Genome engineering using the CRISPR-Cas9 system. *Nat. Protoc.* 8, 2281–2308.
- Scarborough, E.A., Davis, T.N., and Asbury, C.L. (2019). Tight bending of the Ndc80 complex provides intrinsic regulation of its binding to microtubules. *eLife* 8, e44489.
- Scrapanti, E., De Antoni, A., Alushin, G.M., Petrovic, A., Melis, T., Nogales, E., and Musacchio, A. (2011). Direct binding of Cenp-C to the Mis12 complex joins the inner and outer kinetochore. *Curr. Biol.* 21, 391–398.
- Shepherd, L.A., Meadows, J.C., Sochaj, A.M., Lancaster, T.C., Zou, J., Buttrick, G.J., Rappsilber, J., Hardwick, K.G., and Millar, J.B. (2012). Phosphodependent recruitment of Bub1 and Bub3 to Spc7/KNL1 by Mph1 kinase maintains the spindle checkpoint. *Curr. Biol.* 22, 891–899.
- Silió, V., McAinsh, A.D., and Millar, J.B. (2015). KNL1-Bubs and RZZ Provide Two Separable Pathways for Checkpoint Activation at Human Kinetochores. *Dev. Cell* 35, 600–613.
- Sironi, L., Mapelli, M., Knapp, S., De Antoni, A., Jeang, K.T., and Musacchio, A. (2002). Crystal structure of the tetrameric Mad1-Mad2 core complex: implications of a 'safety belt' binding mechanism for the spindle checkpoint. *EMBO J.* 21, 2496–2506.
- Smith, C.A., McAinsh, A.D., and Burroughs, N.J. (2016). Human kinetochores are swivel joints that mediate microtubule attachments. *eLife* 5, e16159.
- Suzuki, A., Hori, T., Nishino, T., Usukura, J., Miyagi, A., Morikawa, K., and Fukagawa, T. (2011). Spindle microtubules generate tension-dependent changes in the distribution of inner kinetochore proteins. *J. Cell Biol.* 193, 125–140.
- Suzuki, A., Badger, B.L., Wan, X., DeLuca, J.G., and Salmon, E.D. (2014). The architecture of CCAN proteins creates a structural integrity to resist spindle forces and achieve proper intrakinetochore stretch. *Dev. Cell* 30, 717–730.
- Suzuki, A., Long, S.K., and Salmon, E.D. (2018). An optimized method for 3D fluorescence co-localization applied to human kinetochore protein architecture. *eLife* 7, e32418.
- Tanaka, T.U., Stark, M.J., and Tanaka, K. (2005). Kinetochore capture and bio-orientation on the mitotic spindle. *Nat. Rev. Mol. Cell Biol.* 6, 929–942.
- Tauchman, E.C., Boehm, F.J., and DeLuca, J.G. (2015). Stable kinetochore-microtubule attachment is sufficient to silence the spindle assembly checkpoint in human cells. *Nat. Commun.* 6, 10036.
- Toso, A., Winter, J.R., Garrod, A.J., Amaro, A.C., Meraldi, P., and McAinsh, A.D. (2009). Kinetochore-generated pushing forces separate centrosomes during bipolar spindle assembly. *J. Cell Biol.* 184, 365–372.
- Uchida, K.S., Takagaki, K., Kumada, K., Hirayama, Y., Noda, T., and Hirota, T. (2009). Kinetochore stretching inactivates the spindle assembly checkpoint. *J. Cell Biol.* 184, 383–390.
- Wan, X., O'Quinn, R.P., Pierce, H.L., Joglekar, A.P., Gall, W.E., DeLuca, J.G., Carroll, C.W., Liu, S.T., Yen, T.J., McEwen, B.F., et al. (2009). Protein architecture of the human kinetochore microtubule attachment site. *Cell* 137, 672–684.
- Wan, X., Cimini, D., Cameron, L.A., and Salmon, E.D. (2012). The coupling between sister kinetochore directional instability and oscillations in centromere stretch in metaphase PtK1 cells. *Mol. Biol. Cell* 23, 1035–1046.
- Wang, H.W., Long, S., Ciferri, C., Westermann, S., Drubin, D., Barnes, G., and Nogales, E. (2008). Architecture and flexibility of the yeast Ndc80 kinetochore complex. *J. Mol. Biol.* 383, 894–903.
- Wei, R.R., Sorger, P.K., and Harrison, S.C. (2005). Molecular organization of the Ndc80 complex, an essential kinetochore component. *Proc. Natl. Acad. Sci. USA* 102, 5363–5367.
- Welburn, J.P., and Cheeseman, I.M. (2008). Toward a molecular structure of the eukaryotic kinetochore. *Dev. Cell* 15, 645–655.
- Welburn, J.P., Vleugel, M., Liu, D., Yates, J.R., 3rd, Lampson, M.A., Fukagawa, T., and Cheeseman, I.M. (2010). Aurora B phosphorylates spatially distinct targets to differentially regulate the kinetochore-microtubule interface. *Mol. Cell* 38, 383–392.
- Wilson-Kubalek, E.M., Cheeseman, I.M., Yoshioka, C., Desai, A., and Milligan, R.A. (2008). Orientation and structure of the Ndc80 complex on the microtubule lattice. *J. Cell Biol.* 182, 1055–1061.
- Yamagishi, Y., Yang, C.H., Tanno, Y., and Watanabe, Y. (2012). MPS1/Mph1 phosphorylates the kinetochore protein KNL1/Spc7 to recruit SAC components. *Nat. Cell Biol.* 14, 746–752.
- Yoo, T.Y., Choi, J.M., Conway, W., Yu, C.H., Pappu, R.V., and Needleman, D.J. (2018). Measuring NDC80 binding reveals the molecular basis of tension-dependent kinetochore-microtubule attachments. *eLife* 7, e36392.
- Zhang, G., Kelstrup, C.D., Hu, X.W., Kaas Hansen, M.J., Singleton, M.R., Olsen, J.V., and Nilsson, J. (2012). The Ndc80 internal loop is required for recruitment of the Ska complex to establish end-on microtubule attachment to kinetochores. *J. Cell Sci.* 125, 3243–3253.
- Zhang, G., Kruse, T., López-Méndez, B., Sylvestersen, K.B., Garvanska, D.H., Schopper, S., Nielsen, M.L., and Nilsson, J. (2017). Bub1 positions Mad1 close to KNL1 MELT repeats to promote checkpoint signalling. *Nat. Commun.* 8, 15822.
- Zhang, G., Kruse, T., Guasch Boldú, C., Garvanska, D.H., Coscia, F., Mann, M., Barisic, M., and Nilsson, J. (2019). Efficient mitotic checkpoint signaling depends on integrated activities of Bub1 and the RZZ complex. *EMBO J.* 38, e100977.

STAR★METHODS

KEY RESOURCES TABLE

REAGENT or RESOURCE	SOURCE	IDENTIFIER
Antibodies		
Guinea Pig polyclonal anti-CenpC (1:2000)	MBL	Cat#PD030; RRID:AB_10693556
Mouse monoclonal anti-CenpA (1:300)	Enzo	Cat#ADI-KAM-CC006-E; RRID:AB_2038993
Mouse monoclonal anti-Hec1 (9G3, 1:1000)	Abcam	Cat#ab3613; RRID:AB_303949
Mouse monoclonal anti-Bub1 (1:200)	Abcam	Cat#ab54893; RRID:AB_940664
Mouse monoclonal anti-Rod (1:50)	Abcam	Cat#ab56745; RRID:AB_943932
Mouse monoclonal anti-alpha tubulin (1:1000)	Sigma	Cat#T6074; RRID:AB_477582
Mouse monoclonal anti-Ska3 (1:2000)	Santa Cruz	Cat#sc-390326
Mouse monoclonal anti-Mad1 (F-7) (1:500)	Santa Cruz	Cat#sc-376613; RRID:AB_11151587
Rabbit polyclonal anti-alpha tubulin (1:1000)	Thermo Fisher	Cat# PA5-19489; RRID:AB_10984311
Rabbit polyclonal anti-Zwilch (1:1000)	A kind gift from Andrea Musacchio	N/A
Rabbit polyclonal anti-Nnf1 (1:1000)	McAinsh et al., 2006	N/A
Rabbit polyclonal anti-Knl1 (amino acids 300-350 MELT2, 1:500)	Abcam	Cat#ab70537; RRID:AB_1209410
Rabbit polyclonal anti-Mad2 (1:500)	BioLegend	Cat#Poly19246; RRID:AB_2565454
Rabbit polyclonal anti-Knl1-pS24 (1:2200)	Welburn et al., 2010	N/A
Rabbit polyclonal anti-CenpT (1:1000)	Gascoigne et al., 2011	N/A
Rabbit polyclonal anti-Mad1pT716 (1:1000)	Allan et al., 2020	N/A
Goat anti-guinea pig AlexaFluor 647 (1:500)	Invitrogen	Cat#A21450; RRID:AB_2735091
Goat anti-guinea pig AlexaFluor 488 (1:500)	Invitrogen	Cat#A11073; RRID:AB_2534117
Goat anti-guinea pig AlexaFluor 568 (1:500)	Invitrogen	Cat#A11075; RRID:AB_2534119
Goat anti-mouse AlexaFluor 488 (1:500)	Invitrogen	Cat#A32723; RRID:AB_2633275
Goat anti-mouse AlexaFluor 647 (1:500)	Invitrogen	Cat#A21235; RRID:AB_2535804
Goat anti-mouse AlexaFluor 594 (1:500)	Invitrogen	Cat# A11032; RRID:AB_2534091
Goat anti-rabbit AlexaFluor 488 (1:500)	Invitrogen	Cat#A11008; RRID:AB_143165
Goat anti-rabbit AlexaFluor 594 (1:500)	Invitrogen	Cat#A11037; RRID:AB_2534095
Chemicals, Peptides, and Recombinant Proteins		
Geneticin (G418)	GIBCO	Cat#10131027
Fugene 6	Promega	Cat#E2691
Oligofectamine	Invitrogen	Cat#12252-011
Nocodazole	Sigma-Aldrich	Cat#M1404
Taxol	Sigma-Aldrich	Cat#PHL89806
DMSO	Sigma-Aldrich	Cat#D2438
DAPI	Sigma-Aldrich	Cat#D9542
VectaShield	Vector	Cat#H-1000; RRID:AB_2336789
Oregon Green (2.5-5μM)	Promega	Cat#G2802
TMR (2μM)	Promega	Cat#G8252
JF549 (250-400nM)	Promega	Cat#GA1110
JF646 (400-800nM)	Promega	Cat#GA1120
SiR-DNA	Spirochrome	Cat#sc007
Reversine	Sigma-Aldrich	Cat#R3904
(S)-MG132	Cayman	Cat#10012628-5

(Continued on next page)



Continued		
REAGENT or RESOURCE	SOURCE	IDENTIFIER
Experimental Models: Cell Lines		
RPE1 HaloTag-CenpA (MC148)	This paper	N/A
RPE1 Ndc80-EGFP (MC191)	This paper	N/A
RPE1 EGFP-Zw10 (MC156)	This paper	N/A
RPE1 (MC133)	ATCC	Cat#CRL-4000; RRID:CVCL_4388
RPE1 <i>bub1</i> 1-23 (MC170)	Currie et al., 2018	N/A
RPE1 Venus-Mad2 (Mad2L1)	Kind gift from Jonathan Pines	N/A
RPE1 Photoactivatable(PA)-GFP-alpha-tubulin (MC021)	Toso et al., 2009	N/A
Oligonucleotides		
Small guide RNA (sgRNA) 5'-caccgATGCATGTTCAGAAGATCTCT-3'	This paper	N/A
Small guide RNA (sgRNA) 5'-aacAGAGATCTTCTGACATGCATc-3'	This paper	N/A
Primer: Fwd_Ndc80EGFP 5'-TAAACTGCAGCCATATGTAGTAAC-3'	This paper	N/A
Primer: Rev_Ndc80EGFP 5'-TTGAAATTAGTAAGAAATGAGAGA-3'	This paper	N/A
Primer: EGFPNtRev 5'-CCGGACACGCTGAACTTG-3'	This paper	N/A
Primer: Rev_Ndc80-EGFP 5'-TTGAAATTAGTAAGAAATGAGAGA-3'	This paper	N/A
CenpT siRNA oligo#1 5'-CAAGAGAGCAGTTGCGGCA-3'	Gascoigne et al., 2011 (obtained from Sigma-Aldrich)	N/A
CenpT siRNA oligo#2 5'-GACGATAGCCAGAGGGCGT-3'	Gascoigne et al., 2011 (obtained from Sigma-Aldrich)	N/A
CenpT siRNA oligo#3 5'-AAGTAGAGCCCTTACACGA-3'	Gascoigne et al., 2011 (obtained from Sigma-Aldrich)	N/A
CenpT siRNA oligo#4 5'-CGGAGAGCCCTGCTTGAAA-3'	Gascoigne et al., 2011 (obtained from Sigma-Aldrich)	N/A
CenpC siRNA oligo 5'-GGATCATCTCAGAATAGAA-3'	Klare et al., 2015 (obtained from Sigma-Aldrich)	N/A
All Star RNAi oligo	QIAGEN	Cat#1027281
Recombinant DNA		
pX330-U6-Chimeric_BB-CBh-hSpCas9	Addgene	Cat#42230; RRID:Addgene_42230
Ndc80 Homology directed repair construct (HDR)	This paper	N/A
EGFP-Zw10 plasmid (pMC453)	Famulski and Chan, 2007	N/A
HaloTag-CenpA (pMC442)	This paper	N/A
Software and Algorithms		
Kit 2.1.10	This paper; Olziersky et al., 2018	https://github.com/cmcb-warwick
Euclidian correction	This paper, on request	N/A
Huygens 4.1 (Deconvolution software)	SVI	N/A
Volocity 6.0 (UltraView microscope software)	PerkinElemer	N/A
MATLAB (2017a and 2018a)	MathWorks	N/A
softWoRX 6.0 (DeltaVision microscope software)	Applied Precision	N/A
SlideBook 6.0 (Marianas microscope software)	3i	N/A
Fiji	Open source	N/A

LEAD CONTACT AND MATERIALS AVAILABILITY

Reagents generated in this study will be made available on request to the Lead Contact, Andrew McAinsh (A.D.McAinsh@warwick.ac.uk), but we may require a payment and/or a completed Materials Transfer Agreement if there is potential for commercial application.

EXPERIMENTAL MODEL AND SUBJECT DETAILS

Immortalized (hTERT) diploid human retinal pigment epithelial (RPE1) cells, RPE1 *bub1 1-23* (MC170; (Currie et al., 2018)), RPE1 Ndc80-EGFP (MC191), RPE1 Venus-Mad2 (Mad2L1 Venus/+; kind gift from Jonathan Pines), RPE1 HaloTag-CenpA (MC148), RPE1 eGFP-Zw10 (MC156) and RPE1 expressing photoactivatable PA-EGFP-alpha-tubulin (MC021, Toso et al., 2009) were grown in DMEM/F-12 medium containing 10% fetal bovine serum (FBS), 2 mM L-glutamine, 100 U/ml penicillin and 100 µg/ml streptomycin. 200 µg/ml and 300 µg/ml Geneticin (G418) were added to the media to maintain MC021 and MC148 cells, respectively. All cell cultures were maintained at 37°C with 5% CO₂ in a humidified incubator.

METHOD DETAILS

Construction and verification of cell lines

The RPE1 HaloTag-CenpA (MC148) cell line was generated by transfecting RPE1 cell with the HaloTag-CenpA (pMC442) plasmid. After 24hr cells were plated in selective media containing 300 µg/ml Geneticin (G418). Subsequently, positive clones were visually selected after addition of 2 µM TMR. To generate the RPE1 eGFP-Zw10 (MC156) cell line, RPE1 cells were transfected with EGFP-Zw10 plasmid (pMC453). After 24 hr, EGFP-expressing cells were isolated by FACS sorting and single clones were selected by visual inspection. For CRISPR engineered RPE1 cell lines small guide RNAs (sgRNAs) (5'-caccgATGCATGTCAGAAGATCTCT-3' and 5'-aaacAGAGATCTTCTGACATGCATc-3') targeting exon 17 of the NDC80 gene were designed using <http://zlab.bio/guide-design-resources> to insert 3xFlagtag-EGFP in frame just prior to the stop codon. sgRNAs were annealed and ligated into pX330 which enables their expression in mammalian cells along with a humanized *S. pyogenes* Cas9 (Ran et al., 2013). A homology Directed Repair (HDR) construct was designed with 800bp homology upstream of the Stop codon and 800 bp downstream of the stop codon. 1 µg of sgRNA construct and 1.5 µg of linearized HDR plasmid were transfected into RPE1 cells using Fugene 6. Positive cells were FACS sorted to isolate the Ndc80-EGFP expressing cells and single clones were identified by visual inspection with confocal microscope, with a further round of clonal selection used to eliminate heterogeneity in the population. PCR analysis of clone MC191 confirmed the presence of a wild-type and EGFP-containing allele (primers: Fwd_Ndc80EGFP, 5'-TAAACTGCAGCCATATG TAGTAAC-3'; Rev_Ndc80EGFP, 5'-TTGAAATTAGTAAGAAATGAGAGA-3'). Individual alleles were then analyzed by cloning PCR products and sequencing the products (primers: EGFPntRev 5'-CCGGACACGCTGAACCTTG-3' for the EGFP containing allele band and Rev_Ndc80-EGFP 5'-TTGAAATTAGTAAGAAATGAGAGA-3' for the wild-type allele band). This confirmed that the EGFP was in-frame with the 3' end of NDC80, although a single amino acid change (Threonine 635 to Alanine, T635A) was identified in the unstructured tail distal to the coiled coils that are required for NDC80 complex tetramerisation. We also note that this variant is found in all primates, except *H. sapiens* and *H. Neanderthalensis*, and that no difference in mitotic timing or multiple delta measurements (Table S1) were detected when compared to parental RPE1 cells (Figure S2). All cell lines were verified by comparing their mitotic timing with parental controls using long term live cell imaging (see below).

Drug treatments and siRNA transfection

For drug treatments, cells were plated on glass coverslips (0.16-0.19 mm) 24 or 48 hr before treatment with 3.3 µM nocodazole (diluted in DMSO) for 2 hr, 1 µM taxol (diluted in DMSO) for 15 min or with 0.1% DMSO for 2 hr as a control. In our experimental set-up, we found that treatment with 3.3 µM nocodazole for 15 min tended to leave microtubules stubs in some kinetochores. Thus, we used a 2 hr nocodazole treatment to ensure depolymerization of all microtubules. We note that a 45 min treatment did also eliminated microtubules and produced similar changes in kinetochores organization. Inhibition of Mps1 was performed using 1 µM reversine in the presence of 3.3 µM nocodazole and 10 µM MG132 for 1 hr. As controls, cells were treated with either DMSO and 10µM MG132 or 3.3 µM nocodazole and 10 µM MG132 for 1hr. To deplete CenpT and CenpC, siRNA oligos targeting their mRNA coding sequences were transfected into RPE1 Ndc80-EGFP (MC191) cells and incubated for 48 hr. For CenpT we used 100 nM of 4 pooled siRNA oligos (25 nM each), whereas for CenpC we transfected 60 nM of a single siRNA oligo. As control, we used 100 nM of the siRNA AllStar oligo. Transfection was performed using oligofectamine following manufacturer's instructions. All depletions were verified by immunofluorescence microscopy (see below).

Immunofluorescence microscopy

Cells were then fixed in 10 mM EGTA, 1 mM MgCl₂, 20 mM PIPES pH 6.8, 0.2% Triton X-100, and 4% formaldehyde for 10 min, washed 3 times in PBS before incubation in PBS supplemented with 3% BSA for 30 min to block non-specific antibody binding. Next, cells were incubated with primary antibodies for 1 hr, washed 3 times in PBS and then incubated for 30 min with secondary antibodies and DAPI (1:1000 dilution); all antibodies were diluted in PBS + 3% BSA. Cells were then washed in PBS and mounted



in Vectashield. For experiments that include Ska staining (i.e., CenpC/Ndc80(C)/Ska3 staining), cells were pre-extracted prior to fixation for 1 min with 10 mM EGTA, 1 mM MgCl₂, 20 mM PIPES pH 6.8, 0.2% Triton X-100. Image stacks were acquired using a confocal spinning-disk microscope (VOX UltraView; PerkinElmer, UK) equipped with a 100X / 1.4 NA oil-immersion objective and a Hamamatsu ORCA-R2 camera, controlled by Volocity 6.0 (PerkinElmer) running on a Windows 7 64-bit (Microsoft, Redmond, WA) PC (IBM, New Castle, NY). Image stacks were acquired over 61 z-slices separated by 0.2 μm (for the samples) or over 121 z-slices separated by 0.1 μm (for the chromatic shift slide, see below) using the 488, 561, 640 and 405 nm wavelength lasers. Acquisition settings were set in order that the kinetochore signals were typically larger than 50 units above background.

Delta distance and intensity measurements

Spinning disc images were exported from Volocity 6.0 in OME.TIFF format (The Open Microscopy Environment, UK) and deconvolved using Huygens 4.1, using point spread functions (PSFs) calculated from 100 nm TetraSpeck fluorescent microspheres using the Huygens 4.1 PSF distiller. Where required, images in the 640 nm wavelength were deconvolved within Huygens 4.1 using a theoretical PSF. Deconvolved images were exported from Huygens 4.1 in r3d format and read into MATLAB using the loci-tools java library (The Open Microscopy Environment). Kinetochore spots were first detected using the 561 or 640 nm channel and then (where appropriate) signals from secondary and tertiary markers were identified (Smith et al., 2016). Initial alignment of all three channels was carried out using images taken from a reference slide (either RPE1 HaloTag-CenpA labeled with Oregon Green, TMR or JF549 and JF646; or anti-CenpA stained with a mix of alexa488, 568 and 647-labeled secondary antibodies) on the day of experiment acquisition (Dudka et al., 2018; Smith et al., 2016). Final outer kinetochore positions were corrected (for chromatic aberrations) per cell so that cell-average intra-kinetochore distance was equal to zero in each the microscope x-, y- and z-coordinates, as is the average orientation previously demonstrated (Dudka et al., 2018; Smith et al., 2016). Kinetochore tracking, sister pairing, 3D delta and intensity measurements were made using KiT (Kinetochore Tracking) v2.1.10. Delta 3D (Δ3D) distances were corrected using an Euclidean correction algorithm (see Methods S1) that outputs the Euclidian corrected delta parameter (termed ΔEC). For measurement of Bub1, Mad2, Mad1-pT716, Zwilch and Knl1-pS24 signal, intensities were background subtracted and then normalized using the CenpC signal as a reference (also background subtracted). For measurement of endogenous Ndc80-EGFP and Venus-Mad2, and CenpT and CenpC within the RNAi experiments, the background subtracted and non-normalized signal is reported.

Assay for spindle assembly checkpoint activity

Cells were cultured in four compartment CELLview dish (627975, Greiner Bio-One Ltd.). Time-lapse imaging was performed on an Olympus DeltaVision microscope (Applied Precision, LLC) equipped with a Photometrics CoolSNAP HQ camera (Roper Scientific) and a stage-top incubator (TokaiHit) to maintain cells at 37°C and 5% CO₂. Temperature was further stabilized using a microscope enclosure (Weather station; Precision Control) held at 37°C. Image stacks (7 × 2 μm optical sections) were acquired using the softWoRX 6.0 software every 3 min using a 40x / 1.3 NA oil-immersion objective. To visualize the DNA, 1 hr before imaging cells were incubated with DMEM/F-12 media containing 0.5 μM SiR-DNA (Spirochrome). In each experiment, only fields (1024 × 1024 pixels) containing at least one metaphase cells were imaged using the point visit function in softWoRX 6.0. Imaging started after the addition of DMSO or 1 μM taxol-containing media. Cells were imaged for 15 min to reproduce the same conditions used for the fixed cell experiments. For experiments with RPE1 bub1 1-23 cells imaging was extended to 24 min because the timing to anaphase onset was slightly delayed with respect to the parental cell line. To inactivate the Spindle Assembly Checkpoint, cells were treated with either DMSO or 1 μM taxol-containing media for 15 min and then 1 μM reversine-containing media was added for 120 min (total imaging time was 135 min) to inhibit Mps1. As control, cells were treated with 1 μM taxol and imaged for 135 min. Images were acquired at 32% solid source illumination with Cy5 and neutral density filters, exposure time 0.05 s. Timing of exit from mitosis was scored by eye.

Long term live-cell imaging

Parental RPE1 and RPE1 stably expressing Ndc80-EGFP were cultured in glass bottom FluoroDish (FD35-100, World Precision Instrument, Inc.). Time-lapse imaging was performed on Olympus DeltaVision microscopes (Applied Precision, LLC) equipped either with Photometrics CoolSNAP HQ (Roper Scientific) or Photometrics CoolSNAP HQ2 cameras (Roper Scientific) and temperature held at 37°C as described above. Image stacks (7 × 2 μm optical sections) were acquired using the SoftWoRX 6.0 software every 3 min using a 40x/1.3 NA oil-immersion objective. To visualize the DNA, 1 hr before imaging RPE1 cells were incubated with DMEM/F-12 media containing 0.5 μM SiR-DNA (Spirochrome). In each experiment, 30 to 40 fields (1024 × 1024 pixels) were imaged using the point visit function in softWoRX 6.0. Images were acquired for 15 hr at 10% solid source illumination with neutral density and Cy5 filter, exposure time 0.05 s. The timing of nuclear envelope breakdown and anaphase onset were scored by eye.

Photoactivation experiments

RPE1 cells stably expressing photoactivatable-(PA)-GFP-alpha-tubulin (Toso et al., 2009) were cultured in Fluorodishes (FD35-100, World Precision Instrument, Inc.) and DNA was visualized by incubation for 30 min with CO₂ independent L15 media (Invitrogen, UK) containing 0.5 μM SiR-DNA (Spirochrome, CH). DMSO or 1 μM taxol was added 15 min prior to imaging. Photoactivation was carried out using a confocal spinning disk microscope (Marianas SDC, 3i, UK) equipped with a Vector module for photoactivation, a 100x / 1.46 NA immersion oil objective and a Photometrics 95B Prime sCMOS camera controlled by Slidebook 6.0 (3i, UK). Cells were maintained at 37°C using a stage top incubator (both Okolab, Italy). PA-GFP-tubulin was activated in an ROI (100x5 pixels, parallel to the

metaphase plate) with 4×2 ms pulses of a 405 nm laser. Images were then acquired (excitation 488 nm) every 15 s for 2 min (150 ms exposure, 3 planes $1 \mu\text{m}$ z-step centered on the photoactivated plane). Images of the DNA staining were acquired (excitation 640nm) at frame 1, 5 and 9. Poleward flux was calculated by measuring the displacement of photoactivated marks over the first 5 frames. To determine the turnover of PA-GFP-alpha-Tubulin the background-subtracted pixel intensity of the photo-activated EGFP-alpha-tubulin over time was measured in ImageJ (averaging the mean intensity of two 7×7 pixels square boxes placed on the photo-activated region). In DMSO, intensity was measured at every time point, whereas, in taxol, intensity was analyzed at time points 0 min, 1 min and 2 min.

QUANTIFICATION AND STATISTICAL ANALYSIS

For all intrakinetochores Δ analysis, expanded kinetochores and kinetochores where the software failed to correctly identify the spot center (as assessed by visual inspection), were excluded to prevent compromising accuracy. All significance tests were done using z-test, except for the microtubule flux rate measurements where we used a t test. Fisher exact test was used to compare the fraction of cells exiting mitosis in live cell imaging experiments. The calculation of Nematic order is defined in [Methods S1](#). In all figures, fluorophores imaged in different experimental conditions are displayed using the same dynamic range for comparison purposes. Effective cell number is calculated as $1/\text{SI}$ where SI is the Simpson Index $\sum_i p_i^2$ where p_i is the fraction of KTs in cell i .

DATA AND CODE AVAILABILITY

Kinetochores Tracking (KIT) 2.1.10 and the Bayesian Euclidean distance correction algorithm (BEDCA) codes are available on our github site: <https://github.com/cmcb-warwick>

Cell Reports, Volume 31

Supplemental Information

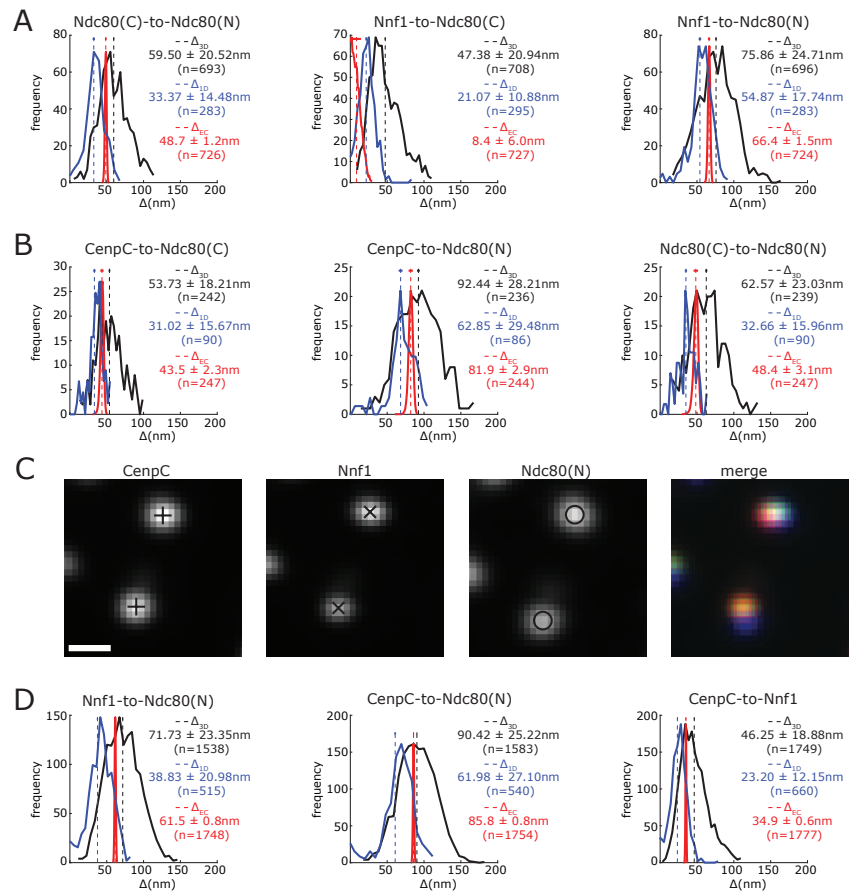
**Ensemble-Level Organization of Human Kinetochores
and Evidence for Distinct Tension
and Attachment Sensors**

Emanuele Roscioli, Tsvetelina E. Germanova, Christopher A. Smith, Peter A. Embacher, Muriel Erent, Amelia I. Thompson, Nigel J. Burroughs, and Andrew D. McAinsh

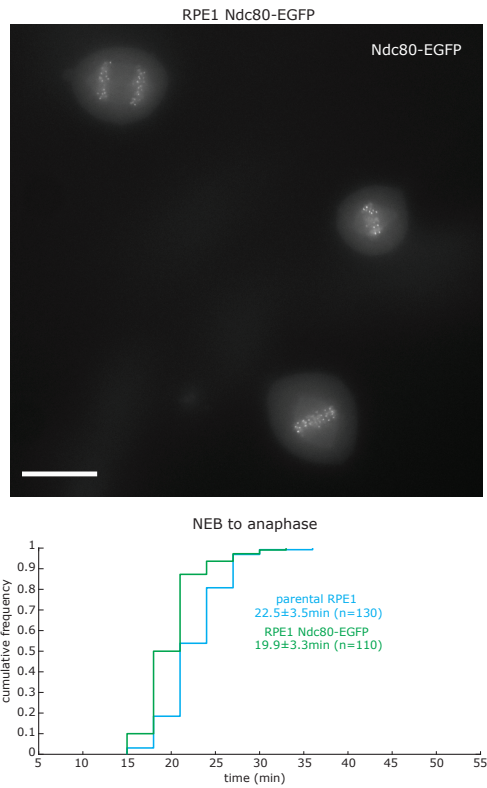
Supplemental figures

Roscioli E., Germanova T., Smith C., Embacher P., Erent M., Thompson A., Burroughs N. J., and McAinsh A. D.

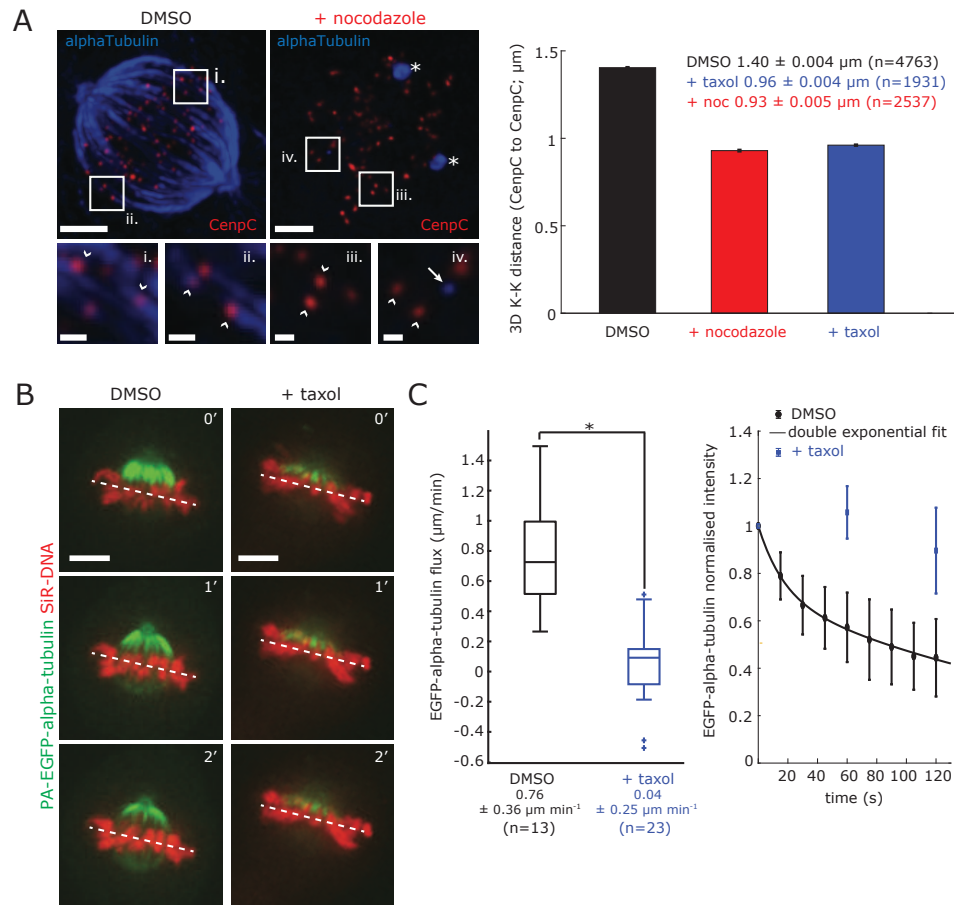
2020



Supplemental Figure 1 related to Figure 1. Comparison of Δ_{1D} , Δ_{3D} and Δ_{EC} measurements. (A) Histograms showing the Ndc80(C)-to-Ndc80(N), Nnf1-to-Ndc80(C) and Nnf1-to-Ndc80(N) Δ_{1D} , Δ_{3D} and Δ_{EC} distances in Ndc80-EGFP cells. (B) Histograms showing the CenpC-to-Ndc80(C), CenpC-to-Ndc80(N) and the Ndc80(C)-to-Ndc80(N) Δ_{1D} , Δ_{3D} and the Δ_{EC} distances in Ndc80-EGFP cells. (C) Kinetochore pair stained with anti-CenpC, anti-Nnf1 and anti-Hec1(9G3) antibodies. Scale bar 500 nm. (D) Histograms show the Nnf1-to-Ndc80(N), CenpC-to-Ndc80(N) and CenpC-to-Nnf1 Δ_{1D} , Δ_{3D} and Δ_{EC} distances in cells. Mean (dashed line) and sd (horizontal bar) values are indicated on the right.

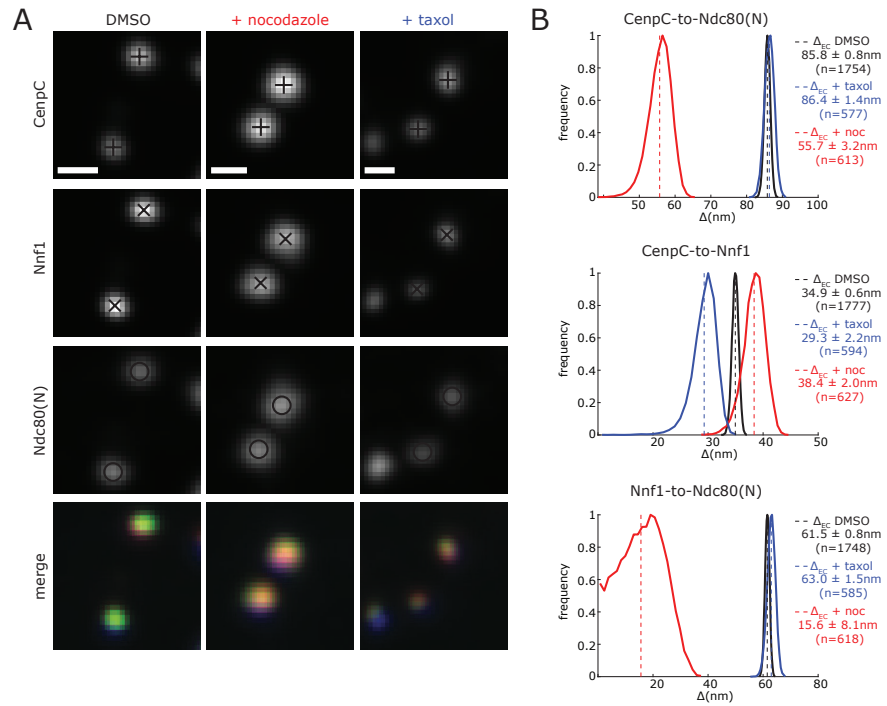


Supplemental Figure 2 related to Figure 1. Parental and Ndc80-EGFP expressing RPE1 cells display the same mitotic timing. Image shows mitotic RPE1 cells expressing Ndc80-EGFP. Scale bar $20 \mu\text{m}$. Cumulative frequency plot displaying the timing between nuclear envelope breakdown (NEB) and anaphase onset in parental RPE1 and RPE1 Ndc80-EGFP cells (MC191). Mean and sd values are indicated on the right.

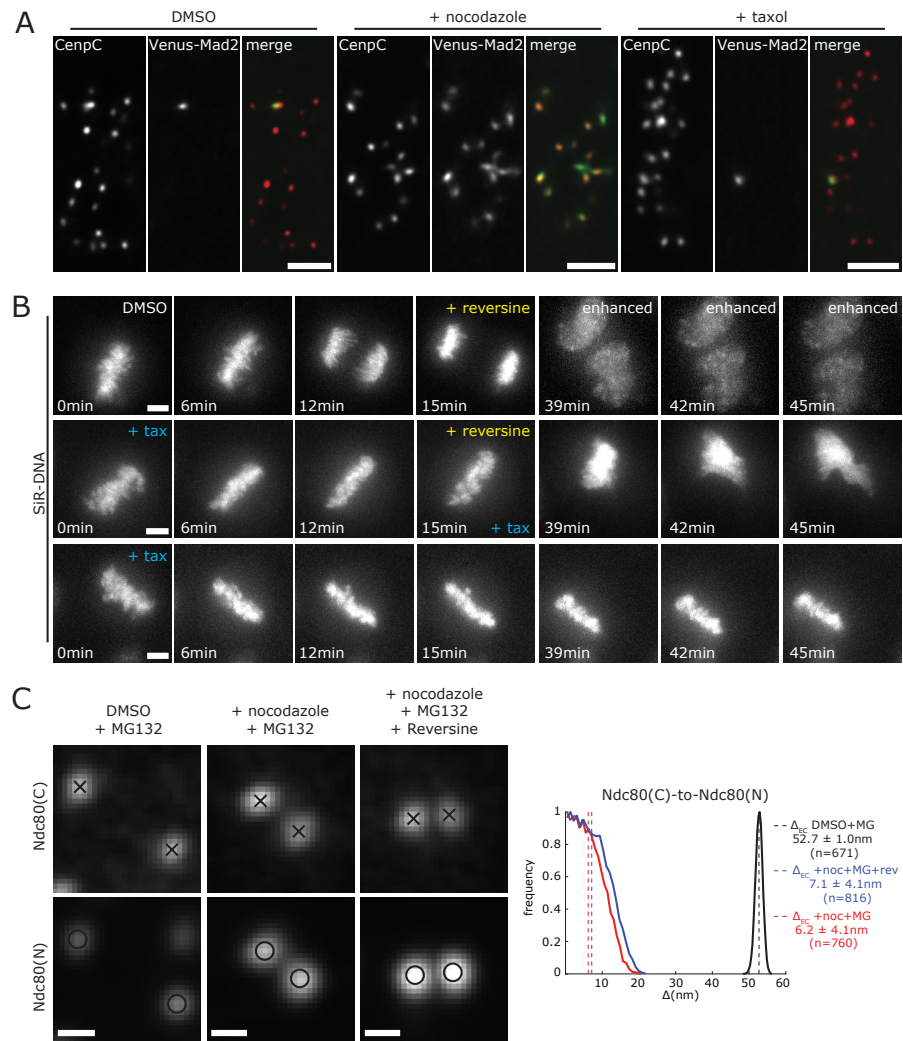


Supplemental Figure 3 related to Figure 4. Nocodazole and taxol reduce inter-sister kinetochore distance and the taxol-dependent loss of inter-sister kinetochore tension is associated with reduced microtubule poleward flux. (A) Example images of RPE1 cells treated with $3.3 \mu\text{M}$ nocodazole for 2 hr and DMSO as control. Scale bars $3 \mu\text{m}$. In control cells, bi-orientated kinetochore pairs (red) are attached to microtubules (blue) and are under tension (white arrowheads in insets i. and ii.; these images were enhanced to better show kinetochores and microtubules). Nocodazole induces full depolymerization of microtubules and reduces the inter-kinetochore distance (white arrowheads in inset iii. and iv.). In this condition, only centrosomes (*) and few rare microtubule stubs (white arrow in inset iv.) remain intact. Scale bar in insets is 500 nm . Bar charts (right) show the 3D K-K distance from CenpC to CenpC in cells treated with $3.3 \mu\text{M}$ nocodazole for 2 hr, $1 \mu\text{M}$ taxol for 15 min and DMSO as control. Mean and SEM values are indicated above the chart. (B) Effect of $1 \mu\text{M}$ taxol treatment on microtubule dynamics was determined by photoactivating PA-EGFP-alpha-tubulin adjacent to the metaphase plate and then measuring its movement to the pole (poleward microtubule flux) and the dissipation of the signal over time (plus-end turnover). Example images of RPE1 expressing photoactivatable PA-EGFP-alpha-tubulin (green) stained with SiR-DNA to visualize the chromosomes (red). Photo-activation was carried out at $T=0$ and cells were imaged every 15 s for 2 min. White dotted lines indicate the centre of the metaphase plate used as reference to measure the position of the PA-EGFP-alpha-tubulin (green). Scale bar $5 \mu\text{m}$. $1 \mu\text{M}$ taxol abolishes plus-end turnover as the tubulin signal is

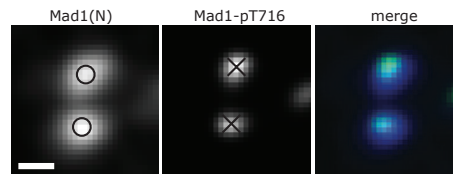
stable for 120 s, while the signal in DMSO treated cells exponentially decays as previously reported (Amaro et al., 2010) (C) Left: Box and whiskers plot showing the measured microtubule poleward flux within the first 60 s in cells treated with 1 μ M taxol or DMSO (see Materials and Methods for details). T-test indicates the difference is significant: (*) $p=3.5 \times 10^{-8}$. Mean and sd values are indicated below the chart. Right: Intensity of PA-EGFP-alpha-tubulin at the indicated times in 1 μ M taxol or DMSO-treated cells (see Materials and Methods for details). Black solid line indicates the double exponential fitting for the DMSO intensities.



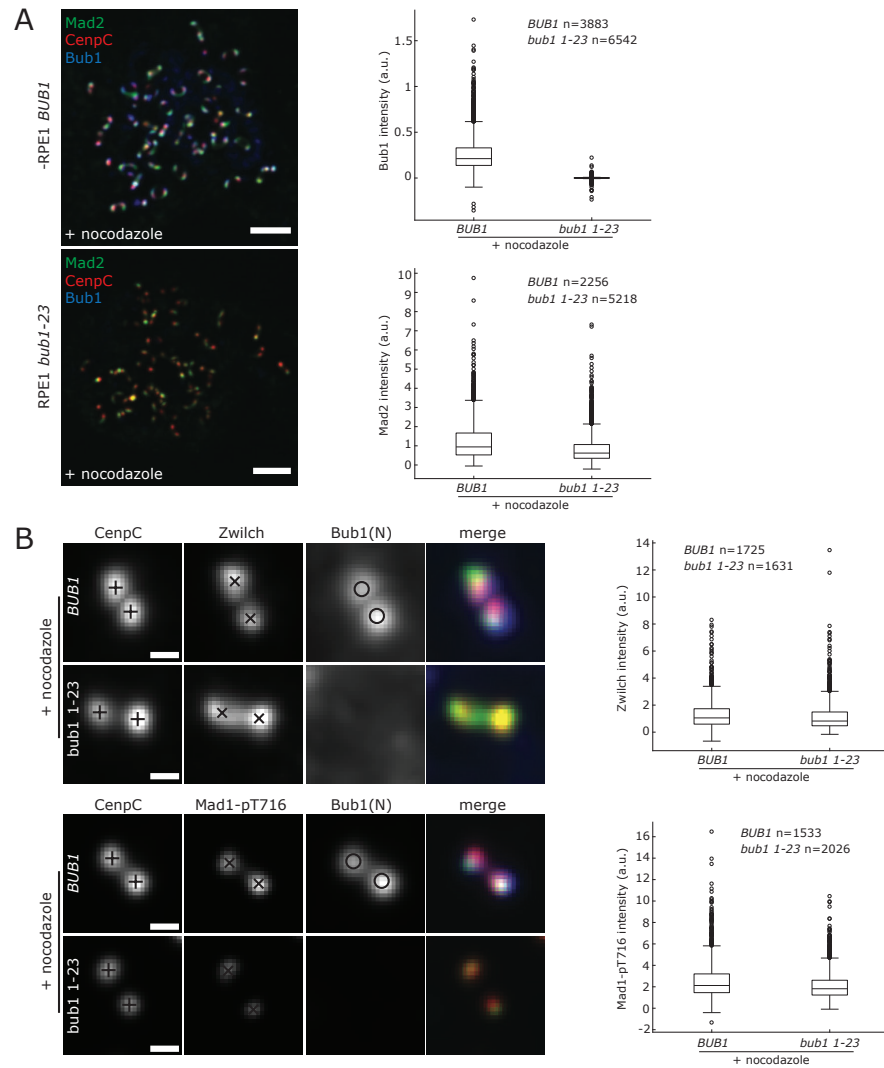
Supplemental Figure 4 related to Figure 4. The Ndc80 N-terminus moves close to Nnf1 in unattached kinetochores. (A) Kinetochores in RPE1 cells stained with anti-CenpC, anti-Nnf1 and anti-Hec1(9G3) antibodies and treated with 3.3 μ M nocodazole for 2 hr, 1 μ M taxol for 15 min and DMSO as control. Scale bar 500 nm. (B) Distribution of the Nnf1-to-Ndc80(N), CenpC-to-Nnf1 and CenpC-to-Ndc80(N) Δ_{EC} distances in DMSO, nocodazole (+noc) and taxol treated cells. Mean (dashed line) and sd values are indicated on the right.



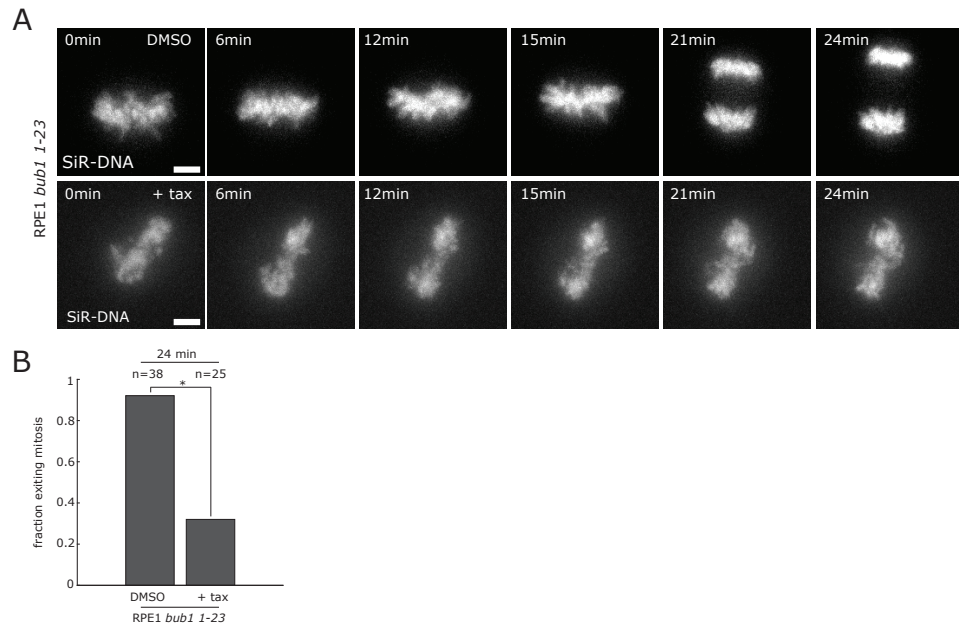
Supplemental Figure 5 related to Figure 5. Taxol-induced mitotic delay is dependent on the activation of the Spindle Assembly Checkpoint. (A) Images of RPE1 Venus-Mad2 cells stained with anti-CenpC antibody and treated with 3.3 μM nocodazole for 2 hr, 1 μM taxol for 15 min and DMSO as control. Scale bars 3 μm . (B) Images of RPE1 cells treated with 1 μM taxol (+tax) or DMSO for 15min and then with 1 μM reversine for 2h. Bottom row shows a cell treated with 1 μM taxol (+tax) only, as negative control. Time frame images at 39, 42 and 45 min in the DMSO sample were enhanced to better display the cell exiting mitosis. To visualize DNA, cells were previously treated with SiR-DNA. Scale bars 5 μm . (C) Kinetochores pair in RPE1 Ndc80-EGFP cells stained with anti-Hec1(9G3) antibodies and treated with 3.3 μM nocodazole + 10 μM MG132 for 1 hr, 3.3 μM nocodazole + 10 μM MG132 + 1 μM reversine for 1 hr and DMSO as control. Scale bar 500 nm. Histograms show the distribution of the Ndc80(C)-to-Ndc80(N) Δ_{EC} in cells treated as above. Mean (dashed line) and sd values are indicated on the right.



Supplemental Figure 6 related to Figure 6. Mad1(N) to Mad1-pT716 Δ_{EC} distance reflects EM structural data. Kinetochore pair stained with antibodies against Mad1 (aa 77-115), here referred as Mad1(N), and Mad1-pT716. Scale bar 500 nm.



Supplemental Figure 7 related to Figure 6. *bub1 1-23* cells can recruit Mad1:Mad2 at kinetochores and are delayed in metaphase upon taxol treatment. (A) Images of parental and RPE1 *bub1 1-23* cells stained with anti-CenpC, anti-Bub1 and anti-Mad2 antibodies and treated with 3.3 μ M nocodazole for 2 hr. Scale bars 500 nm. Box and whiskers plots on the right show Bub1 and Mad2 intensities in parental and RPE1 *bub1 1-23* cells. Bub1 and Mad2 signals were background-subtracted and normalised to CenpC signal (also background corrected). (B) Kinetochore pair stained with anti-CenpC, anti-Zwilch and anti-Bub1(N) antibodies (top) and with anti-CenpC, anti-Mad1-pT716 and anti-Bub1(N) antibodies (bottom) in parental and RPE1 *bub1 1-23* cells treated with 3.3 μ M nocodazole for 2 hr. Scale bars 500 nm. Box and whiskers plots on the right show Zwilch and Mad1-pT716 intensities in parental and RPE1 *bub1 1-23* cells. Zwilch and Mad1-pT716 signals were background-subtracted and normalised to CenpC signal (also background corrected).



Supplemental Figure 8 related to Figure 6. bub1 1-23 cells activate Spindle Assembly Checkpoint in taxol. Images of RPE1 bub1 1-23 cells treated with 1 μ M taxol (+tax) and DMSO as control, for 24 min. To visualize DNA, cells were previously treated with SiR-DNA. Scale bars 3 μ m. Bar chart shows the fraction of cells exiting mitosis within 24 min. Fisher's exact test indicates the differences are significant with 99% confidence interval: (*) $p=7 \times 10^{-7}$.

Methods S1: Δ_{EC} algorithm, Simulation and Nematic order calculations, related to STAR Methods.

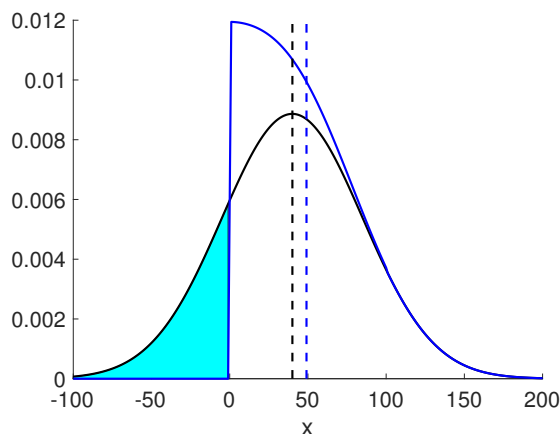
Roscioli E., Germanova T., Smith C., Embacher P., Erent M., Thompson A., Burroughs N. J., and McAinsh A. D.

2020

1 A Bayesian Euclidean distance correction algorithm: paired fluorophores

1.1 Introduction

Errors in the measurement of distances causes an over estimation of those distances which is non-negligible when measurement noise is of a similar order to the true distance, see Figure 1. Thus, distances below the resolution of light will be subject to overestimation/inflation under super resolution methods, the degree of inflation being determined by the spatial accuracy of the measurement. Inflation affects measurements in all dimensions, 1D, 2D and 3D, Churchman et al. (2006). Inflation occurs because measurement error can exceed the actual distance, which could then reverse the orientation along a given axis corresponding to a negative displacement (Figure below, black). Since orientation is however not known, eg kinetochores can twist beyond 90° , Smith et al. (2016), the euclidean distance is used which is always positive. This is subject to the same effect, i.e. there is a shift of the measurements upwards because of noise (Figure below, blue).



Schematic showing inflation under measurement noise of the displacement between 2 fluorophores in 1D. Histograms of displacement measurements under Gaussian noise assuming known orientation (black), and distance distribution under the modulus (absolute value) operation, $|x|$ when orientation unknown (blue). The measurements where noise exceeds the true distance - switching the orientation of the fluorophores (turquoise shaded) - are measured as positive distances causing inflation, e.g. the mean of the distribution (dashed line) is increased.

From multiple samples of intra-kinetochore distance measurements between two fluorophores we present a Bayesian algorithm to infer the true 3D distance. Noise in the measurement means that the measured distance is an over-estimate, e.g. see (Churchman et al., 2005, 2006), a bias that needs to be corrected. Measurement noise comes from both the microscope point spread function (PSF) and the number of emitted photons, which is determined by the brightness of the fluorophores. Thus, measurement noise is both wavelength dependent and protein density dependent. Isotropic measurement errors have been analysed before with published formulae/maximum likelihood correction algorithms in 1-3D (Churchman et al., 2006). However, non-isotropic measurement errors have not been analysed.

In section 1.2 we introduce a 3D model of paired fluorophore measurements. In section 1.3 we derive the associated likelihood. In section 1.4 we present a Markov chain Monte carlo (MCMC) algorithm to sample the posterior distribution of the model parameters. In section 1.5 we demonstrate the algorithm's accuracy on simulated data.

1.2 Euclidean distance model

Let \vec{X} be the observed vector from fluorophore 1 to fluorophore 2. For N measurements, we have samples \vec{X}_i , $i = 1, 2, \dots, N$. Assume that the measurement noise is Gaussian, and if the true displacement is $\mu\vec{n}_i$, with true direction \vec{n}_i (unit vector) and true distance μ , we have

$$\vec{n} \sim \mathcal{P}, \quad \vec{X}_i \sim \mu\vec{n} + N(0, 2\Sigma^{-1})$$

where Σ is the 3D precision matrix (inverse of covariance) for the spot centre accuracy, and direction vector \vec{n}_i is chosen according to a direction distribution \mathcal{P} , e.g. uniform over a sphere. The task is to determine the mean distance $\mu \geq 0$ and the measurement error covariance matrix $2\Sigma^{-1}$. The factor of 2 comes from the fact that both fluorophores have measurement error, so we could write this as the sum of the two measurement errors $2\Sigma^{-1} = \Sigma_1^{-1} + \Sigma_2^{-1}$; however we don't estimate these separately. For isotropic measurements Σ is diagonal; $\Sigma^{-1} = \frac{1}{2}\sigma^2 I$, I is the diagonal matrix and σ is the intradistance error standard deviation. Thus, if spot accuracies are identical, individual spot centres would have variance $\sigma^2/2$. Note that the measurement noise can reverse the orientation, i.e. $\vec{X}_i \cdot \vec{n}_i$ can be negative (see introduction section 1.1).

To quantify distances, it is natural to consider the distribution of $r = |\vec{X}|$; this involves integrating over the orientation distribution \mathcal{P} and the angular components of \vec{X} (i.e. angular measurements are ignored). For the case of isotropic errors we take advantage of the rotational invariance, i.e. choose axes relative to \vec{n} ; thus, the only coordinate is r - the distance between the fluorophores. Then, for isotropic measurement error in 3D we obtain the probability density (Churchman et al., 2006),

$$\pi_{3D}(r) = \frac{1}{\sqrt{2\pi}} \frac{r}{\mu\sigma} \left(e^{-\frac{(r-\mu)^2}{2\sigma^2}} - e^{-\frac{(r+\mu)^2}{2\sigma^2}} \right) \quad (1)$$

This gives for the mean and variance,

$$E[r] = \sqrt{\frac{2}{\pi}} \sigma e^{-\frac{\mu^2}{2\sigma^2}} + \frac{\sigma^2 + \mu^2}{\mu} \operatorname{erf}\left(\frac{\mu}{\sqrt{2}\sigma}\right), \quad \operatorname{var}(r) = 3\sigma^2 + \mu^2 - E[r]^2,$$

which can, for instance, be fitted to data and μ, σ thereby inferred.

1.3 The model likelihood

For N 3D measurements the likelihood of this model is given by,

$$L = \prod_{i=1}^N \left(\frac{1}{(2\pi)^{\frac{3}{2}} \sigma_x^2 \sigma_z} \right) \exp - \left(\vec{X}_i - \mu\vec{n}_i \right)^T \Sigma \left(\vec{X}_i - \mu\vec{n}_i \right),$$

where $2^{-1}\Sigma$ is the 3D precision matrix for the spot centre accuracy (averaged over the two fluorophores), and in microscope coordinates is given by $\Sigma^{-1} = \operatorname{diag}\left(\frac{1}{2}\sigma_x^2, \frac{1}{2}\sigma_x^2, \frac{1}{2}\sigma_z^2\right)$.

We use spherical coordinates to specify the relative position of the two vectors \vec{X}_i, \vec{n}_i ; ϕ_i is the relative angle in the x, y plane between \vec{X}_i, \vec{r}_i , and θ_i, θ_{X_i} are the angles of \vec{n}_i, \vec{X}_i with the z -axis:

$$\vec{n}_i = (\sin \theta_i, 0, \cos \theta_i), \quad \vec{X}_i = r_i(\sin \theta_{X_i} \cos \phi_i, \sin \theta_{X_i} \sin \phi_i, \cos \theta_{X_i})$$

Then the likelihood reads,

$$L = \prod_{i=1}^N \left(\frac{1}{(2\pi)^{\frac{3}{2}} \sigma_x^2 \sigma_z} \right) \exp -\frac{1}{2\sigma_x^2} (\mu^2 \sin^2 \theta_i + r_i^2 \sin^2 \theta_{X_i} - 2\mu r_i \sin \theta_i \sin \theta_{X_i} \cos \phi_i) - \frac{1}{2\sigma_z^2} (\mu \cos \theta_i - r_i \cos \theta_{X_i})^2. \quad (2)$$

This has global parameters μ, σ_x, σ_z and kinetochore specific hidden (unmeasured) variables θ_i, ϕ_i , $i = 1, 2, \dots, N$ to determine (recall r_i, θ_{X_i} are measured).

1.4 Markov chain Monte carlo methods for Bayesian parameter inference

The objective of Bayesian inference is to determine the probability distribution of the model parameters given the data, specifically the posterior density:

$$\pi(\mu, \sigma_x, \sigma_z, \{\vec{n}_i\} | \{\vec{X}_i\}) = \pi(\{\vec{X}_i\} | \mu, \sigma_x, \sigma_z, \{\vec{n}_i\}) \pi(\mu, \sigma_x, \sigma_z, \{\vec{n}_i\}) / \pi(\{\vec{X}_i\})$$

from Bayes theorem, where the first term is the likelihood L above and $\pi(\mu, \sigma_x, \sigma_z, \{\vec{n}_i\})$ are the priors on the parameters. Here we are inferring the model using all the kinetochore data, indicated by the set $\{\vec{X}_i\}$, $i = 1, \dots, n$, i.e. the model assumes all kinetochores are in the same state. This could correspond to all attached, or all detached for example. Using the spherically symmetric measure (solid angle) $d\Omega = \sin \theta d\theta d\phi$, the posterior distribution is thus given up to proportionality,

$$\pi(\mu, \sigma_x, \sigma_z, \vec{n}_i | \vec{X}) \propto \pi(\mu) \pi(\sigma_x, \sigma_z) \prod_{i=1}^N \pi(\theta_i, \phi_i) r_i^2 \sin \theta_i \left(\frac{1}{(2\pi)^{\frac{3}{2}} \sigma_x^2 \sigma_z} \right) \exp -\frac{1}{2\sigma_x^2} (\mu^2 \sin^2 \theta_i + r_i^2 \sin^2 \theta_{X_i} - 2\mu r_i \sin \theta_i \sin \theta_{X_i} \cos \phi_i) - \frac{1}{2\sigma_z^2} (\mu \cos \theta_i - r_i \cos \theta_{X_i})^2, \quad (3)$$

where $\pi(\mu), \pi(\sigma_x, \sigma_z)$ and $\pi(\theta_i, \phi_i)$ are appropriate priors. If $\mathcal{P}(\vec{n}_i)$ is uniform over the surface of the sphere, the prior on $\cos \theta_i$ is $U([1, -1])$. This distribution has 3 global variables μ, σ_x, σ_z , and $2N$ hidden variables ϕ_i, θ_i .

However, the posterior can be marginalised in ϕ_i (integrating out ϕ_i using a uniform prior) to give the alternative form with only N hidden variables θ_i ,

$$\pi(\mu, \sigma_x, \sigma_z, \theta | \vec{X}) \propto \pi(\mu) \pi(\sigma_x, \sigma_z) \prod_{i=1}^N \pi(\theta_i) \sin \theta_i \left(\frac{1}{(2\pi)^{\frac{1}{2}} \sigma_x^2 \sigma_z} \right) I_0 \left(\frac{\mu r_i \sin \theta_i \sin \theta_{X_i}}{\sigma_x^2} \right) \exp -\frac{1}{2\sigma_x^2} (\mu^2 \sin^2 \theta_i + r_i^2 \sin^2 \theta_{X_i}) - \frac{1}{2\sigma_z^2} (\mu \cos \theta_i - r_i \cos \theta_{X_i})^2, \quad (4)$$

where I_0 is the modified Bessel function. If the measurement error is isotropic we can also integrate out the angular variables θ_i to obtain the posterior corresponding to (1).

Neither of these posterior distributions are tractable analytically as far as we are aware, and thus numerical methods are required to generate samples. We use a Markov chain Monte Carlo (MCMC) methodology to sample from these posteriors. The marginalised posterior (4) is computationally more expensive per step but has superior mixing than (3) so convergence is achieved with fewer steps. We thus focus on (4) in the following.

There are a vast number of MCMC algorithms, Craiu and Rosenthal (2014). The fundamental idea of MCMC is that parameters are updated either individually, or in groups, using a proposal and these proposals are accepted or rejected such that the distribution is corrected to conform to the conditional posterior. Specifically, consider sampling from the distribution $\pi(\theta)$ (which could be

our posterior above where θ are our model parameters). If the current state of the markov chain is θ , then propose a new $\theta' \sim q(\theta'|\theta)$, where typically a subset of the θ are changed. Then accept the proposal with probability (the Metropolis-Hastings ratio),

$$\alpha(\theta \rightarrow \theta') = \min \left(1, \frac{\pi(\theta') q(\theta|\theta')}{\pi(\theta) q(\theta'|\theta)} \right)$$

and remain at θ if the proposal is rejected. This is called the update. A number of proposals are needed so that all parameters are updated. Then under fairly weak conditions the resulting Markov chain converges in probability to the target distribution $\pi(\theta)$, Craiu and Rosenthal (2014). Key to the Metropolis-Hastings ratio is that $\pi(\theta)$ only needs to be known up to normalisation. Special cases include the Gibbs update.

1.5 MCMC sampling algorithm

We use a Metropolis-Hastings within Gibbs algorithm, i.e. we have a mix of Metropolis-Hastings and Gibbs proposals. We use an algorithm that updates variables separately except for μ, σ_x that are highly correlated. We switch to precisions $\tau_{x/z} = \sigma_{x/z}^{-1}$ as is typical for models with Gaussian noise since precisions are (conditionally) Gamma distributed under the choice of a conjugate Gamma prior. We use short hand $s_i = \sin \theta_i, c_i = \cos \theta_i, s_{X_i} = \sin \theta_{X_i}, c_{X_i} = \cos \theta_{X_i}$. We use weak conjugate priors, imposing any positivity conditions by truncation. Updates are as follows:

Joint μ, τ_x proposal. We find that μ and τ_x are often highly correlated. Here we describe a twisted random walk along the eigendirections of the covariance matrix. For an estimated covariance matrix C , determined during burnin (computed sequentially 5 times), define the orthonormal eigenvectors $\eta_j, C\eta_j = \lambda_j\eta_j$. Then propose a move in the two directions separately, $j = 1, 2$,

$$\begin{pmatrix} \mu \\ \tau_x \end{pmatrix}' = \begin{pmatrix} \mu \\ \tau_x \end{pmatrix} + N(0, \lambda_j)\eta_j$$

which has an acceptance probability,

$$\begin{aligned} \alpha \left(\begin{pmatrix} \mu \\ \tau_x \end{pmatrix} \rightarrow \begin{pmatrix} \mu' \\ \tau_x' \end{pmatrix} \right) &= \max \left(1, \frac{\pi(\mu')\pi(\tau_x')}{\pi(\mu)\pi(\tau_x)} \left(\frac{\tau_x'}{\tau_x} \right)^N \prod_i \frac{I_0(\mu'\tau_x' r_i s_i s_{X_i})}{I_0(\mu\tau_x r_i s_i s_{X_i})} \right. \\ &\quad \exp -\frac{1}{2}\tau_x' \sum_i ((\mu' s_i)^2 + (r_i s_{X_i})^2) + \frac{1}{2}\tau_x \sum_i ((\mu s_i)^2 + (r_i s_{X_i})^2) \\ &\quad \left. \exp -\frac{1}{2}\tau_x (\mu' - \mu) \sum_i c_i ((\mu' + \mu)c_i - 2c_{X_i} r_i) \right). \end{aligned} \quad (5)$$

The priors enforce rejection of proposals that violate the positivity requirements, $\mu > 0, \tau_x > 0$.

Precision $\tau_z = \sigma_z^{-2}$. Using a conjugate Gamma prior $\Gamma(a_z, k_z)$ we have the Gamma distributed update

$$\tau_z | \cdot \sim \Gamma \left(a_z + \frac{N}{2} - \frac{3}{2}, k_z + \frac{1}{2} \sum_i (\mu c_i - r_i c_{X_i})^2 \right). \quad (6)$$

Hidden variable θ_i . We use a random walk proposal. We used proposal $\theta'_i \sim \theta_i + N(0, w^2)$, with step size $w = 0.75$ giving reasonable acceptance rates. The acceptance probability is,

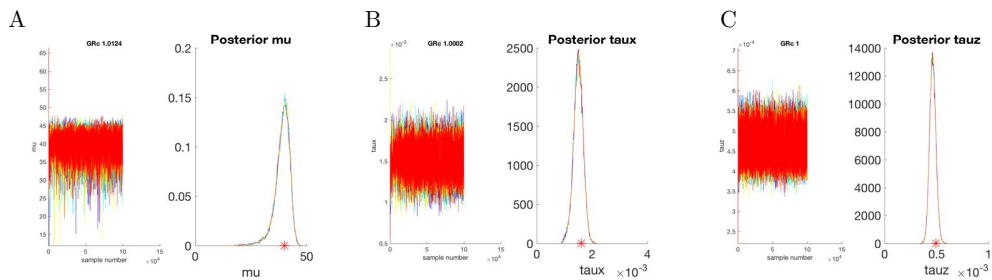
$$\alpha(\theta_i \rightarrow \theta'_i) = \min \left(1, \frac{\pi(\theta') \sin \theta'_i I_0(\mu\tau_x r_i s'_i s_{X_i})}{\pi(\theta) \sin \theta_i I_0(\mu\tau_x r_i s_i s_{X_i})} \exp -\frac{\tau_x \mu^2}{2} ((s'_i)^2 - (s_i)^2) - \frac{\tau_z}{2} ((\mu c'_i - r_i c_{X_i})^2 - (\mu c_i - r_i c_{X_i})^2) \right)$$

Since this is a symmetric random walk, the proposal cancels.

Priors. The prior in μ is a truncated Gaussian ($\mu > 0$) with large standard deviation, $\mu \sim N(60, 100^2)$ (all distances in nm). Priors for τ_x, τ_z are weakly informative Gamma distributions, $\tau_{x/z} \sim \Gamma(a, a s_{x/z}^2)$ (shape and rate), with $a = 10$. This has mean precision s^{-2} and a relative standard deviation $a^{-\frac{1}{2}} = 0.32$. Weaker priors with wider distributions (smaller a , e.g. $a = 1$) worked on some data sets and gave similar results, but $a = 10$ gave good performance on all our data, see convergence discussion below. For τ_x, τ_z we used $s_x = 20, s_z = 40$ nm respectively when both flourophores are antibodies, and $s_x = 25, s_z = 75$ nm if one of them is a fluorescent protein. Our posteriors are always tighter than these priors and typically have posterior means 20-30 nm for σ_x , and 40-55 nm for σ_z .

1.6 MCMC algorithm performance on simulated data

We tested the algorithm on simulated data (see Figure below). Convergence was determined using the Gelman-Rubin diagnostic for multiple chains and determined converged if the corrected Gelman-Rubin statistic was below 1.1. We used 4 chains with chains initialized from the priors. The true parameters are accurately reconstructed, as seen in the following Figure.



Performance on simulated data. Markov chains (4) and posterior distributions shown for distance μ , precision $\tau_x = \sigma_x^{-2}$, precision $\tau_z = \sigma_z^{-2}$. The four chains are shown in different colors. Corrected Gelman Rubin statistic (GRC) for each variable are indicated on top of panel. True values are indicated by red asterisk on the x-axis, *i.e.* $\mu = 40$ nm, $\sigma_x = 25, \sigma_z = 45$ nm. MCMC runs of length 100000 including 50000 burnin. Priors for $\tau_{x,z}$ had $a = 3$. Data set consists of 1000 simulated kinetochores.

1.7 Running the MCMC algorithm on experimental data

We initially filtered the data with the constraint $|X| < \Delta_{max}$ since extremely large measured distances are clearly in error. For most data we used a threshold $\Delta_{max} = 200$ nm; however for KNL1-pS24 the measured 3D distances still had a significant tail population at 200nm. Thus, we used $\Delta_{max} = 250$ nm for pKNL1 data sets. We reduced the threshold to 180 nm for the Ndc80(C) to Ska distance (7 kinetochores were rejected out of 273) because these outliers caused the precision to be abnormally high.

On all runs we used priors with $a = 10$. We used the Gelman-Rubin diagnostic for 4 multiple chains to assess convergence, requiring that the corrected Gelman-Rubin statistic was below 1.1 on all three parameters μ, τ_x, τ_z (typically below 1.02). Burn-in was 50% of the run in all cases. Most data sets converged within 100,000 steps; for datasets that failed to converge within 100,000 the run length was increased until converged attained. The maximum run length (including burn-in) was 2,000,000 for the CenpC-to-Ndc80(C) distance in MC191 cell line under nocodazole treatment. All histograms are based on a single run with 50,000 samples (using subsampling at appropriate rates).

2 Kinetochores architecture simulations

2.1 Structural data

We used kinetochore architectural information and structural data (crystallographic and EM), see Table below, to build a kinetochore simulation. The orientation of the Ndc80/Nuf2 calponin homology (CH) domains with respect to the microtubule lattice, and the extending coiled coils were from Wilson-Kubalek et al. (2008). The Ndc80 hinge (also called loop or kink) was positioned 16 nm from the CH domains and allowed to bend and rotate given the intrinsic flexibility of the hinge and the coiled coil that connects to the Spc24/Spc25 subunits (Maiolica et al., 2007; Huis in 't Veld et al., 2016; Scarborough et al., 2019; Wang et al., 2008). The Ndc80 hinge angle and the elevation angle of the NDC80 complex short arm (the coiled coil between Ndc80 hinge and Ndc80/Nuf2 CH domains) with respect to the microtubule lattice have been measured using purified complexes but not within the context of the intact kinetochore *in vivo*. So this information was not imposed.

Parameter	Value	References for structural biology
Microtubule Bundle (K-fibre)		
K-fibre cross-section area	0.1 μm^2	(Nixon et al., 2015)
Microtubule radius	13 nm	(Ledbetter and Porter, 1963)
Number of microtubules in a K-fibre	20	(Booth et al., 2011)
NDC80 complex		
Number of Ndc80 molecules per microtubule	8	(Joglekar et al., 2006)
NDC80 complex full length (along complex)	60 nm	(Huis in 't Veld et al., 2016; Wang et al., 2008; Wei et al., 2005; Screpanti et al., 2011)
Ndc80(C) to Ndc80(N)*	51 nm	estimated from (Huis in 't Veld et al., 2016; Wang et al., 2008; Wei et al., 2005)
Ndc80(C) to Ndc80 hinge	35 nm	estimated from (Huis in 't Veld et al., 2016)
Ndc80 hinge to Ndc80(N)*	16 nm	(Wang et al., 2008)
Spc24/Spc25 RWD domains	4 nm	(Ciferri et al., 2005)
Ndc80(N)* to microtubule axis	4.25 nm	estimated from (Alushin et al., 2010)
MIS12 complex		
MIS12 complex full length	20 nm	(Huis in 't Veld et al., 2016; Petrovic et al., 2010)
Nnf1** to Ndc80(C)	14 nm	estimated from (Huis in 't Veld et al., 2016; Petrovic et al., 2010; Ciferri et al., 2005)
Nnf1** to Ndc80(N)*	64 nm	estimated from (Petrovic et al., 2014; Screpanti et al., 2011; Musacchio and Desai, 2017; Huis in 't Veld et al., 2016)

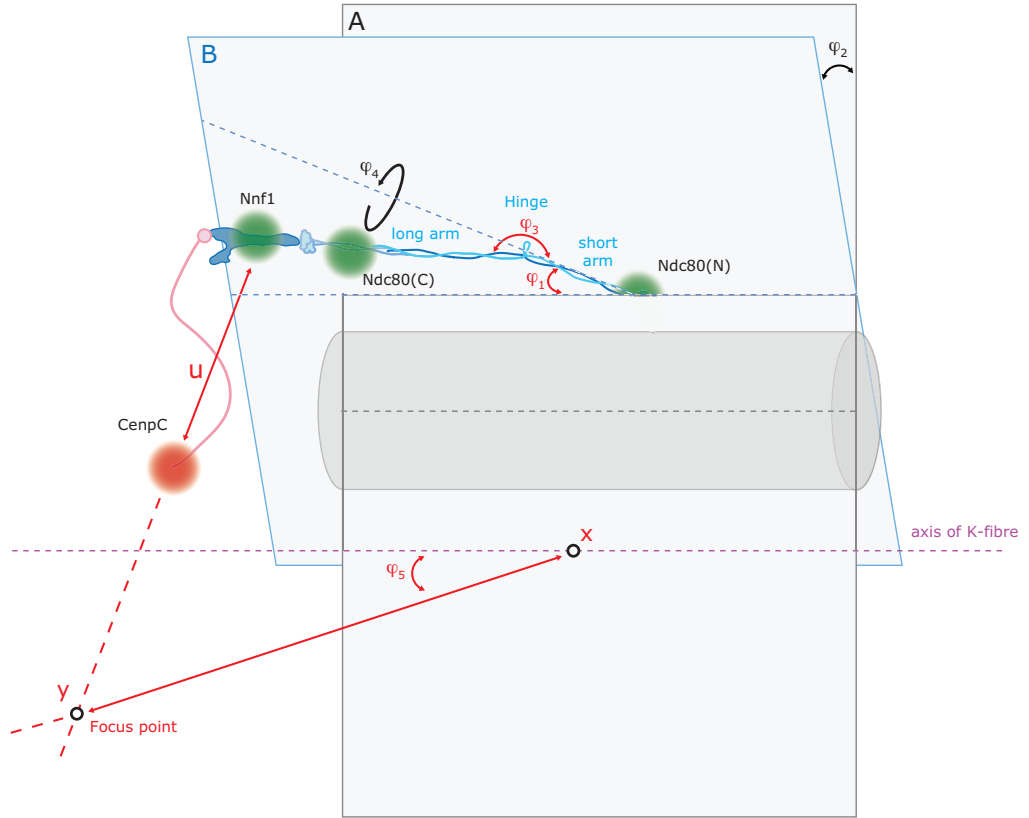
* Ndc80(N) denotes the anti-Hec1 (9G3) antibody binding site (Ndc80 amino acids 200-215; DeLuca et al., 2006)

** The anti-Nnf1 antibody is assumed to bind in the middle of the MIS12 complex

2.2 Simulation

The simulation proceeds as follows. For parameters that are fixed from structural data, the values are described in Section 2.1. Parameters that are fitted to the Ndc80(N)-Ndc80(C)-CenpC triangle distances are indicated below (indicated as 'fitted' in text, and in red color in schematic) and the fitting is described in Section 2.3. Note that variability in angles is set to 10° in absence of constraining data. See schematics below for graphical representation of the incorporated flexibility and annotations.

1. **Microtubule Bundle (K-fibre).** The K-fibre is defined as a disc of diameter 360 nm, centred on the x-axis. Next, 20 microtubules (MT), radius 13 nm, are uniformly distributed within the K-fibre cross-section. Here, the microtubules lie parallel to the x-axis. If there are overlapping microtubules, all positions are rejected and the process is repeated.
2. **NDC80 complex.** The true mean of the Ndc80 attachment points is labelled x along the central axis of the K-fibre. Next, 8 NDC80 complexes are placed on each microtubule as follows:
First, we determine a binding site along the MT (Gaussian, mean x , sd 25 nm) and rotate around the MT axis by angle φ_0 (uniform in $[0, 360^\circ]$). Next, the Ndc80(N) is positioned at 4.25 nm offset from the microtubule surface, considering the 9G3 antibody binding site. This results in 17.25 nm offset from the MT axis (13 nm MT radius). The NDC80 complex short arm is simulated by elevation at angle φ_1 (Gaussian, fitted mean, sd 10°) relative to the microtubule axis, with the Ndc80 hinge oriented towards the inner kinetochore plate. The NDC80 complex short arm can tilt around the axis parallel to the x-axis going through Ndc80(N), angle φ_2 (Gaussian, mean 0° , sd 10°), i.e. the NDC80 complex short arm and the microtubule axes would no longer lie in the same plane for non-zero tilt. The Ndc80 hinge is positioned at a fixed distance of 16 nm from Ndc80(N). The hinge angle between the NDC80 complex short arm and long arm (NDC80 complex coiled coil region between Spc24/Spc25 Head domains and Ndc80 hinge) is defined as φ_3 (Gaussian, fitted mean, sd 10°). We also incorporate rotation of the long arm around the NDC80 complex short arm axis, angle φ_4 (Gaussian, mean 0° , sd 10°). Ndc80(C) is positioned 35 nm from the Ndc80 hinge along the NDC80 complex long arm. Nnf1 is positioned a further 14 nm from Ndc80(C) along the NDC80 complex long arm axis towards the inner kinetochore. Finally, CenpC is positioned as described below.
3. **CenpC-Ndc80(N) axis.** Here, we use a model where the inner kinetochore (detected by the CenpC marker in this study) is off axis relative to the K-fibre. The inner-outer kinetochore axis is defined by elevating a line from the x-axis (pinned at x) at angle φ_5 (Gaussian, fitted mean, sd) and rotating around the K-fibre axis by a random angle φ_6 (uniformly distributed). The focus point y is positioned at a fixed distance (fitted) from x along this inner-outer kinetochore axis. CenpC is placed at a distance u (fitted) along the line joining Nnf1 to the focus point y ; the focus will act to concentrate CenpC molecules relative to Nnf1. If y is at infinity there is no focusing, i.e. the spread of CenpC and Nnf1 will be identical.



Geometrical setup for simulations of the CenpC-MIS12-NDC80 ensembles. Green and red dots represent the positions of the indicated kinetochore proteins. A representative microtubule is shown in grey and its axis (black dotted line) lies on plane A. The purple dotted line indicates the K-fibre axis (x-axis). The NDC80 complex short arm lies on plane B and tilts (φ_2) around the axis (light blue dotted line) that is parallel to the x-axis and goes through Ndc80(N). Fixed angle parameters used in the simulations are shown in black. Fitted parameters obtained from the simulations are displayed in red. For illustration only, the NDC80 MT attachment is shown vertically above the microtubule ($\varphi_0 = 0$).

2.3 Fitting of parameters. Optimisation.

The measured Δ_{EC} distances in DMSO (cell line MC191) of 1. Ndc80(C)-to-Ndc80(N), 2. CenpC-to-Ndc80(N), and 3. CenpC-to-Ndc80(C), were used to fit six parameters: the focus point y (fitting distance from x , and mean and sd of angle φ_5), the distance u from CenpC-to-Nnf1, the means of the short arm elevation angle and the Ndc80 hinge angle. We use a least-squares fitting method to minimise the difference between simulated distances in the triangle Ndc80(N)-Ndc80(C)-CenpC, and those observed. Specifically we minimise:

$$V := (\Delta_{sim}(\text{Ndc80(N)-Ndc80(C)}) - \Delta_{EC}(\text{Ndc80(N)-Ndc80(C)}))^2 + (\Delta_{sim}(\text{Ndc80(C)-CenpC}) - \Delta_{EC}(\text{Ndc80(C)-CenpC}))^2 + (\Delta_{sim}(\text{CenpC-Ndc80(N)}) - \Delta_{EC}(\text{CenpC-Ndc80(N)}))^2,$$

where the Δ_{sim} are the simulated distances, averaged over 20000 independently simulated kinetochores using the algorithm above.

The optimisation procedure is as follows: Starting from the current values of the 6 parameters a new set of these parameters is proposed based on a random walk (Gaussian) around the current values. The random walk has a drift term \vec{v} so that the algorithm continues to move in profitable directions, where the new drift vector is calculated for each jump and given by,

$$\vec{v}' = \frac{1}{2} (\vec{v} + \vec{J})$$

where \vec{v} is the previous drift and \vec{J} is the just accepted jump, if the proposal was accepted, and zero otherwise. The random walk has the following standard deviations: i) 50 nm for the $|x - y|$ distance, ii) 2.5° for all angles except the mean of φ_5 , which was 5° . Larger step sizes were used early on to explore a larger part of the parameter space. A proposal is accepted if the cost function V is reduced. Otherwise, the proposal is rejected and a new proposal is attempted. As the simulations have many stochastic degrees of freedom, the Δ_{sim} are prone to fluctuations (despite the 20000 kinetochore sample size). To remove any bias, we re-evaluate V for a new, independent sample of 20000 kinetochores every time after an acceptance and every second time after a rejection. The process is completed if the results are considered close enough to the minimum of V , or if there is no improvement.

This method gives the following fit, reproducing the observed mean distances in the Ndc80(N)-Ndc80(C)-CenpC triangle to within 3 nm:

- angle φ_1 : mean 22.4° . This is within the range $20-60^\circ$ given by Wilson-Kubalek et al. 2008.
- angle φ_3 : mean 203.5° (where 180° represents straight NDC80 complex conformation and angles $>180^\circ$ denote clockwise bending).
- distance $|x - y|$: 490 nm
- distance u : 37.9 nm
- angle φ_5 : mean 64.2° , sd 18.1° .

Here it needs to be noted that if additional constraints are imposed, a solution can still be found that fits the observed distances. For instance, imposing the elevation of the NDC80 complex short arm relative to the microtubule axis (φ_1) to be 10° , sd 10° (restricted to be positive) gives a solution with Ndc80 hinge angle (φ_3) mean of 177.3° . Therefore, there are nearby solutions that do not require the hinge angle to be above 180° .

3 Nematic order

Nematic order refers to the alignment of the molecules, alignment relative to an orientation axis (the director of Ericksen-Leslie theory). If the alignment distribution is $f(\cos(\theta))$, where θ is the angle between a molecule and the director, alignment order can be quantified in a number of ways. Typically, the distribution $f(\cos(\theta))$ is expanded in Legendre polynomials as follows,

$$f(\cos(\theta)) = \sum_{l=0}^{\infty} \frac{2l+1}{2} N_l P_l(\cos(\theta)).$$

This is analogous to a moment expansion; Legendre polynomials are used because they are orthogonal and $\cos(\theta)$ is valued in $[-1, 1]$. The most common measure of order for uniaxial materials is the second order Legendre polynomial, $N_2 = \mathbf{E}[P_2(\cos(\theta))]$, which can be used for materials with both aligned orientated molecules, eg ferromagnetic, and those with alignment but orientation can be random (no distinguishable head versus tail). For the latter, $f(\cos(\theta))$ is symmetric about zero, so the odd polynomials are zero, including N_1 , limiting their general use. The order parameter N_2 is related

to the alignment tensor Q . The first Legendre polynomial order parameter, $N_1 = \mathbf{E}[P_1(\cos(\theta))] = \mathbf{E}[\cos(\theta)]$, can also be used for aligned orientated molecules, with $N_1 = 1$ full alignment, $N_1 = 0$ no alignment. We use this measure because of its easy relationship to the *structural distance fraction*,

$$SDF = \frac{\Delta_{EC}}{\Delta_{structural}}$$

the ratio of the observed (mean) distance between two fluorophores and the expected structural distance $\Delta_{structural}$. Then $N_1 = SDF$. For Ndc80(N)-Ndc80(C) distance the hinge angle needs to be specified. Because each kinetochore is an ensemble, Δ_{EC} is the (average) distance of the average vector over the ensemble. Thus, N_1 is the proportion of the structural distance recovered by the ensemble average. We cannot use our data to compute N_2 since we only have the average ensemble distance Δ_{EC} .

In the simulations nematic order N is defined as ($|\cdot|$ denotes Euclidean distance, $\langle \cdot \rangle$ denotes average over sample),

$$N = \frac{|\langle \vec{x} \rangle|}{\langle |\vec{x}| \rangle}$$

i.e. the length of the average vector to the average length of those vectors. If all molecules (vectors) have the same length then these formulae are identical, *i.e.* $N = N_1$. They differ when molecule length is not constant, eg for Ndc80 and a variable hinge degree of freedom. If molecule length variation is substantial the SDF and its relation to the order parameter need to be reconsidered as the true structural distance is an ensemble average over these conformations and not known.

Roscioli et al.,

Supplemental Table 1 related to Figure 1: Comparison of $\Delta 1D$, $\Delta 3D$ and ΔEC measurements

Distance		treatment	$\Delta 1D$ mean \forall	sd \dagger	n	$\Delta 3D$ \ddagger	sd \dagger	n	ΔEC mean	sd \ddagger	n (kinetochores)	n cells (ESS \Rightarrow)	cell line
CenpC-A488	CenpC-A568	untreated	-0.62	9.25	1111	91.60	17.64	2279	2.2	1.5	2302	67 (57.5)	
CenpC-A488	CenpC-A647	untreated	-3.33	12.77	631	45.61	23.29	1364	4.3	2.7	1437	38 (33.7)	RPE1
CenpC-A568	CenpC-A647	untreated	-2.74	10.98	653	43.39	21.77	1388	4.5	2.8	1452	38 (33.7)	
Ndc80(C)	Ndc80(N)****	DMSO	33.37	14.48	283	59.50	20.52	693	48.7	1.2	726	25 (19.2)	
		nocodazole	1.12	19.04	227	50.57	23.10	669	7.8	5.0	694	31 (24.2)	
		taxol	27.68	12.86	217	59.96	21.42	582	45.5	1.4	620	32 (23.9)	
Nfn1	Ndc80(N)*	DMSO	54.87	17.74	283	75.86	24.71	696	66.4	1.5	724	25 (19.2)	
		nocodazole	16.04	19.74	218	56.14	24.82	657	12.7	7.2	696	31 (24.0)	RPE1 Ndc80-EGFP (MC191)
		taxol	49.17	15.01	218	74.42	21.91	587	68.3	1.2	624	32 (23.9)	
Nfn1	Ndc80(C)	DMSO	21.07	10.88	295	47.38	20.94	708	8.4	6.0	727	25 (19.2)	
		nocodazole	14.64	16.47	229	51.41	22.62	671	8.7	5.6	699	31 (24.1)	
		taxol	22.76	11.81	226	52.31	22.93	596	11.3	7.0	627	32 (23.9)	
Ndc80(C)	Ndc80(N)****	DMSO	32.66	15.96	90	62.57	23.03	239	48.4	3.1	247	17 (13.1)	
		nocodazole	6.09	16.02	149	52.15	41.32	561	7.3	4.6	600	34 (25.3)	
		taxol	25.09	14.25	238	59.91	21.56	677	44.4	1.6	731	31 (25.7)	
CenpC	Ndc80(N)**	DMSO	62.85	28.48	86	92.44	28.21	236	81.9	2.9	244	17 (13.1)	
		nocodazole	42.19	20.37	150	69.87	23.99	544	56.6	2.0	587	34 (25.2)	RPE1 Ndc80-EGFP (MC191)
		taxol	58.49	17.91	245	87.57	22.93	683	83.0	1.1	732	31 (25.7)	
CenpC	Ndc80(C)	DMSO	31.02	15.67	90	53.73	18.21	242	43.5	2.3	247	17 (13.1)	
		nocodazole	36.79	16.48	154	67.53	38.31	563	40.4	9.3	599	34 (25.3)	
		taxol	33.13	12.80	254	58.55	20.09	695	49.9	1.1	734	31 (25.7)	
Nfn1	Ndc80(N)*	DMSO	38.83	20.98	515	71.73	23.35	1538	61.5	0.8	1748	46 (41.1)	
		nocodazole	12.54	17.59	126	62.76	26.03	513	15.6	8.1	618	33 (23.4)	
		taxol	37.48	17.92	152	74.55	14.13	491	63.0	1.5	585	36 (23.8)	
CenpC	Ndc80(N)**	DMSO	61.98	27.10	540	90.42	25.22	1583	85.8	0.8	1754	46 (41.1)	
		nocodazole	40.25	22.05	126	76.07	28.36	518	55.7	3.2	613	33 (23.5)	RPE1
		taxol	59.22	20.89	136	61.06	24.05	476	65.4	1.4	577	36 (23.9)	
CenpC	Nfn1	DMSO	23.20	12.15	660	46.25	18.88	1749	34.9	0.6	1777	46 (41.2)	
		nocodazole	29.00	15.39	185	55.14	22.66	603	38.4	2.0	627	33 (23.5)	
		taxol	21.21	10.86	195	46.37	19.85	576	29.3	2.2	594	36 (24.0)	
CenpC	Ndc80(C)	siAlliStar	46.56	20.21	344	72.56	31.50	814	61.1	1.4	875	22 (19.5)	
		siCenpT	64.04	24.58	90	89.21	32.67	229	71.6	0.9	280	12 (8.7)	
		siAlliStar	11.83	14.98	386	43.61	30.60	856	5.7	4.0	894	22 (15.5)	RPE1 Ndc80-EGFP (MC191)
		siCenpC	22.82	14.68	235	52.85	22.14	649	20.2	9.1	689	24 (20.9)	
		siAlliStar	34.21	15.05	336	64.44	23.72	807	47.9	1.6	882	22 (19.6)	
CenpC	Sk3 #	DMSO	53.08	30.79	41	91.31	29.28	207	84.9	3.0	265	16 (11.6)	
		DMSO	26.88	15.00	91	54.00	20.82	299	39.2	2.1	314	17 (12.0)	RPE1 Ndc80-EGFP (MC191)
		taxol	23.37	33.80	40	75.35	48.00	209	35.9	12.4	266	17 (12.1)	
Ndc80(C)	Sk3 #	DMSO	33.87	15.96	252	61.92	19.84	642	52.7	1.0	671	23 (19.6)	
		nocodazole+MG	-1.34	15.68	270	49.41	24.49	705	6.2	4.1	760	36 (30.2)	RPE1 Ndc80-EGFP (MC191)
		nocodazole+MG+rev	9.17	14.51	309	49.62	23.00	765	7.1	4.6	816	28 (22.2)	
CenpC	Bub1(N)	DMSO	37.81	21.07	902	72.03	25.41	2053	58.9	1.1	2232	69 (51.8)	
		nocodazole	44.27	22.69	360	70.39	23.38	1048	60.7	1.1	1137	38 (34.6)	RPE1
		taxol	36.53	25.84	190	82.45	44.60	684	63.1	2.8	816	70 (43.4)	
CenpC	Rod(C)	DMSO	47.95	23.39	389	85.62	31.24	1073	71.4	1.9	1294	52 (35.2)	
		nocodazole	46.55	26.34	16	89.03	48.42	91	65.6	8.3	112	14 (8.2)	RPE1
		taxol	37.77	27.91	56	84.14	31.31	282	70.5	3.6	350	38 (25.0)	
CenpC	EGFP-Zw10	DMSO	40.54	40.26	20	93.40	31.02	273	82.9	3.1	334	51 (32.0)	RPE1 EGFP-Zw10 (MC156)
		DMSO	73.41	19.35	408	100.01	28.30	1090	96.3	1.0	1292	32 (27.9)	
		nocodazole	63.29	30.83	66	103.91	43.57	331	89.4	3.2	397	39 (30.1)	
		taxol	67.89	22.22	100	97.53	26.30	440	96.6	1.4	565	32 (25.4)	RPE1
CenpC	Knl1-pS24	DMSO	33.48	40.20	263	89.48	45.03	959	26.1	12.5	1260	54 (41.8)	
		nocodazole	68.87	43.85	47	115.75	52.84	346	91.7	6.3	472	47 (31.4)	RPE1
		taxol	86.12	39.89	51	124.92	43.96	409	119.1	2.7	547	55 (37.7)	
CenpC	Knl1 - MELT 2	DMSO	51.89	13.19	445	72.76	23.49	1012	65.4	1.0	1066	34 (26.2)	
		nocodazole	56.72	28.23	136	90.87	39.82	487	82.5	2.2	605	37 (26.7)	RPE1
		taxol	51.47	15.61	166	78.10	37.45	411	68.5	1.9	443	33 (17.1)	
CenpC	Zw1ch**	DMSO	68.40	23.36	49	100.82	37.32	244	92.1	2.9	296	34 (24.1)	RPE1 and RPE1 <i>bub1 1-23</i> (MC170)
		nocodazole <i>bub1 1-23</i>	74.52	44.07	15	119.93	58.78	111	97.2	5.8	133	27 (14.6)	
CenpC	Mad1-pT716	DMSO	38.45	20.84	342	69.67	24.90	843	54.4	2.0	911	35 (29.4)	RPE1 and RPE1 <i>bub1 1-23</i> (MC170)
		nocodazole <i>bub1 1-23</i>	49.34	21.61	412	75.85	23.46	948	68.1	1.1	1008	37 (28.7)	
Mad1-pT716	Mad1(N)	DMSO	-15.54	42.93	26	95.42	70.00	174	48.4	13.7	235	31 (22)	RPE1
		nocodazole <i>bub1 1-23</i>	51.97	19.68	105	80.07	26.25	478	70.3	1.8	550	34 (24.6)	RPE1 and RPE1 <i>bub1 1-23</i> (MC170)
		nocodazole <i>bub1 1-23</i>	58.70	32.28	220	97.18	36.74	1016	84.1	1.8	1265	68 (51.5)	
CenpC	Ndc80(N)**	DMSO - Mad2+	45.52	25.71	5	71.85	22.58	68	66.2	3.7	74	18 (10.5)	
		DMSO - Mad2-	66.08	15.20	278	86.59	22.06	685	82.4	1.0	721	25 (19.9)	
		DMSO - pool Mad2+/-	63.76	16.70	334	85.26	22.50	753	81.0	1.0	795	25 (20.7)	
		nocodazole - Mad2+	43.73	18.86	510	70.89	25.73	1218	59.3	1.3	1322	33 (31.4)	
		taxol - Mad2+	45.06	39.48	5	84.33	26.96	54	80.5	4.9	64	20 (13.9)	
		taxol - Mad2-	69.63	14.14	194	94.78	23.92	498	92.0	1.3	558	21 (16.5)	
		taxol - pool Mad2+/-	68.42	15.44	234	93.76	24.41	552	90.9	1.3	622	21 (16.8)	RPE1 Venus-Mad2

All measurements from at least two independent experiments for each marker pair. Multiple marker pairs (indicated with *, **, ***) also determined in different RPE1 clonal lines or independent sets of experiments (****)

¶ for $\Delta 3D$ measurements, kinetochores were omitted from the analysis where the z-offset between two markers was >100 nm in the z-axis.

\Rightarrow Effective Sample Size (ESS)

‡ 1D measurements determined as Smith et al., 2016.

† sd of dataset samples

§ sd of posterior (estimated parameter sd)

samples were pre-extracted before fixation

**Roscioli et al.,
Supplemental Table 2 related to Figure 4: Nematic order of MIS12-NDC80, RZZ and Mad1:Mad2 complexes**

Distance (vector)	treatment	Δ expected (nm)	Δ EC observed (nm)#	nematic order (N)§	markers labelled	cell line	
Ndc80(C)	Ndc80(N)†	DMSO	50.1	48.7±1.2	0.97±0.02	Nnf1-Ndc80(C)-Ndc80(N)	RPE1 Ndc80-EGFP (MC191)
		nocodazole	19	7.8±5.0	0.41±0.26		
		taxol	50.1	45.5±1.4	0.91±0.03		
		DMSO	50.1	48.4±3.1	0.97±0.06	CenpC-Ndc80(C)-Ndc80(N)	RPE1 Ndc80-EGFP (MC191)
		nocodazole	19	7.3±4.6	0.38±0.24		
		taxol	50.1	44.4±1.6	0.89±0.03		
Nnf1*	Ndc80(N)†	DMSO	65	66.4±1.5	1.02±0.02	Nnf1-Ndc80(C)-Ndc80(N)	RPE1 Ndc80-EGFP (MC191)
		nocodazole	34	12.7±7.2	0.37±0.21		
		taxol	65	68.3±1.2	1.05±0.02		
		DMSO	65	61.5±0.8	0.95±0.01	CenpC-Nnf1-Ndc80(N)	RPE1
		nocodazole	34	15.6±8.1	0.46±0.24		
		taxol	65	63.0±1.5	0.97±0.02		
Rod(C)¥	Zwilch**	DMSO	31.4	24.9±2.1	0.79±0.07	CenpC-Rod(C) and CenpC-Zwilch	RPE1
		nocodazole	31.4	23.8±8.9	0.76 ±0.28		
		taxol	31.4	26.1±3.9	0.83±0.12		
Mad1-pT716	Mad1(N)	nocodazole	57	48.4±13.7	0.85±0.24	Mad1-pT716 and Mad1(N)	RPE1

* distances estimated considering the Nnf1 antibody binding the central region of the MIS12 complex

** distances estimated considering the Zwilch antibody binding the central region of the protein

† vector calculated considering Ndc80 hinge angle of 203.5° for DMSO and taxol and 0° for nocodazole samples

¥ distances between Zwilch and Rod derived by subtracting the CenpC-to-Rod(C) from CenpC-to-Zwilch distances

mean±sd is displayed for each measurement

B.2 Subcellular Euclidean distance measurements with Multicolor Fluorescence localization imaging

Subcellular Euclidean distance measurements with Multicolor Fluorescence localization imaging

Germanova T.E.^{1,2,5}, Roscioli E.^{1,2,4}, Harrison J.U.³, McAinsh A.D.^{1,2} and Burroughs, N.J.^{1,3,6*}

¹Centre for Mechanochemical Cell Biology, University of Warwick, Coventry, CV47AL

²Division of Biomedical Sciences, Warwick Medical School, University of Warwick, Coventry CV4 7AL, UK.

³Warwick Mathematics Institute, University of Warwick, Coventry CV4 7AL, UK.

⁴Monoclonal Antibody Discovery (MAD) Lab, Fondazione Toscana Life Sciences, Via Fiorentina 1, 53100 Siena, Italy

⁵Technical Contact

⁶Lead Contact

*Correspondence: N.J.Burroughs@warwick.ac.uk

SUMMARY

This protocol measures the 3D Euclidean distance (Δ_{3D}) between two or three fluorescently labelled kinetochore components in fixed samples using Kinetochore Delta software (KiD, Kit 2.1.10). Overestimation of mean Δ_{3D} is corrected through a Bayesian algorithm, with Δ_{EC} distances reflecting the ensemble average positions of fluorophores within a population of kinetochores. This package also enables measurement of kinetochore intensities, information which can be used to sub-sample kinetochores and measure Δ_{EC} . Together, this allows the dynamic architecture of the human kinetochores to be investigated. For complete details on the use and execution of this protocol, please refer to Roscioli et al. (2020).

GRAPHICAL ABSTRACT

BEFORE YOU BEGIN

Software installation in Matlab and recommended controls

Timing: [30 min]

1) Matlab preparation

Note: the software has been developed on Mac (latest version checked is) and not all user interfaces display fully on Windows. The user is recommended to use Mac if possible.

a. **Optional:** Install Matlab.

Note: If you already have Matlab installed proceed to step b.

Download Matlab. Matlab R2020a is the latest version on which the software has been tested, and thus is recommended. During Matlab installation the user will be prompted to select the packages to be installed. Check the boxes for the following packages:

MATLAB
Simulink
Control System Toolbox
Curve Fitting Toolbox
DSP System Toolbox
Global Optimization Toolbox
Image Processing Toolbox
Instrument Control Toolbox
Deep Learning Toolbox
Optimization Toolbox
Parallel Computing Toolbox
Partial Differential Equation Toolbox
Signal Processing Toolbox
Statistics and Machine Learning Toolbox
Symbolic Math Toolbox

Note: In later versions of Matlab the toolboxes may be re-named. If you cannot find one of the toolboxes check in MathWorks for alternative name.

Note: Once Matlab is installed, a “Matlab” named folder will appear in the Documents folder on your computer.

- b. Check what packages are installed. In the command window type `ver` and press `Enter`. If not all of the packages stated in a. are installed, navigate to the Matlab tab `Home` -> `Add ons` -> `Get Add ons`. In the `Search field` type the name of the missing package and press `Enter`. Navigate to the correct package and press `Install`. Repeat these steps for all packages that need to be added.

Note: Every time the user types a command (here highlighted in pink) in the Command window, the user should press Enter to execute the command.

2) Add KiD and BEDCA Software to Matlab.

- a. Download KiD and the BEDCA software from the following link <https://github.com/cmcb-warwick/KiD-also-known-as-KiT2.1.10-and-BEDCA> in “.zip” format. Extract the content of the downloaded folder. Open the folder and copy the “KiDv1.0.1” and “BEDCA” folder into the “Matlab” folder.
- b. Allow Matlab to access the code: Open MATLAB, and within the Current Folder panel, locate the “KiD” folder, right-click on it and select `Add to Path` -> `Selected Folders and Subfolders`. Do the same for the “BEDCA” folder.

Critical: Every time the user closes and re-opens Matlab when doing this protocol, the user should add the “KiD” and “BEDCA” folders to the Matlab path as described in this step.

3) Recommended controls

- a. Software functionality control: We recommend for the user to download the provided dataset from the following link: <https://omero.warwick.ac.uk/webclient/?show=project-4752>. The provided dataset has been published in Roscioli et al., 2020. The “Approximate Chromatic shift” data contains hTERT Rpe1 cells stained with a-CenpA primary antibody, that is then labelled with mixture of A-488, A-568, and A-647 secondary antibodies. The “Rpe1 Nnf1/CenpC/9G3” data contains hTERT Rpe1 cells stained with a-Nnf1, a-CenpC, and a-Ndc80N primary antibodies, that are then labelled with A-488, A-568, and A-647 secondary antibodies, respectively. Then follow the protocol for measuring three-channel Delta measurement, or the desired functionality. That will ensure that the software is running properly on the user computer. The examples in that protocol follow analysis of the provided dataset where possible.
- b. Experimental control: We recommend the user to stain the same kinetochore marker in three colors and measure the Delta distance between all pairs of fluorescent channels. The expected results are in the range of 0 – 6 nm distance, where the true distance is 0 nm. That will ensure the immunofluorescence protocol used by the user does not significantly affect the Delta distances measured, as previous study suggested that sample preparation can affect Delta

measurements (Suzuki et al., 2018). See Figure 1 for the results of that experiment performed in Roscioli *et al.*

STEP-BY-STEP METHOD DETAILS

In this protocol the user will find instructions how to:

- A. Measure intra-kinetochore Delta Euclidian distance between two fluorescently-labelled kinetochore markers – steps 1, 2, 3, 4, 5, 6, 10, 11, 13, 14, 15
- B. Measure intra-kinetochore Delta Euclidian distances between three fluorescently-labelled kinetochore markers – steps 1, 2, 3, 4, 5, 6, 7, 10, 11, 13, 14, 15
- C. Measure intra-kinetochore Delta Euclidian distance between two fluorescently-labelled kinetochore markers at kinetochores positive and negative for a third fluorescently-labelled kinetochore marker – steps 1, 2, 3, 4, 5, 6, 8, 10, 11, 13, 14, 15
- D. Quantify kinetochore marker intensity – steps 1, 2, 3, 4, 9, 12 or completing step 12 after any of the above analysis.

For more information on the workflows see Figure 2.

Raw data collection

Timing: [2h – 3 days]

This section describes how to prepare, image and export the data for the approximate chromatic shift (ACS) correction and the sample of interest.

- 1) Approximate chromatic shift (ACS) slide preparation and imaging.

Note: The ACS analysis (step 3) detects the shift between the kinetochore spots detected in different fluorescent channels for the same marker, i.e. if there is no chromatic shift the spots should perfectly colocalize. Next, in the sample analysis (step 4), the detected sample spot coordinates are corrected for the calculated shift. However, the ACS alone is not sufficiently precise for Delta analysis and further chromatic shift correction is applied in step 10.

- a. Stain with a primary antibody against a kinetochore marker, and then use a mix of secondary antibodies directed against the primary antibody and emitting in the same fluorescent channels as the sample.

Critical: the stained kinetochore marker needs to (1) be present in interphase cells and (2) stain well in gaussian spot shape manner, i.e. CenpA or CenpC (avoid use of CREST which often results in a “spread” signal).

- b. Image the ACS slide with 100x objective, N.A ≥ 1.4 , ideally on a spinning disk confocal microscope. Widefield confocal microscope could also be used. Take 12 μm z-stack, at 100 nm z-steps (121 images), aiming for one or two interphase cells in the center of the field of view. Take a dataset of 10 to 15 images for a given day of imaging.

Note: Field of view size 512x512 pixels is recommended.

Note: Always use a piezo stage for accurate z-sectioning.

Note: To ease analysis, image in the following fluorescent channel order: 488 nm, 561 nm, 647 nm. If only two channels are used, keep the same relative order.

Critical: If the user images the sample slides in more than one day, an ACS dataset must be acquired for each day of sample imaging.

Critical: The KiD software supports only three fluorescent channels and any additional channels are not seen in the analysis. If the user would like to acquire images in channels that would not be used in analysis (such as DAPI), the user should acquire in those channels last, i.e. the first three acquired channels should be the channels used for analysis if more than three channels are acquired.

- c. Export all images as **ome.tif** or **.r3d** files.

Note: If the microscope does not support one of those formats (such as 3i systems which use SlideBook), open the image in Fiji and save it as **ome.tif** file.

Note: Number the images with consecutive numbers, starting from 1 to facilitate relating the analysis number in KiD to the original file number.

2) Sample preparation.

- a. The fixation and staining or use of fluorescent proteins is up to the user to implement. Tested fixation protocol is available in Roscioli et al. If the user chooses a different protocol, step 3b. from the “Before you begin” section is highly recommended.

- b. Image the sample with the same microscope set up as the ACS slide, i.e. 100x objective, N.A ≥ 1.4 , spinning disk or widefield confocal microscope, piezo stage and the following fluorescent channel order: 488 nm, 561 nm, 647 nm.

Note: Field of view size 512x512 pixels is recommended.

Note: In our experience, dataset of 17 to 24 cells per experiment is typically sufficient to produce a dataset of 300-500 kinetochores, depending on the quality of the signal.

Critical: in difference to step 1, take 12um z-stack, at 200nm z-steps (61 images) in the channels of interest.

Critical: The KiD software supports only three fluorescent channels and any additional channels are not seen in the analysis. If the user would like acquire images in channels that would not be used in analysis (such as DAPI), the user should acquire in those channels last, i.e. the first three acquired channels should be the channels used for analysis if more than three channels are used.

- c. Export all images as **ome.tif** or **.r3d** files.

Note: Number the images with consecutive numbers, starting from 1 to facilitate relating the analysis number in KiD to the original file number.

Entering raw data in KiD and setting up the analysis

Timing: [1 – 4 h]

This section provides instructions how to (1) use the KiD Graphical User Interface (GUI), (2) input raw data and specifications and (3) select the analysis to perform. All of this information is saved in a **jobset** file.

Critical: Every time the user closes and opens Matlab, the user should add the “KiD” and “BEDCA” folders to the Matlab path, see step 2b. from the before you begin section.

3) Processing the ACS data

Timing [0.5 – 1 hour]

In this step the user will input the ACS images in KiD in the form of a **jobset** (jS) file that contains information about the data, analysis set up, and once it is processed at the end of step 3, also the initial raw data analysis. For more information about the ACS correction see step 1.

Note: at the end of step 3, the **jobset** analysis will be automatically saved in the folder with the raw data.

- a. Creating a **jobset** (jS) file. In the Command window type `jS_Name = kitGUI`, where `jS_Name` is the name under which the analysis performed in this section will be saved. This command will open a GUI where the user sets up the ACS analysis for the day of imaging (see Figure 3 and Supplemental Figures 1 and 2).

Note: We suggest the name to be in the following format: `jS_expN_DateofImaging_ACS`

For example: `jS_exp1_13042020_ACS`

Note: The user is advised to use informative naming. Here, we suggest a naming system that has been used for the set of experiments in Roscioli *et al.* However, the user can develop their own naming system as appropriate.

- b. Movie and ROI selection

- i. Click on **Select directory**. Select the folder that contains the ACS images and click on **Select Folder**. You can now see the path of the selected folder on the right of the **Select directory** button, and all of the files in the selected folder in the **Available movies** window.
Optional: If the user has already saved a **jobset** (at the end of step 3) and wishes to edit it, the user can click on **Open existing jobset**.
- ii. In the **Available movies** window, select the image stacks that are to be used for ACS correction by clicking with left button on it – it will become highlighted in blue.
Note: You can select multiple image stacks at once by selecting the first image, holding **shift** and selecting the last image, or by selecting one image and holding **Command** to select the rest.
- iii. Click on **Add full**. This will enter the full image size for each selected image stack to the bottom of the list in the **ROIs** window. The image stacks used for ACS correction contain interphase cells and thus cropping is not required.
Note: If the user has made a mistake, an ROI can be deleted by selecting it with left mouse button and clicking **Delete**. The ROI can also be viewed in similar manner using the **View**

button.

- iv. Repeat steps ii. and iii. until all ACS images are added to the ROIs window.

c. Process setup

- i. In the **Process type** drop down menu select **Chromatic Shift**.
- ii. In the **coordinate system (CS) channel** pick the fluorophore channel with the best signal. Here **O1** is the first, **O2** is the second, and **O3** is the third acquired channel.
For example: for ACS correction slide, cells are stained with anti-CenpA primary antibody labelled with a mixture of A488-, A561- and A647-conjugated secondary antibodies. In this case, the best channel is Channel2 (CenpC-A561), and **O2** is chosen as CS channel.
- iii. The detection method for the **CS channel** is automatically set to **Histogram** and the refinement to **MMF**. Using these parameters, KiD will first detect spots in the **CS channel** via unimodal histogram thresholding. In this method, the histogram of all signal intensities is used to determine the threshold that discriminates between signal and background noise. Next, KiD models the spots based on the default PSF and detects the likely candidates. Finally, the detected spots are refined using Gaussian mixture model fitting (MMF) and their centers are detected. The MMF function checks how many gaussian spots best explain the detected signal and improves kinetochore detection in cases of two nearby or overlapping kinetochore signals.
- iv. Set the detection in the non-coordinate system (NCS) channels with kinetochore marker to **Neighbour** and the refinement to **MMF**. The NCS channels are all acquired channels with kinetochore marker except the channel selected as CS channel in step ii. The option **Neighbour** allows the software to search for the spot signal in a NCS channel within a **Circle** or **Semi-circle** (see mask options, step d ii.) centered at the corresponding spot coordinates in the CS channel.

For example: for CenpA-A488-A561-A647, the NCS channels are Channel1 (CenpA-A488) and Channel3 (CenpA-A647) because Channel2 (CenpA_A561) is the CS channel.

Note: Through this setup the best signal is used for primary spot detection, while the detection in the other channels is facilitated by searching only in a mask with a set shape and radius from the primary identified spot.

d. Options

The options have been optimized for kinetochores in human cells. If the user studies another model organism, they should input what seems best for their setting.

- i. **Spot Detection and Refinement.**
Min spots per frame 20 denotes that KiD will aim to use a **Histogram** threshold such that a minimum of 20 spots are detected in the image stack.
Max spots per frame 150 denotes that KiD will aim to use a threshold such that a maximum of 150 spots are detected in the image stack.

Max MMF time per frame (min) 300 denotes that the MMF algorithm in KiD will try to refine the spots for a maximum of 300 mins.

Weight for intensity restriction – signal weight is applied as the signal in the 488 nm channel is typically the strongest, followed by the 561 nm channel, and the 647 nm channel which is the weakest.

ii. **Neighbour spot detection**

Mask shape – KiD starts from the kinetochore center location in the CS channel and searches in **Circle** (only mask available for ACS processing) to find the spots in the **Neighbour** system channel.

Mask radius (μm) – defines the radius of the mask in which KiD will search for the neighbor spot.

Channel number: type the order of channels from inner toward the outer kinetochore components. If only two channels are detected, one box will remain greyed out.

Note: For ACS correction, the same marker is stained in three colors so the order can be left as default.

iii. **Intensity measurements.** The user can choose to make intensity measurements in any of the channels by clicking on the box next to the channel number.

Note: Intensity measurements are not typically useful for the ACS Correction.

Mask shape – KiD starts from the kinetochore center location in the CS channel and measures the intensity in a **Circle** (only mask available for ACS processing) in the specified channels for intensity measurements.

Mask radius (μm) – defines the radius of the mask in which KiD will measure intensity.

e. Execution

i. Type or paste the **jobset** name defined in step 3a in the **Jobset name** field.

ii. Click on **Validate metadata** and check that the metadata is read in correctly.
[Troubleshooting](#)

iii. Click **Execute**

Note: by default Matlab will hint all functions and variables that start with the typed phrase if the user presses tab. Matlab will display the associated with a function help, if the user types in the Command window **help** followed by **name of the function**.

4) Processing the Sample data

Timing [0.5 – 1.5 hours]

In this step the user will input the raw Sample data in KiD by creating a **jobset (.js)** file that contains information about the data, analysis set up, and once it is processed at the end of step 4, also the initial raw data analysis.

Note: at the end of step 4, the **jobset** analysis will be automatically saved in the folder with the raw data.

- a. In the Command window type `js_Name = kitGUI`, where `js_Name` is the name under which the analysis performed in this step will be saved. This will open a GUI where the user can set up the sample analysis for the day of imaging (see Figure 3 and Supplemental Figures 1 and 2).

Note: We suggest the name to be in the following format:

`js_expN_DateOfImaging_ProteinsInChannelOrder_Treatment`

For example: in the provided experiment, hTERT Rpe1 cell line is stained with anti-Nnf1, anti-CenpC and anti-Ndc80 N-terminus (Ndc80(N), 9G3 antibody) primary antibodies which are then labelled with Alexa 488-, Alexa 561- and Alexa 647-conjugated secondary antibodies, respectively. The respective `jobset` can be named:

`js_exp1_13042020_Nnf1CenpCNdc80N_DMSO` and will identify Nnf1, CenpC and Ndc80(N) in the 488nm, 561nm and 647nm fluorescent channels, respectively.

- b. Movie and ROI selection

- i. Click on `Select directory`. Select the folder that contains the Sample images and click on `Select Folder`. The user can now see the path of the selected folder on the right of the `Select directory` button, and all of the files within the selected folder in the **Available movies** window (as in 3b)

Optional: If the user has already saved a `jobset` (at the end of step 3 or 4) and wishes to edit it, the user can click on `Open existing jobset` and load it. If ACS `jobsets` have been loaded, KiD will open a browser window where the user is to select the ACS `jobset`.

- ii. Select all of the movies to be used for Sample analysis as in 3b ii.

Crucial: Make sure that the cells are added in the order of the raw image numbering, i.e. Raw cell 1 is added first and so on. This way the movie numbering in the analysis will correspond to the image stack numbering of the raw data.

- iii. Click on `Add Crop`. To facilitate spot tracking of the sample, it is advisable to use only the part of the image where the mitotic cell is located. This button will open a figure with a maximum Z projection of the image stack.

Note: If the user has used field of view size such that only the cell of interest and a little bit of background is captured (such as 256x256 pixels), the user can add the full image as described for ACS images in in steps 1 b. ii., iii., and iv. and continue to step 2 c.

- iv. Click on `Add ROI` and make a rectangle around the mitotic cell including some background. Avoid high background signals and other nearby cells.

- v. Double click in the rectangle to confirm it. Click `Finish`.

Note: The user can also add a second ROI in one image by clicking `Add ROI` again. In that case, make a note of the image stack with more than one ROI as now the number of ROIs will be more than raw image stacks and thus the numbering in the analysis and raw data will differ.

Note: After step v., the ROI will appear at the bottom of the list in the **ROIs** window. Here, if the user has made a mistake, an ROI can be deleted by selecting it with left mouse button

and clicking **Delete**. The ROI can also be viewed in similar manner using the **View** button.

vi. Repeat steps ii. to v. until all cells are added to the **ROIs** list.

c. Process setup

i. **Process type**. Select **2D/3D only**.

ii. **Coordinate system**. Select **Metaphase plate** if the kinetochores are aligned in a metaphase plate. Select **Centre of mass** if metaphase plate is not clearly present, such as in prometaphase cells and cells treated with nocodazole.

Note: The software does not currently support analysis of anaphase cells.

iii. **Coordinate system channel**. Choose a coordinate system (CS) channel based on the following criteria: (1) the protein is a robust kinetochore marker, i.e. does not get loaded/unloaded dynamically, (2) has a clear kinetochore-localized signal, (3) if relevant, can serve as a reference in multiple experiments.

For example: for Nnf1-A488, CenpC-A561, Ndc80(N)-A647, the best marker to use as CS channel is Channel2 (CenpC-A561).

iv. Set the detection in the non-coordinate system (NCS) channels to **Neighbour** and the refinement to **MMF** (see step 3c iii. and iv. for description of these options). NCS channels are all acquired channels with a kinetochore marker **except** the channel selected as CS channel in step iii.

v. Leave the detection to **None** and the refinement to **None** in channels with no staining or no kinetochore marker stained.

For example: for Nnf1-A488, CenpC-A561, Tubulin-A647: CenpC produces the most robust kinetochore staining and, therefore, Channel2 is set as the CS channel. Nnf1 is a kinetochore marker and Channel2 is the CS channel, therefore, Channel1 is set as NCS channel. Tubulin is not a kinetochore marker and, therefore, no detection is set in Channel3.

d. Options

The following options have been optimized for kinetochores in human cells. If the user studies another model organism, they should input what seems best for their setting.

i. **Spot detection and refinement** – do not change these options for human cells unless there is an issue. See 3d for explanation of the options.

ii. **Chromatic shift**

Check the box next to **Provide chromatic shift correction**.

Next, the user loads the ACS jobset created in Step 3.

- To run detection in two channels, click on the field under Jobset positioned on the right of the used channel pair (i.e. channel vector 1-2).

- To run detection in three channels, load the ACS jobset into all jobset fields (1-2; 1-3; 2-3).

For example: for Nnf1-A488, CenpC-A561, Ndc80(N)-A647, spot detection is set for all channels and the ACS **jobset** is loaded into all **jobset** fields.

Note: ACS dataset is required for each day of sample imaging.

Check the box for **Filter chromatic shift spots**.

Min spot intensity (% of max) – enter **25**. Now, only chromatic shift spots that have intensity of 25% or higher of the maximum image intensity will be used. In essence, very weak intensity spots will be discarded.

Min spot separation – enter **0.75**. ACS spots closer than 0.75 μm will be discarded. This parameter filters background and overlapping spots based on the fact that the kinetochore sister-sister pair distance at rest is 0.75 μm .

iii. **Neighbor spot detection**

Mask shape – KiD starts from the kinetochore center location in the CS channel and searches in **Semi-Circle** or **Circle** to find the spots in the Neighbour system channels. The **Semi-Circle** can be used when **Metaphase plate** option is given in step 4c ii and is orientated relative to the metaphase plate. **Circle** is used in all other situations.

Mask radius (μm) – defines the radius of the mask in which KiD will search for the neighbor spot.

Channel number: type the order of channels from inner toward the outer kinetochore components. If only two channels are detected, one box will be greyed out.

For example: for Nnf1-A488, CenpC-A561, Ndc80(N)-A647, the channel order will be **2 1 3**

iv. **Intensity measurements.** The user can choose to make intensity measurements in any of the channels by clicking on the box next to the channel number.

Mask shape – KiD starts from the kinetochore center location in the CS channel and measures the intensity in a **Circle** or in a **Semi-Circle** in the specified channels for intensity measurements. The Semi-Circle is oriented as described in for Neighbour spot detection above (see step 4 d. iii.). For the work in Roscioli et al., 2020, all intensities were measured using the **Circle** option as it gives better intensity coverage.

Mask radius (μm) – defines the radius of the mask in which KiD will measure intensity.

Critical: This approach to intensity measurements is to be used for kinetochore-localized markers **only**.

Note: Check all the boxes if in the future intensity measurement may become useful as these are quick to run and if afterwards such analysis is required, the full **jobset** will need to be re-analyzed.

e. Execution

i. Put the **Jobset_Name** chosen in step 4a. in the **Jobset name** field.

For example: **jS_exp1_13042020_Nnf1CenpCNdc80N_DMSO**

ii. Click on **Validate metadata** and check that the metadata is read in correctly.

- iii. Click **Execute**

Note: The jobset is now saved in the folder where the source images are. It will also appear in the Workspace window signifying that it is accessible from Matlab at the moment.

Note: The user can also click **Save** to save the **jobset** and execute it at another time after re-loading it into the GUI as described in step 4bi.

Crucial: if the user closes and then re-opens Matlab, the jobset will not appear in the Workspace window, i.e. the user will need to load it into Matlab for further analysis. To do that, type **jS_Name = kitLoadJobset**. Navigate to the raw data window and select the **jobset** saved in iii. Click **Open**. The **jobset** is now loaded and you can see it in your **Workspace** window.

For example: **jS_exp1_13042020_Nnf1CenpCNdc80N_DMSO = kitLoadJobset**

- f. **Detection Quality.** Once tracking is complete, KiD will display in the Command window **“Tracking complete”**. Scroll up in the Command window and check how many spots have been detected. If more than 60% of the cells have more than 20 spots detected, continue to:
- Step 5 for Delta distance analysis
 - Step 9 for kinetochore marker intensity analysis **only**, i.e. no intra-kinetochore measurement.
- If the detection of spots did not meet the above criteria see the associated Troubleshooting.
- Note:** The statistics of spot detection are also saved in a .txt file in the raw data folder.

Quality control of detected kinetochore spots and cells

Cell selection, sister kinetochore pairing and quality control of detected spots are essential steps to improve the calculation of intra-kinetochore distances. This section provides instructions to select cells, to pair sister kinetochores and to run spot quality control in experiments where two/three kinetochore markers are stained. This section also includes instructions on kinetochore marker spot categorization by eye (see step 8).

- 5) Cell selection, manual kinetochore sister pairing and spot quality control in the CS channel

Timing [0.5 - 1 hour]

Critical: If the user has closed Matlab and re-opened it after step 4, the user should load the **jobset** analysis from step 4 as described in step 4eiii.

For example: the staining is Nnf1-A488, CenpC-A561, Ndc80(N)-A647 and the CS channel for primary spot detection is Channel2 (CenpC-A561). The goal is to select the “good” cells for the analysis, pair the detected sister kinetochores and select the good quality spots in the CS channel. Here, as “good” cells we refer to cells that the user thinks look appropriate for the used treatment. For example, a selection of cells with no microtubule stubs in Nocodazole or cells with no unaligned kinetochore pairs in untreated metaphase cells.

Note: The kinetochore sister pairing is automatically saved in the **jobset** during the analysis.

Note: The user can stop the pairing at any point by simultaneously pressing on the keyboard

Command and **C**. The user can then continue the analysis from the next cell by using the **‘Subset’** option (see a iii. below).

Note: The user can redo the pairing for one or more cells by using the **‘Subset’** option and

indicating those cells. KiD will display the previous pairing, and any subsequent changes will overwrite the existing pairing and will be automatically saved.

- a. In the Command window type: `dublManualPairSisters(jS_Name, options)`, where in brackets is the **jobset** name chosen in 4 a. and the **options** are described next. See step a iv. for example of the function with options.
 - i. **'imageChans', vector** – here the **vector** contains the channel(s) that KiD will display for cell inspection and kinetochore pairing. The user should plot the CS channel for pairing. If useful, the user can plot other channels in addition.
For example: `'imageChans', [2]` will display only Channel2; `'imageChans', [1 2 3]` will display the markers acquired in Channel1, Channel2 and Channel3.
 - ii. **'plotChan', number** – here **number** is the CS channel in which the kinetochore spot centers will be plotted for assessment of the spot quality and pairing.
For example: if the CS channel is Channel2 (CenpC-A561), this will be given as `'plotChan', 2`
 - iii. **'Subset', vector** – use this option to do or repeat cell selection on a subset of cells specified in the **vector**.
For example: `'Subset', [5 6 7 8]` will prompt cell selection and pairing only for cells 5, 6, 7 and 8.
Note: In Matlab typing `[5 6 7 8]` is the same as typing `[5:8]`
 - iv. **Example:** `dublManualPairSisters(jS_exp1_13042020_Nnf1CenpCNdc80N_DMSO, 'imageChans', [1 2 3], 'plotChan', 2)` will display Nnf1-A488, CenpC-A561 and Ndc80(N)-A647 and the spot centers will be plotted for the CenpC-A561 channel.
- b. Cell quality control: Window with a maximum projection of the first cell will appear after step a. To accept the cell in the analysis press **y** (keyboard). To discard the cell press **n** (keyboard). See Figure 4.
Critical: Make a note of the accepted and discarded cells. KiD will display in the Command window in which cell the user is pairing the kinetochores at the moment. Make sure to check the cell number as KiD will skip any cells where no kinetochores have been detected.
Note: in this stage, the user performs a quality control on the acquired cells.
Critical: if the user presses by mistake a keyboard key other than **y** or **n**, KiD can automatically accept it as **y** and continue the analysis. If the user wishes to discard the cell instead, the function can be terminated by simultaneously pressing on the keyboard **Command** and **C**. In that case any previous analysis will be saved and the user can continue from that cell by using the **'Subset'** option (see a.).
For example: if the mistake happened at cell 3, use the **'Subset'** option to avoid repeating the analysis for cells 1 and 2.
- c. Spot quality control and kinetochore sister pairing in the CS channel.
 Once a cell is accepted, a figure will appear (see Figure 4). The right side shows the full cell,

projection of 5 z-slices around the coordinates of the spot under consideration. The left side shows a zoom-in on the spot under consideration (white cross), projection of five z-slices as above. Here, green crosses mark suggested spots within 2.5 μm radius from the kinetochore spot under consideration, yellow crosses mark spots within 2.5 μm radius that have been previously ignored by the user, and red crosses mark spots within 2.5 μm radius that have been previously paired by the user.

Note: To facilitate choosing the correct pairing, the user is suggested to first observe the full image projection in the right panel of the figure. If required, more advice on sister-pairing is available next.

Note: The position of the mouse cursor is visualized as a blue cross spanning the full image.

Advice on kinetochore sister-sister pairing:

If there is a metaphase plate: (1) in the right figure panel, identify the direction of the metaphase plate if there is such, i.e. the direction of the plane on which the kinetochore pairs are aligned, (2) in the left figure panel, identify the kinetochore pair such that the K-K axis would lie roughly perpendicular to the metaphase plate, and (3) follow one of the actions below the advice box.

If there is no metaphase plate present: (1) in the left figure panel, observe the kinetochore spots close to the one to be paired, (2) in the left figure panel, identify one or more best candidates, (3) see if there is a more suitable pair for some of the candidates in the case where the sister pair is not imminently clear (if the user is really doubtful on which is the correct pair, the user should discard the spot), and (4) follow one of the actions below the advice box.

- if none of the suggested kinetochore spots (green crosses) is the sister pair, press `space` to exclude the spot.

- if the kinetochore spot under consideration (white cross) or the suggested kinetochore spots (green crosses) are distorted or the center of the spots is not detected correctly, press `space` to exclude the spot.

- if both the kinetochore spot under consideration (white cross) and the sister kinetochore spot identified by the user are correctly recognized and not distorted, press on the respective green cross to pair the two kinetochore spots.

Note: Any kinetochore spot previously discarded will appear marked with a yellow cross.

Note: To aid visualization, KiD auto-scales the intensity of the images to the spot to be paired.

- d. Repeat steps b. and c. for all cells. This will conclude cell selection, manual sister pairing and kinetochore spot quality control in the CS channel.
- 6) Kinetochore spot quality control in one NCS channel for two/three-color Delta measurements. This section illustrates the steps to discard “bad” spots acquired in one NCS channel when at least two

kinetochore markers are stained. Here as “bad” spots we refer to spots with non-gaussian shape and spots with wrong center detection.

Timing [1 - 2 hours]

For example: the staining is Nnf1-A488, CenpC-A561, Ndc80(N)-A647 and the goal of the experiment is to measure the intra-kinetochore distance between CenpC-A561 and Ndc80(N)-647. The CS channel is Channel2 (CenpC-A561) and is used for primary spot detection. Channel3 (Ndc80(N)-647) is one NCS channel to be explored for spot quality.

- a. Create a **movieStructure (mS)**. The purpose of this structure is to extract the analysis of the image stacks (movies) completed so far and saved in the **jobset**. The **mS** structure will be used as input for further analysis.
In the Command window type: **mS_Name = kitLoadAllJobs(jS_Name)**, where on the right is the name of the **mS** structure and in brackets is the name of the **jobset** as given in step 4a. This will load all of the analysis from the **jobset** into the movie structure.
Note: we suggest the **mS** structure to be named as the **jobset except** starting with **mS**:
mS_expN_DateOfImaging_ProteinsInChannelOrder_Treatment.
For example: **mS_exp1_13042020_Nnf1CenpCNdc80N_DMSO**
- b. Save the **movieStructure**. In the Workspace window select the **mS** structure created in a. and click with right mouse button on it, then click with left mouse button on **Save as**. A window will pop-up. In the “Save as” field type the name of the **mS** structure as defined in a. Then navigate to the folder with raw data and press **Save**. Now the **mS** structure is saved in the folder with raw data.
Note: After closing and re-opening Matlab the user can load the saved **mS** structure by dragging it from the folder where it is saved into the Workspace window.
- c. Create a vector denoting the cells that have been selected for analysis.
Use the list of selected cells made in step 5b and type in the Command window:
SelectedCells_Name = [index number of cells that are accepted], where on the left is the name of the vector and on the right in square brackets are the numbers of the selected cells.
Note: We suggest to name the vector as the **jobset except** starting with **SelectedCells**:
SelectedCells_expN_DateOfImaging_ProteinsInChannelOrder_Treatment
For example: **SelectedCells_exp1_13042020_Nnf1CenpCNdc80N_DMSO = [1 2 3 4 5 9 12 15]**, if cells 1, 2, 3, 4, 5, 9, 12, and 15 were selected for analysis.
- d. Save the **SelectedCells** vector as described for the **mS** structure (6b.) but with the name chosen in 6c.
- e. Create a **mS** structure that contains **only** the cells selected for analysis in step 5a. In the Command window type: **mS_Name_sel = mS_Name(SelectedCells_Name)**, where on the left is the name of the sub-selection.
Note: We suggest to name the structure as the **mS** structure created in 6a **except** ending with **_sel**: **mS_expN_DateOfImaging_ProteinsInChannelOrder_Treatment_sel**.

For example: `mS_exp1_13042020_Nnf1CenpCNdc80N_DMSO_sel = mS_exp1_13042020_Nnf1CenpCNdc80N_DMSO(SelectedCells_exp1_13042020_Nnf1CenpCNdc80N_DMSO)`. This `mS` structure now contains only cells 1, 2, 3, 4, 5, 9, 12, and 15.

f. Save the `mS_Name_sel` as described for the `mS` structure (6b.) but with the name chosen in 6e.

g. Spot quality control in one NCS channel – creating a spot selection structure (`sS`).

Note: the spot selection is saved by KiD as set up in step ii. below at the end of the spot selection. If the function is terminated by the user by simultaneously pressing `Command` and `C` on the keyboard, step g. should be repeated from the beginning.

i. In the Command window type:

`sS_Name_sel = kitSelectData(mS_Name_sel, 'channel', x, 'method', 'deselect')`, where on the left side is the name of the spot selection, and `x` is the NCS channel under consideration.

Note: We suggest naming the list as the `jobset` **except** starting with `sS`, indicating the channel used for spot selection (`SpotsChannel`), omitting the date to reduce the length of the name, and ending the structure with `_sel`:

`sS_expN_ProteinsInChannelOrder_Treatment_SpotsChannel_sel`

For example: `sS_exp1_Nnf1CenpCNdc80N_DMSO_SpotsNdc80N_sel =`

`kitSelectData(mS_exp1_13042020_Nnf1CenpCNdc80N_DMSO_sel, 'channel', 3, 'method', 'deselect')`

Note: The `'deselect'` option allows the user to make a list of all spots that are not suitable for analysis and that will be ignored (bad spots). Use of the `'select'` option instead of `'deselect'` allows the user to make a list of the spots suitable for the analysis (good spots).

ii. KiD will prompt a window and ask the user to save the `sS` structure file. Navigate to the folder containing the raw images, input name chosen in i., and press `Save`.

iii. Next, KiD will open a figure with all spots that have been paired in the first accepted cell, and their index numbers on top. See figure 5.

Make a table with rows corresponding to each cell analyzed and two columns either for “bad” (ignored) and “good” (selected) spots. Identify “bad” and “good” spots from each cell and write down their index number in the relevant box in the table.

Critical: classification of “good” and “bad” spots should take into account: (1) the shape of the spot, i.e. expanded or not round spots should be ignored, and (2) the center detection of the spot, i.e. when the cross marking the spot is not in the center, the spot should be ignored. See Figure 5.

Note: If no spots were detected or paired in a cell, KiD will skip that cell.

iv. In the Command window, the user will be prompted to input either the “Spots to be ignored” or the “Spots to be selected” depending on which method was chosen in step 6g. i.

Input the relevant spots by typing in the Command window: [index numbers of spots to be ignored/selected]. If no spots are to be ignored/selected, type [].

For example: in cell1, the user explores signals in Channel 3(Ndc80(N)-647) and ignores spots 3, 7 and 8 by typing: [3 7 8] and pressing Enter. In this case, all Ndc80(N)-647 spots detected and paired in cell1 will be selected as “good” spots **except** spots 3, 7 and 8.

- v. Repeat steps iii. and iv. until KiD displays in the Command window: “Data selection complete”
 - vi. Update metadata in the list of selected spots (`sS_sel` structure, created in g.) such that cell numbers correspond to raw image cell numbers. In the Command window type: `sS_Name = kitUpdateSpotSelections(sS_Name_sel, mS_Name, SelectedCells_Name)`, where on the left is the name of the updated structure

Note: We suggest naming the updated structure as in 6 g i. **but** omitting the `_sel`:
`sS_expN_ProteinsInChannelOrder_Treatment_SpotsChannel`

For example: `sS_exp1_Nnf1CenpCNdc80N_DMSO_SpotsNdc80N = (sS_exp1_Nnf1CenpCNdc80N_DMSO_SpotsNdc80N_sel, mS_exp1_13042020_Nnf1CenpCNdc80N_DMSO, SelectedCells_exp1_13042020_Nnf1CenpCNdc80N_DMSO)`
 - h. Save the `sS` structure as described for the `mS` structure (6b.) but with the name chosen in 6 g vi.
 - i. -For analysis of intra-kinetochore distances in two-fluorophore-detection experiments proceed to Step 11.
 -To pool data from experiments with biological replicates perform step 10, and then proceed to step 11 for Intra-kinetochore Delta measurements of the pooled dataset.
 -For spot quality control in three-fluorophore-detection experiments proceed to step 7
 -To make categories based on the presence/absence of a kinetochore marker in the third fluorescent channel in combination with two fluorophore Delta experiments proceed to step 8.
- 7) Kinetochore spot quality control in the second NCS channel to measure the intra-kinetochore distances between three-fluorescently labelled kinetochore markers in pairwise manner. This section illustrates the steps to discard “bad” spots acquired in the second NCS channel when three kinetochore markers are stained.

Timing [1 - 2 hours]

For example: the staining is Nnf1-A488, CenpC-A561, Ndc80(N)-A647 and the goal of the experiment is to measure pairwise intra-kinetochore distances between the three markers. Channel2 (CenpC-A561) is the CS channel used for primary spot detection. The NCS channels for spot quality control are Channel1 (Nnf1-A488) and Channel3 (Ndc80(N)-A647). Spot quality control in only one NCS channel, i.e. Channel 3 (Ndc80(N)-647), has been described at step 6. Channel1 (Nnf1-A488) is the second NCS channel to be explored for spot quality here.

Note: If the user has closed and re-opened Matlab, the user needs to load the `mS` structure saved in step 6b. See step 6b. for instruction.

- a. Inspect spots in the second NCS channel and make a list of the “good”/”bad” spots, also taking into account the NCS channel previously analyzed (step 6).
Note: the spot selection is saved by KiD as set up in step ii. below at the end of the spot selection. If the function is terminated by the user by simultaneously pressing `Command` and `C` on the keyboard, step a. should be repeated from the beginning.
- i. In the Command window type: `sS_Name_sel = kitSelectData(mS_Name_sel, 'channel', x, 'method', 'deselect')`, where, as in step 6 d ii., on the left is the name of the spot selection and `x` is the NCS channel under consideration – choose the NCS channel different than the one analyzed in step 6.
Note: We suggest to name the structure as in 6 i. **but** also indicating the second NCS channel in which spot selection will be done here:
`sS_expN_ProteinsInChannelOrder_Treatment_SpotsChannelSpotsChannel_sel`
- ii. KiD will prompt a window and ask the user to save the `sS` structure file. Navigate to the folder containing the raw images, input the name chosen in i., and press Save.
- iii. KiD will open a figure with all spots that have been paired in the first accepted cell, and their index numbers on top. Identify the kinetochores to discard in the second **NCS** channel and mark the respective indexes in the table made in step 6 g. iii. (see Figure 5)
Note: If no spots were detected or paired in a cell, KiD will skip that cell.
- iv. In the Command window, the user will be asked to input the “Spots to be ignored”.
 In the Command window type: `[indexes of spots to be discarded]`, where in brackets are the “bad” spots in the previously analyzed **NCS** channel (step 6) and the additional “bad” spots identified here. If no spots are to be discarded type `[]`.
For example: in cell1, spots 3, 7 and 8 were initially ignored because of their signal in Channel 3(Ndc80(N)-647). However, when exploring the signal in Channel1 (Nnf1-A488), spots 3, 4 and 5 were classified as bad spots. The new list of ignored spots will be `[3 7 8 4 5]` and will result from the union of spots ignored in both NCS channels.
- v. Repeat steps iii. and iv. until KiD displays in the Command window: “Data selection complete.”
- b. Update metadata in list of selected spots such that cell numbers correspond to raw image cell numbers. In the Command window type: `sS_Name = kitUpdateSpotSelections(sS_Name_sel, mS_Name, SelectedCells_Name)`, where on the left is the name of the updated spot selection.
Note: we suggest to name the update spot selection as the one created in step a. **but** omitting `_sel`: `sS_expN_ProteinsInChannelOrder_Treatment_SpotsChannelSpotsChannel`
Note: The created `sS` structure specifies the list of spots that have good labelling in both NCS channels and will be used for analysis.
For example: `sS_exp1_Nnf1CenpCNdc80N_DMSO_SpotsNdc80NNnf1 = kitUpdateSpotSelections(sS_exp1_Nnf1CenpCNdc80N_DMSO_SpotsNdc80NNnf1_sel, mS_exp1_15042020_Nnf1CenpCNdc80N_DMSO,`

SelectedCells_exp1_15042020_Nnf1CenpCNdc80N_DMSO)

- c. Save the **sS** structure as described for the **mS** structure (see step 6b.) but with the name chosen in step 7 b.
 - d. - For analysis of intra-kinetochore distances in three-fluorescent channels experiments proceed to step 11.
 - To pool data from experiments with biological replicates perform step 10, and then proceed to step 11 for Intra-kinetochore Delta measurements of the pooled dataset.
 - For kinetochore intensity measurements proceed to step 12.
- 8) Kinetochore spot categorization. This part illustrates the steps to make categories based on the presence/absence of a kinetochore marker. Kinetochores are categorized as “positive” in the presence of the marker and “negative” when the marker is absent. The analysis is made by eye. These categories can then be used in step 11 to measure Delta distance between the non-categorized fluorescent channels at kinetochore marker positive and negative kinetochores.

Timing [1 - 2 hours]

For example: the staining is Venus-Mad2, CenpC-A561, Ndc80(N)-A647 and the goal is to compare the intra-kinetochore CenpC-A561 to Ndc80(N)-A647 distance at Mad2 positive and negative kinetochores. Channel2 (CenpC-A561) is the CS channel and its spot quality control was done in step 5. Channel3 (Ndc80(N)-A647) is NCS channel and its spot quality control was done in step 6. Channel1 (Venus-Mad2) is the kinetochore marker to be used to categorize positive/negative kinetochores as follows.

Note: If the user has closed and re-opened Matlab, the user needs to load the **mS** structure saved in step 6b. See step 6b. for instruction.

- a. Making “Marker Positive kinetochores” category.

Note: the spot selection is saved by KiD as set up in step ii. below at the end of the spot selection. If the function is terminated by the user by simultaneously pressing **Command** and **C** on the keyboard, step a. should be repeated from the beginning.
- i. In the Command window type: `sS_Name_sel = kitSelectData(mS_Name_sel, 'channel', x, 'method', 'select')`, where on the left is the name of the spot selection, and **x** is the channel that will be used to categorize kinetochores.

Note: We suggest to name the spot selection as the one made in step 6 but indicating the category made: `sS_expN_ProteinsInChannelOrder_Treatment_SpotsChannelMarkerP_sel`

For example: `sS_exp1_Mad2CenpCNdc80N_DMSO_SpotsNdc80NMad2P_sel = kitSelectData(mS_exp1_2004202_Mad2CenpCNdc80N_DMSO_sel, 'channel', 1, 'method', 'select')`
- ii. KiD will prompt a window and ask the user to save the **sS** structure file. Navigate to the folder containing the raw images, input name chosen in i., and press **Save**.

- iii. Next, KiD will open a figure with all spots that have been paired in the first accepted cell, and their index numbers on top. Identify the spots that can be categorized as “positive” and mark their indexes in the column of “good” (selected) spots in the table made at steps 6g. iii.

Note: If no spots were detected or paired in a cell, KiD will skip that cell.
 - iv. In the Command window, the user will be asked to input the “Spots to be selected”. In the Command window type: [indexes of spots to be selected], where the indexes of spots to be selected will include only those ones categorized as “positive” within the good (selected) spots at step 6d. v. If no spots are to be selected, type [].

For example: in cell1, all spots detected and paired in Channel3 (Ndc80(N)-A647) were selected as good spots **except** spots 3, 7 and 8. When exploring Channel1 (Venus-Mad2) signal, spots 1, 2, 6, 8 were categorized as “positive” but spots 8 was in the list of ignored spots. Thus, the list of positive spots will be [1 2 6].
 - v. Repeat steps iii. and iv. until KiD displays in the Command window: “Data selection complete.”
- b. Making “Marker Negative kinetochores” category.

Note: the spot selection is saved by KiD as set up in step ii. below at the end of the spot selection. If the function is terminated by the user by simultaneously pressing `Command` and `C` on the keyboard, step b. should be repeated from the beginning.

 - i. In the Command window type: `sS_Name_sel = kitSelectData(mS_Name_sel, 'channel', x, 'method', 'select')`, where on the left is the name of the spot selection, and `x` is the channel that will be used to categorize kinetochores as negative.

Note: We suggest to name the spot selection as the one made in step 6g iii. but indicating the category made:

`sS_expN_ProteinsInChannelOrder_Treatment_SpotsChannelMarkerN_sel`

For example: `sS_exp1_Mad2CenpCNdc80N_DMSO_SpotsNdc80NMad2Negative_sel = kitSelectData(mS_exp1_2004202_Mad2CenpCNdc80N_DMSO_sel, 'channel', 1, 'method', 'select')`
 - ii. KiD will prompt a window and ask the user to save the `sS` structure file. Navigate to the folder containing the raw images, input name chosen in i., and press `Save`.
 - iii. Next, KiD will open a figure with all spots that have been paired in the first accepted cell, and their index numbers on top. Identify the spots that can be categorized as “negative” and mark their indexes in the column of “good” (selected) spots in the table made at steps 8g. iii.

Note: If no spots were detected or paired in a cell, KiD will skip that cell. Identify the spots that can be categorized as “negative”
 - iv. In the command window, the user will be asked to input the “Spots to be selected”.

In the Command window type: [indexes of spots to be selected], where the indexes of spots to be selected will include only those ones categorized as “negative” within the good (selected) spots at step 6 g. iii. If no spots are to be selected type [].

For example: in cell1, all spots detected and paired in Channel3 (Ndc80(N)-A647) were selected as good spots **except** spots 3, 7 and 8. When exploring Channel1 (VenusMad2) signal, spots 3, 4, 5, 9, 10 were categorized as “negative” but spots 3 was in the list of ignored spots. Thus, the list of negative spots will be [4 5 9 10].

- v. Repeat steps iii. and iv. until KiD displays in the command window: “Data selection complete.”
- c. Update metadata in list of selected spots such that cell numbers correspond to raw image cell numbers. Here the user will update both the list of marker “positive” and of marker “negative” kinetochores.
 - i. Updating the list of Marker “positive” kinetochores. In the Command window type: `sS_Name= kitUpdateSpotSelections(sS_Name_sel, mS_Name, SelectedCells_Name)`, where on the left is the name of the updated spot selection.
Note: we suggest to name the update spot selection as the one created in step b. **but** omitting `_sel`: `sS_expN_ProteinsInChannelOrder_Treatment_SpotsChannelMarkerP_sel`
For example: `sS_exp1_Mad2CenpCNdc80N_DMSO_SpotsNdc80NMad2P = kitUpdateSpotSelections(sS_exp1_Mad2CenpCNdc80N_DMSO_SpotsNdc80NMad2P_sel, mS_exp1_2004202_Mad2CenpCNdc80N_DMSO, SelectedCells_exp1_2004202_Mad2CenpCNdc80N_DMSO)`
 - ii. Updating the list of Marker “negative” kinetochores. In the Command window type: `sS_Name = kitUpdateSpotSelections(sS_Name_sel, mS_Name, SelectedCells_Name)`, where on the left is the name of the updated spot selection.
Note: we suggest to name the update spot selection as the one created in step a. **but** omitting `_sel`: `sS_expN_ProteinsInChannelOrder_Treatment_SpotsChannelMarkerN_sel`
For example: `sS_exp1_Mad2CenpCNdc80N_DMSO_SpotsNdc80NMad2N = kitUpdateSpotSelections(sS_exp1_Mad2CenpCNdc80N_DMSO_SpotsNdc80NMad2N_sel, mS_exp1_2004202_Mad2CenpCNdc80N_DMSO, SelectedCells_exp1_2004202_Mad2CenpCNdc80N_DMSO)`
 - iii. Save the `sS` structures as described for the `mS` structure (see step 6b.) but with the name chosen in 8 c i. and ii.

Lists of spot selection categories created in this step:

(1) Marker positive. Here, the user created a list of spots that are positive for the kinetochore marker of interest, and have good spot quality in the NCS channel that will be used for Delta measurements. That list has the suggested name of:

`sS_expN_ProteinsInChannelOrder_Treatment_SpotsChannelMarkerP`

(2) Marker negative. The user also created a list of spots that are negative for the kinetochore marker of interest, and have good spot quality in the NCS channel that will be used for Delta measurements. That list has the suggested name of:

`sS_expN_ProteinsInChannelOrder_Treatment_SpotsChannelMarkerN`

- d. - For analysis of intra-kinetochore Delta between two fluorescently labelled kinetochore markers at kinetochores “positive” and “negative” for a third fluorescently labelled kinetochore marker proceed to step 11.
 - To pool data from experiments with biological replicates perform step 10 and then proceed to step 11 for Intra-kinetochore Delta measurements.
 - For intensity measurements proceed to step 12.

9) Spot quality control for **kinetochore intensity measurement only**.

Timing [20 min - 1 hour]

Here, the user performs spot quality control in the CS channel **only**.

Note: The quality control for intensity measurements only is a quicker than that used for Delta measurements as it skips cell selection, pairing of the kinetochores, and quality control in the remaining channels.

Crucial: if the user has closed and then re-opened Matlab after step 4, the **jobset** will not appear in the Workspace window, i.e. the user will need to load it into Matlab for further analysis. For instructions on how to load the **jobset** see step 4 e. iii.

For example: the staining is Venus-Mad2, CenpC-A561 and Ndc80(N)-A647. The goal is to measure the intensity of VenusMad2 and Ndc80(N)-A647. Channel2 (CenpC-A561) is the CS channel used for primary spot detection. Following step 4. the user has created a **jobset** named:

`jS_exp2_25042020_Mad2CenpCNdc80N_DMSO`

- a. In the Command window type:

`sS_Name = kitFilterSpots(jS_Name, 'channel', x)`, where on the left is the name of the spot selection, and **x** is the channel to explore for spot quality.

Note: we suggest to name the list of selected spots as the **jobset** (see step 4., and the example above), **except** starting with **sS**, indicating in which channel spots are to be selected, and omitting the date to reduce the length of the name:

`sS_expN_ProteinsInChannelOrder_Treatment_SpotsChannel`

For example: the staining is Venus-Mad2, CenpC-A561 and Ndc80(N)-A647. The aim is to measure the intensities of Mad2 and Ndc80(N), and CenpC is the reference kinetochore marker. Perform spot quality control in the CenpC channel by typing in the command line:

`sS_exp1_Mad2CenpCNdc80N_DMSO_SpotsCenpC=kitFilterSpots(jS_exp1_25042020_Mad2CenpCNdc80N_DMSO,'channel',2)`

- b. KiD will prompt a GUI with all spots detected in the first cell in the fluorescent channel specified in 9a (See Figure 6). All detected spots will appear in boxes with green outline. The green outline indicates that the spot has been selected as a “good” spot and will be used for analysis. Red outline indicates that the spot will be ignored.

Critical: classification of “good” and “bad” spots should take into account: (1) the shape of the spot, i.e. expanded spots or spots that are not round should be ignored, and (2) the center

detection of the spot, i.e. when the cross marking the spot is not in the center, the spot should be ignored.

Click with left mouse button on the spot to change the color between green and red. Press **Invert all** to invert the box outline colors of all spots. Press **Next** to proceed to the next cell.
Note: if a cell has to be discarded **all spots** must be outlined in red.

- c. Repeat step 9b. for all cells until KiD displays “**Manual filtering complete**” in the Command window, stating that the selection is complete for all cells in the channel.
- d. Make a movie structure (**mS**) to use as input for intensity measurements (step 11).
 The movie structure will contain the spot detection and raw intensity measurements from the **jobset**.
 In the Command window type: **mS_Name = kitLoadAllJobs(jS_Name)**, where on the left is the name of the movie structure, and on the right side is the name of the **jobset** created in step 4.
Note: We suggest to name this structure as the **jobset** **except** starting with **mS**:
mS_expN_DateOfImaging_ProteinsInChannelOrder_Treatment.
For example: **mS_exp1_25042020_Mad2CenpCNdc80N_DMSO**

Continue to step 12.

Pooling the data of experiment biological replicates for kinetochore intra-measurements

The BEDCA correction algorithm requires a minimum of 300 kinetochores to reliably correct the inflation (based on our experience with our fluorophores), depending on the length of the distance and other factors (see BEDCA, step 13). To increase the number of kinetochores for an experimental set up, several biological replicates can be pooled together.

Critical: The experiments to be pooled must be biological replicates.

- 10) Pooling of the data. The kinetochore intra-measurement function (**dublIntraMeasurements**) requires as input the **mS** structure (movie structure, created in step 5) and the **sS** structure (spot selection, step 6, 7 or 8), see step 11. Therefore, to make a unique intra-kinetochore measurement output for several experiment repeats, the **mS** and **sS** structures of the individual experiments (each created by following the steps above) are pooled. The pooled **mS** and **sS** structures are analyzed with the **dublIntraMeasurements** function (step 11).

Timing [10 min – 20 min]

- a. Pooling of the **sS** structures.
Critical: If the **sS** structures to be pooled do not appear in the user Workspace window, load the **sS** structures, one by one, by dragging the file from the folder with raw data into the Workspace window. The **sS** structure will be loaded with name **spotSelection**. Rename the variable by typing in the Command Window: **sS_Name = spotSelection**, where **sS_Name** is the name under which the **sS** structure was saved.

Pool the **sS** structures by typing the following command: `sS_Pool_Name = kitCombineSpotSelections({sS_Name, sS_Name, sS_Name})`, where on the left is the name of the pooled structure and in curly brackets are the **sS** structures to be pooled.

Note: We suggest the pooled structure to be named as `sS_Pool_expN_expN_expN_ProteinsInChannelOrder_Treatment_SpotsChannels`, i.e. as the individual **sS** structures but indicating which experiments have been pooled.

- b. Pooling of the **mS** structures.

Critical: If the **mS** structures to be pooled do not appear in the user Workspace window, load the **mS** structures by dragging the file from the folder with raw data into the Workspace window.

In the command window type: `mS_Pool_Name = {mS_Name, mS_Name, mS_Name}`, where on the left is the name of the pooled **mS** structure, and in the curly brackets are the **mS** structures to be pooled.

Critical: the order of **sS** and **mS** structures in a iii. and c ii. with respect to which experiment is analyzed **must** be the same.

Note: We suggest to name the **mS** structure of the pooled experiments as `mS_Pool_expN_expN_expN_ProteinsInChannelOrder_Treatment`, i.e. as the individual **mS** structures but omitting the date and indicating which experiments have been pooled.

- c. Save the structure(s) as described in step 6b with the appropriate names.

- d. - To make intra-kinetochore measurements of the pooled data (**iM**) in step 11 use as input the created pooled **mS** and **sS** structures and the options that were used for analysis of the individual experimental repeats.

- To make intensity measurements of the pooled data (**IntiM**) in step 12 use as input the created pooled **mS** and **sS** structures and the options that were used for analysis of the individual experimental repeats.

Intra-kinetochore measurements, basic raw Delta statistics and plots

- 11) Making Intra-kinetochore measurements. Delta is measured between two channels. For three-channel datasets, Delta is measured between each pair of channels. For marker positive/negative datasets (Delta of a category of spots), Delta is measured between the non-categorized fluorescent marker channels at marker “positive” and “negative” kinetochores.

Timing [10 min – 20 min]

Note: If the **mS** and **sS** structures that the user has created before do not appear in the workspace, the user needs to load the structures as described in steps 6b. and 6d.

- a. Measure Delta. In the Command window type: `iM_Name = dublIntraMeasurements(mS_Name, 'centralise', 1, 'channels', [a b], 'spotSelection', sS_Name)`, where on the left is the name of the intra-kinetochore measurements variable, **a** and **b** are the channels between which Delta will be measured, and `sS_Name` is the list of selected spots created in step 6, 7 or 8.

Critical: In the name include the treatment name flanked by underscores. If no treatment is applied use: “_untreated_”. Annotation of treatment is critical for data recognition by the BEDCA software.

Note: We suggest to name the intra-kinetochore measurement structure as follows:

`iM_expN_ProteinsInChannelOrder_Treatment_ProteinProtein`, where `ProteinProtein` are the two proteins between which Delta is measured.

For example: `iM_exp1_Nnf1CenpCndc80N_DMSO_CenpCndc80N`

Note: Add `_MarkerP` or `_MarkerN` if you are analyzing a dataset of marker positive/negative kinetochores (continuing here from step 8).

For example: `iM_exp1_Mad2CenpCndc80N_DMSO_CenpCndc80N_Mad2P` for Mad2 positive kinetochore dataset.

Explanation of the options:

- i. `'centralise', 1` will prompt KiD to use data centralisation. Centralisation is the fine chromatic shift correction. Here, KiD detects the center of mass of the analyzed kinetochores in each channel, and aligns the centers of mass in the different channels to correct the chromatic shift. Always switch on the centralization for this method.
- ii. `'channels', [a b]` This option defines the channels between which the user will measure Delta. If the user is measuring Delta between channels 2 and 3, the user needs to specify: `'channels', [2 3]`
- iii. `'spotSelection', sS_Name` This option allows the user to specify a list of kinetochores for which the measurement is to be done. For `vector` use the `sS` list made in step 6 for two-channel Delta measurement, in step 7 for three-channel Delta measurement, and in step 8 for Delta measurement of a spot category.

iv. **Examples:**

(1) Two channel Delta measurement – use the `sS` list from step 6:

Type: `iM_exp1_Nnf1CenpCndc80N_DMSO_CenpCndc80N = dublIntraMeasurements(mS_exp1_13042020_Nnf1CenpCndc80N_DMSO, 'centralise', 1, 'channels', [2 3], 'spotSelection', sS_exp1_Nnf1CenpCndc80N_DMSO_SpotsNdc80NNnf1)`

(2) Three channel Delta measurement – use the `sS` list from step 7 and do step (1) for the three combinations:

Type: `iM_exp1_Nnf1CenpCndc80N_DMSO_Nnf1CenpC = dublIntraMeasurements(mS_exp1_13042020_Nnf1CenpCndc80N_DMSO, 'centralise', 1, 'channels', [1 2], 'spotSelection', sS_exp1_Nnf1CenpCndc80N_DMSO_SpotsNdc80NNnf1)`

Type: `iM_exp1_Nnf1CenpCndc80N_DMSO_CenpCndc80N = dublIntraMeasurements(mS_exp1_13042020_Nnf1CenpCndc80N_DMSO, 'centralise', 1, 'channels', [2 3], 'spotSelection', sS_exp1_Nnf1CenpCndc80N_DMSO_SpotsNdc80NNnf1)`

Type: `iM_exp1_Nnf1CenpCndc80N_DMSO_Nnf1Ndc80N = dublIntraMeasurements(mS_exp1_13042020_Nnf1CenpCndc80N_DMSO, 'centralise', 1, 'channels', [1 3], 'spotSelection', sS_exp1_Nnf1CenpCndc80N_DMSO_SpotsNdc80NNnf1)`

(3) Delta measurement for Spot category – use the `ss` lists from step 8 and do step (1) for each category:

Type: `iM_exp1_Mad2CenpCNdc80N_DMSO_CenpCNdc80N_Mad2P = dublIntraMeasurements(mS_exp1_2004202_Mad2CenpCNdc80N_DMSO, 'centralise', 1, 'channels', [1 2], 'spotSelection', ss_exp1_Mad2CenpCNdc80N_DMSO_SpotsNdc80NMad2P)`

Type: `iM_exp1_Mad2CenpCNdc80N_DMSO_CenpCNdc80N_Mad2N = dublIntraMeasurements(mS_exp1_2004202_Mad2CenpCNdc80N_DMSO, 'centralise', 1, 'channels', [1 2], 'spotSelection', ss_exp1_Mad2CenpCNdc80N_DMSO_SpotsNdc80NMad2N)`

- b. Quick statistics and plots of the non-inflation corrected Delta measurements and kinetochore pair statistics.
 - i. To quickly access the mean, median and standard deviation of these measurements per kinetochore, type: `dublBasicStats(iM_Name)`, where in brackets is the `iM` name given in step 11a. KiD will display a list of the characteristics in the Command window. Choose the desired measurement and type its number in the Command window.
For example: to access the non-corrected Delta 3D statistics, type `1` and press `Enter`
 - ii. To quickly visualize a plot of these measurements per kinetochore, type: `dublBasicPlots(iM_Name)` and press `Enter`, where in brackets is the `iM` name given in step 11a. KiD will display a list of the characteristics in the Command window. Choose the desired measurement and type its number in the Command window.
For example: to plot the non-corrected Delta 3D, type `1` and press `Enter`
- c. Accessing the non-inflation corrected Delta and kinetochore pair data saved in the `iM` structures created in step 11a.
Critical: the inflation of the Delta measurements in the `iM` structures makes them non-informative *per se* and is to be used only for comparison to other studies that use non-inflation corrected measurements.

The detected kinetochore positions and distances are saved in the `iM_Name.microscope` structure.

- i. To access the kinetochore coordinates use `.coords`, followed by `.x`, `.y` or `.z` for the corresponding dimension. This will render a list with four columns, where the first two columns are the coordinates of the inner and outer markers of one of the sister kinetochores, and the third and fourth column are the inner and outer marker coordinates at the second sister kinetochore.
For example: to access the x coordinate of Nnf1 (column 2 and 4) and CenpC (column 1 and 3), type: `iM_exp1_Nnf1CenpCNdc80N_DMSO_Nnf1CenpC.microscope.coords.x`
- ii. To access the Delta 1D measurement vector with Delta>200nm filtered out, type: `iM_Name.microscope.depthFilter.delta.oneD`

- iii. To access the Delta 2D measurement vector with Delta>200nm filtered out, type:
`iM_Name.depthFilter.delta.twoD.all`
- iv. To access the Delta 3D measurement vector with Delta>200nm filtered out, type:
`iM_Name.microscope.depthFilter.delta.threeD.all`
- v. To access the raw Delta 1D measurement vector, type:
`iM_Name.raw.microscope.delta.oneD`
- vi. To access the raw Delta 2D measurement vector, type:
`iM_Name.raw.microscope.delta.twoD.all`
- vii. To access the raw Delta 3D measurement vector, type:
`iM_Name.raw.microscope.delta.threeD.all`
- viii. To access the 3D kinetochore sister-sister separation, type:
`iM_Name.microscope.sisSep.threeD`

Intensity measurements

- 12) Measurement of kinetochore marker fluorescent intensity. Here, we describe how to perform automated kinetochore intensity measurements in KiD and the different options that can be used.
Timing [10 min – 20 min]

Functionality:

- KiD measures the intensity in a sphere 300 nm radius (default, other mask and radius can be specified in the `jobset`) centered at the detected kinetochore centers.

- KiD uses the detected kinetochore centers of a reference kinetochore marker in one channel to measure the intensity in a sphere with the same center and 300 nm radius (default, other mask and radius can be specified in the `jobset`) in another channel.

For example: the staining is Ndc80(C)-eGFP, CenpC-A561 and Ndc80(N)-A647. The goal is to measure the intensity of Mad2 at kinetochores. Channel2 (CenpC-A561) is the CS channel used for primary spot detection. Kit can measure the intensity of Mad2 in a sphere with 300nm radius centered at the detected centers of CenpC kinetochores.

- a. In the Command window type: `IntiM_Name = dublIntensityMeasurements(mS_Name, 'channels', [a b], 'paired', 0 or 1, 'refMarker', 'option', 'spotSelection', sS_Name)`, where on the left is the name of the intensity measurement structure, `mS_Name` is the `mS` structure generated in 5a, 9d or 10b, and `sS_Name` is the spot selection made in step 6, 7, 8, 9 or 10.
Note: We suggest to name the intensity measurement

`IntiM_expN_ProteinsInChannelOrder_Treatment_Marker1Marker2`, where `Marker1` and `Marker2` are two channels in which the user will measure intensity.

For example: `IntiM_exp1_Nnf1CenpCNdc80N_DMSO_Nnf1CenpC`

Explanation and use of the options:

- i. `a` and `b` are the channels in which KiD will measure the intensity.
For example: `'channels', [1 2]` indicates channels 1 and 2.
 - ii. `'paired', 1` will prompt kit to use only the kinetochores paired in step 5. `'paired', 0` will prompt kit to use all spots detected irrespective of previous pairing,
Critical: The user should state `'paired', 0` if kinetochore pairing has not been performed, i.e. the user is continuing here from step 9.
 - iii. `'refMarker' – 'self'` prompts KiD to measure the intensity in a mask centered at the detected kinetochore center. The mask is defined in the `jobset`. The default mask is a sphere with 300 nm radius, see step 4 d iii.
`'inner'` or `'outer'` prompts KiD to use the spot centers detected in the inner or the outer of the two given channels (the user stated the order of kinetochore markers in step 4. d. iii.) to measure the intensity in a mask in both `'channels'`. As above, the mask is defined in the `jobset`. The default mask is a sphere with 300 nm radius, see step 4 d iii.
For example: the staining is Nnf1-A488, CenpC-A561 and Ndc80(N)-A647. The goal is to measure the intensity of Nnf1 around kinetochores. CenpC is positioned inner of Nnf1. Use `'refMarker', 'inner'` to measure the intensity of Nnf1 in a sphere with 300 nm radius, centered at the detected spot centers of CenpC kinetochores.
 - iv. If the user wishes to measure the intensity of a selection of kinetochores made in the “Spot quality control” section (step 6, 7, 8, or 9), the user can state the `sS` list at the place of `sS_Name`. Otherwise, use `[]` (an empty vector) instead of `sS_Name`.
- b. Accessing the intensity measurements. The `IntiM` structures, created in step 12a. contains the background and the background subtracted kinetochore intensity measurements in the selected fluorescent channels.
- i. To access the inner kinetochore marker background intensity type:
`IntiM_Name.intensity.bg.inner`
For example: To access the background intensity of the inner kinetochore marker (CenpC), type: `IntiM_exp1_Nnf1CenpCNdc80N_DMSO_Nnf1CenpC.intensity.bg.inner`
 - ii. To access the inner kinetochore marker mean intensity measurements (per kinetochore), type: `IntiM_Name.intensity.mean.inner`
 - iii. To access the inner kinetochore marker maximum intensity measurements (per kinetochore), type: `IntiM_Name.intensity.max.inner`

- iv. To access the outer kinetochore marker background intensity measurements (per kinetochore), type: `IntiM_Name.intensity.bg.outer`
- v. To access the outer kinetochore marker mean intensity measurements (per kinetochore), type: `IntiM_Name.intensity.mean.outer`
- vi. To access the outer kinetochore marker maximum intensity measurements (per kinetochore), type: `IntiM_Name.intensity.max.outer`

Bayesian Euclidian distances correction algorithm (BEDCA)

Distances between fluorescent spots are inflated (Suzuki et al., 2018), and thus need correction. In 3D, with an anisotropic PSF there is no analytical method. BEDCA is a sampling algorithm providing samples of the true distance which can be used to generate the posterior distribution. BEDCA is a Markov chain Monte Carlo (MCMC) algorithm and the Bayesian framework in BEDCA gives tighter confidence intervals than previous methods (Churchman et al., 2005; Suzuki et al., 2018; see Figure1, for testing of BEDCA data see Roscioli et al., 2020)

Critical: In order to produce reliable results, the kinetochore and cell sample sizes need to be sufficient. The kinetochore sample size should be increased for distances in the range of 0 to 30 nm and at that length scale, for instance a sample size of 500 kinetochores may be required in this range. Cell sizes should be greater than 5 (ideally as quantified by the diversity measures to allow for unequal kinetochore counts). To make sure the correction parameters and sample size are appropriate, the user should always check the quality of the correction by following the advice in step 15.

13) Input the 3D delta information from step 10. into the BEDCA algorithm

Timing [20 min – 30 min]

- a. Input the `iM` file in the BEDCA directory: Load the `iM` structures saved in step 11 into Matlab by dragging them in the Workspace window.
 - Analysis of the same Delta distance in samples with more than one treatment done in parallel. If more than one treatment is analyzed, in the Workspace window select all treatments that correspond to the same experiment and the same protein-protein distance by holding down `Command` and clicking on each `iM` structure with the left mouse button. Then save the structure selection in one file by clicking with right mouse button on the selection and choosing `Save as`. Choose as destination `MATLAB/BEDCA/ExptData` and as name choose the name of the individual `iM` structures **without Treatment** annotation (the structures saved together should be of the same distance, same experiment but different treatment only, see Example below). **For example:** the Ndc80N-CenpC distance is measured in cells treated with DMSO and with nocodazole, creating the `iM` structures: `iM_exp1_Nnf1CenpCNdc80N_DMSO_CenpCNdc80N` and `iM_exp1_Nnf1CenpCNdc80N_noc_CenpCNdc80N`. As all other parameters are the same except for treatment, the two structures can be saved in a single file, named

`iM_exp1_Nnf1CenpCNdc80N_CenpCNdc80N`. Then the single file is input into BEDCA as described above, and each treatment is accessed in BEDCA using the “treatment” input in the `Run_BEDCA` function.

- Analysis of experiment with only one treatment.

If only one treatment is used for the analyzed distance, in the Workspace window click with right mouse button on the `iM` structure, click on `Save as`, for name type the `iM` structure name **without** `Treatment` annotation (see example below) and for saving directory choose: `MATLAB/BEDCA/ExptData`. Repeat that for all `iM` structures to be corrected, i.e. all protein-protein distance measurements.

For example: The `iM` structure created in step 11 is named `iM_exp1_Nnf1CenpCNdc80N_DMSO_CenpCNdc80N`. Save the structure as: `iM_exp1_Nnf1CenpCNdc80N_CenpCNdc80N`. The structure will still appear in the Workspace window with name `iM_exp1_Nnf1CenpCNdc80N_DMSO_CenpCNdc80N` while the file will be named `iM_exp1_Nnf1CenpCNdc80N_CenpCNdc80N`.

Critical: Do not include annotation of the treatment in the `iM` structure saved in the `ExptData` folder. In case of multiple treatments, the `iM` structure contains all treatments of the same intra-kinetochore pair measurement in an individual or pooled experiment.

Note: We suggest the user to name this structure file `iM_expN_ProteinsInChannelOrder_ProteinProtein`, denoting the experiment number, the proteins imaged in channel order and the protein-protein distance.

- b. Input information about the data location and characteristics to BEDCA.
 - i. Open the `BEDCA` folder in the Matlab Current Folder window by double-clicking with the right mouse button.
 - ii. Open the `ExptData_list` file in the same manner. The `ExptData_list` file will appear in the Editor window. Here, the user enters information about the location of the data and the staining.
 - iii. Add any treatments used for first time with the software in the treatments library: At the top of the list the user will see `TreatmentLib = {'DMSO', 'DMSO'}, {'DMSO', 'untreated'}, {'Taxol15min', 'tax15min', 'tax'} ...`. To add a new treatment, after the first curly bracket, type in curly brackets the `'Treatment'` and any synonyms used, separated by commas (see example in the file and in the previous sentence). Make sure the treatment name input matches exactly the treatment name in the `iM` structure, saved in step 11. The treatments that have already been included can be seen in the curly brackets after `TreatmentLib`.
 - iv. Indicate the `iM` file name saved in the `ExptData` folder that will be used for correction: `FileNames{n} = 'iM_expN_ProteinsInChannelOrder_ProteinProtein.mat'`, where `n` is the item number in the list and the expression after is the name of the `iM` file.

Note: The user can leave comments in the list by using % sign before the text. That text will appear in green and will not be read as code by Matlab.

- v. Indicate the name of the analysis. To do so navigate to the **ExptDats** section. Provide the name of the sample by typing: `Expt_Dats{n}.name = AnalysisName`, where **n** is the item number in the list as chosen in 13 b. iv. and the expression after is the name of the Delta distances analysis. After running, BEDCA will automatically create a folder named as the **AnalysisName** input that will contain all figures and data of the BEDCA run. The analysis folder will be situated within the “MCMCruns” folder that is automatically created in the “Matlab” folder after the first BEDCA run.
- vi. Indicate the treatment. To do so navigate to the **Treatments** section of the **ExptData_list** file. At the bottom of the section type: `ExptDats{n}.treatment = 'Treatment'`; , where **n** is the item number in the list as chosen in step 13 b. iv. , and **'Treatment'** is the treatment of the sample as saved in the **iM** structure(s) (created in step 11.) and in the **TreatmentLib** (step 13 b. iii.). If the input **iM** file (created in step 13 a.) contains more than one treatment (see step 13. a.), type `ExptDats{n}.treatment = 'Treatment'`; for each treatment, keeping the same **n** number as chosen in step 13 b. iv.
For example: In step 11, the user created the structures:
`iM_exp1_Nnf1CenpCNdc80N_DMSO_Nnf1CenpC` and
`iM_exp1_Nnf1CenpCNdc80N_tax_Nnf1CenpC`. In step 13 a., the user created a combined **iM** file named: `iM_exp1_Nnf1CenpCNdc80N_Nnf1CenpC`. For this example, the item number of the distance is **1**. To indicate the treatments, the user is required to type:
`ExptDats{1}.treatment = 'DMSO'; ExptDats{1}.treatment = 'tax';`
- vii. Indicate the source of fluorescence in the sample. Navigate to the **Staining** section of the **ExptData_list** file and type: `ExptDats{n}.fluorophore = 'stain'`; , where **n** is the item number in the list as chosen in step 13 b. iv. , and **'stain'** is **'Ab'** if both proteins are labelled via indirect immunofluorescence (antibody staining) and **'GFP'** if one or both of the proteins are labelled with a fluorescent protein.
Note: In general, staining with an antibody provides better signal-to-noise ratio than using fluorescent protein labelling. Therefore, the BEDCA algorithm uses different parameters if one or both of the analyzed kinetochore markers is labelled with a fluorescent protein (see 14 b. i.).
- viii. Save the changes to the **Expt_Data_list** file by simultaneously pressing **Command** and **S** on the keyboard.

14) Use of BEDCA

Timing [30 min – 1 hour]

Run BEDCA. In the command window type: `Run_BEDCA(n, 'treatment', [], struct('filterdist', 200), struct('nsteps', value, 'a', 4))`, where **n** is the experiment item number in the **ExptData_list**, **'treatment'** is the treatment to be analyzed and **value** relates to the number of steps the BEDCA algorithm will take in attempt to infer the Delta distance (see 14 b. iii.). In first instance a **value** of

100000 is suggested, i.e. 100,000 steps. See next for more information on the parameters and filters used.

a. Parameters used by BEDCA

- i. Priors. The BEDCA algorithm uses priors (prior knowledge) for the spot spread in the x/y, and z directions, specifically for the precisions (inverse variances) τ_{aux} (the noise is assumed to be the same in x and y) and τ_{az} . Priors are needed as there is typically insufficient information in the data to use uninformed priors. Prior experimental knowledge, for instance, can be gleaned from Roscioli et al, 2020. The prior means for the standard deviations of the spot gaussian in x (sd_x , σ_x) and in z (sd_z , σ_z) are set to 20 nm and 40 nm, respectively, for antibody-stained samples. As antibody staining in general results in better signal-to-noise ratio as compared to fluorescent protein labels, the sd_x and sd_z prior means are set to 25 nm and 75 nm, respectively, when one or both of the proteins are tagged with fluorescent protein. In addition, the sd_z prior mean is twice sd_x reflecting the poorer resolution in z (at least two-fold lower than in x/y).
- ii. Alpha (α). The α parameter controls the prior variance; the relative error (of the prior) is $1/\sqrt{\alpha}$. A relative error of 30% ($\alpha=3$) seems to work on the majority of the data, whilst 100% ($\alpha=1$) is advised if possible. The α value by default is set to 4 and allows for 50% relative error in the τ_{aux} and τ_{az} prior. The user is recommended to use lower α value, although to compare across experiments using the same α is recommended.
- iii. The affect of your priors (means of τ_{aux} , τ_{az} , and α) should be checked post run. The posterior distribution should lie within the prior distribution, i.e. the data has improved the estimates (from prior knowledge) whilst being consistent with that prior knowledge. See Figure 7.
- iv. Chains. By default, BEDCA uses four independent runs (chains), i.e. using the same data input. This allows convergence of the algorithm to be assessed. Sampling algorithms need to converge to the desired distribution. In absence of convergence the results are UNRELIABLE. Convergence is thus essential for accurate distance correction.
- v. Number of steps. The number of steps is the number of iterations BEDCA uses of the underlying Markov chain. In case of a lack of convergence, the number of steps should be increased and the algorithm rerun. It is advised to increase by multiples of 2 or 5. Convergence is slower for smaller data sets and smaller distances.

b. Filters

- i. Z filter. The z filter is optional and removes any distances where the 100 nanometers or more of the distance is in the z-plane. That is used only for comparison in plots such that the user can check for effects on the distribution from kinetochores lying in the z-plane where the resolution is poorer as compared to the x/y plane.
- ii. 3D distance filter. Any uncorrected 3D Delta distances above 200 nm are filtered out by default. Delta distances rarely go beyond 200 nm given the size of the kinetochore (although

corona proteins may be this distance from the CCAN), and thus such measurements in most cases reflect outliers in the data. The 3D Delta filter by default removes KT measurements above this threshold (see 15 ii.). The user can increase the distance filter to appropriate value by replacing 200 with a desired distance in nanometers.

15) BEDCA output

Timing [10 min – 20 min]

a. Quality control

- i. BEDCA can alert the user of a problem by displaying in the Command window the following warnings:
 - **taux too strong or inappropriate** and **tauz too strong or inappropriate**. The data isn't consistent with your prior choices (either taux, tauz means or a). Check that the **a** parameter is set to 4 as default, and if a=4, try a smaller a, such as a=1. Check your prior estimates of spot center accuracy (mean taux, tauz). Alternatively, the user should check if the staining is annotated correctly, i.e. the input of 'Ab' or 'GFP' stain in the **ExptData_list** file. If neither of these resolves the warning, the user should go back to step 2 and optimize the imaging conditions such that the signal-to-noise ratio is improved.
 - **Fewer than 300 KT. Algorithm performance poor especially for distances < 50nm and Effective number of cells is <5. Biological variation will not be averaged out, so estimates are unreliable**. In that case, the user should perform another biological replicate, analyze it (KiD) and pool the data as described in step 9 above before running the BEDCA correction.

ii. Evaluation of the BEDCA run.

Critical: The user should **always** evaluate the run to make sure the obtained results are informative.

(1) Distribution. See Figure 8A.

The distributions of the inflated (input) and corrected Delta (output) are automatically plotted and the figure is saved in Matlab\MCMCrans**AnalysisName**\Figures under the name "DataWithPostEsts". Here, **AnalysisName** refers to the name under which the analysis is saved (see step 14 b. v.)

- Check that part of the distance distribution has not been cut off by the filtering of Delta 3D distances over 200nm (i.e. does not lie in the obvious tail of the distribution and is only removing what look like outliers). If the distribution has been cut off by the filter, change the filter as appropriate (see 14 c. ii.) and rerun the algorithm again (see 14 a).
- Check that the (uncorrected) distance distribution does not display more than one obvious peak. That would suggest a mixture of two distances which is inappropriate for BEDCA (we have not yet observed such case).

(2) Convergence. See Figure 8B.

Figure with the convergence characteristics is automatically saved in Matlab\MCMCrans**name**\Figures under the name "ConvPosteriorSummary". Here,

name refers to the name under which the analysis is saved (see step 14 b. v.). The Figure displays three plots: the convergence of the mean (μ), of τ_{aux} and τ_{z} (for more information on priors and convergence see 14 b. i. and 14 b. iii.).

- Check the convergence value is displayed at the top of each plot. If the convergence value (GRc) for all parameters is below 1.02, convergence has been successful and the user can proceed to step (3). Otherwise, the algorithm has not converged and the results are UNRELIABLE. If not converged, set the Number of steps (see 14 b. iv.) to a higher value, i.e. if the user has ran BEDCA with '**nsteps**', 100000, the user could attempt 300000. The maximum number of iterations that we have used for problematic datasets is 1,000,000. If that does not lead to convergence, increase the sample size if it is below 1000 kinetochores as too small kinetochore and cell sample size can also lead to lack of convergence.
- Check if the estimated τ_{aux} is smaller than τ_{z} . τ_{aux} and τ_{z} quantify the detection accuracy in the x/y and z axes, respectively. The resolution in x/y is in principle better than the one in z. Thus, the error in the x/y direction (τ_{aux}) should be smaller than the error in the z-direction (τ_{z}). In Roscioli et al., we observed orders of τ_{aux} to be 10^{-3} nm^2 and for τ_{z} 10^{-4} nm^2 .
- Check the shape of the mean, τ_{aux} and τ_{z} distributions. The distributions should not display multiple peaks or have a shape strongly deviating from gaussian.

Note: If the true distance mean Euclidian distance is very close to 0, the gaussian distribution of the mean Euclidian distance (μ) will be centered close to 0 value and thus the user will see only the positive values of the distribution, i.e. the distribution should resemble gaussian distribution cut-off at 0 on the left side. Such appearance is normal and the user should not classify this scenario as abnormal distribution shape.

b. Accessing the data

- i. Accessing the corrected distribution of Delta values. The distribution after Euclidian correction is saved as .csv file under the name of "MCMCSamples_chain1" in Matlab\MCMCruns**AnalysisName**, where **AnalysisName** refers to the name under which the analysis is saved (see step 14 b. v.).
- ii. Accessing the statistics of the corrected Delta distribution and the statistics of the BEDCA run. The statistics of the distribution mean, τ_{aux} and τ_{z} (see step 14 b. i.), and estimated sd_x and sd_z is saved as .csv file under the name of "MCMCSamples_chain1" in Matlab\MCMCruns**AnalysisName**, where **AnalysisName** refers to the name under which the analysis is saved (see step 14 b. v.).
- iii. Kinetochore and cell sample size. The number of cells, number of kinetochores (KTs), average kinetochores per cell (average KT/cell), number of kinetochore pairs (number pairs of KT), and the effective cell sample size (Effective (cell) sample size) numbers of the analyzed dataset are stated at beginning of each BEDCA run in the Command Window.

If the user wishes to display these characteristics again after the run, the user can type: `preRunchecks(n, 'treatment', [], struct('filterdist', 200), struct('nsteps', value, 'a', 4))`, where the input of the function is the same as the one used in `Run_BEDCA` previously (see step 14). Here, BEDCA will only display the characteristics without running again the analysis.

Note: Additional figures saved in the BEDCA run are depicted in Supplemental Figures 3 to 6.

Making figures of cells and kinetochore pairs used in the analysis

Critical: For steps 16 and 17, the user is required to open again the KiD folder in the Current folder panel (see step 3).

- 16) Plotting a kinetochore sister pair with at least one of the kinetochores used for analysis. In the command window type: `dublShowSisterPair(mS_Name{i}, 'sisterPair', XX)`, where `mS_Name` is the structure created in step 5 or 9, `i` is the cell number, `XX` is the kinetochore pair number.

Timing [15 min – 30 min]

Additional function options:

- a. Channels to be plotted. The user can specify which channels to be plotted by using option `'channels', [a]`, where `a` are the image channels to be plotted.

For example: `'channels', [1 2 3]` will prompt KiD to plot three of the imaged channels, while `'channels', [1 2]` will prompt KiD to plot the first and second acquired channel.
- a. Changing the image contrast.

The input for the `'contrast'` option is in the form of `{[0.1 1] [0.1 1] [0.1 1]}`, where each bracket corresponds to a fluorescent channel in the order 488 nm, 561 nm, 647 nm. The contrast input is in the borders between 0.1 and 1.

Increase in the lower limit will increase contrast in the corresponding channel.

For example: `'contrast', {[0.1 1] [0.2 1] [0.1 1]}` will increase the contrast in the 561 nm channel

Decrease in the upper limit will lower the contrast in the corresponding channel.

For example: `'contrast', {[0.1 1] [0.1 1] [0.1 0.9]}` will lower the contrast in the 647 nm channel.
- b. Plotting two images at the same intensity scale. The user can obtain the true intensity value of each fluorescent channel by using `'contrast', 'help'`. Next, the user needs to calculate by what percentage the contrast of the second image needs to be adjusted to match the first image intensity scale.

Note: after input of `'contrast', 'help'`, KiD will prompt the user to choose contrast scale. If the user has not yet calculated the wanted scale, input of `[0.1 1]` will allow KiD to continue to the next channel.

For example: The first image intensity is 50 and the second image intensity is 100. To be on the same intensity scale, the intensity of the second image needs to be decreased by 50%. In the scale of 0.1 to 1 that corresponds to 0.5. Therefore, the user can plot the second image with option `'contrast', [0.1 0.5]` for the respective channel and the two images will be on the same

intensity scale.

- c. Zoom. The user can choose to plot an image zoomed in at the kinetochore pair by using option 'zoom', 1 or to plot the full cell using option 'zoom', 0. In each of the cases KiD will mark the detected kinetochore centers of the 'sisterPair'.
 - d. Z projection. By default, KiD plots maximum intensity projection over five z slices surrounding the kinetochore pair center z-slice. The user can choose to plot a single Z slice containing the detected kinetochore pair center by using the option 'zProject', 0. Alternatively, the user can plot a maximum intensity projection of all z slices by using option 'zProject', 1, or a maximum projection of 5 slices total centered at the kinetochore-pair slice by using 'zProject', -1.
 - e. Example. `dublShowSisterPair(mS_exp1_13042020_Nnf1CenpCNdc80N_DMSO{1}, 'sisterPair', 5, 'imageChans', [1 2 3], 'contrast', {[0.1 1] [0.2 1] [0.1 1]}, 'zoom', 1, 'zProject', -1)`. With such stated options, KiD will display the first movie of the `Nnf1CenpCNdc80N` analysis, the 5th kinetochore pair as detected in the CS channel in all three fluorescent channels, the contrast is default for the 488 nm and 647 nm channels and enhanced in the 561 nm channel. Further, the image is a zoom-in at the kinetochore pair and represents a maximum intensity z-projection over 5 slices.
- 17) Plot one of the analyzed cells. In the command window type: `kitShowImage(mS_Name{i})`, where `mS_Name` is the structure created in step 5 or step 9, and `i` is the cell number.
Note: The additional options are inputted separated by commas as in step 16).
Timing [15 min – 30 min]

Additional function options:

- a. Channels to be plotted. The user can specify which channels to be plotted by using option 'imageChans', [a], where `a` are the image channels to be plotted.
For example: 'imageChans', [1 2 3] will prompt KiD to plot three of the imaged channels, while 'imageChans', [1 2] will prompt KiD to plot the first and second acquired channel.
- b. Coordinate system. By default, KiD will display the image in the x and y coordinates. The user can plot the x and z or y and z coordinates by using option 'coords', 'xz' or 'coords', 'yz', respectively.
- c. Crop. By default, KiD shows crop of the image corresponding to the ROI selected in the `jobset` set up. The user can display the full image or the full image with the selected crop annotated by using option 'crop', 0 or 'crop', -1, respectively.
- d. Projection range. By default, KiD will not project over the third axis not given by 'coords'. To make a maximum intensity projection, the user can use 'projectionRange', 'help'. Next, KiD will display the possible values the range can take in pixels and request a range from the user. The user should input the two values in square parentheses.

- e. Changing the image contrast.
 The input for the 'contrast' option is in the form of `{[0.1 1] [0.1 1] [0.1 1]}`, where each bracket corresponds to a fluorescent channel in the order 488 nm, 561 nm, 647 nm. The contrast input is in the borders between 0.1 and 1.
 Increase in the lower limit will increase contrast in the corresponding channel.
For example: 'contrast', `{[0.1 1] [0.2 1] [0.1 1]}` will increase the contrast in the 561 nm channel
 Decrease in the upper limit will lower the contrast in the corresponding channel.
For example: 'contrast', `{[0.1 1] [0.1 1] [0.1 0.9]}` will lower the contrast in the 647 nm channel.
- f. Plotting two images at the same intensity scale. The user can obtain the true intensity value of each fluorescent channel by using 'contrast', 'help'. Next, the user needs to calculate by what percentage the contrast of the second image needs to be adjusted to match the first image intensity scale.
Note: after input of 'contrast', 'help', KiD will prompt the user to choose contrast scale. If the user has not yet calculated the wanted scale, input of `[0.1 1]` will allow KiD to continue to the next channel.
For example: The first image intensity is 50 and the second image intensity is 100. To be on the same intensity scale, the intensity of the second image needs to be decreased by 50%. In the scale of 0.1 to 1 that corresponds to 0.5. Therefore, the user can plot the second image with option 'contrast', `[0.1 0.5]` for the respective channel and the two images will be on the same intensity scale.
- g. Scale Bar. By default, KiD will display scale bar of 3 μm at the bottom right of the image, without length label. To change the length of the scale bar use option 'scaleBarSize', `x`, where `x` is the desired length in μm . To display label of the scale bar length, use option 'scaleBarLabel', `1`.
- h. Labelling on the image. To display text overlaid with the image use option 'textNorthWest', 'textNorthEast' or 'textSouthEast' to display the text in the upper left corner, upper right corner or bottom right corner, respectively. Input the text in the form `{'label'}`, where label is the text, or to separate the text in multiple line use `{'label1', 'label2', 'label3'}` where each label will appear on separate line.
For example: 'textNorthEast', `{'Nnf1-A488', 'CenpC-A561', 'Ndc80(N)-A647'}` will display in the upper right corner Nnf1-A488, CenpC-A561 and Ndc80(N)-A647, each on a new line.
- i. Transpose the image. To transpose the image, i.e. flip the image on its main diagonal axis, use option 'transpose', `1`
- 18) Bibliography.
- Abbreviations in text:
 ACS – approximate chromatic shift
 CS channel – coordinate system channel.
 NCS – non-coordinate system channel.
 - Variable functional name abbreviations

jS – jobset, created in step 3 and 4.
mS – movie structure, created in step 6 and 9.
sS_sel – spot selection **before** the metadata is updated to adhere to raw movie numbers, created in steps 6, 7, 8 and
sS – spot selection **after** the metadata is updated to adhere to raw movie numbers, created in steps 6, 7, 8 and
iM – intra-measurements, file that contains intra-kinetochore Delta measurements, created in step 11.
IntiM – intensity intra-measurements, file that contains kinetochore intensity measurements, created in step 12. The kinetochore sample can be chosen to be the kinetochore subset used for intra-kinetochore Delta measurements, created in step 6, 7 or 8.

- c. List of functions used and their syntax, refer to the protocol for complete information on the available options.

```

jS_Name = kitGUI
dublManualPairSisters(jS_Name, 'imageChans', [x], 'plotChan', x)
sS_Name_sel = kitSelectData(mS_Name_sel, 'channel', x, 'method', 'deselect')
sS_Name = kitUpdateSpotSelelections(sS_Name_sel, mS_Name, SelectedCells_Name)
sS_Name = kitFilterSpots(jS_Name, 'channel', x)
iM_Name = dublIntraMeasurements(mS_Name, 'centralise', 1, 'channels', [a b],
'spotSelection', sS_Name)
dublBasicStats(iM_Name)
dublBasicPlots(iM_Name)
IntiM_Name = dublIntensityMeasurements(mS_Name, 'channels', [a b], 'paired', 0 or 1,
'refMarker', 'option', 'spotSelection', sS_Name)
sS_Pool_Name = kitCombineSpotSelections({sS_Name, sS_Name, sS_Name})
Run_BEDCA(n, 'treatment', [], struct('filterdist', 200), struct('nsteps', value))
preRunchecks(n, 'treatment', [], struct('filterdist', 200), struct('nsteps', value))
dublShowSisterPair(mS_Name{i}, 'sisterPair', XX)
kitShowImage(mS_Name{i})
  
```

LIMITATIONS

The user should abstain for using the above protocol for analysis of structures that produce non-gaussian shaped staining. For example, kinetochore components can form crescents. The KiD software cannot detect the center of crescents accurately and thus the results are unreliable.

TROUBLESHOOTING

Problem:

Metadata not read in correctly or at all.

Potential Solution:

Open the image via BioFormats import in Fiji, do not use virtual hyperstack here. Once opened, the image should have the correct Z sectioning and channels. If not, re-order the movie and save it as **ome.tif**. If the problem persists, make sure you followed steps 1 and 2 accurately.

Problem:

No or very few spots detected in the majority of jobs (images).

Potential Solution:

KiD is most effective in a range of signal to noise ratio. However, because of the different default offset of signal units being different in alternative microscope set ups, that range is not unique. To deduce the range for your system, image metaphase cells with different exposure and laser power. Use appropriate ACS as described in steps 1 - 4. Analyze the cells as suggested in step 4 and note which conditions give close to the expected number of spots (KiD will display in the Command window number of spots detected in each movie). Use the condition with best quality spots from the ones with acceptable amount of detected spots.

ACKNOWLEDGMENTS

We thank Alessio Inchingolo for testing the protocol and providing suggestions for improvement. We also thank Laura Cooper from Warwick CAMDU for help with depositing the code on GitHub. This work was supported by the Leverhulme Trust (RPG-2017-349 to AM and NJB). Work in the AM lab was also supported by a Wellcome Trust Senior Investigator Award (106151/Z/14/Z) and a Royal Society Wolfson Research Merit Award (WM150020). TG is funded by the Medical Research Council Doctoral Training Partnership grant MR/J003964/1.

AUTHOR CONTRIBUTIONS

A.D.M. and N.J.B. were responsible for the project conception, planning, and supervision. The manuscript was developed and written by T.G. and edited by A.M., N.B., E.R. and J.H. Modifications to the KiD GUIs were made by J.H. with input from T.G.

DECLARATION OF INTERESTS

The authors declare no competing interests.

REFERENCES

1. Churchman, L., Okten, Z., Rock, R., Dawson, J. and Spudich, J., 2005. Single molecule high-resolution colocalization of Cy3 and Cy5 attached to macromolecules measures intramolecular distances through time. *Proceedings of the National Academy of Sciences*, 102(5), pp.1419-1423.
2. Roscioli, E., Germanova, T., Smith, C., Embacher, P., Erent, M., Thompson, A., Burroughs, N. and McAinsh, A., 2020. Ensemble-Level Organization of Human Kinetochores and Evidence for Distinct Tension and Attachment Sensors. *Cell Reports*, 31(4), p.107535.
3. Suzuki, A., Long, S. and Salmon, E., 2018. An optimized method for 3D fluorescence co-localization applied to human kinetochore protein architecture. *eLife*, 7.

FIGURE LEGENDS

Figure 1: 3D Delta Euclidian distance measurements of CenpC to CenpC (0 nm true distance). Comparison between the measurement before and after BEDCA inflation correction. A) Example images of CenpC labelled with a-CenpC primary antibody and mix of A488, A568 and A647 secondary antibodies. B) Delta 3D distance measurements of the CenpC-A488-to-CenpCA568, CenpC-A488-to-CenpCA647, and CenpC-A568-to-CenpCA647 distances. The measured 3D Euclidian distance distribution ($\Delta 3D$) prior to BEDCA distance inflation correction is shown in black. The 3D Euclidian distance distribution after BEDCA distance inflation correction (ΔEC) is shown in red. Mean, standard deviation and sample size for each distribution is indicated on the right. (Adapted from Roscioli et al., 2020)

Figure 2: Workflows for Delta Euclidian distance inflation corrected measurements (ΔEC) between kinetochore components and kinetochore intensity measurements. The protocol contains the steps for four workflows depending on the desired output: (1) For ΔEC measurement between two fluorescently labelled kinetochore proteins, follow steps 1, 2, 3, 4, 5, 6, 10, 11, 13, 14 and 15. (2) For ΔEC measurements between three fluorescently labelled kinetochore proteins (in pairs), follow steps 1, 2, 3, 4, 5, 6, 7, 10, 11, 13, 14 and 15. (3) For ΔEC measurements between two fluorescently labelled kinetochore proteins at kinetochore marker positive and negative kinetochores, follow steps 1, 2, 3, 4, 5, 6, 7, 10, 11, 13, 14 and 15. (4) For kinetochore intensity measurements, follow steps 1, 2, 3, 4, 9, and 12, or perform step 12 after any of the previous workflows.

Figure 3: Kinetochore Delta (KiD) software graphic user interphase (GUI) for data analysis set up. The parameters of data analysis are set up and saved in a jobset as described in steps 3 and 4. The figure displays the jobset analysis set up of the provided Nnf1-CenpC-Ndc80N sample dataset as described in step 4. (See also Supplemental Figures 1 and 2)

Figure 4: Kinetochore sister-sister pairing and spot quality control in the Coordinate system channel (CSC). A) Kinetochore sister-sister pairing. Left: zoom-in at the kinetochore spot under consideration (white cross) and spots within two microns that are suggested for pairing (green cross), already paired (red cross) or previously ignored for pairing (yellow cross). The image is projection of 5 z-slices around the spot under consideration. Right: image region of interest as set by the user in step 4, projection of 5 z-slices around the spot under consideration. B) Examples of kinetochores that should be ignored in the analysis due to spot distortion in the kinetochore under consideration or its kinetochore sister

pair (2 and 4), wrong detection of the kinetochore spot center (1), and no sister kinetochore spot detection (3, 5 and 6).

Figure 5: **Kinetochore spot selection for spot quality control in ΔEC measurements.** A. and B. show examples of spot selection GUI using `kitSelectData` function in two analyzed cells from the exemplar dataset after KiD spot detection and manual sister-sister pairing. The user is required to evaluate the spot shape and center detection, and to discard non-gaussian shaped asymmetric spots and spots with wrong center detection. A. Spots 1, 31, 40 and 47 are to be discarded. Spot 1 is distorted. Spots 31, 40 and 47 are too close to a neighboring spot and the center may not be detected appropriately. B. Spots 4, 18, 28, 33 and 49 are to be discarded. These spots are distorted.

Figure 6: **Kinetochore spot selection for spot quality control in intensity measurements.** A. and B. show examples of spot selection GUI using `kitFilterSpots` function in two analyzed cells from the exemplar dataset after KiD spot detection. The user is required to evaluate the spot shape and center detection, and to discard non-gaussian shaped asymmetric spots and spots with wrong center detection. Spots with green outline will be accepted and spots with red outline will be discarded in the analysis. The user can change the outline of one spot by clicking on it and of all spots by clicking on "Invert All". In the figure example, the spots have been evaluated and selected accordingly.

Figure 7: **Quality control of BEDCA run. Position of posterior distributions of the ΔEC mean, τ_{aux} , and τ_{tauz} in relation to boundaries of set prior distributions.** A) Example of figure saved as "Posterior_mu" in "MCMC_EuclDistMargFigs" folder using Nnf1-to-Ndc80N distance correction from provided dataset. Histogram of corrected mean (μ) distance (blue). Red line indicates the boundary of the mean prior. Prior used is indicated in the legend (60 nm). The estimated mean and sd. of the posterior μ distribution are stated above (mean 57.4496 nm, sd. 1.214). B) Example of figure saved as "Posterior_taux" in "MCMC_EuclDistMargFigs" folder, dataset as in A. Histogram of estimated τ_{aux} (precision in x) measurements (blue). Red line indicates the boundary of the τ_{aux} prior. Prior used is indicated in the legend (0.0025 nm). The estimated mean and sd. of the posterior τ_{aux} distribution are stated above (mean 0.002594 nm, sd. 0.00021498). C) Example of figure saved as "Posterior_tauz" in "MCMC_EuclDistMargFigs" folder, dataset as in A. Histogram of estimated τ_{tauz} (precision in z) measurements (blue). Red line indicates the boundary of the τ_{tauz} prior. Prior used is indicated in the legend (0.000625 nm). The estimated mean and sd. of the posterior τ_{tauz} distribution are stated above (mean 0.00036346 nm, sd. 0.000023406).

Figure 8: **Quality control of BEDCA run. $\Delta 3D$ and ΔEC distributions, and convergence.** A) 3D Delta Euclidian distance distribution of the Nnf1-to-Ndc80N distance from the provided dataset. The figure is automatically saved by the algorithm under the name "DataWithPostEsts". The figure shows histogram of the 3D distance measurements before (blue) and after (red) BEDCA correction. The uncorrected 3D Delta distribution (blue) lies before the 200 nm cutoff imposed in BEDCA. B) Convergence of the mean, τ_{aux} (precision in x), and τ_{tauz} (precision in z) of the Nnf1-to-Ndc80N distance measurements from the provided dataset (see A.). The figure is automatically saved as "ConvPosteriorSummary". BEDCA is ran with default parameters. GRc numbers below 1.01 indicate successful convergence. τ_{aux} is in the order of magnitude of 10^{-3} . τ_{tauz} is in order of magnitude of 10^{-4} .

Supplemental figures:

Supplemental Figure 1: **Kinetochores Delta (KiD) software graphic user interphase (GUI)**. Instructions on: A) Entering imaging data in KiD. B) Spot detection process set up for the acquired imaging channels. C) Set up of chromatic shift correction. For full details see steps 3 and 4 from the protocol.

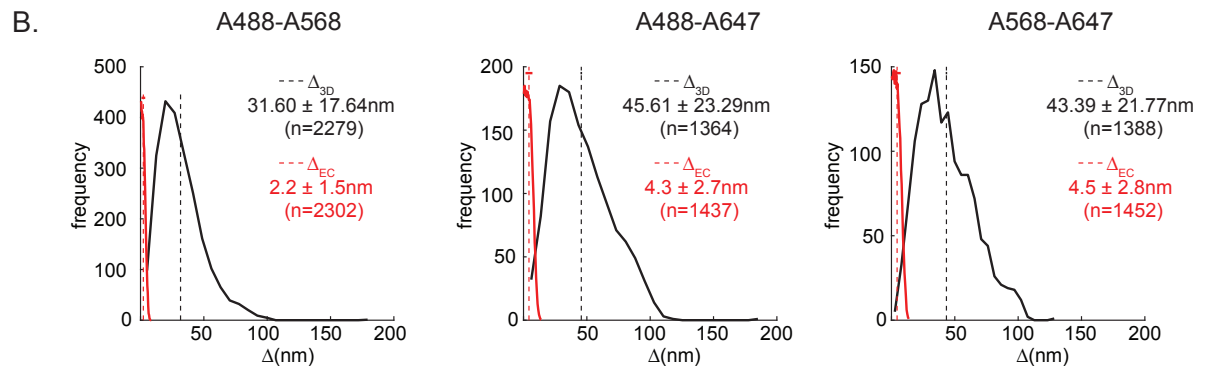
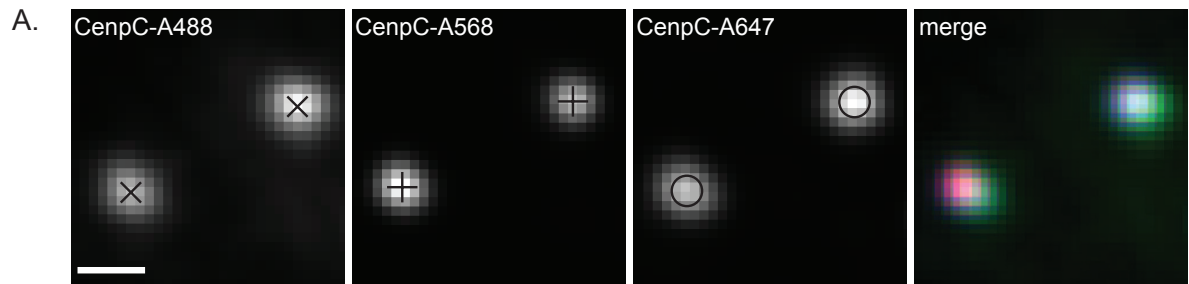
Supplemental Figure 2: **Kinetochores Delta (KiD) software graphic user interphase (GUI)**. Instructions on: A) Set up of parameters for Neighbour spot detection and intensity measurements. B) Saving and executing the jobset analysis.

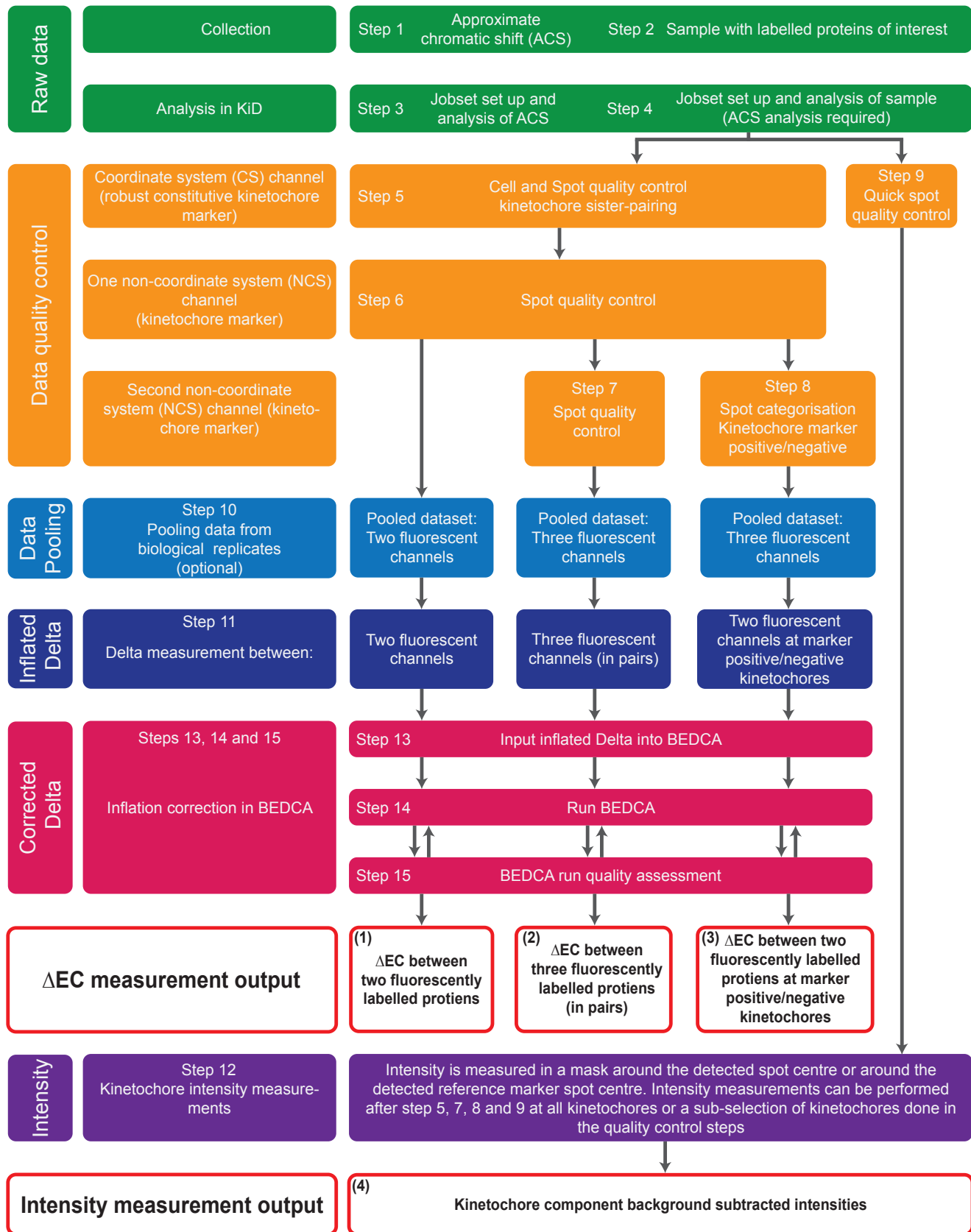
Supplemental Figure 3: **Posterior distributions and samples of μ , τ_{ax} and τ_{az}** . A) Example of figure saved as "Posterior_μ" in "MCMC_EuclDistMargFigsConv" folder, using Nnf1-to-Ndc80N distance correction from provided dataset. Left: μ estimation at each sample, GRc shown above is below 1.01 and indicates convergence. Colors indicate the four runs Right: Histogram of corrected mean (μ) in each of the four runs (red, yellow, dark and light blue). B) Example of figure saved as "Posterior_τ_{ax}" in "MCMC_EuclDistMargFigsConv" folder, dataset as in A. Left: τ_{ax} (precision in x) estimation at each sample, GRc shown above is below 1.01 and indicates convergence. Red, yellow, dark and light blue colours indicate the four runs. Right: Histogram of corrected τ_{ax} (precision in x) in each of the four runs (red, yellow, dark and light blue). C) Example of figure saved as "Posterior_τ_{az}" in "MCMC_EuclDistMargFigsConv" folder, dataset as in A. Left: τ_{az} (precision in z) estimation at each sample, GRc shown above is below 1.01 and indicates convergence. Red, yellow, dark and light blue colours indicate the four runs. Right: Histogram of corrected τ_{az} (precision in z) in each of the four runs (red, yellow, dark and light blue).

Supplemental Figure 4: **$\Delta 3\text{D}$ distance distributions and simulation**. A) Example of figure saved as "DataSimComp" in "Figures" folder, using Nnf1-to-Ndc80N distance correction from provided dataset. Histogram of the measured 3D delta distance distribution (black) and the simulated 3D delta distance distribution in BEDCA after sampling. B) Example of figure saved as "MCMC_EuclDistMarg3DrData", dataset as in A. Histogram of the 3D delta distance measurements that are input in BEDCA.

Supplemental Figure 5: **Kinetochores-Kinetochores distance and Intra-kinetochores Delta distance spherical angles**. A) Schematic showing the theta and phi angle annotation as related to K-K and Delta vector angles inferred by BEDCA B) Example of figure saved as "ConvPosterior_hiddenstates" in "MCMC_EuclDistMargFigsConv" folder, as automatically saved for Nnf1-Ndc80N measurement from the provided dataset. The figure shows average inferred theta per run (red, yellow light and dark blue) versus the mean of inferred theta over the four runs. C) Example of figure saved as "MCMC_EuclDistMarg_angularData", dataset as in B. The figure shows histograms of the inferred theta, cosine(theta) and phi (see A.).

Supplemental Figure 6: **ΔEC mean, τ_{ax} and τ_{az} inference per sample per run and histograms of the posteriors**. A) Example of figure saved as "DataSimComp" in "Figures" folder, using Nnf1-to-Ndc80N distance correction from provided dataset. Inference of the mean (μ), τ_{ax} (precision in x) and τ_{az} (precision in z) at each sample for each run (red, yellow, light and dark blue). B) Example of figure saved as "PosteriorParams" in "Figures" folder, dataset as in A. Histogram of estimated posterior distribution of μ , sig_x (standard deviation of spot gaussian in x), and sig_z (standard deviation of spot gaussian in z), respectively left to right. X axis values are shown in nm.





KID 1.0.1

Open existing jobset

1. Movie and ROI

Select directory /Users/u1693259/Dropbox/My Mac (007522)/Dx

Available movies:

ER_170804_MC133_9G3Nnf1CenpC_14_dms0_05/ER_170804_MK
ER_170804_MC133_9G3Nnf1CenpC_14_dms0_06/ER_170804_MK
ER_170804_MC133_9G3Nnf1CenpC_14_dms0_07/ER_170804_MK
ER_170804_MC133_9G3Nnf1CenpC_14_dms0_08/ER_170804_MK
ER_170804_MC133_9G3Nnf1CenpC_14_dms0_09/ER_170804_MK
ER_170804_MC133_9G3Nnf1CenpC_14_dms0_10/ER_170804_MK
ER_170804_MC133_9G3Nnf1CenpC_14_dms0_11/ER_170804_MK
ER_170804_MC133_9G3Nnf1CenpC_14_dms0_12/ER_170804_MK
ER_170804_MC133_9G3Nnf1CenpC_14_dms0_13/ER_170804_MK
ER_170804_MC133_9G3Nnf1CenpC_14_dms0_14/ER_170804_MK
ER_170804_MC133_9G3Nnf1CenpC_14_dms0_15/ER_170804_MK
ER_170804_MC133_9G3Nnf1CenpC_14_dms0_16/ER_170804_MK
ER_170804_MC133_9G3Nnf1CenpC_14_dms0_17/ER_170804_MK

ROIs:

Add crop Add full Delete View

ER_170804_MC13...01.ome.ome.rdd [124 141 284 262]
ER_170804_MC13...02.ome.ome.rdd [168 127 256 225]
ER_170804_MC13...03.ome.ome.rdd [135 125 265 269]
ER_170804_MC13...04.ome.ome.rdd [145 146 262 252]
ER_170804_MC13...05.ome.ome.rdd [121 121 292 262]
ER_170804_MC13...06.ome.ome.rdd [112 122 258 273]
ER_170804_MC13...07.ome.ome.rdd [152 134 239 272]
ER_170804_MC13...08.ome.ome.rdd [145 124 239 251]
ER_170804_MC13...09.ome.ome.rdd [105 140 278 271]
ER_170804_MC13...10.ome.ome.rdd [115 132 254 257]
ER_170804_MC13...11.ome.ome.rdd [110 122 256 253]
ER_170804_MC13...12.ome.ome.rdd [149 143 244 241]
ER_170804_MC13...13.ome.ome.rdd [133 134 250 253]
ER_170804_MC13...14.ome.ome.rdd [116 114 257 263]
ER_170804_MC13...15.ome.ome.rdd [137 102 248 279]
ER_170804_MC13...16.ome.ome.rdd [134 133 252 244]
ER_170804_MC13...17.ome.ome.rdd [131 126 265 255]
ER_170804_MC13...18.ome.ome.rdd [143 125 251 238]
ER_170804_MC13...19.ome.ome.rdd [120 76 284 238]
ER_170804_MC13...20.ome.ome.rdd [95 123 278 263]

2. Process setup

Process type 2D/3D only

Coordinate system Metaphase plate

Coordinate system channel 1 2 3

Channel 1
Spot detection Neighbour
Spot refinement MMF

Channel 2
Spot detection Histogram
Spot refinement MMF

Channel 3
Spot detection Neighbour
Spot refinement MMF

3. Options

Spot detection & refinement

Min spots per frame 20
Max spots per frame 1000

Max MMF time per frame (min) 300

Weight for intensity restriction: Ch.1 0.05
Ch.2 0.075
Ch.3 0.1

Chromatic shift

Provide chromatic shift correction

Chromatic shift jobsets

Channel vector	Jobset	Channel order
1 -> 2	JS_170804_chrs.tif...	1 -> 2
1 -> 3	JS_170804_chrs.tif...	1 -> 3
2 -> 3	JS_170804_chrs.tif...	2 -> 3

Filter chromatic shift spots

Min spot intensity (% of max) 25
Min spot separation (um) 0.75

Neighbour spot detection

Mask shape Semi-circle
Mask radius (um) 0.3

Neighbour orientation

inner khore	Channel number	outer khore
2	1	3

Intensity measurement

Measure in channels... 1 2 3

Mask shape Circle
Mask radius (um) 0.3

4. Execution

Jobset name JS_170804_Nnf19G3

Validate metadata

Save

Execute



A.

Locate the white cross' sister.
Click on an: unallocated (g), ignored (y) or pre-paired (r) cross.
Press **backspace** if none applicable.

Zoom-in at the kinetochore under consideration

Image crop showing the spot under consideration in the context of the full cell

X - Suggested kinetochore pair spots

X - Spot under consideration

X - Previously ignored spot

X - Already paired kinetochore spots. Pairing can be over-written by clicking on red-cross marked spot

X - Spot under consideration

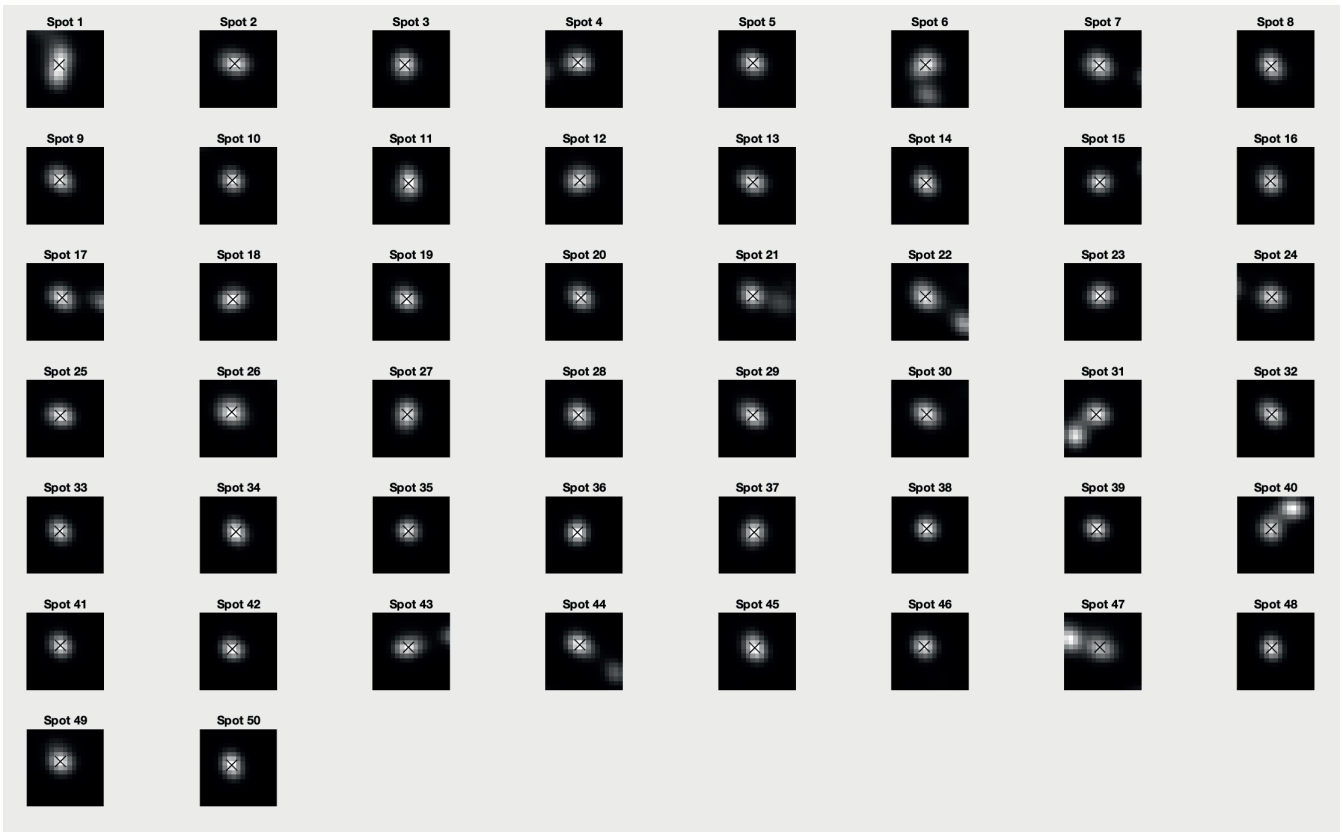
Left figure panel

Right figure panel

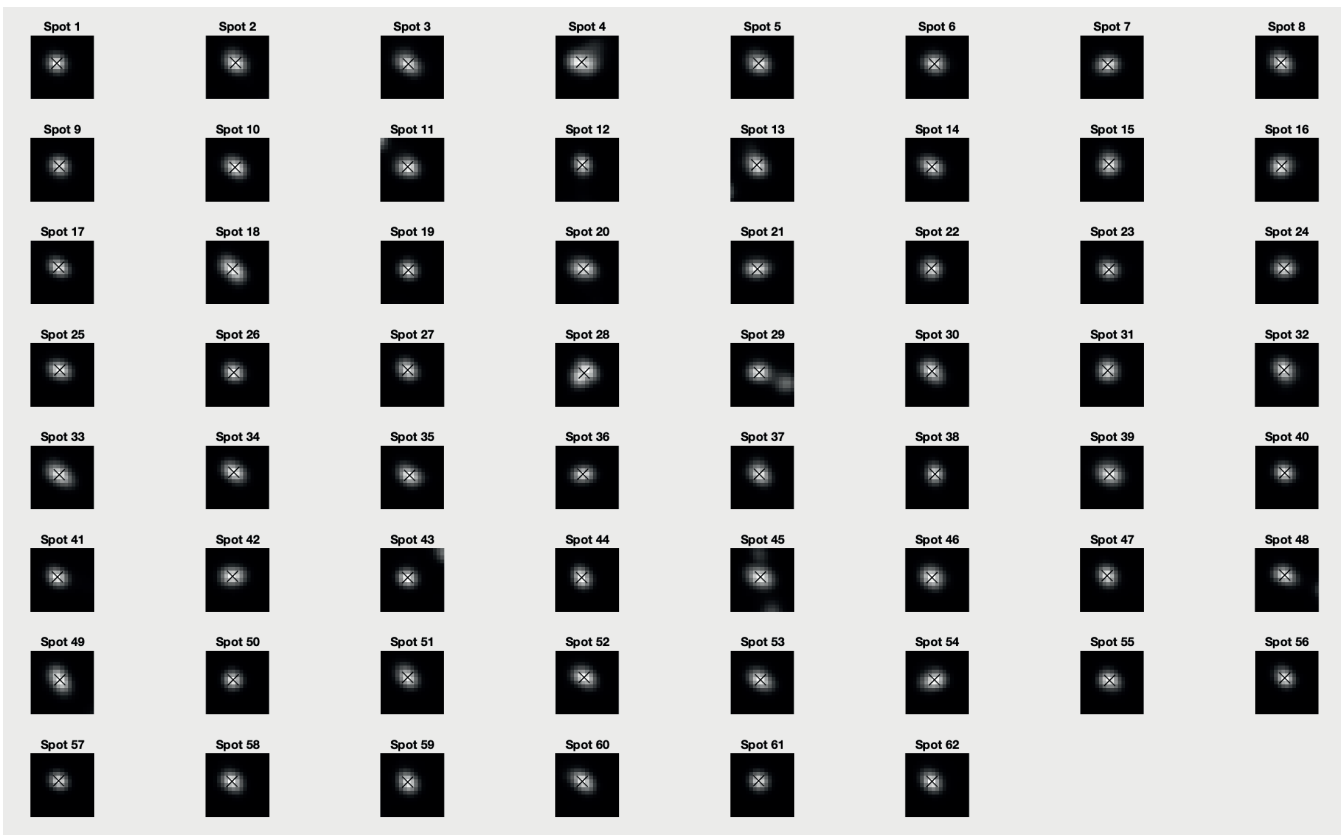
B.



A.



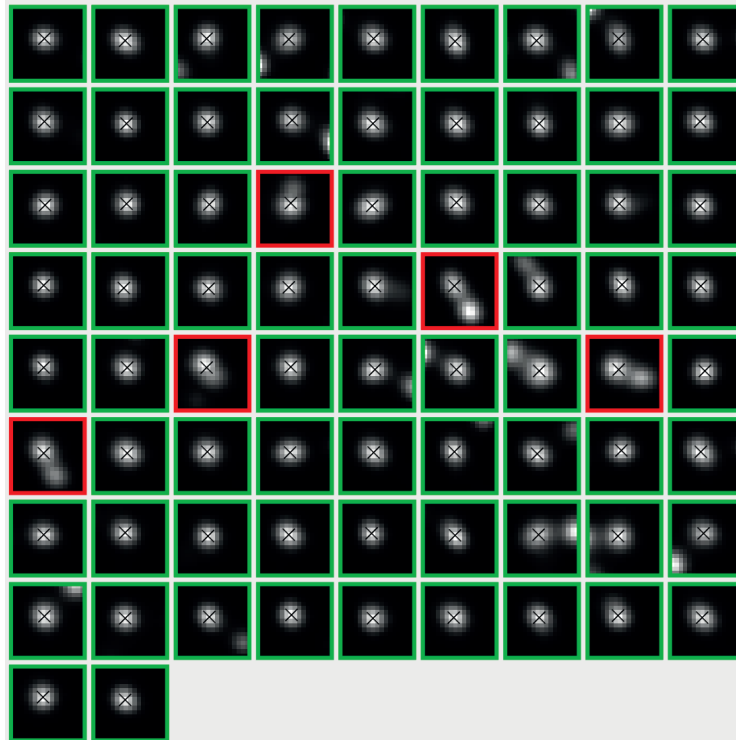
B.



A.

Click on spots to keep (green) or remove (red).

Next

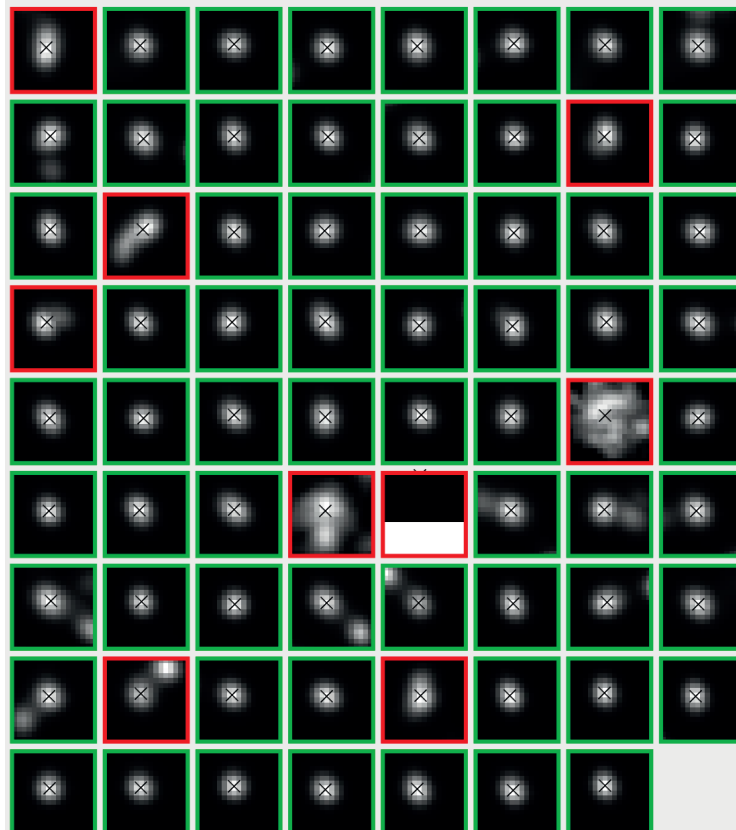


Invert all

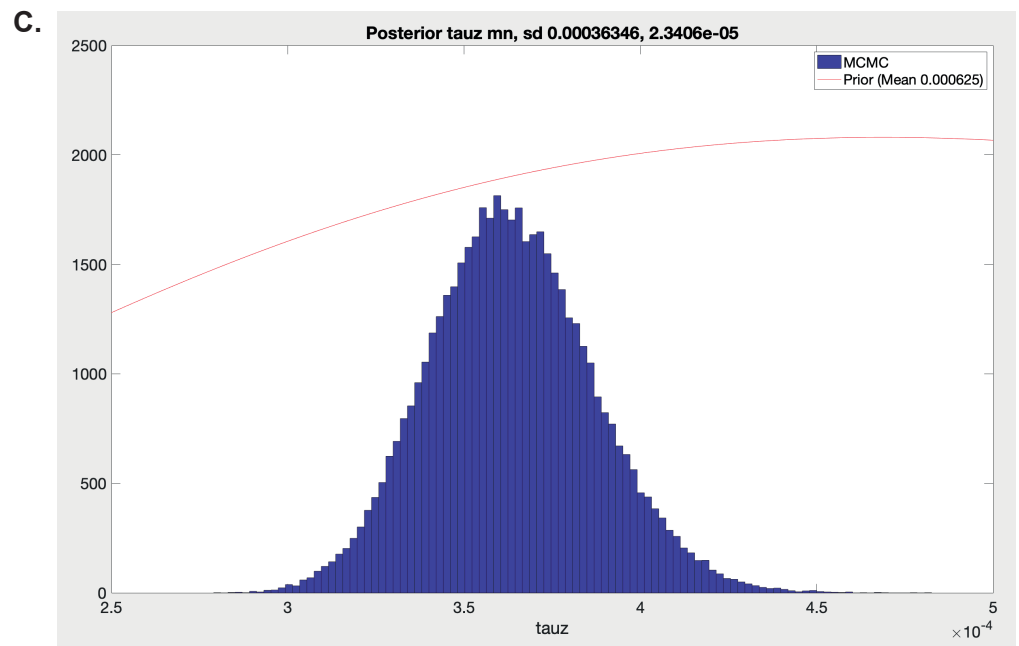
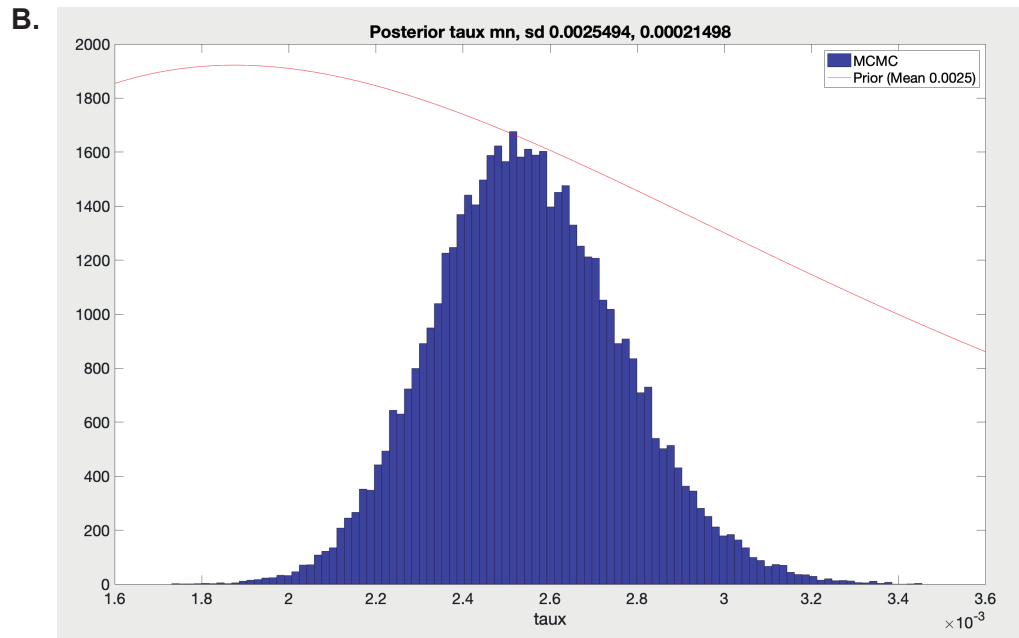
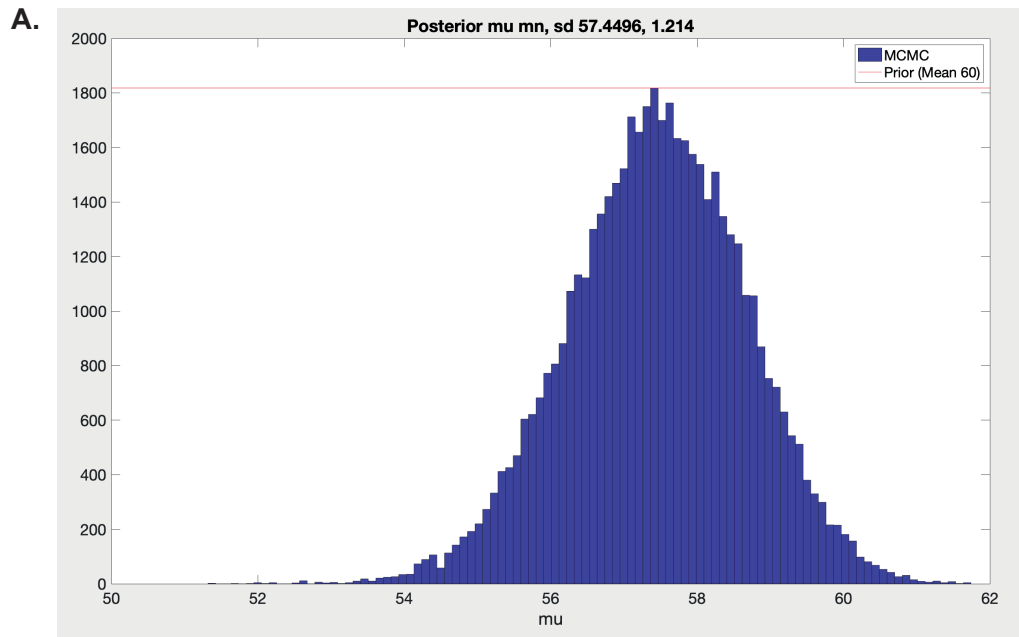
B.

Click on spots to keep (green) or remove (red).

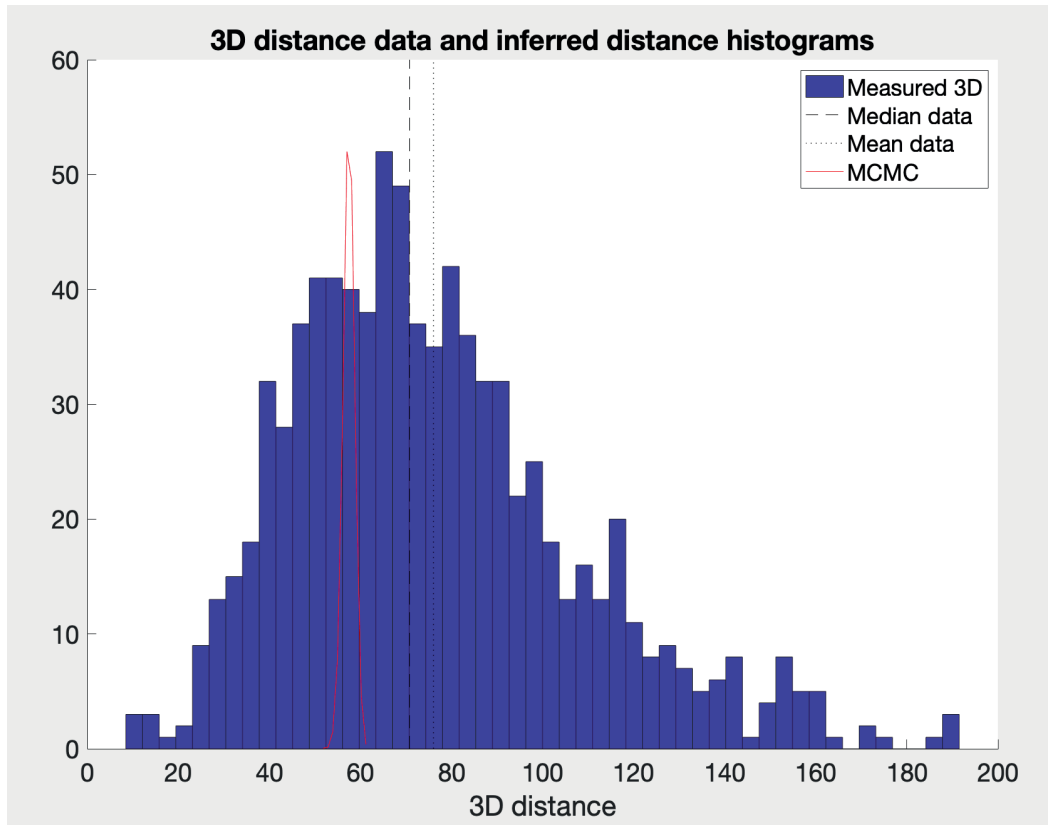
Next



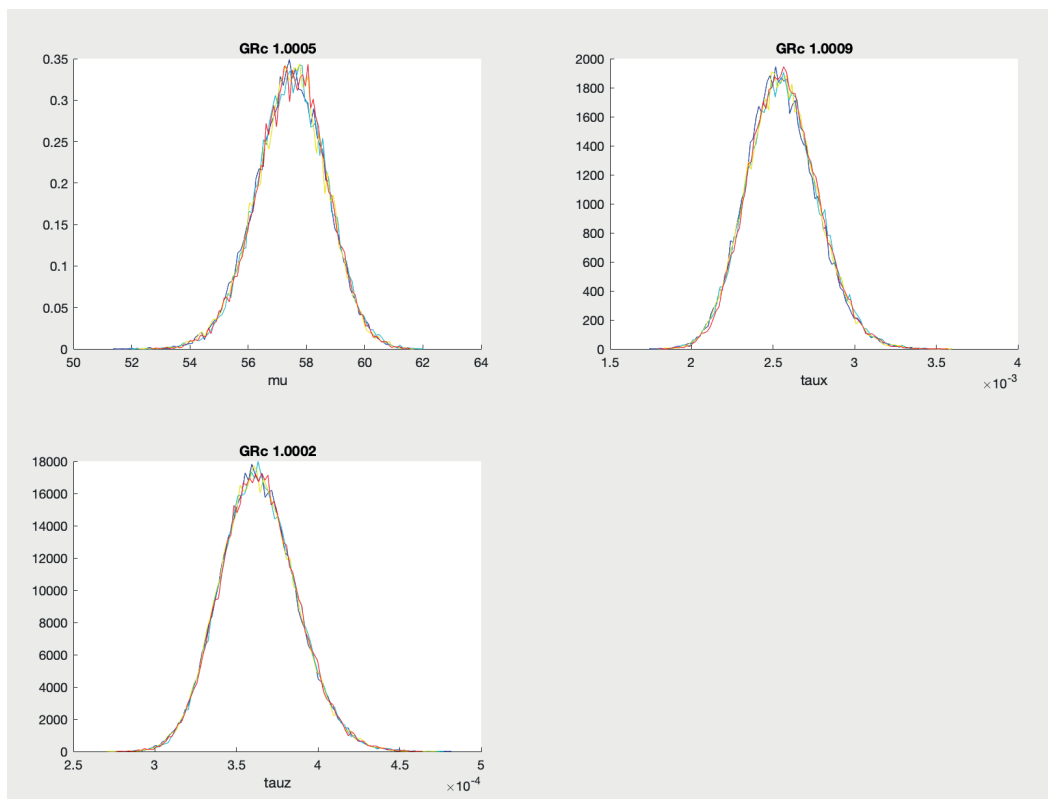
Invert all

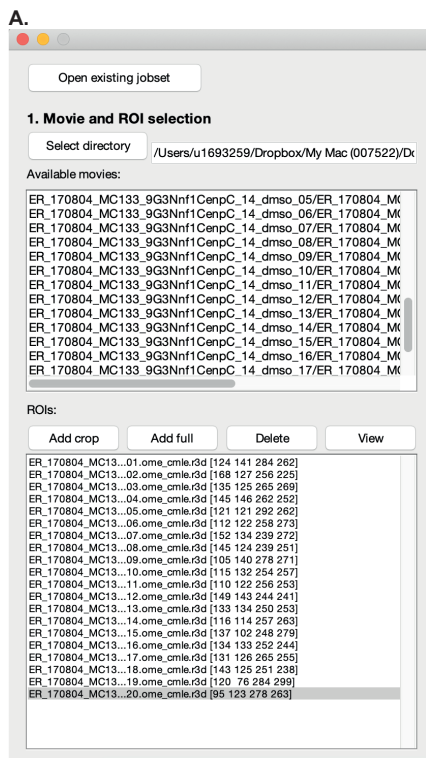


A.



B.





Click on **Select directory** and choose the folder containing the raw data

The **Available movies** (image stacks) will appear here. Left-click with the mouse on a movie to select it.

Click **Add full** to enter the full image (for ACS analysis) or **Add crop** to analyse only the region containing the cell of interest (the ROI, for Sample analysis), see below.

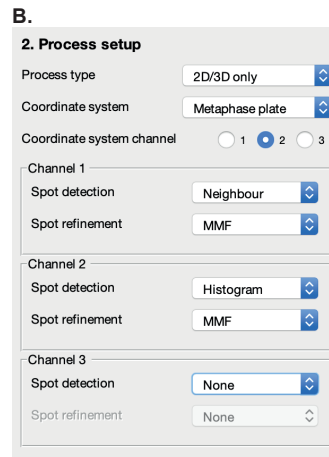
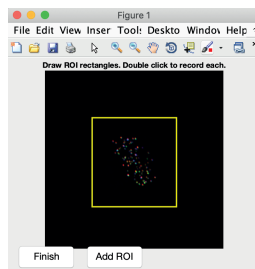
The user can select a **ROI** and click **Delete** to delete it and **View** to view it.

If **Add crop** is clicked, Window with maximum Z-projection of the selected image stack will appear.

Use the left mouse button to make a rectangle around the cell of interest. Double-click with left mouse button on the rectangle to confirm it (it will become yellow), see example on the right.

Click **Finish**.

The added ROI will now appear in the **ROIs window**



Select **2D/3D only** for sample analysis and **Chromatic shift** for ACS analysis

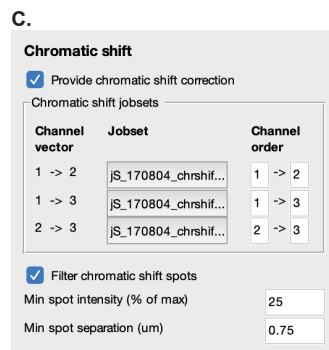
Choose **Metaphase plate** if the kinetochores are aligned and **Centre of mass** otherwise.

Select **coordinate system channel** based on criteria in step 7 c iii. Numbers relate to order of acquisition.

Set the detection to **Neighbour** and the refinement to **MMF** if the channel is non-coordinate system channel and contains kinetochore marker staining.

Set the detection to **Histogram** and the refinement to **MMF** if the channel is coordinate system channel.

Set the detection to **None** if there is no kinetochore marker imaged.



Click on the box to **Provide chromatic shift correction** for Sample analysis.

Click on one of the boxes below **Jobset** to provide the ACS jobset created in step 4. Load the created jobset for all used channel combinations (**channel vectors**).

Click on the box to **Filter chromatic shift spots**

Set the **Min spot intensity** to 25, i.e. 25% from the max intensity in the image. Set the **Min spot separation** to 0.75 μm - the resting inter-sister distance.

Click on the blue arrows to see the available options

A.

Neighbour spot detection

Mask shape

Mask radius (um)

Neighbour orientation

Channel number				
inner kchore	<input type="text" value="2"/>	<input type="text" value="1"/>	<input type="text" value="3"/>	outer kchore

Intensity measurement

Measure in channels... 1 2 3

Mask shape

Mask radius (um)

Indicates the **mask shape** in which KiD will scan for spots starting with the ACS-transformed spot coordinates of the CS channel and searching in the channels where Neighbor spot detection is specified. **Semi-circle** uses the detected plate to inform direction of the mask in semi-circle outwards of the plate. **Circle** denotes circle mask around the spot in the CS channel coordinates.

The **mask radius** indicates in what radius KiD will scan for spots in the neighbour NCS channel starting from the ACS transformed spot coordinates in the CS channel. The default is **0.3** micrometer, chosen as kinetochores are largely diffraction-limited spot, i.e. with size below 250nm.

Indicate order of channels based on approximate location of the kinetochore markers relative to each other. Results are not affected by the order. Note the chosen order.

Click on the boxes next to the channels for which **Intensity measurement** is desired.

Intensity is measured in the indicated **mask shape** around the coordinates of the spot in CS channel transformed after ACS in the neighbour NCS channel. The default option is **Circle** but **Semi-circle** and **Cone** are also available as options.

The **mask radius** indicates in what radius KiD will measure the spot intensity in the neighbour NCS channel starting from the ACS transformed spot coordinates in the CS channel. The default is **0.3** micrometer, chosen for the reason stated above.

B.

4. Execution

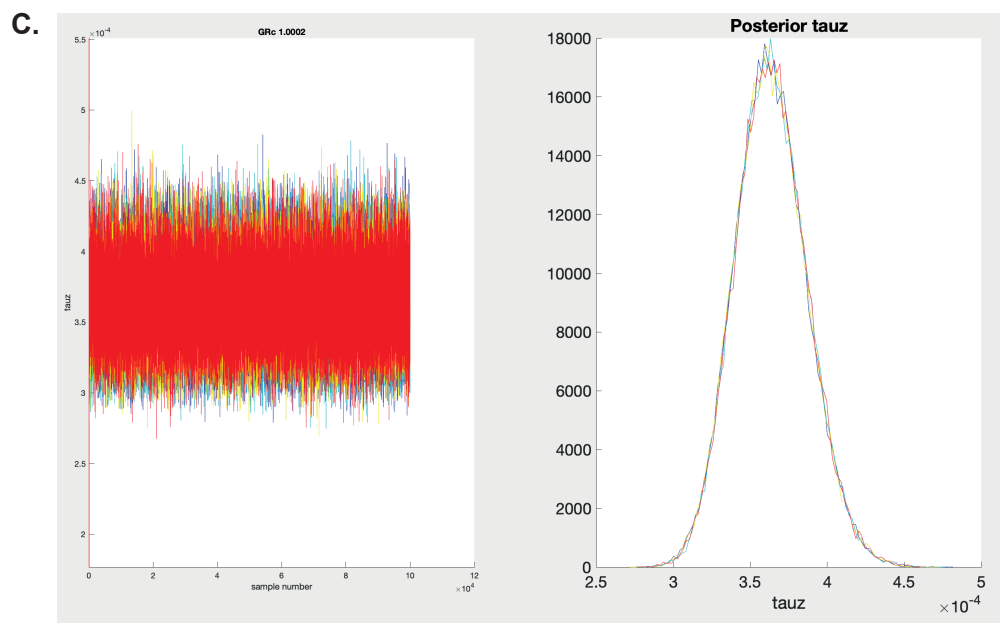
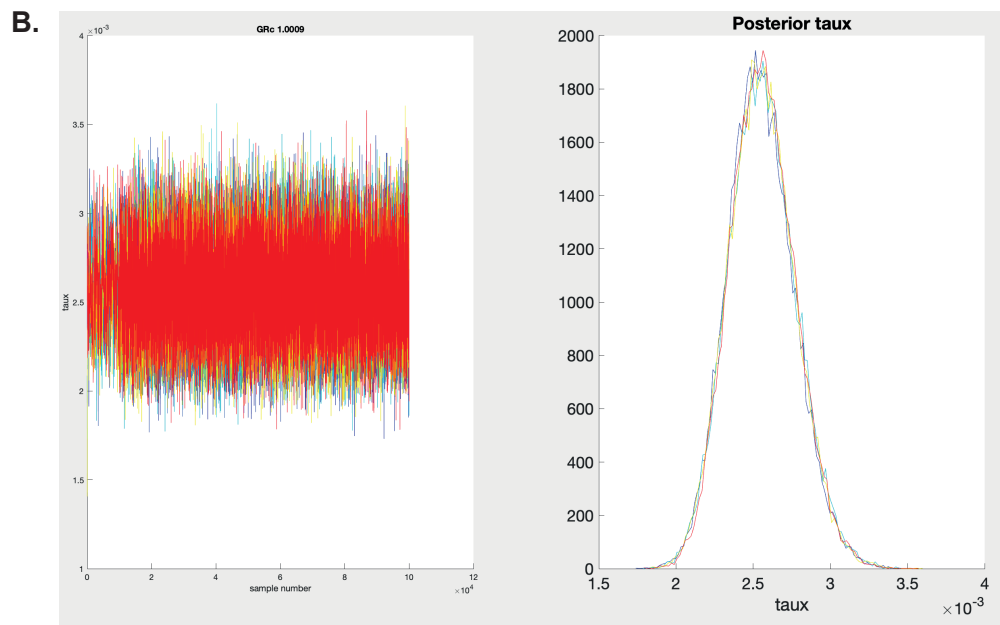
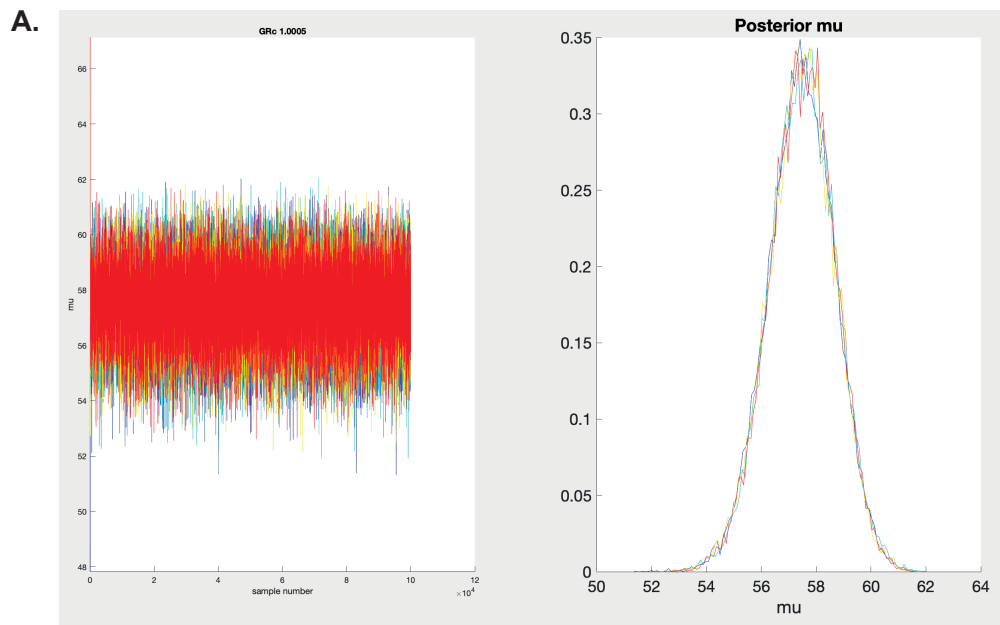
Jobset name

Type the **Jobset name** as chosen in 3a or 4a.

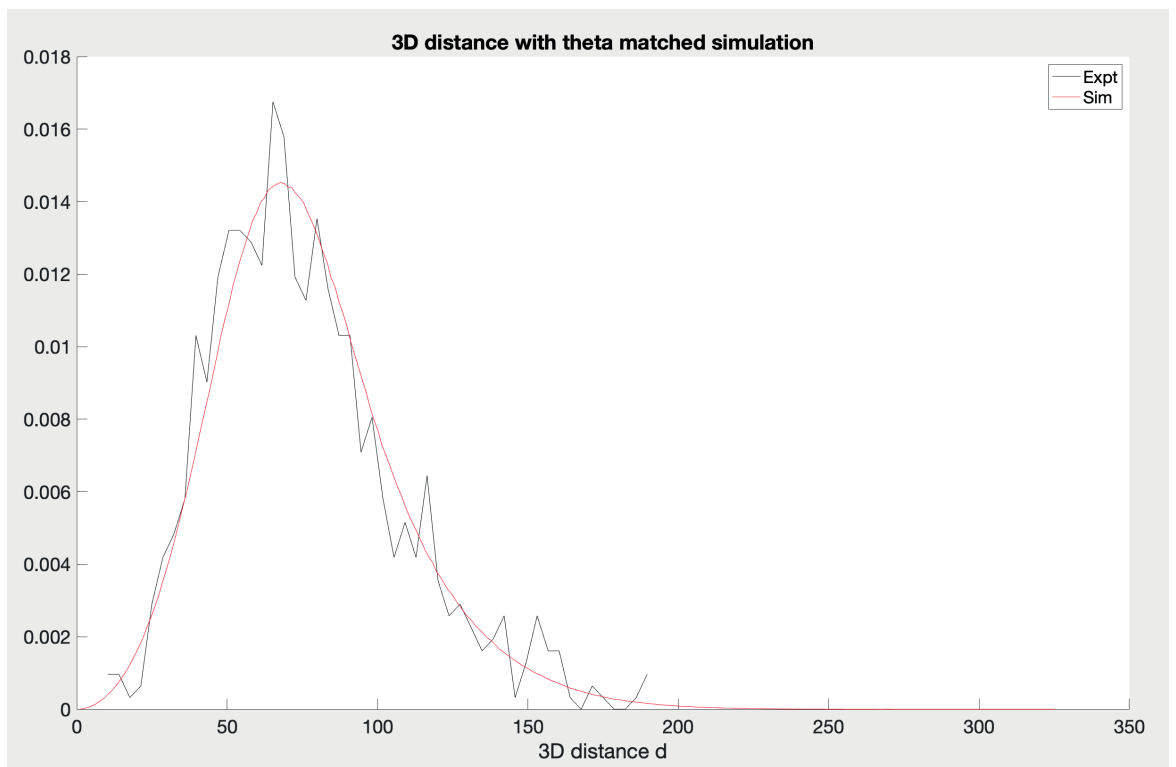
Click on **Validate**. A window with the image stack metadata will pop-up. If the metadata is correct, click on the box next to **Apply to all movies** and then click **Validate**. Otherwise make sure the data is exported as stated in step 1 and 2.

Press **Save** to save the Jobset and run the analysis at a later time.

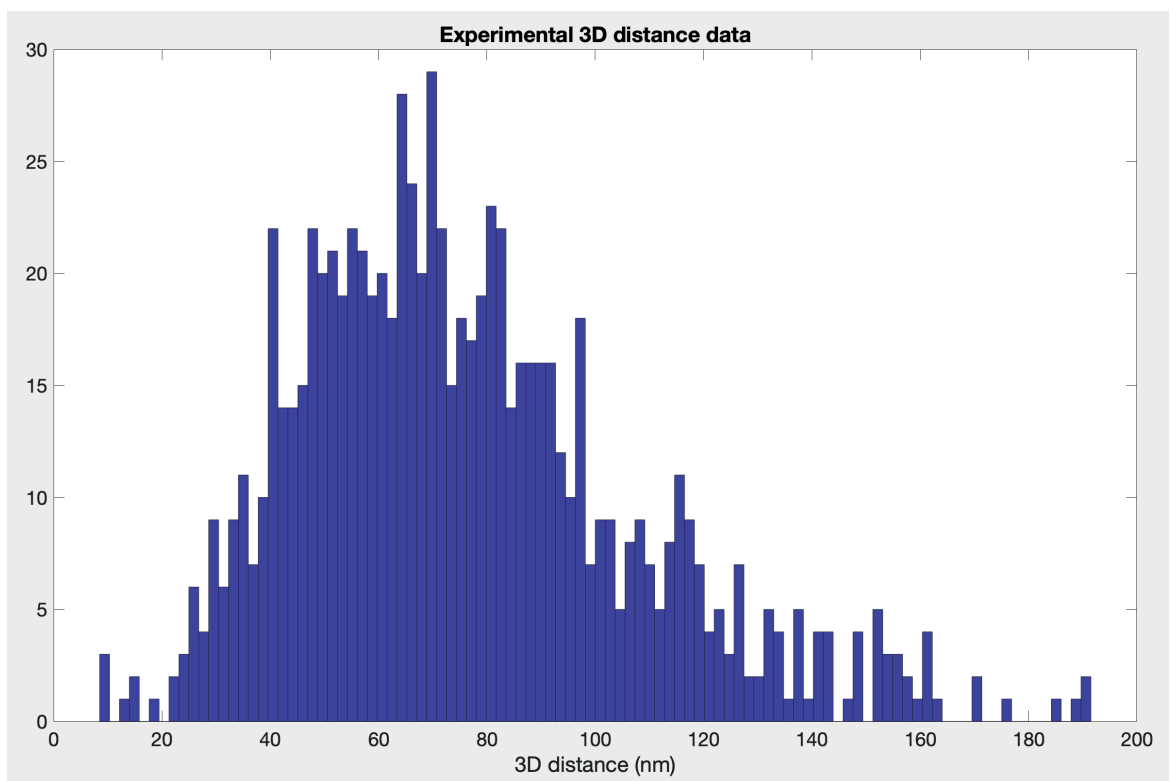
Press **Execute** to run the analysis. The Jobset is now automatically saved in the folder with raw data.

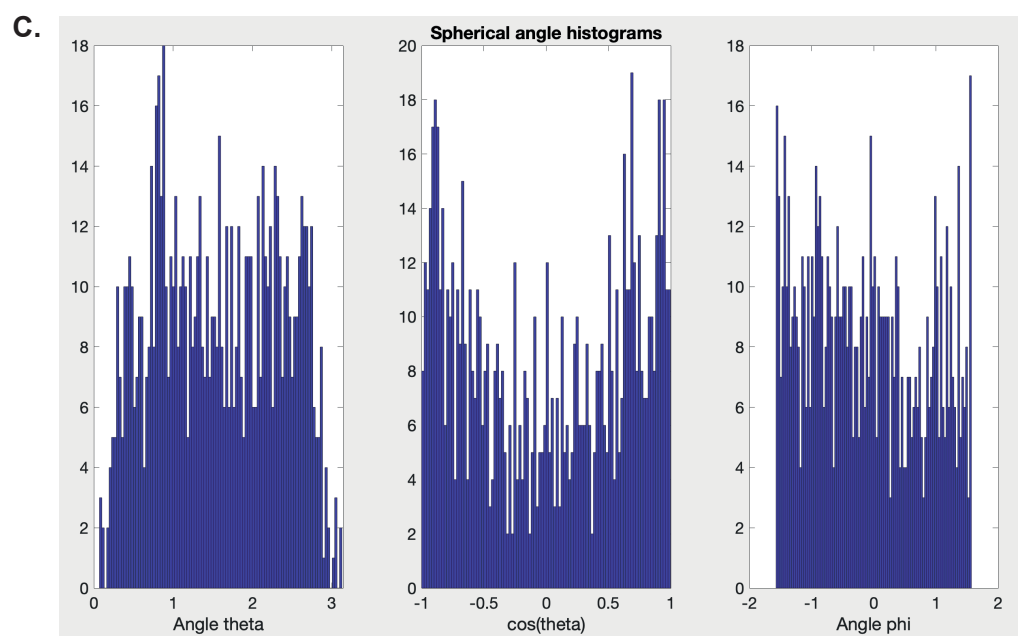
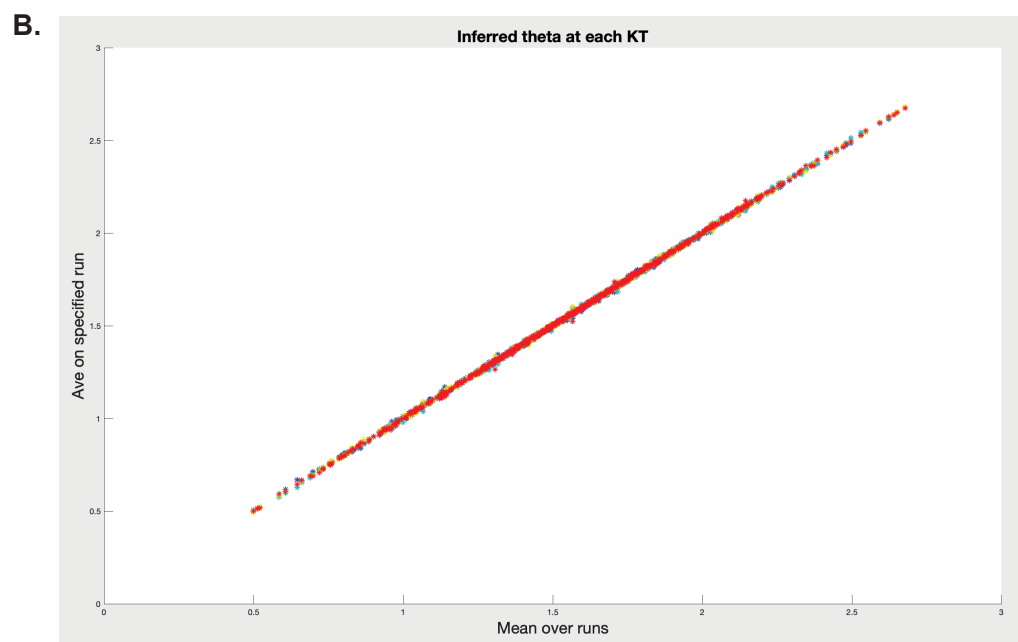
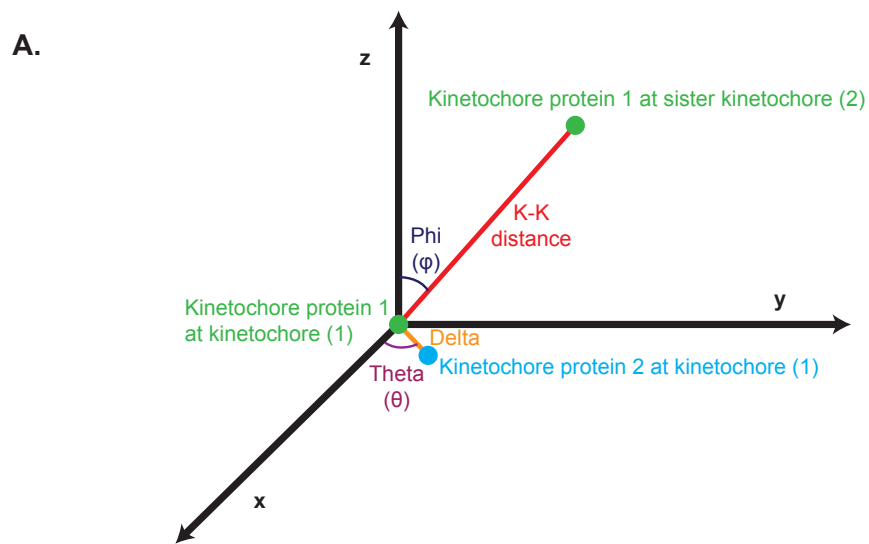


A.

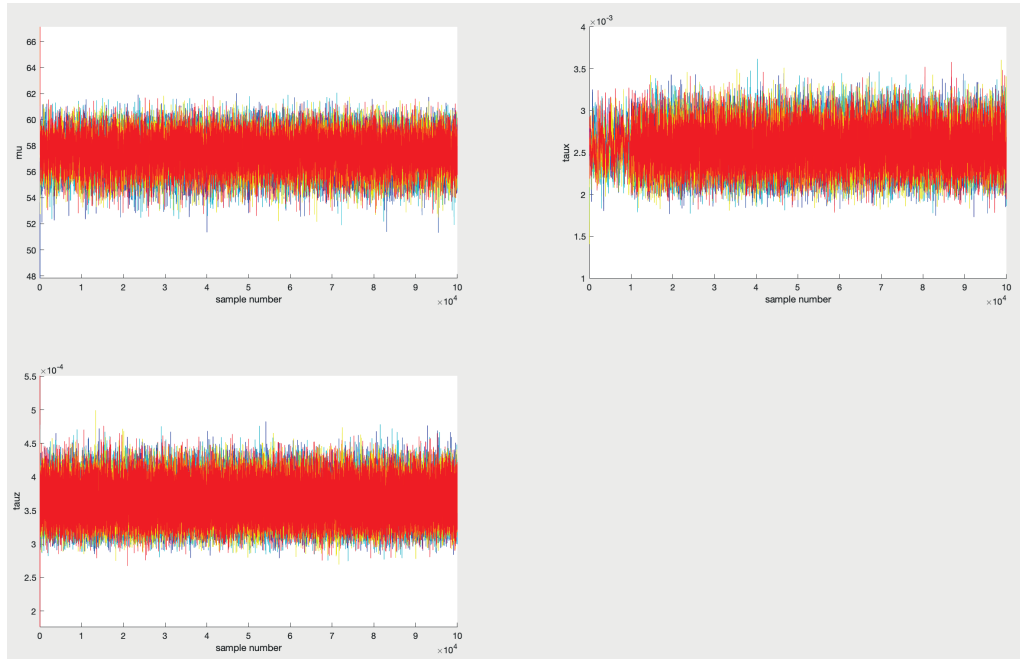


B.

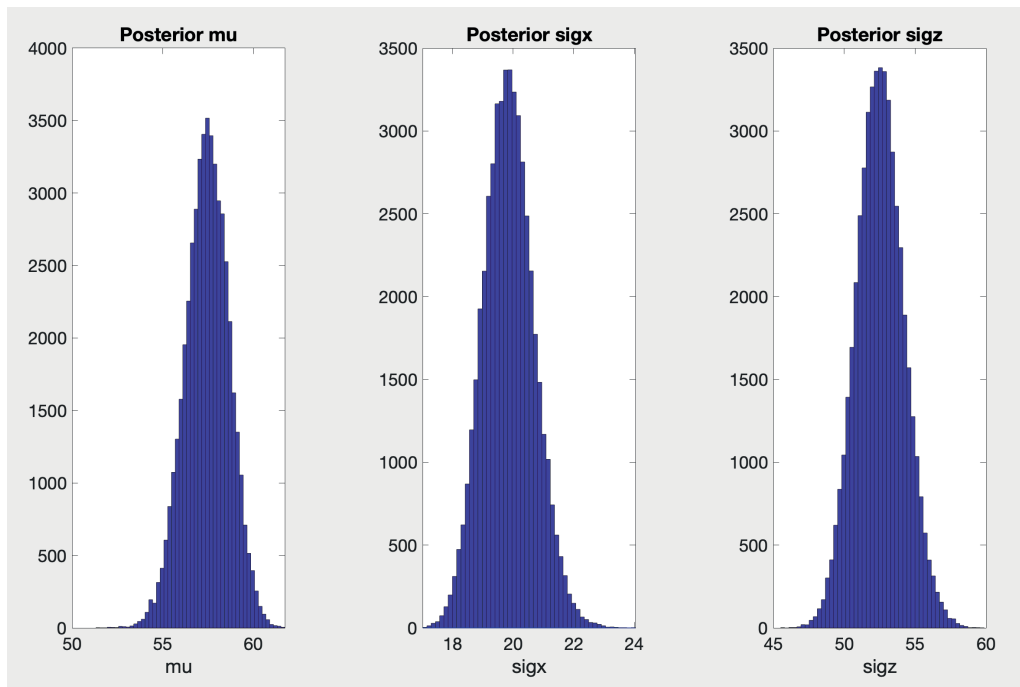




A.



B.



Bibliography

1. Abad, M., Medina, B., Santamaria, A., Zou, J., Plasberg-Hill, C., Madhumalar, A., Jayachandran, U., Redli, P., Rappsilber, J., Nigg, E. and Jeyaprakash, A. (2014). Structural basis for microtubule recognition by the human kinetochore Ska complex. *Nature Communications*, 5(1).
2. Abad, M., Zou, J., Medina-Pritchard, B., Nigg, E., Rappsilber, J., Santamaria, A. and Jeyaprakash, A. (2016). Ska3 Ensures Timely Mitotic Progression by Interacting Directly With Microtubules and Ska1 Microtubule Binding Domain. *Scientific Reports*, 6(1).
3. Alberts B, Johnson A, Lewis J, et al. *Molecular Biology of the Cell*. 4th edition. New York: Garland Science; 2002. Intracellular Control of Cell-Cycle Events. Available from:
<https://www.ncbi.nlm.nih.gov/books/NBK26856/>
4. Allu, P., Dawicki-McKenna, J., Van Eeuwen, T., Slavin, M., Braitbard, M., Xu, C., Kalisman, N., Murakami, K. and Black, B., 2019. Structure of the Human Core Centromeric Nucleosome Complex. *Current Biology*, 29(16), pp.2625-2639.e5.
5. Alushin, G., Musinipally, V., Matson, D., Tooley, J., Stukenberg, P. and Nogales, E. (2012). Multimodal microtubule binding by the Ndc80 kinetochore complex. *Nature Structural & Molecular Biology*, 19(11), pp.1161-1167.
6. Alushin, G., Ramey, V., Pasqualato, S., Ball, D., Grigorieff, N., Musacchio, A. and Nogales, E. (2010). The Ndc80 kinetochore complex forms oligomeric arrays along microtubules. *Nature*, 467(7317), pp.805-810.
7. Auckland, P. and McAinsh, A. (2015). Building an integrated model of chromosome congression. *Journal of Cell Science*, 128(18), pp.3363-3374.

8. Bajaj, R. *et al.* (2018) 'KNL1 Binding to PP1 and Microtubules Is Mutually Exclusive', *Structure*, 26(10), pp. 1327-1336.e4. doi: [10.1016/j.str.2018.06.013](https://doi.org/10.1016/j.str.2018.06.013).
9. Bharadwaj, R., Qi, W. and Yu, H. (2003). Identification of Two Novel Components of the Human NDC80 Kinetochores Complex. *Journal of Biological Chemistry*, 279(13), pp.13076-13085.
10. Bharadwaj, R., Yu, H., (2004). The spindle checkpoint, aneuploidy, and cancer. *Oncogene* 23, 2016–2027. <https://doi.org/10.1038/sj.onc.1207374>
11. Booth, D., Hood, F., Prior, I. and Royle, S., (2011). A TACC3/ch-TOG/clathrin complex stabilises kinetochore fibres by inter-microtubule bridging. *The EMBO Journal*, 30(5), pp.906-919.
12. Brinkley BR, Stubblefield E. (1966); The fine structure of the kinetochore of a mammalian cell in vitro. *Chromosoma*. 19(1):28-43. doi: 10.1007/BF00332792. PMID: 5912064
13. Brouhard, G. and Rice, L. (2018). Microtubule dynamics: an interplay of biochemistry and mechanics. *Nature Reviews Molecular Cell Biology*, 19(7), pp.451-463.
14. Caldas, G.V., DeLuca, K.F., DeLuca, J.G., (2013). KNL1 facilitates phosphorylation of outer kinetochore proteins by promoting Aurora B kinase activity. *Journal of Cell Biology* 203, 957–969. <https://doi.org/10.1083/jcb.201306054>
15. Chan, Y. W., Jeyaprasath, A. A., Nigg, E. A. and Santamaria, A. (2012). Aurora B controls kinetochore-microtubule attachments by inhibiting Ska complex-KMN network interaction. *Journal of Cell Biology* 196, 563-571. doi:10.1083/jcb.201109001
16. Cheerambathur, D., Prevo, B., Hattersley, N., Lewellyn, L., Corbett, K., Oegema, K. and Desai, A. (2017). Dephosphorylation of the Ndc80 Tail Stabilizes Kinetochore-Microtubule Attachments via the Ska Complex. *Developmental Cell*, 41(4), pp.424-437.e4.

17. Cheeseman, I. and Desai, A. (2008). Molecular architecture of the kinetochore–microtubule interface. *Nature Reviews Molecular Cell Biology*, 9(1), pp.33-46.
18. Cheeseman, I. M. (2004) 'A conserved protein network controls assembly of the outer kinetochore and its ability to sustain tension', *Genes & Development*, 18(18), pp. 2255–2268. doi: [10.1101/gad.1234104](https://doi.org/10.1101/gad.1234104).
19. Cheeseman, I. M., Enquist-Newman, M., Müller-Reichert, T., Drubin, D. G. and Barnes, G. (2001). Mitotic spindle integrity and kinetochore function linked by the Duo1p/Dam1p complex. *Journal of Cell Biology* 152, 197-212. doi:10.1083/jcb.152.1.197
20. Cheeseman, I.M., Chappie, J.S., Wilson-Kubalek, E.M., Desai, A., (2006). The Conserved KMN Network Constitutes the Core Microtubule-Binding Site of the Kinetochore. *Cell* 127, 983–997. <https://doi.org/10.1016/j.cell.2006.09.039>
21. Chik, J., Moiseeva, V., Goel, P., Meinen, B., Koldewey, P., An, S., Mellone, B., Subramanian, L. and Cho, U., (2019). Structures of CENP-C cupin domains at regional centromeres reveal unique patterns of dimerization and recruitment functions for the inner pocket. *Journal of Biological Chemistry*, 294(38), pp.14119-14134.
22. Churchman, L.S., Okten, Z., Rock, R.S., Dawson, J.F., Spudich, J.A., (2005). Single molecule high-resolution colocalization of Cy3 and Cy5 attached to macromolecules measures intramolecular distances through time. *Proceedings of the National Academy of Sciences* 102, 1419–1423. <https://doi.org/10.1073/pnas.0409487102>
23. Ciferri, C. *et al.* (2008) 'Implications for Kinetochore-Microtubule Attachment from the Structure of an Engineered Ndc80 Complex', *Cell*, 133(3), pp. 427–439. doi: [10.1016/j.cell.2008.03.020](https://doi.org/10.1016/j.cell.2008.03.020).
24. Ciferri, C., De Luca, J., Monzani, S., Ferrari, K., Ristic, D., Wyman, C., Stark, H., Kilmartin, J., Salmon, E. and Musacchio, A., (2005). Architecture of the Human Ndc80-Hec1 Complex, a Critical Constituent

- of the Outer Kinetochore. *Journal of Biological Chemistry*, 280(32), pp.29088-29095.
25. Ciferri, C., Musacchio, A., Petrovic, A., (2007). The Ndc80 complex: Hub of kinetochore activity. *FEBS Letters* 581, 2862–2869.
<https://doi.org/10.1016/j.febslet.2007.05.012>
26. Currie, C.E., Mora-Santos, M., Smith, C.A., McAinsh, A.D., Millar, J.B.A., (2018). Bub1 is not essential for the checkpoint response to unattached kinetochores in diploid human cells. *Current Biology* 28, R929–R930.
<https://doi.org/10.1016/j.cub.2018.07.040>
27. Daum, J., Potapova, T., Sivakumar, S., Daniel, J., Flynn, J., Rankin, S. and Gorbsky, G. (2011). Cohesion Fatigue Induces Chromatid Separation in Cells Delayed at Metaphase. *Current Biology*, 21(12), pp.1018-1024.
28. Dawson, I.A., Roth, S., Artavanis-Tsakonas, S., (1995). The *Drosophila* cell cycle gene *fizzy* is required for normal degradation of cyclins A and B during mitosis and has homology to the CDC20 gene of *Saccharomyces cerevisiae*. *Journal of Cell Biology* 129, 725–737.
<https://doi.org/10.1083/jcb.129.3.725>
29. De Antoni, A., Pearson, C.G., Cimini, D., Canman, J.C., Sala, V., Nezi, L., Mapelli, M., Sironi, L., Faretta, M., Salmon, E.D., Musacchio, A., (2005). The Mad1/Mad2 Complex as a Template for Mad2 Activation in the Spindle Assembly Checkpoint. *Current Biology* 15, 214–225.
<https://doi.org/10.1016/j.cub.2005.01.038>
30. De Wulf, P., (2003). Hierarchical assembly of the budding yeast kinetochore from multiple subcomplexes. *Genes & Development* 17, 2902–2921. <https://doi.org/10.1101/gad.1144403>
31. DeLuca, J., Gall, W., Ciferri, C., Cimini, D., Musacchio, A. and Salmon, E., (2006). Kinetochore Microtubule Dynamics and Attachment Stability Are Regulated by Hec1. *Cell*, 127(5), pp.969-982.
32. DeLuca, K.F., Lens, S.M.A., DeLuca, J.G., (2011). Temporal changes in Hec1 phosphorylation control kinetochore-microtubule attachment

- stability during mitosis. *Journal of Cell Science* 124, 622–634.
<https://doi.org/10.1242/jcs.072629>
33. Desai, A. and Mitchison, T. (1997). Microtubule polymerization dynamics. *Annual Review of Cell and Developmental Biology*, 13(1), pp.83-117.
34. Dong, Y., Vanden Beldt, K.J., Meng, X., Khodjakov, A., McEwen, B.F., 2007. The outer plate in vertebrate kinetochores is a flexible network with multiple microtubule interactions. *Nature Cell Biology* 9, 516–522.
<https://doi.org/10.1038/ncb1576>
35. Dudka, D., Noatynska, A., Smith, C.A., Liaudet, N., McAinsh, A.D., Meraldi, P., (2018). Complete microtubule–kinetochore occupancy favours the segregation of merotelic attachments. *Nature Communications* 9, 2042. <https://doi.org/10.1038/s41467-018-04427-x>
36. Dumont, S., Salmon, E. and Mitchison, T. (2012). Deformations Within Moving Kinetochores Reveal Different Sites of Active and Passive Force Generation. *Science*, 337(6092), pp.355-358.
37. Espert, A., Uluocak, P., Bastos, R.N., Mangat, D., Graab, P., Gruneberg, U., (2014). PP2A-B56 opposes Mps1 phosphorylation of Knl1 and thereby promotes spindle assembly checkpoint silencing. *Journal of Cell Biology* 206, 833–842. <https://doi.org/10.1083/jcb.201406109>
38. Espeut J, Cheerambathur DK, Krenning L, Oegema K, Desai A (2012) Microtubule binding by KNL-1 contributes to spindle checkpoint silencing at the kinetochore. *Journal of Cell Biology*
doi:[10.1083/jcb.201111107](https://doi.org/10.1083/jcb.201111107)
39. Etemad, B., Vertesy, A., Kuijt, T.E.F., Sacristan, C., van Oudenaarden, A., Kops, G.J.P.L., (2019). Correction: Spindle checkpoint silencing at kinetochores with submaximal microtubule occupancy (doi:10.1242/jcs.231589). *Journal of Cell Science* 132, jcs237750.
<https://doi.org/10.1242/jcs.237750>
40. Fang, G., (2002). Checkpoint Protein BubR1 Acts Synergistically with Mad2 to Inhibit Anaphase-promoting Complex. *Molecular Biology of the Cell* 13, 755–766. <https://doi.org/10.1091/mbc.01-09-0437>

41. Flemming, W. (1882). Zellsubstanz, Kern und Zelltheilung. Leipzig
42. Fonseca, C.L., Malaby, H.L.H., Sepaniac, L.A., Martin, W., Byers, C., Czechanski, A., Messinger, D., Tang, M., Ohi, R., Reinholdt, L.G., Stumpff, J., (2019). Mitotic chromosome alignment ensures mitotic fidelity by promoting interchromosomal compaction during anaphase. *Journal of Cell Biology* 218, 1148–1163.
<https://doi.org/10.1083/jcb.201807228>
43. Gaitanos, T. N., Santamaria, A., Jeyaprakash, A. A., Wang, B., Conti, E. and Nigg, E. A. (2009). Stable kinetochore–microtubule interactions depend on the Ska complex and its new component Ska3/C13Orf3. *EMBO Journal* 28, 1442–1452. doi:10.1038/emboj.2009.96
44. Gascoigne, K., Takeuchi, K., Suzuki, A., Hori, T., Fukagawa, T. and Cheeseman, I., (2011). Induced Ectopic Kinetochore Assembly Bypasses the Requirement for CENP-A Nucleosomes. *Cell*, 145(3), pp.410–422.
45. Gassmann, R., Holland, A.J., Varma, D., Wan, X., Civril, F., Cleveland, D.W., Oegema, K., Salmon, E.D., Desai, A., (2010). Removal of Spindly from microtubule-attached kinetochores controls spindle checkpoint silencing in human cells. *Genes & Development* 24, 957–971.
<https://doi.org/10.1101/gad.1886810>
46. Gelman, A., and Rubin, D. (1992), Inference from Iterative Simulation using Multiple Sequences, *Statistical Science*, 7, 457–511
47. Ghongane, P. et al. (2014) ‘The dynamic protein Knl1 - a kinetochore rendezvous’, *Journal of Cell Science*, 127(16), pp. 3415–3423. doi: [10.1242/jcs.149922](https://doi.org/10.1242/jcs.149922).
48. Gorbsky, G. J., Sammak, P. J. and Borisy, G. G. (1987). Chromosomes move poleward in anaphase along stationary microtubules that coordinately disassemble from their kinetochore ends. *Journal of Cell Biology* 104, 9–18. doi:10.1083/jcb.104.1.9
49. Green, R., Paluch, E. and Oegema, K. (2012). Cytokinesis in Animal Cells. *Annual Review of Cell and Developmental Biology*, 28(1), pp.29–58.

50. Grishchuk, E. L., Spiridonov, I. S., Volkov, V. A., Efremov, A., Westermann, S., Drubin, D., Barnes, G., Ataullakhanov, F. I. and McIntosh, J. R. (2008). Different assemblies of the DAM1 complex follow shortening microtubules by distinct mechanisms. *Proceedings of the National Academy of Sciences USA* 105, 6918-6923.
doi:10.1073/pnas.0801811105
51. Grishchuk, E., Molodtsov, M., Ataullakhanov, F. and McIntosh, J. (2005). Force production by disassembling microtubules. *Nature*, 438(7066), pp.384-388.
52. Gui, P., Sedzro, D.M., Yuan, X., Liu, S., Hei, M., Tian, W., Zohbi, N., Wang, F., Yao, Y., Aikhionbare, F.O., Gao, X., Wang, D., Yao, X., Dou, Z., (2020). Mps1 dimerization and multisite interactions with Ndc80 complex enable responsive spindle assembly checkpoint signaling. *Journal of Molecular Cell Biology* 12, 486–498.
<https://doi.org/10.1093/jmcb/mjaa006>
53. Hanisch, A., Silljé, H. H. W. and Nigg, E. A. (2006). Timely anaphase onset requires a novel spindle and kinetochore complex comprising Ska1 and Ska2. *EMBO Journal* 25, 5504-5515.
doi:10.1038/sj.emboj.7601426
54. Hara, M., Fukagawa, T., (2020). Dynamics of kinetochore structure and its regulations during mitotic progression. *Cellular and Molecular Life Sciences* 77, 2981–2995. <https://doi.org/10.1007/s00018-020-03472-4>
55. Heald, R., Khodjakov, A., (2015). Thirty years of search and capture: The complex simplicity of mitotic spindle assembly. *Journal of Cell Biology* 211, 1103–1111. <https://doi.org/10.1083/jcb.201510015>
56. Helgeson, L., Zelter, A., Riffle, M., MacCoss, M., Asbury, C. and Davis, T. (2018). Human Ska complex and Ndc80 complex interact to form a load-bearing assembly that strengthens kinetochore–microtubule attachments. *Proceedings of the National Academy of Sciences*, 115(11), pp.2740-2745.

57. Hershko, A., 1999. Mechanisms and regulation of the degradation of cyclin B. *Phil. Trans. R. Soc. Lond. B* 354, 1571–1576.
<https://doi.org/10.1098/rstb.1999.0500>
58. Heyrovská, R. (2018). Atomic and Ionic Radii in the Structures of Inorganic, Organic and Biological Molecules: Reference Papers with Data and Figures. *viXra*.
59. Hill, T. (1985). Theoretical problems related to the attachment of microtubules to kinetochores. *Proceedings of the National Academy of Sciences*, 82(13), pp.4404-4408.
60. Hori, T., Amano, M., Suzuki, A., Backer, C., Welburn, J., Dong, Y., McEwen, B., Shang, W., Suzuki, E., Okawa, K., Cheeseman, I. and Fukagawa, T., (2008). CCAN Makes Multiple Contacts with Centromeric DNA to Provide Distinct Pathways to the Outer Kinetochores. *Cell*, 135(6), pp.1039-1052.
61. Huis in 't Veld, P. J. *et al.* (2016) 'Molecular basis of outer kinetochore assembly on CENP-T', *eLife*, 5, p. e21007. doi: [10.7554/eLife.21007](https://doi.org/10.7554/eLife.21007).
62. Huis in 't Veld, P.J., Volkov, V.A., Stender, I.D., Musacchio, A., Dogterom, M., (2019). Molecular determinants of the Ska-Ndc80 interaction and their influence on microtubule tracking and force-coupling. *eLife* 8, e49539. <https://doi.org/10.7554/eLife.49539>
63. Im, H., (2011). The Inoue Method for Preparation and Transformation of Competent *E. coli*: 'Ultra Competent' Cells. *BIO-PROTOCOL*, 1(20).
64. Janczyk, P., Skorupka, K., Tooley, J., Matson, D., Kestner, C., West, T., Pornillos, O. and Stukenberg, P. (2017). Mechanism of Ska Recruitment by Ndc80 Complexes to Kinetochores. *Developmental Cell*, 41(4), pp.438-449.e4.
65. Jeyapakash, A., Santamaria, A., Jayachandran, U., Chan, Y., Benda, C., Nigg, E. and Conti, E. (2012). Structural and Functional Organization of the Ska Complex, a Key Component of the Kinetochores-Microtubule Interface. *Molecular Cell*, 46(3), pp.274-286.

66. Ji, Z., Gao, H., Jia, L., Li, B., Yu, H., (2017). A sequential multi-target Mps1 phosphorylation cascade promotes spindle checkpoint signaling. *eLife* 6, e22513. <https://doi.org/10.7554/eLife.22513>
67. Joglekar, A., Bouck, D., Molk, J., Bloom, K. and Salmon, E., (2006). Molecular architecture of a kinetochore–microtubule attachment site. *Nature Cell Biology*, 8(6), pp.581-585.
68. Johnston, K., Joglekar, A., Hori, T., Suzuki, A., Fukagawa, T. and Salmon, E. D. (2010). Vertebrate kinetochore protein architecture: protein copy number. *Journal of Cell Biology* 189, 937-943. doi:10.1083/jcb.200912022
69. Kang, J., Chen, Y., Zhao, Y., Yu, H., (2007). Autophosphorylation-dependent activation of human Mps1 is required for the spindle checkpoint. *Proceedings of the National Academy of Sciences* 104, 20232–20237. <https://doi.org/10.1073/pnas.0710519105>
70. Kang, M., Tanaka, K., (2017). Plk1 bound to Bub1 contributes to spindle assembly checkpoint activity during mitosis. *Science Reports* 7, 8794. <https://doi.org/10.1038/s41598-017-09114-3>
71. Kato, H., Jiang, J., Zhou, B., Rozendaal, M., Feng, H., Ghirlando, R., Xiao, T., Straight, A. and Bai, Y., (2013). A Conserved Mechanism for Centromeric Nucleosome Recognition by Centromere Protein CENP-C. *Science*, 340(6136), pp.1110-1113.
72. Kixmoeller K, Allu PK, BlackBE. (2020) The centromere comes into focus:from CENP-A nucleosomes to kinetochoreconnections with the spindle. *Open Biology*10:200051.
73. Kiyomitsu T., Murakami H., Yanagida M. (2011). Protein interaction domain mapping of human kinetochore protein Blinkin reveals a consensus motif for binding of spindle assembly checkpoint proteins Bub1 and BubR1. *Molecular Cell Biology* 31:998–1011
10.1128/MCB.00815-10
74. Kiyomitsu T., Obuse C., Yanagida M. (2007). Human Blinkin/AF15q14 is required for chromosome alignment and the mitotic checkpoint through

- direct interaction with Bub1 and BubR1. *Developmental Cell* 13:663–676
10.1016/j.devcel.2007.09.005
75. Klare, K., Weir, J., Basilico, F., Zimniak, T., Massimiliano, L., Ludwigs, N., Herzog, F. and Musacchio, A., (2015). CENP-C is a blueprint for constitutive centromere-associated network assembly within human kinetochores. *Journal of Cell Biology*, 210(1), pp.11-22.
76. Kline, S. L. *et al.* (2006) 'The human Mis12 complex is required for kinetochore assembly and proper chromosome segregation', *Journal of Cell Biology*, 173(1), pp. 9–17. doi: [10.1083/jcb.200509158](https://doi.org/10.1083/jcb.200509158).
77. Kops, G.J.P.L., Kim, Y., Weaver, B.A.A., Mao, Y., McLeod, I., Yates, J.R., Tagaya, M., Cleveland, D.W., (2005). ZW10 links mitotic checkpoint signaling to the structural kinetochore. *Journal of Cell Biology* 169, 49–60. <https://doi.org/10.1083/jcb.200411118>
78. Kramer, E.R., Scheuringer, N., Podtelejnikov, A.V., Mann, M., Peters, J.-M., (2000). Mitotic Regulation of the APC Activator Proteins CDC20 and CDH1. *MBoC* 11, 1555–1569. <https://doi.org/10.1091/mbc.11.5.1555>
79. Krenn V., Wehenkel A., Li X., Santaguida S., Musacchio A. (2012). Structural analysis reveals features of the spindle checkpoint kinase Bub1-kinetochore subunit Knl1 interaction. *Journal of Cell Biology* 196:451–467 10.1083/jcb.201110013
80. Kuhn, J., Dumont, S., 2017. Spindle assembly checkpoint satisfaction occurs via end-on but not lateral attachments under tension. *Journal of Cell Biology* 216, 1533–1542. <https://doi.org/10.1083/jcb.201611104>
81. Kukreja, A., Kavuri, S. and Joglekar, A., (2020). Microtubule Attachment and Centromeric Tension Shape the Protein Architecture of the Human Kinetochore. *Current Biology*, 30(24), pp.4869-4881.e5.
82. Ledbetter, M. and Porter, K., (1963). A "MICROTUBULE" IN PLANT CELL FINE STRUCTURE. *Journal of Cell Biology*, 19(1), pp.239-250.
83. Lesage B, Qian J, Bollen M (2011) Spindle checkpoint silencing: PP1 tips the balance. *Curr Biol* 21(21):R898–R903.
doi:[10.1016/j.cub.2011.08.063](https://doi.org/10.1016/j.cub.2011.08.063)

84. Liu D., Vleugel M., Backer C.B., Hori T., Fukagawa T., Cheeseman I.M., Lampson M.A. (2010). Regulated targeting of protein phosphatase 1 to the outer kinetochore by KNL1 opposes Aurora B kinase. *Journal of Cell Biology* 188:809–820 10.1083/jcb.201001006
85. London, N., Biggins, S., (2014). Mad1 kinetochore recruitment by Mps1-mediated phosphorylation of Bub1 signals the spindle checkpoint. *Genes & Development* 28, 140–152.
<https://doi.org/10.1101/gad.233700.113>
86. London, N., Ceto, S., Ranish, J.A., Biggins, S., (2012). Phosphoregulation of Spc105 by Mps1 and PP1 Regulates Bub1 Localization to Kinetochores. *Current Biology* 22, 900–906.
<https://doi.org/10.1016/j.cub.2012.03.052>
87. Long, A.F., Kuhn, J., Dumont, S., (2019). The mammalian kinetochore–microtubule interface: robust mechanics and computation with many microtubules. *Current Opinion in Cell Biology* 60, 60–67.
<https://doi.org/10.1016/j.ceb.2019.04.004>
88. Luo, X., Tang, Z., Rizo, J., Yu, H., n.d. (2002) The Mad2 Spindle Checkpoint Protein Undergoes Similar Major Conformational Changes Upon Binding to Either Mad1 or Cdc20. *Molecular Cell* 13.
89. Maciejowski, J., Drechsler, H., Grundner-Culemann, K., Ballister, E., Rodriguez-Rodriguez, J., Rodriguez-Bravo, V., Jones, M., Foley, E., Lampson, M., Daub, H., McAinsh, A. and Jallepalli, P. (2017). Mps1 Regulates Kinetochore-Microtubule Attachment Stability via the Ska Complex to Ensure Error-Free Chromosome Segregation. *Developmental Cell*, 41(2), pp.143-156.e6.
90. Magidson, V., He, J., Ault, J., O’Connell, C., Yang, N., Tikhonenko, I., McEwen, B., Sui, H. and Khodjakov, A. (2016). Unattached kinetochores rather than intrakinetochore tension arrest mitosis in taxol-treated cells. *The Journal of Cell Biology*, 212(3), pp.307-319.
91. Maiolica, A., Cittaro, D., Borsotti, D., Sennels, L., Ciferri, C., Tarricone, C., Musacchio, A., Rappsilber, J., (2007). Structural Analysis of Multiprotein Complexes by Cross-linking, Mass Spectrometry, and

Database Searching. *Molecular Cell Proteomics* 6, 2200–2211.

<https://doi.org/10.1074/mcp.M700274-MCP200>

92. Malvezzi, F., Litos, G., Schleiffer, A., Heuck, A., Mechtler, K., Clausen, T., Westermann, S., (2013). A structural basis for kinetochore recruitment of the Ndc80 complex via two distinct centromere receptors. *EMBO Journal* 32, 409–423.
<https://doi.org/10.1038/emboj.2012.356>
93. Maresca, T. and Salmon, E. (2009). Intrakinetochore stretch is associated with changes in kinetochore phosphorylation and spindle assembly checkpoint activity. *The Journal of Cell Biology*, 184(3), pp.373-381.
94. Maskell, D. P., Hu, X.-W. and Singleton, M. R. (2010) Molecular architecture and assembly of the yeast kinetochore MIND complex, *Journal of Cell Biology* 190(5):823-34
95. Maure, J.F., Komoto, S., Oku, Y., Mino, A., Pasqualato, S., Natsume, K., Clayton, L., Musacchio, A., Tanaka, T., U. (2011) The Ndc80 loop region facilitates formation of kinetochore attachment to the dynamic microtubule plus end. *Current Biology* 21: 207-213
96. McAinsh, A., Meraldi, P., Draviam, V., Toso, A. and Sorger, P., (2006). The human kinetochore proteins Nnf1R and Mcm21R are required for accurate chromosome segregation. *The EMBO Journal*, 25(17), pp.4033-4049.
97. McAinsh, A.D., Tytell, J.D., Sorger, P.K., (2003). Structure, Function, and Regulation of Budding Yeast Kinetochores. *Annual Reviews Cell Developmental Biology* 19, 519–539.
<https://doi.org/10.1146/annurev.cellbio.19.111301.155607>
98. McEwen, B., Heagle, A., Cassels, G., Buttle, K. and Rieder, C. (1997). Kinetochore Fiber Maturation in PtK1 Cells and Its Implications for the Mechanisms of Chromosome Congression and Anaphase Onset. *The Journal of Cell Biology*, 137(7), pp.1567-1580.
99. McIntosh, J. (2016). Mitosis. *Cold Spring Harbor Perspectives in Biology*, 8(9), p.a023218.
100. McIntosh, J., Grishchuk, E., Mophew, M., Efremov, A., Zhudenkov, K., Volkov, V., Cheeseman, I., Desai, A., Mastrorarde, D.

- and Ataullakhanov, F. (2008). Fibrils Connect Microtubule Tips with Kinetochores: A Mechanism to Couple Tubulin Dynamics to Chromosome Motion. *Cell*, 135(2), pp.322-333.
101. Miranda, J. J. L., De Wulf, P., Sorger, P. K. and Harrison, S. C. (2005). The yeast DASH complex forms closed rings on microtubules. *Nat. Struct. Mol. Biol.* 12, 138-143. doi:10.1038/nsmb896
102. Mitchison, T., Evans, L., Schulze, E. and Kirschner, M. (1986). Sites of microtubule assembly and disassembly in the mitotic spindle. *Cell* 45, 515-527.
103. Mora-Santos, M. del M., Hervás-Aguilar, A., Sewart, K., Lancaster, T.C., Meadows, J.C., Millar, J.B.A., (2016). Bub3-Bub1 Binding to Spc7/KNL1 Toggles the Spindle Checkpoint Switch by Licensing the Interaction of Bub1 with Mad1-Mad2. *Current Biology* 26, 2642–2650. <https://doi.org/10.1016/j.cub.2016.07.040>
104. Morin, V., Prieto, S., Melines, S., Hem, S., Rossignol, M., Lorca, T., Espeut, J., Morin, N., Abrieu, A., (2012). CDK-Dependent Potentiation of MPS1 Kinase Activity Is Essential to the Mitotic Checkpoint. *Current Biology* 22, 289–295. <https://doi.org/10.1016/j.cub.2011.12.048>
105. Mosalaganti, S., Keller, J., Altenfeld, A., Winzker, M., Rombaut, P., Saur, M., Petrovic, A., Wehenkel, A., Wohlgemuth, S., Müller, F., Maffini, S., Bange, T., Herzog, F., Waldmann, H., Raunser, S., Musacchio, A., (2017). Structure of the RZZ complex and molecular basis of its interaction with Spindly. *Journal of Cell Biology* 216, 961–981. <https://doi.org/10.1083/jcb.201611060>
106. Musacchio, A., Desai, A., (2017). A Molecular View of Kinetochores Assembly and Function. *Biology* 6, 5. <https://doi.org/10.3390/biology6010005>
107. Ng, C.T., Deng, L., Chen, C., Lim, H.H., Shi, J., Surana, U., Gan, L., (2019). Electron cryotomography analysis of Dam1C/DASH at the kinetochores–spindle interface in situ. *Journal of Cell Biology* 218, 455–473. <https://doi.org/10.1083/jcb.201809088>

108. Nicklas, R. and Koch, C., (1969). CHROMOSOME MICROMANIPULATION. *Journal of Cell Biology*, 43(1), pp.40-50.
109. Nicklas, R. B. (1988). The forces that move chromosomes in mitosis. *Annual Reviews in Biophysics and Biophysical Chemistry* 17, 431-449. doi:10.1146/annurev.bb.17.060188.002243
110. Nicklas, R., Ward, S. and Gorbsky, G., (1995). Kinetochore chemistry is sensitive to tension and may link mitotic forces to a cell cycle checkpoint. *Journal of Cell Biology*, 130(4), pp.929-939.
111. Nicklas, R.B., Arana, P., (1992). Evolution and the meaning of metaphase. *Journal of Cell Science* 10. 102 681-690.
112. Nijenhuis, W., Vallardi, G., Teixeira, A., Kops, G.J.P.L., Saurin, A.T., (2014). Negative feedback at kinetochores underlies a responsive spindle checkpoint signal. *Nature Cell Biology* 16, 1257–1264.
<https://doi.org/10.1038/ncb3065>
113. Nilsson, J. (2015) ‘Mps1-Ndc80: one interaction to rule them all’, *Oncotarget*, 6(19), pp. 16822–16823. doi: [10.18632/oncotarget.4837](https://doi.org/10.18632/oncotarget.4837).
114. Nishino, T., Rago, F., Hori, T., Tomii, K., Cheeseman, I.M., Fukagawa, T., (2013). CENP-T provides a structural platform for outer kinetochore assembly. *EMBO Journal* 32, 424–436.
<https://doi.org/10.1038/emboj.2012.348>
115. Nishino, T., Takeuchi, K., Gascoigne, K.E., Suzuki, A., Hori, T., Oyama, T., Morikawa, K., Cheeseman, I.M., Fukagawa, T., (2012). CENP-T-W-S-X Forms a Unique Centromeric Chromatin Structure with a Histone-like Fold. *Cell* 148, 487–501.
<https://doi.org/10.1016/j.cell.2011.11.061>
116. Nixon, F., Gutiérrez-Caballero, C., Hood, F., Booth, D., Prior, I. and Royle, S., (2015). The mesh is a network of microtubule connectors that stabilizes individual kinetochore fibers of the mitotic spindle. *eLife*, 4.
117. Nogales, E., Ramey, V.H. (2009) Structure-function insights into the yeast Dam1 kinetochore complex. *Journal of Cell Science* 122: 3831-3836

118. Obuse, C., Iwasaki, O., Kiyomitsu, T., Goshima, G., Toyoda, Y., Yanagida, M., (2004). A conserved Mis12 centromere complex is linked to heterochromatic HP1 and outer kinetochore protein Zwint-1. *Nature Cell Biology* 6, 1135–1141. <https://doi.org/10.1038/ncb1187>
119. Paweletz, N. (2001). Walther Flemming: pioneer of mitosis research. *Nature Reviews Molecular Cell Biology*, 2(1), pp.72-75.
120. Pekgöz Altunkaya, G., Malvezzi, F., Demianova, Z., Zimniak, T., Litos, G., Weissmann, F., Mechtler, K., Herzog, F., Westermann, S., (2016). CCAN Assembly Configures Composite Binding Interfaces to Promote Cross-Linking of Ndc80 Complexes at the Kinetochore. *Current Biology* 26, 2370–2378. <https://doi.org/10.1016/j.cub.2016.07.005>
121. Pentakota, S., Zhou, K., Smith, C., Maffini, S., Petrovic, A., Morgan, G., Weir, J., Vetter, I., Musacchio, A. and Luger, K., (2017). Decoding the centromeric nucleosome through CENP-N. *eLife*, 6.
122. Pesenti, M., Prumbaum, D., Auckland, P., Smith, C., Faesen, A., Petrovic, A., Erent, M., Maffini, S., Pentakota, S., Weir, J., Lin, Y., Raunser, S., McAinsh, A. and Musacchio, A., (2018). Reconstitution of a 26-Subunit Human Kinetochore Reveals Cooperative Microtubule Binding by CENP-OPQUR and NDC80. *Molecular Cell*, 71(6), pp.923-939.e10.
123. Pesenti, M., Weir, J. and Musacchio, A., (2016). Progress in the structural and functional characterization of kinetochores. *Current Opinion in Structural Biology*, 37, pp.152-163.
124. Petrovic, A. et al. (2010) 'The MIS12 complex is a protein interaction hub for outer kinetochore assembly', *Journal of Cell Biology*, 190(5), pp. 835–852. doi: [10.1083/jcb.201002070](https://doi.org/10.1083/jcb.201002070).
125. Petrovic, A. et al. (2014) 'Modular Assembly of RWD Domains on the Mis12 Complex Underlies Outer Kinetochore Organization', *Molecular Cell*, 53(4), pp. 591–605. doi: [10.1016/j.molcel.2014.01.019](https://doi.org/10.1016/j.molcel.2014.01.019).
126. Petrovic, A., Keller, J., Liu, Y., Overlack, K., John, J., Dimitrova, Y., Jenni, S., van Gerwen, S., Stege, P., Wohlgemuth, S., Rombaut, P.,

- Herzog, F., Harrison, S., Vetter, I. and Musacchio, A., (2016). Structure of the MIS12 Complex and Molecular Basis of Its Interaction with CENP-C at Human Kinetochores. *Cell*, 167(4), pp.1028-1040.e15.
127. Powers, A., Franck, A., Gestaut, D., Cooper, J., Graczyk, B., Wei, R., Wordeman, L., Davis, T. and Asbury, C. (2009). The Ndc80 Kinetochores Complex Forms Load-Bearing Attachments to Dynamic Microtubule Tips via Biased Diffusion. *Cell*, 136(5), pp.865-875.
128. Prendergast, L., Müller, S., Liu, Y., Huang, H., Dingli, F., Loew, D., Vassias, I., Patel, D., Sullivan, K. and Almouzni, G., (2016). The CENP-T/-W complex is a binding partner of the histone chaperone FACT. *Genes & Development*, 30(11), pp.1313-1326.
129. Primorac, I., Weir, J.R., Chiroli, E., Gross, F., Hoffmann, I., van Gerwen, S., Ciliberto, A., Musacchio, A., (2013). Bub3 reads phosphorylated MELT repeats to promote spindle assembly checkpoint signaling. *eLife* 2, e01030. <https://doi.org/10.7554/eLife.01030>
130. Rago, F., Gascoigne, K. E. and Cheeseman, I. M. (2015) 'Distinct Organization and Regulation of the Outer Kinetochores KMN Network Downstream of CENP-C and CENP-T', *Current Biology*, 25(5), pp. 671–677. doi: [10.1016/j.cub.2015.01.059](https://doi.org/10.1016/j.cub.2015.01.059).
131. Ran, F.A., Hsu, P.D., Wright, J., Agarwala, V., Scott, D.A., Zhang, F., (2013). Genome engineering using the CRISPR-Cas9 system. *Nature Protocols* 8, 2281–2308. <https://doi.org/10.1038/nprot.2013.143>
132. Renda, F., Magidson, V., Tikhonenko, I., Fisher, R., Miles, C., Mogilner, A., Khodjakov, A., (2020). Effects of malleable kinetochores morphology on measurements of intrakinetochores tension. *Open Biology* 10, 200101. <https://doi.org/10.1098/rsob.200101>
133. Rieder CL. (1982) The formation, structure, and composition of the mammalian kinetochores and kinetochores fiber. *International Review of Cytology* 1982;79:1-58. doi: 10.1016/s0074-7696(08)61672-1. PMID: 6185450.
134. Rieder, C.L., Schultz, A., Cole, R., Sluder, G., (1994). Anaphase onset in vertebrate somatic cells is controlled by a checkpoint that

- monitors sister kinetochore attachment to the spindle. *Journal of Cell Biology* 127, 1301–1310. <https://doi.org/10.1083/jcb.127.5.1301>
135. Rosenberg J.S., Cross F.R., Funabiki H. (2011). KNL1/Spc105 recruits PP1 to silence the spindle assembly checkpoint. *Current Biology* 21:942–947 [10.1016/j.cub.2011.04.011](https://doi.org/10.1016/j.cub.2011.04.011)
136. Santaguida, S., Tighe, A., D’Alise, A.M., Taylor, S.S., Musacchio, A., (2010). Dissecting the role of MPS1 in chromosome biorientation and the spindle checkpoint through the small molecule inhibitor reversine. *Journal of Cell Biology* 190, 73–87. <https://doi.org/10.1083/jcb.201001036>
137. Saurin, A.T., (2018). Kinase and Phosphatase Cross-Talk at the Kinetochore. *Frontiers in Cell Developmental Biology* 6, 62. <https://doi.org/10.3389/fcell.2018.00062>
138. Saurin, A.T., van der Waal, M.S., Medema, R.H., Lens, S.M.A., Kops, G.J.P.L., (2011). Aurora B potentiates Mps1 activation to ensure rapid checkpoint establishment at the onset of mitosis. *Nature Communications* 2, 316. <https://doi.org/10.1038/ncomms1319>
139. Scarborough, E.A., Davis, T.N., Asbury, C.L., (2019). Tight bending of the Ndc80 complex provides intrinsic regulation of its binding to microtubules. *eLife* 8, e44489. <https://doi.org/10.7554/eLife.44489>
140. Schmidt, J., Arthanari, H., Boeszoermenyi, A., Dashkevich, N., Wilson-Kubalek, E., Monnier, N., Markus, M., Oberer, M., Milligan, R., Bathe, M., Wagner, G., Grishchuk, E. and Cheeseman, I. (2012). The Kinetochore-Bound Ska1 Complex Tracks Depolymerizing Microtubules and Binds to Curved Protofilaments. *Developmental Cell*, 23(5), pp.968-980.
141. Screpanti, E., De Antoni, A., Alushin, G., Petrovic, A., Melis, T., Nogales, E. and Musacchio, A., (2011). Direct Binding of Cenp-C to the Mis12 Complex Joins the Inner and Outer Kinetochore. *Current Biology*, 21(5), pp.391-398.

142. Shepperd, L.A., Meadows, J.C., Sochaj, A.M., Lancaster, T.C., Zou, J., Buttrick, G.J., Rappsilber, J., Hardwick, K.G., Millar, J.B.A., (2012). Phosphodependent Recruitment of Bub1 and Bub3 to Spc7/KNL1 by Mph1 Kinase Maintains the Spindle Checkpoint. *Current Biology* 22, 891–899. <https://doi.org/10.1016/j.cub.2012.03.051>
143. Shepperd, L.A., Meadows, J.C., Sochaj, A.M., Lancaster, T.C., Zou, J., Buttrick, G.J., Rappsilber, J., Hardwick, K.G., Millar, J.B.A., (2012). Phosphodependent Recruitment of Bub1 and Bub3 to Spc7/KNL1 by Mph1 Kinase Maintains the Spindle Checkpoint. *Current Biology* 22, 891–899. <https://doi.org/10.1016/j.cub.2012.03.051>
144. Silió, V., McAinsh, A.D., Millar, J.B., (2015). KNL1-Bubs and RZZ Provide Two Separable Pathways for Checkpoint Activation at Human Kinetochores. *Developmental Cell* 35, 600–613. <https://doi.org/10.1016/j.devcel.2015.11.012>
145. Silió, V., McAinsh, A.D., Millar, J.B., (2015). KNL1-Bubs and RZZ Provide Two Separable Pathways for Checkpoint Activation at Human Kinetochores. *Developmental Cell* 35, 600–613. <https://doi.org/10.1016/j.devcel.2015.11.012>
146. Simon, J. R. and Salmon, E. D. (1990). The structure of microtubule ends during the elongation and shortening phases of dynamic instability examined by negative-stain electron microscopy. *Journal of Cell Science* 96, 571-582
147. Sivakumar, S., Janczyk, P.Ł., Qu, Q., Brautigam, C.A., Stukenberg, P.T., Yu, H., Gorbsky, G.J., (2016). The human SKA complex drives the metaphase-anaphase cell cycle transition by recruiting protein phosphatase 1 to kinetochores. *eLife* 5, e12902. <https://doi.org/10.7554/eLife.12902>
148. Smith, C., McAinsh, A. and Burroughs, N. (2016). Human kinetochores are swivel joints that mediate microtubule attachments. *eLife*, 5.
149. Stucke, VolkerM., Baumann, C., Nigg, ErichA., (2004). Kinetochores localization and microtubule interaction of the human

spindle checkpoint kinase Mps1. *Chromosoma* 113.

<https://doi.org/10.1007/s00412-004-0288-2>

150. Sudakin, V., Chan, G.K.T., Yen, T.J., (2001). Checkpoint inhibition of the APC/C in HeLa cells is mediated by a complex of BUBR1, BUB3, CDC20, and MAD2. *Journal of Cell Biology* 154, 925–936.
<https://doi.org/10.1083/jcb.200102093>
151. Sullivan, K.F., Hechenberger, M., Masri, K., (1994). Human CENP-A contains a histone H3 related histone fold domain that is required for targeting to the centromere. *Journal of Cell Biology* 127, 581–592.
<https://doi.org/10.1083/jcb.127.3.581>
152. Suzuki, A., Badger, B. and Salmon, E., (2015). A quantitative description of Ndc80 complex linkage to human kinetochores. *Nature Communications*, 6(1).
153. Suzuki, A., Long, S. and Salmon, E. (2018). An optimized method for 3D fluorescence co-localization applied to human kinetochore protein architecture. *eLife*, 7.
154. Takeuchi, K., Nishino, T., Mayanagi, K., Horikoshi, N., Osakabe, A., Tachiwana, H., Hori, T., Kurumizaka, H., Fukagawa, T., (2014). The centromeric nucleosome-like CENP–T–W–S–X complex induces positive supercoils into DNA. *Nucleic Acids Research* 42, 1644–1655.
<https://doi.org/10.1093/nar/gkt1124>
155. Theis, M., Slabicki, M., Junqueira, M., Paszkowski-Rogacz, M., Sontheimer, J., Kittler, R., Heninger, A., Glatter, T., Kruusmaa, K., Poser, I., Hyman, A., Pisabarro, M., Gstaiger, M., Aebersold, R., Shevchenko, A. and Buchholz, F. (2009). Comparative profiling identifies C13orf3 as a component of the Ska complex required for mammalian cell division. *The EMBO Journal*, 28(10), pp.1453-1465.
156. Tooley, J. and Stukenberg, P. T. (2011) ‘The Ndc80 complex: integrating the kinetochore’s many movements’, *Chromosome Research*, 19(3), pp. 377–391. doi: [10.1007/s10577-010-9180-5](https://doi.org/10.1007/s10577-010-9180-5).
157. Trazzi, S., Perini, G., Bernardoni, R., Zoli, M., Reese, J., Musacchio, A. and Valle, G., (2009). The C-Terminal Domain of CENP-C

Displays Multiple and Critical Functions for Mammalian Centromere Formation. *PLoS ONE*, 4(6), p.e5832.

158. Uhlmann, F., Wernic, D., Poupard, M.-A., Koonin, E.V., Nasmyth, K., (2000). Cleavage of Cohesin by the CD Clan Protease Separin Triggers Anaphase in Yeast. *Cell* 103, 375–386.
[https://doi.org/10.1016/S0092-8674\(00\)00130-6](https://doi.org/10.1016/S0092-8674(00)00130-6)
159. Umbreit, N. T., Miller, M. P., Tien, J. F., Cattin Ortolá, J., Gui, L., Lee, K. K., Biggins, S., Asbury, C. L. and Davis, T. N. (2014). Kinetochores require oligomerization of Dam1 complex to maintain microtubule attachments against tension and promote biorientation. *Nature Communications* 5, 4951. doi:10.1038/ncomms5951
160. Umbreit, N.T., Gestaut, D.R., Tien, J.F., Vollmar, B.S., Gonen, T., Asbury, C.L., Davis, T.N., (2012). The Ndc80 kinetochore complex directly modulates microtubule dynamics. *Proceedings of the National Academy of Sciences* 109, 16113–16118.
<https://doi.org/10.1073/pnas.1209615109>
161. Valverde, R., Ingram, J. and Harrison, S. (2016). Conserved Tetramer Junction in the Kinetochore Ndc80 Complex. *Cell Reports*, 17(8), pp.1915-1922.
162. Vleugel, M., Omerzu, M., Groenewold, V., Hadders, M.A., Lens, S.M.A., Kops, G.J.P.L., 2015. Sequential Multisite Phospho-Regulation of KNL1-BUB3 Interfaces at Mitotic Kinetochores. *Molecular Cell* 57, 824–835. <https://doi.org/10.1016/j.molcel.2014.12.036>
163. Volkov, V. A., Grissom, P. M., Arzhanik, V. K., Zaytsev, A. V., Renganathan, K., McClure-Begley, T., Old, W. M., Ahn, N. and McIntosh, J. R. (2015). Centromere protein F includes two sites that couple efficiently to depolymerizing microtubules. *Journal of Cell Biology* 209, 813-828. doi:10.1083/jcb.201408083
164. Wäldchen, F., Schlegel, J., Götz, R., Luciano, M., Schnermann, M., Doose, S., Sauer, M., (2020). Whole-cell imaging of plasma membrane receptors by 3D lattice light-sheet dSTORM. *Nature Communications* 11, 887. <https://doi.org/10.1038/s41467-020-14731-0>

165. Walstein, K., Petrovic, A., Pan, D., Hagemeyer, B., Vogt, D., Vetter, I. and Musacchio, A., (2020). Assembly principles and stoichiometry of a complete human kinetochore module. *BioRxiv*
166. Wan, X., O'Quinn, R., Pierce, H., Joglekar, A., Gall, W., DeLuca, J., Carroll, C., Liu, S., Yen, T., McEwen, B., Stukenberg, P., Desai, A. and Salmon, E. (2009). Protein Architecture of the Human Kinetochore Microtubule Attachment Site. *Cell*, 137(4), pp.672-684.
167. Wang, H.-W., Long, S., Ciferri, C., Westermann, S., Drubin, D., Barnes, G., Nogales, E., (2008). Architecture and Flexibility of the Yeast Ndc80 Kinetochore Complex. *Journal of Molecular Biology* 383, 894–903. <https://doi.org/10.1016/j.jmb.2008.08.077>
168. Wei, R., Al-Bassam, J. and Harrison, S. (2007). The Ndc80/HEC1 complex is a contact point for kinetochore-microtubule attachment. *Nature Structural & Molecular Biology*, 14(1), pp.54-59.
169. Wei, R., Sorger, P. and Harrison, S. (2005). Molecular organization of the Ndc80 complex, an essential kinetochore component. *Proceedings of the National Academy of Sciences*, 102(15), pp.5363-5367.
170. Welburn, J. P. I., Grishchuk, E. L., Backer, C. B., Wilson-Kubalek, E. M., Yates, J. R., 3rd. and Cheeseman, I. M. (2009). The human kinetochore Ska1 complex facilitates microtubule depolymerization-coupled motility. *Developmental Cell* 16, 374-385.
171. Westermann, S., Avila-Sakar, A., Wang, H.-W., Niederstrasser, H., Wong, J., Drubin, D. G., Nogales, E. and Barnes, G. (2005). Formation of a dynamic kinetochore- microtubule interface through assembly of the Dam1 ring complex. *Molecular Cell* 17, 277-290. doi:10.1016/j.molcel.2004.12.019
172. Wilson-Kubalek, E.M., Cheeseman, I.M., Yoshioka, C., Desai, A., Milligan, R.A., (2008). Orientation and structure of the Ndc80 complex on the microtubule lattice. *Journal of Cell Biology* 182, 1055–1061. <https://doi.org/10.1083/jcb.200804170>

173. Wimbish, R.T., DeLuca, K.F., Mick, J.E., Himes, J., Jiménez-Sánchez, I., Jeyaprakash, A.A., DeLuca, J.G., (2020). The Hec1/Ndc80 tail domain is required for force generation at kinetochores, but is dispensable for kinetochore–microtubule attachment formation and Ska complex recruitment. *MBoC* 31, 1453–1473.
<https://doi.org/10.1091/mbc.E20-05-0286>
174. Wordeman, L., Steuer, E., Sheetz, M. and Mitchison, T. (1991). Chemical subdomains within the kinetochore domain of isolated CHO mitotic chromosomes. *The Journal of Cell Biology*, 114(2), pp.285-294.
175. Wynne, D. and Funabiki, H., (2016). Heterogeneous architecture of vertebrate kinetochores revealed by three-dimensional superresolution fluorescence microscopy. *Molecular Biology of the Cell*, 27(22), pp.3395-3404.
176. Yamagishi, Y., Yang, CH., Tanno, Y. *et al.* MPS1/Mph1 phosphorylates the kinetochore protein KNL1/Spc7 to recruit SAC components. *Nature Cell Biology* **14**, 746–752 (2012).
<https://doi.org/10.1038/ncb2515>
177. Zaytsev, A.V., Mick, J.E., Maslennikov, E., Nikashin, B., DeLuca, J.G., Grishchuk, E.L., 2015. Multisite phosphorylation of the NDC80 complex gradually tunes its microtubule-binding affinity. *MBoC* 26, 1829–1844. <https://doi.org/10.1091/mbc.E14-11-1539>
178. Zhang, G., Kelstrup, C., Hu, X., Kaas Hansen, M., Singleton, M., Olsen, J. and Nilsson, J. (2012). The Ndc80 internal loop is required for recruitment of the Ska complex to establish end-on microtubule attachment to kinetochores. *Journal of Cell Science*, 125(13), pp.3243-3253.
179. Zhang, G., Kruse, T., Guasch Boldú, C., Garvanska, D.H., Coscia, F., Mann, M., Barisic, M., Nilsson, J., (2019). Efficient mitotic checkpoint signaling depends on integrated activities of Bub1 and the RZZ complex. *EMBO Journal* 38. <https://doi.org/10.15252/emj.2018100977>
180. Zhang, G., Lischetti, T., Nilsson, J., (2014). A minimal number of MELT repeats supports all the functions of KNL1 in chromosome

segregation. *Journal of Cell Science* 127, 871–884.

<https://doi.org/10.1242/jcs.139725>

181. Zhang, Q., Sivakumar, S., Chen, Y., Gao, H., Yang, L., Yuan, Z., Yu, H., Liu, H., (2017). Ska3 Phosphorylated by Cdk1 Binds Ndc80 and Recruits Ska to Kinetochores to Promote Mitotic Progression. *Current Biology* 27, 1477-1484.e4. <https://doi.org/10.1016/j.cub.2017.03.060>
182. Zhang, Z., Bellini, D. and Barford, D., (2020). Crystal structure of the Cenp-HIKHead-TW sub-module of the inner kinetochore CCAN complex. *Nucleic Acids Research*, 48(19), pp.11172-11184.